Delft University of Technology

Document Version
Final published version

Citation (APA)
ten Haaf, S. L. D. (2026). *Majoranas can be lonely: Engineering the Kitaev chain in a two-dimensional electron gas*. [Dissertation (TU Delft), Delft University of Technology]. https://doi.org/10.4233/uuid:fbf5ce51-595a-4ddf-b862-d6c71f1a016b

Important note
To cite this publication, please use the final published version (if applicable).
Please check the document version above.

Copyright
In case the licence states “Dutch Copyright Act (Article 25fa)”, this publication was made available Green Open Access via the TU Delft Institutional Repository pursuant to Dutch Copyright Act (Article 25fa, the Taverne amendment). This provision does not affect copyright ownership.
Unless copyright is transferred by contract or statute, it remains with the copyright holder.

Sharing and reuse
Other than for strictly personal use, it is not permitted to download, forward or distribute the text or part of it, without the consent of the author(s) and/or copyright holder(s), unless the work is under an open content license such as Creative Commons.

Takedown policy
Please contact us and provide details if you believe this document breaches copyrights.
We will remove access to the work immediately and investigate your claim.

This work is downloaded from Delft University of Technology.

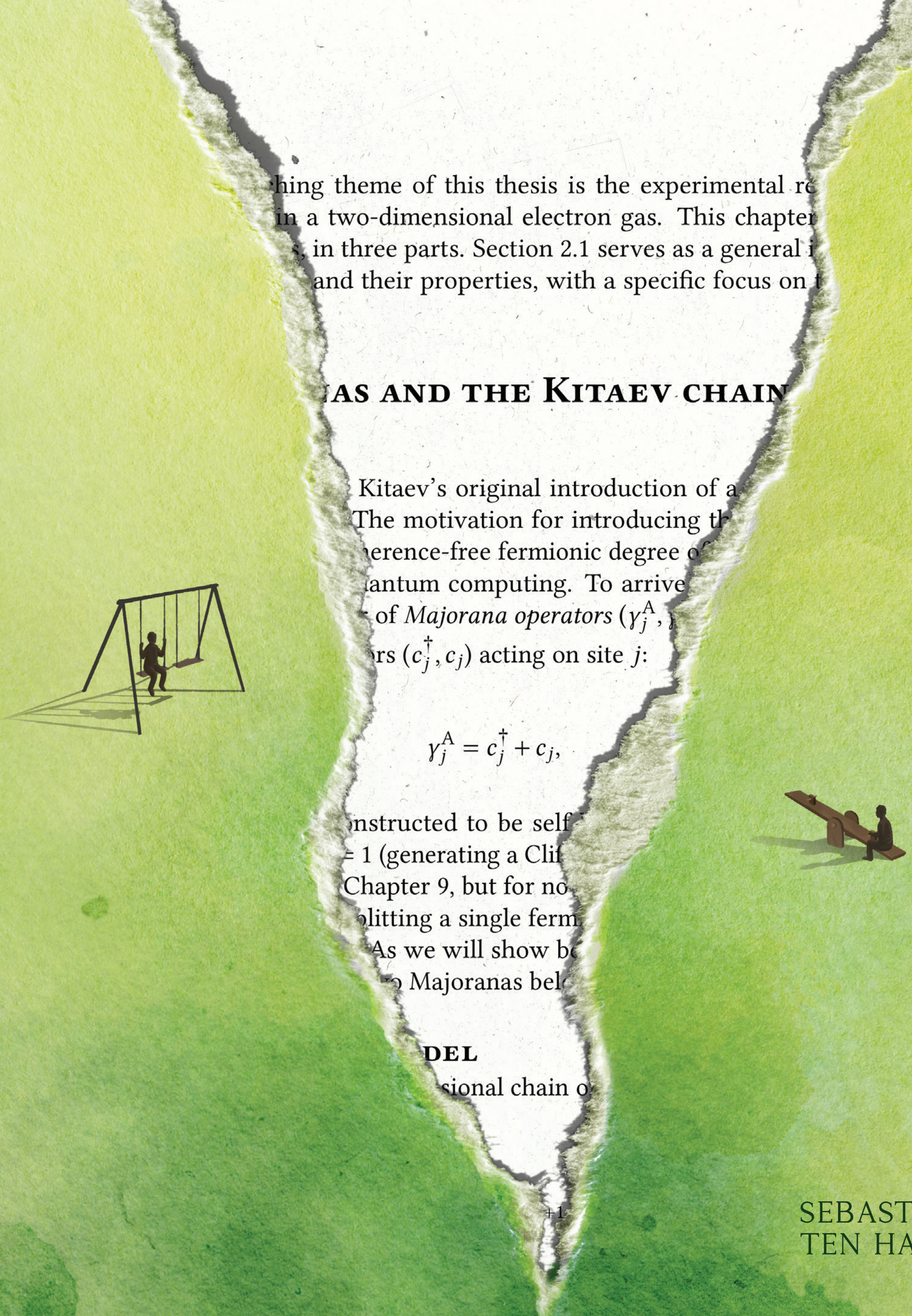
hing theme of this thesis is the experimental r
in a two-dimensional electron gas. This chapte
, in three parts. Section 2.1 serves as a general
and their properties, with a specific focus on
AS AND THE KITAEV CHAIN
Kitaev's original introduction of a
The motivation for introducing t
erence-free fermionic degree o
antum computing. To arrive
of Majorana operators (γ_j^A,
rs ($c_j^\dagger, c_j$) acting on site j:
$\gamma_j^A = c_j^\dagger + c_j,$
nstructed to be self
= 1 (generating a Cli
Chapter 9, but for no
litting a single ferm
As we will show b
Majoranas bel
DEL
sional chain o

SEBASTIAAN
TEN HAAF

Majoranas
can be
Lonely

MAJORANAS CAN BE LONELY

ENGINEERING THE KITAEV CHAIN IN A TWO-DIMENSIONAL ELECTRON GAS

MAJORANAS CAN BE LONELY

ENGINEERING THE KITAEV CHAIN IN A TWO-DIMENSIONAL ELECTRON GAS

Dissertation

for the purpose of obtaining the degree of doctor
at Delft University of Technology,
by the authority of the Rector Magnificus, Prof.dr.ir. H. Bijl,
chair of the Board for Doctorates,
to be defended publicly on
Friday 27th of March 2026 at 10:00 o' clock

by

Sebastiaan Laurens Daniël TEN HAAF

Master of Science in Physics,
Universiteit Leiden
born in Rijswijk, The Netherlands.

This dissertation has been approved by the promotors.

Composition of the doctoral committee:

Rector Magnificus,	Chairperson
Prof. dr. M.T. Wimmer,	Delft University of Technology, promotor
Dr. S. Goswami,	Delft University of Technology, copromotor
Independent members:	
Prof. dr. ir. L.P. Kouwenhoven,	Delft University of Technology
Prof. dr. J.A. Folk,	University of British Colombia, Canada
Prof. dr. K. Flensberg,	University of Copenhagen, Denmark
Prof. dr. C.W.J. Beenakker,	Leiden University
Prof. dr. ir. L.M.K. Vandersypen,	Delft University of Technology

Keywords: Two dimensional electron gas, quantum dots, superconductivity, Cooper pair splitting, Kitaev chain, Majorana zero modes

Printed by: ProefschriftMaken

Cover: *Life is better with friends*

Designed by Hester Lincke

Copyright © 2026 by S.L.D. ten Haaf
ISBN: 978-94-6384-897-8

An electronic version of this dissertation is available at `http://repository.tudelft.nl/`.

CONTENTS

Summary **ix**

Samenvatting **xi**

1 Introduction **1**

2 Theoretical background **7**
2.1 Majoranas and the Kitaev chain 8
2.1.1 Kitaev's toy model 8
2.1.2 Properties of the finite-size Kitaev chain 11
2.2 Building a Kitaev chain. 15
2.2.1 Sub-gap transport in a superconductor 16
2.2.2 Proximitized quantum dots. 17
2.2.3 Transport in a QD-ABS-QD junction 19
2.2.4 Approximating the Kitaev chain 24
2.3 Majorana Kramers pairs and Parafermions 27
2.3.1 Duality of the Kitaev chain and the Ising spin chain 28
2.3.2 The $\mathbb{Z}_n$ clock model 30
2.3.3 Poor man's Majorana Kramers pairs 31
2.3.4 Building a $\mathbb{Z}_3$-parafermion chain. 35

3 Experimental methods **41**
3.1 The experimental setup 42
3.1.1 Properties of InSbAs with epitaxial aluminium 42
3.1.2 Multi-terminal DC and AC measurements 43
3.1.3 Radio frequency lead reflectometry. 45
3.2 Characterising a QD-ABS-QD system 47
3.2.1 Forming a one-dimensional channel 48
3.2.2 Forming quantum dots 50
3.2.3 Superconductivity and Andreev bound states 53
3.2.4 RF charge-stability diagrams 55
3.2.5 Calibrating the QD-ABS coupling 56

4 Probing elastic co-tunneling and crossed Andreev reflection **59**
4.1 Introduction 60
4.2 Device and experimental set-up 61
4.3 Results 62
4.3.1 Signatures of ECT and CAR 62
4.3.2 Zero field spin blockade 63
4.3.3 Singlet and triplet ECT/CAR 65

4.4 Summary. 67
4.5 Discussion 67
4.6 Methods 68
4.7 Extended Data 69

5 Engineering a two-site Kitaev chain 77
5.1 Introduction 78
5.2 The Kitaev chain with strongly coupled dots 78
5.3 Device and measurement set-up 80
5.4 Results 80
  5.4.1 Tuning to the Majorana sweet spot. 80
  5.4.2 Estimating the Majorana polarisation 83
5.5 Discussion 85
5.6 Summary. 86
5.7 Methods 86
5.8 Extended Data 91

6 Majoranas at the edges of a three-site Kitaev chain 99
6.1 Introduction 100
6.2 The Kitaev model for a three-site QD chain 100
6.3 Device and experimental set-up 101
6.4 Results 102
  6.4.1 Tuning the two-site pairs. 102
  6.4.2 Phase control and probing the bulk excitation gap 103
  6.4.3 Shifting the Majorana wavefunctions. 104
  6.4.4 ZBPs outside the sweet spot 106
6.5 Summary. 107
6.6 Methods 108
6.7 Extended Data 115

7 The spinful Kitaev chain 127
7.1 Introduction 128
7.2 The spinful QD chain model 129
7.3 Device and experimental setup 129
7.4 Results 130
  7.4.1 The two-site sweet spot at zero field 130
  7.4.2 Naive scaling from two to three sites 132
  7.4.3 Superconducting phase control. 133
  7.4.4 Finetuned strong degeneracies 134
7.5 Summary. 136
7.6 Methods 137
7.7 Extended Data 141

8 Removing domain walls in longer chains 149
8.1 Introduction 150
8.2 The scaling protocol 150
8.3 Device and experimental setup 152

8.4 Results 152
8.4.1 Spin-induced phase shifts 152
8.4.2 ABS-induced phase shifts 154
8.4.3 Possible origin of smooth phase evolution 155
8.5 Discussion 156
8.6 Summary. 157
8.7 Methods 158
8.8 Extended Data 164

9 Outlook **173**
9.1 Scaling beyond short 1D chains 174
9.1.1 Tuning up a six-site chain 175
9.1.2 Spin-orbit interactions in 2D arrays 177
9.1.3 Hidden π-phase in a Kitaev T-junction 178
9.2 Non-abelian anyonic exchange of Majoranas 180
9.2.1 Gate-based braiding 181
9.3 Observing the fractional entropy of Majoranas 182

Acknowledgments **185**

A Numerical transport calculations **189**

B Topology in the Kitaev chain **193**

C Miscellaneous results **195**

Bibliography **201**

Curriculum Vitæ **221**

List of Publications **223**

SUMMARY

At a fundamental level, a fermionic excitation can be represented as two Majorana quasiparticles. Studying the properties of these Majoranas in isolation is of interest to a wide range of applications. From a theoretical perspective, they can be used to study the behaviour of particles that lie outside the typical boson-fermion classification: Majoranas are expected to exhibit non-abelian, anyonic exchange statistics. Practically, these properties could enable the construction of new types of intrinsically stable qubits and robust qubit operations, making Majoranas a potential building block for a topological quantum computer.

These compelling prospects have driven significant experimental efforts over the past decades. While the experimental realization of Majoranas has historically been challenging, recent advances have introduced techniques that allow for the reliable creation of these modes. Notably, the team of Leo Kouwenhoven in Delft pioneered an approach that combines quantum dots with superconductivity to construct a so-called Kitaev chain, providing a systematic method to isolate Majorana modes. In such chains, Majoranas are expected to localize at the edges, appearing as zero-energy excitations in tunneling spectroscopy measurements.

This thesis extends the development of these experimental techniques to a new material platform, with the goal of probing the fundamental properties of Majoranas. To do so, we implement a series of experiments demonstrating the construction of a Kitaev chain in an InSbAs two-dimensional electron gas. As first experiment, we couple two quantum dots to either side of a small semiconducting segment in proximity to a superconductor. In this setup, we demonstrate that elastic co-tunnelling and crossed Andreev reflection can be mediated by an Andreev bound state, that their relative amplitudes can be controlled and that spin-orbit interactions enable spin-triplet processes. Leveraging this system, we show that a minimal two-site Kitaev chain can be created, as evidenced by the study of zero-bias conductance features. Building on these results, we investigate extending the system to implement a three-site Kitaev chain. This allows us to show experimentally that the edges of the system, where Majoranas are expected to appear, have distinct properties from the middle of the system, demonstrating a key property of the Kitaev chain. The results in this thesis hope to provide a solid understanding for creating Majoranas in a two-dimensional system, opening up the path toward more complex configurations and the systematic exploration of Majorana physics.

SAMENVATTING

Op een fundamenteel niveau kan een fermionische excitatie worden weergegeven als twee Majorana quasideeltjes. Het bestuderen van de eigenschappen van deze Majorana's is van belang voor een breed scala aan toepassingen. Op theoretisch vlak kunnen zij worden gebruikt om het gedrag te onderzoeken van deeltjes die buiten de gebruikelijk boson of fermion classificatie vallen: Majorana's vertonen naar verwachting een niet-abelse, anyonische uitwisselingsstatistiek. Praktisch gezien kunnen deze eigenschappen de constructie van nieuwe typen stabiele qubits en robuuste qubit-operaties mogelijk maken. Dit maken Majorana's een potentiële bouwsteen voor een topologische kwantumcomputer.

Deze veelbelovende perspectieven hebben in de afgelopen decennia geleid tot aanzienlijke experimentele inspanningen. Hoewel de experimentele realisatie van Majorana's historisch gezien uitdagend is gebleken, hebben recente ontwikkelingen technieken geïntroduceerd die een betrouwbare creatie mogelijk maken. Met name de groep van Leo Kouwenhoven in Delft heeft een benadering ontwikkeld waarin kwantumstippen worden gecombineerd met supergeleiding om een zogeheten Kitaev-keten te construeren, wat een systematische methode biedt om Majorana's te isoleren. In dergelijke ketens worden Majorana's verwacht zich aan de randen te lokaliseren, waar zij verschijnen als excitaties met nul energie in spectroscopiemetingen.

Dit proefschrift breidt de ontwikkeling van deze experimentele technieken uit naar een nieuw materiaalplatform, met als doel de fundamentele eigenschappen van Majorana's te onderzoeken. Daartoe voeren wij een reeks experimenten uit bij cryogene temperaturen die de constructie van een Kitaev-keten in een InSbAs-tweedimensionaal elektrongas demonstreren. In het eerste experiment koppelen wij twee kwantumstippen aan weerszijden van een klein halfgeleidersegment dat zich in nabijheid van een supergeleider bevindt. In deze opstelling laten wij zien dat elastische co-tunneling en gekruiste Andreev-reflectie bemiddeld kunnen worden door een Andreev-gebonden toestand, dat hun relatieve amplituden controleerbaar zijn en dat spin-orbitaal-interacties spin-triplet processen mogelijk kunnen maken. Met dit systeem tonen wij aan dat een Kitaev-keten met twee roosterplaatsen kan worden gerealiseerd, wat blijkt uit de studie van geleidingskenmerken bij nul spanning. Voortbouwend op deze resultaten onderzoeken wij vervolgens hoe dit systeem kan worden opgeschaald naar een Kitaev-keten met drie roosterplaatsen. Dit stelt ons in staat om aan te tonen dat de randen van het systeem, waar Majorana's worden verwacht te verschijnen, andere eigenschappen vertonen dan het middelste gedeelte van de keten. Deze resultaten bieden een solide basis voor het creëren van Majorana's in een tweedimensionaal systeem en leggen een fundament voor het bestuderen van complexere configuraties en een systematische verkenning van Majorana-fysica.

1

INTRODUCTION

THE work presented in this thesis centres around an experimental study of the interaction between quantum dots and superconductors. The goal of this investigation is to trick electrons into revealing their Majorana nature and, as the title of this thesis suggests, demonstrate that these Majoranas can be unpaired, or *lonely*. One way to explain what this means and why this is interesting, can be: "Well, because Majoranas are non-Abelian anyonic quasiparticles, that can arise at the edges of one-dimensional topological p-wave superconductors."[1] This may be a sufficient answer for condensed matter physicists, but it is likely not a satisfying explanation in general (it certainly would not be to me four years ago!). To introduce the overarching goals of this thesis, we will therefore start from a more zoomed out point of view. The Majoranas in our context have a deep connection to the construction of a suitable quantum computing platform, which has been an exciting ongoing line of research over the past decades. Below, we will first discuss why there is a large effort towards building a quantum computer and why this is not an easy task. Next, we will discuss where Majoranas come into play and how they can offer a potential solution to the challenges in quantum computing. Finally, we detail the contents of this thesis and their relation to these broader research directions.

ORDINARY COMPUTERS AND ELECTRONS

In starting our introduction of quantum computing and Majoranas, it can be helpful to first mention a more familiar piece of equipment: the classical computer. Classical computers have advanced rapidly in complexity since their theoretical conception in the 1930's: today, even disposable devices like vape pens can run video games and send text messages. In a classical, *digital* computer, information is translated into a sequence of 0's and 1's and then transmitted as two different values in some physical signal. For example, such a signal can be created by sending a sequence of low (0) and high (1) voltages on an electrical wire, which carries the signal via the flow of electrons through the wire. This technique is reliable, because the interpretation of the signal is *digital*. When sending a '1' as a high-voltage signal, a small amount of noise in the signal will not hinder the ability to deduce that the signal was meant to represent a '1', even if the actual signal fluctuates.

---

[1] In a similar vain: "A monad is just a monoid in the category of endofunctors" [1].

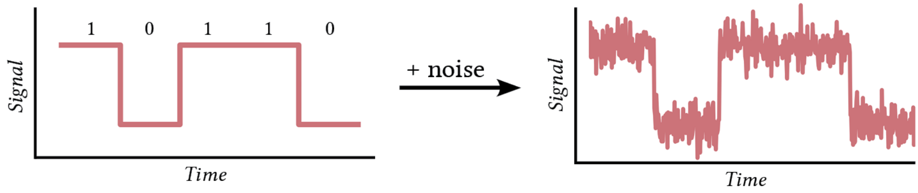

In a computer chip, these types of electrical signals are stored and handled with transistors: nanoscale objects that can be ‘on’ or ‘off’, like tiny light-switches. By combining millions of transistors in complex networks, such chips allow to implement basic operations whereby large amounts of information can be processed extremely fast. The digital implementation (among other reasons) allows this processing to be done very reliably - every calculation yields the same, deterministic outcome.

The computer has certainly made our lives easier in many facets and is very good at performing many types of calculations, such as deciding which pixels on your screen should be which colour. However, not every problem can be solved (efficiently) by a classical computer. Specific problems exist, which have been proven to not be solvable by classical computers in any reasonable time-frame, but which may be solvable by an entirely different approach [2–4]: using a quantum computer. One type of problem relates to the modelling of nature itself at a particle level, such as calculating the interactions between large collections of electrons. The behaviour of these particles is best described by the theory of quantum mechanics, which does not lend itself well to our classical computing power. The general idea is that a new type of computer that fundamentally uses quantum mechanics in its operation will be better suited to perform these calculations and can therefore solve specific problems that are inaccessible using a classical computer.

Why is quantum computing so hard?

Unlike classical computers, quantum computers at a basic level are not digital machines. Instead of relying on large-scale electrical signals involving trillions of electrons, quantum computers operate at the level of individual particles, for example by using individual electrons to store and manipulate information. This approach leverages the distinct behaviour of particles at the quantum scale, which differs markedly from the macroscopic world we are used to. At this scale, particles do not behave like billiard balls bouncing around, but rather have ‘wave-like’ properties. This means that particles interfere with each other, like waves merging with each other in an ocean as they collide. Furthermore, the particles can be in *superpositions* of possible states, rather than having single well-defined properties. As an example: electrons have a property called spin, which one can picture as a rotating arrow pointing ‘up’ (state 0) or ‘down’ (state 1). Counterintuitively, this property can behave as if the electron is pointing in both directions at the same time, or any combination in between. We say that it is in a superposition state, which we denote as $a|0\rangle + b|1\rangle$ (where a and b are complex values that satisfy $|a|^2 + |b|^2 = 1$). This system is an example of a *qubit*.

It is these properties of superposition and interference that can make a quantum computer more effective at solving specific problems compared to a classical computer. They allow for more complex ways to establish and evolve the information that we encode in these systems. Unfortunately, this comes with a big drawback: the calculations are also much more sensitive to errors. As we discussed above, a binary computer can get away with transmitting 5.1 volts instead of 5 volts to indicate a '1'; for a quantum computer this is not so simple. Quantum information is stored in a state that covers a continuous range of values. When using the spin of an electron to store information, tuning it accidentally to a state of $0.501|0\rangle+0.499|1\rangle$ instead of $0.5|0\rangle+0.5|1\rangle$ can have a real impact on the outcome of a calculation. Any useful calculation may require thousands to millions of qubits, all individually controlled to the highest precision to get a correct, reliable result. Meanwhile, errors arise due to interactions with the environment, or due to imperfections in the control signals that are used to steer the system. Ultimately, such an implementation of a quantum computer behaves more like an *analogue* machine, as opposed to a classical computer that runs on *digital* logic. In an analogue system, errors tend to accumulate and grow as a calculation grows in duration or complexity. This greatly complicates any attempt to scale such a system [5–7], not to mention the fact that things like trapping and manipulating electrons are not trivial tasks to begin with.

The goal in the past three decades has thus been to develop a platform that overcomes these fundamental challenges. To do so, there are a few actively pursued strategies:

1. Develop the quality of individual qubits and push the precision of control over operations to extremely high levels.
2. Detect and correct for errors when they happen through quantum error correction [8–10], somewhat analogous to Hamming codes in digital computers [11].
3. Store and manipulate quantum information in a way that does not suffer from the aforementioned errors to begin with.

The third point brings us a step closer to the central focus of this thesis. It may sound like an obvious strategy ("to overcome the errors, just make sure there are no errors"), but it is easier said than done. A realistic quantum system couples easily to its environment, which affects the quantum information stored in the system and causes errors. Creating a quantum system that is robust against such external factors is a key goal of *topological quantum computation* [12, 13], which leads us to the topics of Majoranas and Kitaev chains.

TOPOLOGY TO THE RESCUE?

Topology is a part of mathematics that studies properties of objects which do not change under certain specified deformations. It studies, for example, whether a given shape can be stretched or squeezed to become another shape. For instance, one can imagine deforming a football into a rugby ball[2], but turning a football into a swimming-tube would require tearing the football to create a hole. While these are clearly different deformations, it is challenging to determine what properties are retained in the first transformation, but not in the second transformation. Properties that are unchanged under deformations are called *invariants*, which allows for classifying objects that otherwise may seem hard to classify.

---

[2] Or as many kids will have heard: "Do not sit on the football, or it will become an egg."

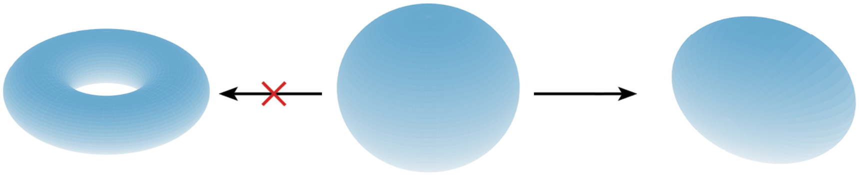

In analogy, in our context of quantum computing, it would be very helpful to have a quantum system that can be 'stretched' or 'squeezed' without changing the properties that represent the quantum information. It would be very desirable if one could for instance create a system of electrons where one does not need to worry about disruptions from the environment or from imperfections in the signals used to control the system. This is where topology enters the story - certain quantum systems were found to have stable, *topologically protected* features. These systems can similarly be classified by invariants, offering a more robust foundation for quantum computation. Connecting again to the above picture: if we prepare a quantum system with useful, invariant properties in the 'swimming-tube' state, we can be more certain that a noisy environment will not transform it into a 'football'-state by accident.

KITAEV CHAINS AND MAJORANAS

The topological system central to this thesis is called the Kitaev chain, after Alexei Kitaev who introduced the model and its properties [14]. The interest in this model arises from the finding that an electron can be described as a pair of *quasiparticles* called Majoranas. These are not particles in the real sense; the behaviour of a system of electrons and a system of Majorana pairs is in principle just two different ways to sketch the same problem. What Kitaev showed, however, is that exotic circumstances can be created under which Majorana pairs arranged in a chain can be restructured, such that two Majoranas are left over at the edges of the chain:

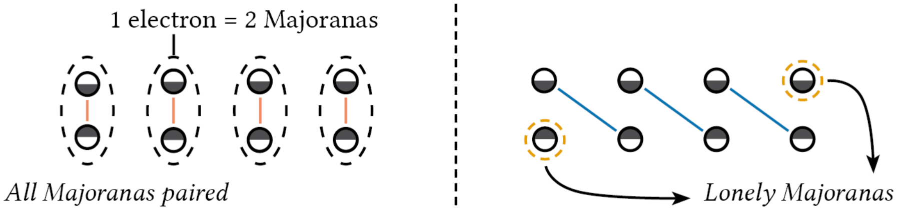

The consequences of this rearrangement turn out to be very significant: the leftover Majoranas at the ends only behave like a normal electron when they form a pair. Without forming a pair, they cannot couple to the environment: the system is said to be in a *topologically protected* state. This allows a system with unpaired Majoranas to store quantum information in a way that is protected from environmental noise. The further the two Majoranas are separated, the more stable the system becomes. Additionally, quantum information stored in this system can be reliably manipulated by exchanging the positions of two Majoranas [15], without relying on precise control signals. In theory, this can address the two major challenges in quantum computing mentioned above: the instability of encoded information and the errors introduced during manipulation. Topological quantum computing, therefore, aims to avoid analogue-like fragility by building a more ‘digital’, robust foundation.

The above is of course a very simplified sketch and creating this situation in an experimental system of electrons is not straightforward. The way we proceed this study experimentally, has undergone a great transformation in the past years. The field of Majorana research initially exploded with attention when proposals showed that the system proposed by Kitaev could in fact be build from ‘household’ materials [16, 17], by introducing a superconductor to a semiconductor nanowire and applying a large magnetic field. The relative simplicity of this approach and the promise that it held, spurred a great amount of activity on developing these ideas [18–20]. Initial observations were promising, suggesting that Majoranas could indeed by created in such systems. Reality, however, turned out more complicated than initially anticipated: disorder and impurities would lead to false positives, or even prevent the observation of Majoranas [21–24]. By 2020, it became clear that material disorder would be a major obstacle for topological quantum computing, leading to a decline in attention. This prompted a renewed focus on the original Kitaev model, with breakthroughs showing that non-Majorana states in a superconductor could be used to fine-tune key interactions between quantum dots [25–27]. In 2022, this led to the first experimental realization of a short Kitaev chain in a semiconductor nanowire in Delft [28].

Majoranas can be lonely

The first reliable implementation of a short Kitaev chain opened up the path to consider many new experiments that were previously inaccessible. This thesis builds on these techniques, to develop a system that enables the study fundamental predictions concerning Majoranas. In particular, we aim to show that unpaired Majoranas can indeed be isolated in space if all conditions imposed by the Kitaev chain model are met: we want to show that Majoranas can be lonely. To perform these experiments, we first extend the original techniques to a new material platform - an InSbAs two-dimensional electron gas - which offers more flexibility in the types of possible experiments that can be realized compared to the original one-dimensional nanowires. We build to the central experiment through the following chapters:

- Chapter 2 and Chapter 3 explore the theoretical background and detail the experimental building blocks used in this thesis.
- In Chapter 4, we use quantum dots on either side of a superconductor to study two important sub-gap processes mediated by Andreev bound states: crossed Andreev reflection and elastic co-tunneling.
- Chapter 5 shows that the processes studied in Chapter 4 can be used to create a minimal, two-site Kitaev chain, where clear signatures of Majoranas can be observed.

- Chapter 6 demonstrates the technique can be scaled to longer systems, by constructing a three-site Kitaev chain. Using this system, we show that the signatures of Majoranas appear localized at the edges of the chain. This marks the central result of this thesis.

Finally, we detail two experimental investigations that expand on the Kitaev chain model:

- In Chapter 7, we extend the experiments beyond the settings prescribed by the Kitaev model. Instead, we study what happens when the magnetic field is removed from the equation, which leads to a surprising connection to Majorana Kramers pairs and parafermions.
- Chapter 8 works towards future experiments by studying how the complex phases in a three-site Kitaev chain device are affected by intrinsic device properties. Using this, we study a proposal that would simplify scaling the developed systems to make longer chains.

To conclude, Chapter 9 highlights interesting future experiments that may be within reach via the experimental developments presented in this thesis.

2

THEORETICAL BACKGROUND

“Es steht alles schon bei Dedekind”

- Emmy Noether

The overarching theme of this thesis is the experimental realization of the Kitaev chain [14] in a two-dimensional electron gas. This chapter aims to introduce the relevant concepts, in three parts. Section 2.1 serves as a general introduction to Kitaev's model and Majoranas and their properties, with a specific focus on the properties of finite-length chains. Next, section 2.2 discusses the relevant ingredients for the specific experimental realization that is studied in this thesis: quantum dots coupled via superconductors. Finally, section 2.3 generalizes the concepts of the Kitaev chain to higher dimensional degeneracies. Each section serves to build a basic intuition for the experimental results, by studying the properties of a few simple fermionic Hamiltonians in the formalism of second quantization.

2.1 MAJORANAS AND THE KITAEV CHAIN

Below, we will follow Kitaev's original introduction of a toy model for topological superconductivity [14]. The motivation for introducing this system was the search for a way to generate a decoherence-free fermionic degree of freedom, as a platform for intrinsically fault-tolerant quantum computing. To arrive there, we utilize the fact that it is possible to define a pair of *Majorana operators* ($\gamma_j^{\mathrm{A}}, \gamma_j^{\mathrm{B}}$) from a pair of fermionic creation and annihilation operators ($c_j^\dagger, c_j$) acting on site j:

$$\gamma_j^{\mathrm{A}} = c_j^\dagger + c_j, \qquad \gamma_j^{\mathrm{B}} = \frac{c_j^\dagger - c_j}{i} \tag{2.1}$$

Such operators are constructed to be self-hermitian ($\gamma^\dagger = \gamma$) and satisfy the relations $\{\gamma_j, \gamma_k\} = 2\delta_{jk}$ and $\gamma^2 = 1$ (generating a Clifford algebra). We will go over the consequences of these properties in Chapter 9, but for now the rewriting of the fermionic operators has no immediate effect - splitting a single fermion into two Majoranas on a single site is just a basis transformation. As we will show below, the interesting physics arises if one can create a fermion out of two Majoranas belonging to different fermionic sites.

2.1.1 KITAEV'S TOY MODEL

Kitaev introduced a one-dimensional chain of N spinless fermionic sites with two nearest neighbour coupling terms:

$$H_{\mathrm{kitaev}} = \sum_{j=1}^{N} \mu_j c_j^\dagger c_j + \sum_{j=1}^{N-1} (t_j c_j^\dagger c_{j+1} + t_j^* c_{j+1}^\dagger c_i) + \sum_{j=1}^{N-1} (\Delta_j c_j^\dagger c_{j+1}^\dagger - \Delta_j^* c_i c_{j+1}) \tag{2.2}$$

Here, μ_j denotes the chemical potential energy of site j. Two neighbouring sites interact via two mechanisms: a hopping term with amplitude t_j and an effective superconducting pairing term with amplitude Δ_j. In general t_j and Δ_j can be complex values. Due to the pairing term, which creates or destroys particles in pairs, the total particle number is not conserved (U(1) symmetry is broken). Instead, the conserved quantity of interest is the fermionic parity[1], which takes just two values corresponding to an even or odd parity.

---

[1] Fermionic parity is determined by the parity operator $\hat{P} = (-1)^{\hat{N}}$ with $\hat{N} = \sum_{j=1}^{N} c_j^\dagger c_j$. This quantity is conserved, corresponding to the remaining $\mathbb{Z}_2$ symmetry in the system.

The utility of the Hamiltonian in equation (2.2) becomes apparent when writing each fermionic operator as the sum of two Majorana operators, by applying the inverse transformation of equation (2.1) for each set of fermionic operators:

$$c_j^\dagger = \frac{1}{2}(\gamma_j^{\mathrm{A}} - i\gamma_j^{\mathrm{B}}), \qquad c_j = \frac{1}{2}(\gamma_j^{\mathrm{A}} + i\gamma_j^{\mathrm{B}}) \tag{2.3}$$

In this new basis, equation (2.2) becomes:

$$H_{\mathrm{kitaev}} = -i\sum_{j=1}^{N}\mu_j\gamma_j^{\mathrm{A}}\gamma_j^{\mathrm{B}} + i\sum_{j=1}^{N-1}(t_j-\Delta_j)\gamma_j^{\mathrm{A}}\gamma_{j+1}^{\mathrm{B}} + i\sum_{j=1}^{N-1}(t_j+\Delta_j)\gamma_j^{\mathrm{B}}\gamma_{j+1}^{\mathrm{A}} \tag{2.4}$$

where the nearest-neighbour couplings now correspond to bilinear terms of Majorana operators from neighbouring sites. To illustrate the effect of this transformation, it is helpful to consider a schematic representation of this change of basis (figure 2.1):

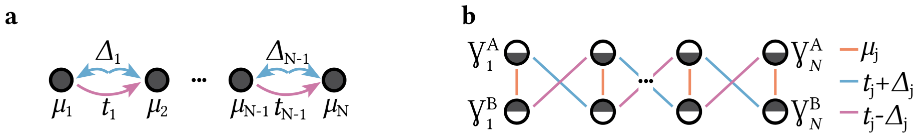

Figure 2.1: **Schematic representations of the Kitaev chain. (a)** Representation of the fermionic Hamiltonian in equation (2.2), where each circle represents a fermionic site with chemical potential μ_i. **(b)** Representation of the rewritten Hamiltonian in the Majorana basis (Equation (2.4)), where each site is now represented by two Majorana operators ($\gamma_j^{\mathrm{A}}, \gamma_j^{\mathrm{B}}$). Lines represent a non-zero term that couples the connected Majorana operators.

So far, the Hamiltonian has just been rewritten in terms of the new Majorana operators. The interesting physics arises when considering two different limits. In the first, trivial limit, we turn off the nearest-neighbour couplings ($t_j = \Delta_j = 0$) and leave only the on-site energy μ_j, which yields:

$$H_{\mathrm{kitaev}} = -i\sum_{j=1}^{N}\mu_j\gamma_j^{\mathrm{A}}\gamma_j^{\mathrm{B}} \qquad (\mu_j \neq 0 \quad t_j = \Delta_j = 0) \tag{2.5}$$

In this limit, Majoranas from the same original site are paired (illustrated in figure 2.2a), leaving just a chain of uncoupled sites. The second, more interesting limit, occurs when setting $\mu_j = 0$ and turning on the coupling terms $t_j = \Delta_j \neq 0$, resulting in:

$$H_{\mathrm{kitaev}} = i\sum_{j=1}^{N-1}2t_j\gamma_j^{\mathrm{B}}\gamma_{j+1}^{\mathrm{A}} \qquad (\mu_j = 0 \quad t_j = \Delta_j \neq 0) \tag{2.6}$$

Now, only a coupling between Majoranas from neighbouring sites remains, illustrated in figure 2.2b. Crucially, this leaves two Majoranas at the edge of the chain unpaired. The Majorana operators γ_1^{A} and γ_N^{B} at opposite ends of the chain have dropped out of the Hamiltonian completely, so that $\left[H_{\mathrm{kitaev}}, \gamma_1^{\mathrm{A}}\right] = \left[H_{\mathrm{kitaev}}, \gamma_N^{\mathrm{B}}\right] = 0$. In combination with the fact that a Majorana operator flips the fermionic parity of the system, commuting with the Hamiltonian enforces that the unpaired Majoranas act as zero-energy excitations that map between the even and odd eigenstates. Indeed, the presence of unpaired Majoranas goes hand-in-hand with a two-fold degeneracy of the odd and even-parity sectors in the fermionic language. This ground state degeneracy allows for the construction of a non-local fermionic excitation from the unpaired Majoranas:

$$c^\dagger_{\mathrm{non-local}} = \frac{1}{2}(\gamma_1^{\mathrm{A}} - i\gamma_N^{\mathrm{B}}), \qquad c_{\mathrm{non-local}} = \frac{1}{2}(\gamma_1^{\mathrm{A}} + i\gamma_N^{\mathrm{B}}) \tag{2.7}$$

This is precisely what Kitaev was after: a non-local fermionic degree of freedom arises, manifested as a zero-energy excitation between two degenerate ground states. Critically, the zero-energy excitation is protected from local perturbations on μ_j or t_j, Δ_j. Any perturbation involving γ_1^{A} or γ_N^{B} alone is unrealistic, since these operators do not conserve fermionic parity. Nor can they be removed through coupling to any of the other Majoranas, which all pair up to form fermionic excitations with energy $2t$. The only possible perturbation is a term $\propto i\gamma_1^{\mathrm{A}}\gamma_N^{\mathrm{B}}$, which is inherently non-local.

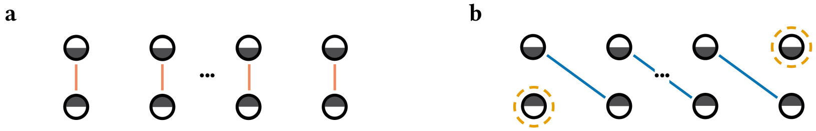

Figure 2.2: **Schematic representations of two different limits of the Kitaev chain**. **(a)** When $\mu_j \neq 0$ and $t_j = \Delta_j = 0$, Majoranas belonging to the same site couple to form ordinary local fermions. **(b)** When $\mu_j = 0$ and $t_j = \Delta_j \neq 0$, each Majorana couples to a neighbouring partner leaving two Majoranas unpaired at either end of the chain. The unpaired Majoranas form a non-local fermionic excitation.

The above discussion focusses on the special point $t_j = \Delta_j$, $\mu_j = 0$, where it is easy to see in the schematic above how unpaired Majoranas arise at the edges of the chain. What makes the Kitaev chain particularly interesting, is that the parameter space where Majorana edge modes are present forms a large continuous phase when the number of sites $N \to \infty$. In this limit, a phase transition takes place when going from $|\mu| > |2t|$, where no Majoranas are present, to $|\mu| < |2t|$, where Majoranas are always present at the edge. This is an example of a *topological* phase transition. How and why topology enters the discussion is treated seperately in appendix B, but the aspects that are of experimental interest should be clear:

1. The ability to create a non-local fermionic degree of freedom.

2. Independent of finetuned microscopic parameters or external perturbations.

Notably, the circumstances giving rise to unpaired Majoranas in equation (2.6) do not depend on the number of sites in the chain. In fact, the analysis holds even if $N = 2$, which is sufficient to create Majoranas with some minimal degree of protection to perturbations. This is best introduced by exploring the spectral properties of the finite-size Kitaev chain, central to the experimental investigations in Chapters 5 and 6.

2.1.2 Properties of the finite-size Kitaev chain

While the infinite Kitaev chain hosts robust Majorana zero modes at its edges, real devices are inevitably finite. In this thesis we study the extreme case of chains with only two or three sites. This raises a natural question: do such minimal systems host Majorana edge modes, and if so, how do they hold up against external perturbations? To examine this, we set for convenience all parameters in the Kitaev chain (equation (2.2)) to be real and set all terms of the same type to be equal along the chain ($t_j = t$, $\Delta_j = \Delta$, $\mu_j = \mu$ for all $j \in [1, N]$). An exact solution can then be obtained for the parameters that allow for zero-energy excitations [29][2]:

$$\mu = 2\sqrt{t^2 - \Delta^2}\cos\left(\frac{n\pi}{N+1}\right) \qquad n = 1, \ldots, N \tag{2.8}$$

For fixed Δ and N, this corresponds to a series of $N/2$ hyperbolic solutions in the μ vs t-plane (figure 2.3).

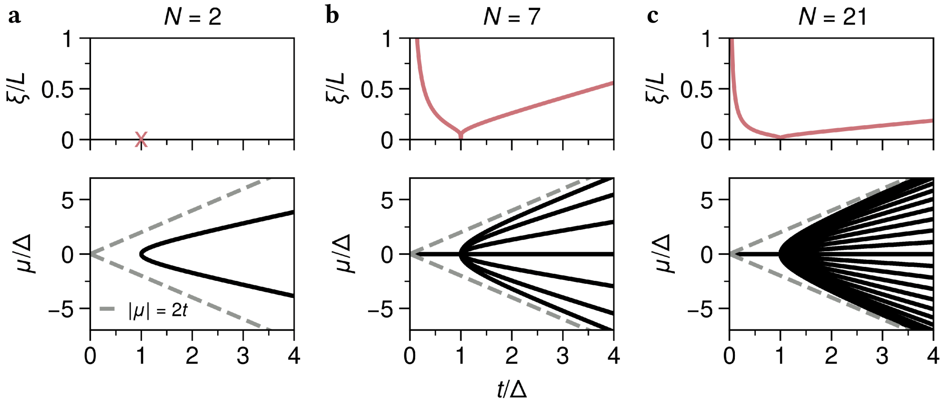

Figure 2.3: **Majorana solutions of the Kitaev chain for varying N.** Bottom row: solutions to equation (2.8) as a function of μ and t, for a fixed pairing interaction Δ. Top row: the corresponding localisation length ξ for the solutions along $\mu = 0$, relative to the length of the chain L. The solutions are shown for **(a)** $N = 2$, **(b)** $N = 7$ and **(c)** $N = 21$. Dashed gray lines indicate the topological phase boundary that forms when $N \to \infty$ (see appendix B).

Each solution corresponds to parameter values where the Hamiltonian admits zero-energy excitations, which can be constructed from a pair of Majorana operators that combine into a non-local fermion. For large N, the entire region inside $|\mu| = 2t$ forms a continuous solution, referred to as a topological phase in the previous section. The important differentiating factor between the discrete solutions is the amount of overlap between the Majorana wavefunctions. To capture this difference, we show the localisation length ξ of the Majorana wavefunctions, which can be derived exactly for the solution along $\mu = 0$ [29]:

$$\xi/L = 2\left|\ln^{-1}\left(\frac{|t/\Delta - 1|}{t/\Delta + 1}\right)\right| \tag{2.9}$$

---

[2] The solution uses the fact that the Kitaev chain in the Majorana basis can be written as two coupled SSH chains - a 1D topological insulator introduced as effective model for polyacetylene [30, 31].

The localisation length captures how quickly the wavefunctions of the Majoranas decay to zero ($\propto e^{-\xi/L}$) as one moves away from the outermost sites, where L is the length of the chain aN with a the lattice spacing. Notably, at the point $t = \Delta$, $\mu = 0$ the Majorana wavefunctions are perfectly localized on the outermost sites, regardless of the number of sites in the chain. As discussed in section 2.1.1, if a perturbation does not directly couple the two unpaired Majoranas, they are resilient against the perturbation. We therefore refer to the configuration where the Majoranas are maximally separated as the 'sweet spot', as they are maximally robust against local perturbations.

Outside of the sweet spot, there will be a finite overlap between Majoranas on opposite ends of the chain, due to their finite localisation length. This overlap means that perturbations in μ can directly affect the zero-energy modes. We can see the effect of this by numerically calculating the full excitation spectra of the system. In the many-body basis, this corresponds to the expectation values of adding a hole or electron on site j to the ground-state $|\phi^{\mathrm{gs}}_{e,o}\rangle$ and ending up in a higher energy state $|\phi_{e,o}\rangle$ in the opposite parity sector. The energy of such a transition E_{T} is equal to the energy difference between the ground state $E^{gs}_{o,e}$ and the excited state $E_{e,o}$.

$$E_{\mathrm{T}} = |E^{\mathrm{gs}}_{o,e} - E_{e,o}| \qquad w_{\mathrm{T}} = |\langle \Phi_{o,e}| c_j^{\dagger} |\Phi^{\mathrm{gs}}_{e,o}\rangle|^2, |\langle \Phi_{o,e}| c_j |\Phi^{\mathrm{gs}}_{e,o}\rangle|^2 \tag{2.10}$$

The result for different N and different ratios of t/Δ is shown in figure 2.4, where all excitations with non-zero probability amplitude w_{T} are shown. Hole excitations correspond to a negative E_{T}. For full details of the numerical transport calculations we refer to appendix A. The Majorana solutions appear naturally at $E_{\mathrm{T}} = 0$.

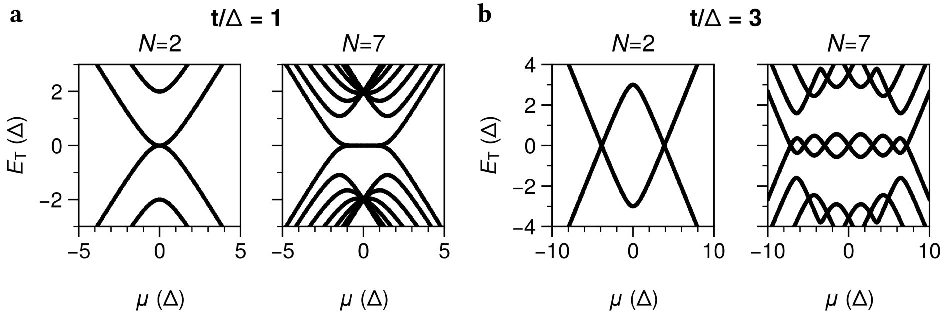

Figure 2.4: **Low-energy spectra as a function of μ.** In the finite-size Kitaev chain, the 'robustness' of the Majorana modes can be captured by their response to detuning μ. **(a)** When $t/\Delta = 1$, the smallest possible chain (N=2) shows a quadratic dispersion of the zero-energy excitations with μ. Extending the chain increases this protection to a higher-order polynomial. **(b)** When $t/\Delta \neq 1$, perturbing μ always results in an immediate linear splitting, due to finite overlap of the Majoranas. For larger N this leads to oscillations around zero-energy, which evolve again into a constant zero-energy plateau in the limit $N \to \infty$. These oscillations are also known as 'finite size oscillations' [32].

When $t = \Delta$, zero-energy excitations persist when detuning μ over a region that grows with N (figure 2.4a). In contrast, when $t \neq \Delta$, detuning μ results in an immediate linear splitting (figure 2.4b), as a consequence of the finite overlap of the Majorana edge modes.

Summarizing the key properties of the finite-length Kitaev chain:

- For general parameters, the number of Majorana solutions grows linearly with N, evolving into a topological phase within $|\mu| = 2t$ as $N \to \infty$.
- For any N, a sweet-spot exists at $t = \Delta \neq 0$, $\mu = 0$, where two unpaired Majoranas are perfectly localised on the outermost sites.
- The protection of the Majoranas against detuning μ grows as N increases.

The perfect localisation of the Majoranas at the 'sweet spot' for any N is what makes it worthwhile to experimentally consider studying shorter chains. To conclude, we turn to the simplest non-trivial case of $N = 2$.

THE TWO-SITE KITAEV CHAIN: POOR MAN'S MAJORANAS

The smallest possible Kitaev chain of two sites was first explored by Leijnse and Flensberg [33]. In this work, they coined the phrase "Poor Man's Majoranas" (PMMs), to stress that there are no *topologically* protected Majoranas in this small system. Nevertheless there is a degree of protection, as long as one can prevent creating a coupling between the unpaired Majoranas. Additionally, the system provides a simple playground to go over some important concepts in more detail.

With only two sites, the Kitaev chain Hamiltonian (equation (2.2)) is:

$$H_{\text{PMM}} = \mu_1 c_1^\dagger c_1 + \mu_2 c_2^\dagger c_2 + (t c_1^\dagger c_2 + t^* c_2^\dagger c_1) + (\Delta c_1^\dagger c_2^\dagger + \Delta^* c_1 c_2) \tag{2.11}$$

In the many-body basis $\{|00\rangle, |11\rangle, |10\rangle, |01\rangle\}$ this can be written in matrix form:

$$H_{\text{PMM}} = \begin{bmatrix} 0 & \Delta & & \\ \Delta^* & \mu_1 + \mu_2 & & \\ & & \mu_1 & t \\ & & t^* & \mu_2 \end{bmatrix} \tag{2.12}$$

The block-diagonal structure follows directly from the fact that there are two independent parity sectors. Diagonalizing each block individually gives two eigenvalues per sector:

$$E^{\pm}_{\text{even}} = (\mu_1 + \mu_2)/2 \pm \sqrt{(\mu_1 + \mu_2)^2/4 + \Delta^2} \quad E^{\pm}_{\text{odd}} = (\mu_1 + \mu_2)/2 \pm \sqrt{(\mu_1 - \mu_2)^2/4 + t^2} \tag{2.13}$$

The global ground state corresponds to the lowest energy between E^-_{odd} and E^-_{even}. Since exciting the system with a single electron results in a transition between parity sectors, the quantity of interest is the difference between even and odd eigenvalues. Majorana excitations flip the parity of the system and additionally have zero energy, so that they will arise whenever there is a ground state degeneracy. This requires $E^-_{\text{odd}} = E^-_{\text{even}}$, leading to the degeneracy condition $\mu_1\mu_2 = t^2 - \Delta^2$. From the degeneracy condition, we can see that perturbing either μ_1 or μ_2 from the sweet spot ($t = \Delta$, $\mu_1 = \mu_2 = 0$) maintains the ground state degeneracy. On the other hand, perturbing both μ_1 and μ_2 simultaneously or detuning away from $t = \Delta$ does *not* maintain the degeneracy. Excitation spectra as a function of these perturbations are shown in figure 2.5, demonstrating the robustness of this minimal system.

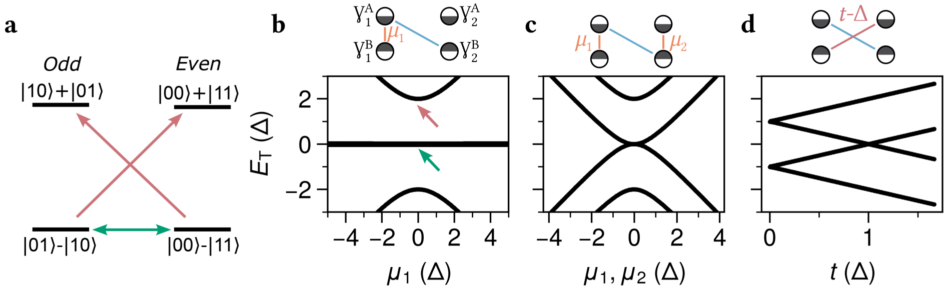

Figure 2.5: **Perturbations in the two-site Kitaev chain.** Numerically calculated energy spectra for various deviations from the two-site sweet spot. **(a)** Energy level diagram at the sweet spot, showing possible single-electron transitions between the odd and even parity sector (omitting pre-factors). **(b)** Detuning a single chemical potential does not couple the two Majoranas - a zero energy excitation remains in the system. **(c)** Finite overlap is only created when detuning both chemical potential energies, resulting in the lowest energy excitation splitting in energy quadratically. **(d)** Detuning away from the $t = \Delta$ point creates a direct coupling, which results in an immediate linear splitting.

Invoking the schematics of the Majorana basis from figure 2.1 provides a second, intuitive way to see which perturbations will preserve the zero-energy excitations. When detuning μ_1 for instance (figure 2.5b), a connection is created between three Majoranas (γ_1^A, γ_1^B and γ_2^B), while γ_2^A remains unpaired. Any coupling terms connecting an odd number of Majorana operators necessarily leave a zero-energy excitation in the system[3]. Only additionally detuning μ_2 in the above example gives rise to a finite energy splitting (figure 2.5c), since an even number of Majoranas becomes connected. In contrast, detuning the nearest neighbour couplings such that $t \neq \Delta$ result in an immediate linear splitting $\propto |t - \Delta|$ (figure 2.5d). This can be understood from the fact that γ_1^B and γ_2^A are directly coupled by such a deviation. Notably, this is already avoided by extending the chain to three sites [34].

At the $\mu = 0, t = \Delta$ sweet spot, we have the following eigenvectors:

$$|\text{even}, \pm\rangle = \frac{1}{\sqrt{2}}(|00\rangle \pm |11\rangle), \qquad |\text{odd}, \pm\rangle = \frac{1}{\sqrt{2}}(|01\rangle \pm |10\rangle) \tag{2.14}$$

Here, it is straightforward to confirm the action of an unpaired Majorana operator on the ground states:

$$\gamma_1^B|\text{even}, -\rangle = |\text{odd}, -\rangle \qquad \gamma_1^B|\text{odd}, -\rangle = |\text{even}, -\rangle \tag{2.15}$$

The excited states $|\text{even}, +\rangle$ and $|\text{odd}, +\rangle$ are also degenerate at the sweet spot, and the Majorana operators will similarly map between these states. A system where every subspace is N-fold degenerate is called *strongly degenerate*, the significance of which will be further explored in section 2.3. First, we will discuss how the above system may be created experimentally.

---

[3] This arises from particle-hole symmetry imposing that the energies in the excitation spectrum are symmetric around zero (invariant under mapping all $E \to -E$). When an odd number of Majoranas is connected, at least one eigenvalue will remain unpaired, which can therefore only have a value of 0.

2.2 Building a Kitaev chain

So far, we have considered Kitaev's model at the theoretical level. The next topic of interest is the experimental realization of the system. As discussed in Chapter 1, initial proposals focussed primarily on combinations of bulk materials that would approach the Kitaev chain in the thermodynamic limit. Disorder in the materials and their interfaces has so far complicated such approaches, motivating a shift to bottom-up strategies where the system is assembled site by site, with direct control over the relevant parameters. There, the aim is to directly implement and control all the parameters in Kitaev's original Hamiltonian. In this section we will build up the intuition for the components that underlie the experimental work in this thesis, which consists of arrays of quantum dots and superconductors (figure 2.6).

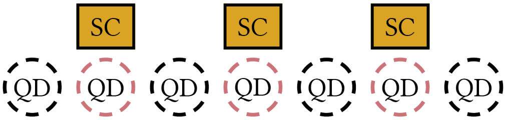

Figure 2.6: **The Kitaev chain as an array of normal and proximitized quantum dots.** To construct the Kitaev chain experimentally, a chain of spin-polarised quantum dots is alternated with quantum dots strongly tunnel-coupled to a superconductor. These additional, *proximitized* quantum dots can effectively facilitate the nearest neighbour t and Δ couplings, which will be detailed in this section. In the limit of large E_z, U, this system can approximate the Kitaev chain [35, 36]. Limitations of the approximation are discussed in section 2.2.4.

The goal of this section is to detail how the building blocks in figure 2.6 can be used to engineer an effectively spinless system with nearest-neighbour hopping and pairing interactions. Already pointed out early on [33, 37, 38], quantum dots (QDs) are a natural candidate to consider for implementing a spinless fermionic chain. QDs can be constructed by creating a confining potential in a semiconductor through electrostatic gating, and are readily spin-polarised by an external magnetic field. For the purposes of this section, we will treat quantum dots as a single spinful fermionic site with possible occupations $\{|0\rangle, |\downarrow\rangle, |\uparrow\rangle, |2\rangle\}$, where the doubly occupied $|2\rangle$ state is the spin-singlet state $\frac{1}{\sqrt{2}}(|\uparrow\downarrow\rangle$-$|\downarrow\uparrow\rangle)$, as enforced by Pauli exclusion. The Hamiltonian description then includes a chemical potential energy μ, a charging energy U and the Zeeman energy E_z:

$$H_\mathrm{QD} = U c_\downarrow^\dagger c_\uparrow^\dagger c_\downarrow c_\uparrow + (\mu - E_\mathrm{z}) c_\downarrow^\dagger c_\downarrow + (\mu + E_\mathrm{z}) c_\uparrow^\dagger c_\uparrow \tag{2.16}$$

The Zeeman energy $E_z = \frac{1}{2} g \mu_B |B|$ depends on the strength of an external magnetic field B, the Bohr Magneton μ_B and the g-factor, which is a material specific property (such experimental details will be treated in Chapter 3). The role of U is to penalize the presence of two electrons in the quantum dot, while the Zeeman energy favours the $|\downarrow\rangle$ occupation. In the limit of large U and large E_z, the QD has a degeneracy between $|0\rangle$ and $|\downarrow\rangle$ occupation at $\mu = E_z$. The QD then reduces to an effective two-level system spanned by $\{|0\rangle,|\downarrow\rangle\}$ so that the system is effectively spinless, fulfilling a first requirement for building the Kitaev chain. The remaining challenge is implementing the t and Δ hopping and pairing interactions.

To do so, we introduce two processes that occur when introducing a superconductor between two electron reservoirs.

2.2.1 SUB-GAP TRANSPORT IN A SUPERCONDUCTOR

In conventional superconductors at low temperatures, electron-phonon interactions can induce an attractive interaction between electrons. This results in the formation of Cooper pairs, correlated pairs of electrons that can travel through the superconductor coherently without dissipation [39]. When this happens, a particle-hole symmetric energy gap (Δ_{SC}) opens around the Fermi energy E_{F} and the ground state is formed by a condensate of Cooper pairs. Typically, electrons are paired with opposite spin and their combined state has net zero momentum. Such superconductors are called *s-wave*, referring to the symmetry of the momentum component of their Cooper pair wavefunctions. In contrast, the Kitaev chain includes *p-wave* superconductivity, where pairing occurs between same-spin electrons. In that case, the orbital symmetry of the Cooper pair wavefunction must be odd, corresponding to a p-wave momentum component. The lowest energy single electron excitations (typically called quasiparticles) lie at the superconducting gap edge Δ_{SC}, where the quasiparticle density of states diverges. As a result, regular single-electron transport from a metal or a quantum dot into a superconductor is blocked for electrons with energies below Δ_{SC}, as there are no states available for an electron to tunnel into. Nevertheless, single electron transport can be facilitated by higher-order mechanisms, referred to as sub-gap processes.

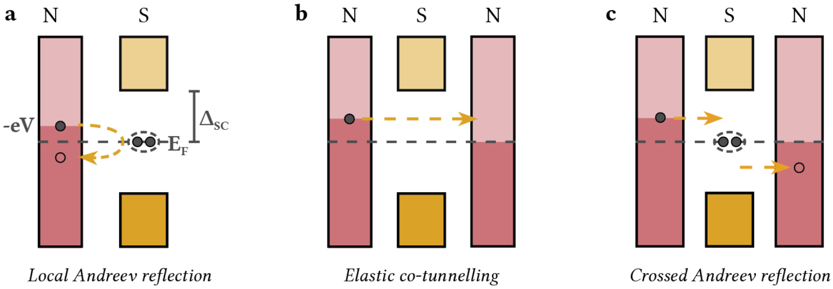

Figure 2.7: **Sub-gap transport processes in a superconductor (S) coupled to electron reservoirs (N). (a)** An incoming electron is reflected as a hole, transferring a Cooper pair to the superconductor. **(b)** An electron virtually tunnel across the superconductor to an opposing lead. **(c)** An electron is transmitted as a hole into an opposing lead, again transferring a Cooper pair to the superconductor.

Three important processes are depicted in the energy level diagrams in figure 2.7. In this so-called semiconductor picture, the metal is represented as a continuum of filled states up to energy $-eV$ with respect to the Fermi level, where V is an applied voltage bias. The superconductor is described by an energy gap around E_{F}, with occupied quasiparticle states below $-\Delta_{\mathrm{SC}}$ and unoccupied states above Δ_{SC}. At energies below $|\Delta_{\mathrm{SC}}|$, electrons can only enter the superconductor in pairs. In local Andreev reflection, an incoming electron at energy E gets retroreflected as a hole with energy $-E$, with opposite spin and momentum [40]. This process effectively transfers two electrons to the superconductor, creating a Cooper pair. Repeated Andreev reflections off of a second superconductor interface results in a special type of confined state known as an Andreev bound state (ABS) [41–44]. Adding a second reservoir enables two additional sub-gap processes. First, an electron can tunnel through the superconductor without breaking a Cooper pair: it virtually occupies a quasiparticle state above the gap and reappears in the opposite lead with the same spin and energy. This process is known as elastic co-tunneling (ECT); inelastic tunneling is in principle possible but strongly suppressed at energies below the superconducting gap. Second, the incoming electron can be converted into a hole in the opposite lead, while a Cooper pair is deposited into the superconductor. This non-local analogue of Andreev reflection is called crossed Andreev reflection (CAR).

The geometry with two reservoirs coupled to a superconductor has been studied extensively in the context of Cooper pair splitting [45–49]. In this process, the roles are reversed: a Cooper pair in the superconductor is split into two spatially separated electrons, one entering each metallic lead. To explore this experimentally, quantum dots are typically placed between the reservoirs and the superconductor. The QDs can act as charge and spin filters [50, 51], allowing fine control over the injection of electrons into the superconductor, which we will exploit in Chapter 4. The large charging energy of quantum dots ($U \gg \Delta_{\mathrm{SC}}$) in such a set-up suppresses local Andreev reflection, since a retroreflected hole would require the doubly occupied state which is energetically unfavourable. This leaves CAR and ECT as the dominant sub-gap processes - precisely the pairing and hopping interactions required to emulate the Kitaev chain. However, mediating these processes with a superconductor raises three challenges in this context:

- Spin mismatch: in an s-wave superconductor, Cooper pairs are opposite-spin, while the Kitaev chain requires an equal-spin coupling.
- Geometric limitations: the strength of CAR and ECT is limited by the superconducting coherence length and the overlap of the quasiparticle states with both QDs.
- Control: there is no straightforward independent way to tune the relative amplitudes of the CAR and ECT processes, which is required for the ($t = \Delta$) sweet spot[4].

A key development to overcome these issues was the realization that an Andreev bound state in the superconductor can mediate effective interactions with greater tunability [25], providing a practical route to implement Kitaev's Hamiltonian. To see this, we introduce first a simple model describing a quantum dot strongly coupled to a superconductor.

2.2.2 PROXIMITIZED QUANTUM DOTS

To obtain a simple description of a quantum dot in proximity to a superconductor, we invoke the *superconducting atomic limit* [52, 53]. In this approximation, the presence of the superconductor is included solely as an effective pairing term with strength Γ_{S}, reflecting the possible transfer of two electrons into/from the superconductor as a Cooper pair:

$$H_{\mathrm{ABS}} = H_{\mathrm{QD}} + \Gamma_{\mathrm{S}} c_{\downarrow}^{\dagger} c_{\uparrow}^{\dagger} - \Gamma_{\mathrm{S}}^{*} c_{\downarrow} c_{\uparrow} \tag{2.17}$$

---

[4] Ref. [33] proposes to use non-collinear fields to polarise the two QDs along different axis, but this is not so trivial to implement experimentally.

This extra term couples the empty state $|0\rangle$ and the doubly-occupied state $|2\rangle$. In the basis $\{|0\rangle, |2\rangle, |\uparrow\rangle, |\downarrow\rangle\}$, the Hamiltonian takes the matrix form:

$$H_{\text{ABS}} = \begin{bmatrix} 0 & \Gamma_S & & \\ \Gamma_S^* & 2\mu + U & & \\ & & \mu - E_z & 0 \\ & & 0 & \mu + E_z \end{bmatrix} \tag{2.18}$$

The even parity ground state is a spin-singlet state of the form $|S\rangle$ = $u|0\rangle$ - $v|2\rangle$, typically called a BCS-singlet (see section 2.2.4). The odd parity states are the spin-doublet states $|D\rangle$ = $|\downarrow\rangle$,$|\uparrow\rangle$, which are degenerate in the absence of a magnetic field ($E_z = 0$). The interplay of charging energy and a superconducting pairing leads to a competition between these odd- and even-parity states. Normally, the charging energy of the quantum dots favours odd occupancy, whereas the superconducting term favours an even occupancy. Depending on μ and the ratio Γ_S/U, the ground state parity can switch between these regimes. This competition produces the phase diagram shown in figure 2.8a.

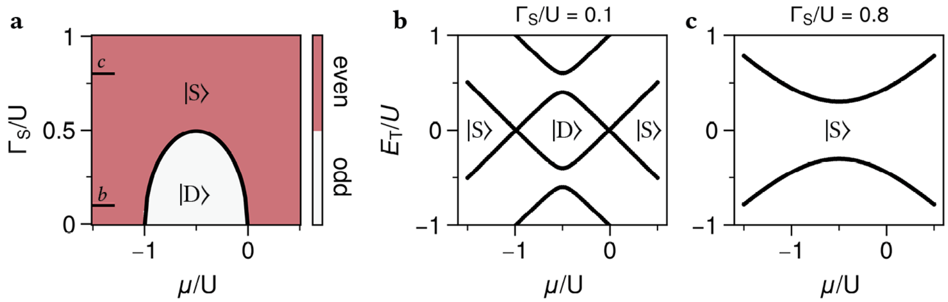

Figure 2.8: **Singlet to doublet transition in a proximitized QD.** **(a)** Phase diagram of H_{ABS} ($E_z = 0$), showing the parity of the ground state as a function of μ/U and Γ_S/U. **(b)** Excitation spectrum as a function of μ, for Γ_S/U=0.1. Two ground state parity transitions occur, driven by μ. **(c)** Excitation spectrum as a function of μ, for Γ_S/U=0.8. The system remains in the singlet ground state and the excitations do not cross zero-energy.

In this phase diagram, two distinct regimes can be identified where the ground-state is either the singlet or the doublet state. Figures 2.8b,c show excitation spectra for two cuts across the phase diagram, at different ratios of Γ_S/U. When the quantum dot is weakly coupled to the superconductor, tuning μ drives a singlet-doublet-singlet transition, signified by two zero-energy crossings. In the strong coupling limit, the system remains in the singlet ground state and no zero-energy crossing occurs. The sub-gap excitations in this limit are typically called Andreev bound states, like the confined states arising in an S-N-S geometry described in the previous section. The properties of this system and the singlet-doublet transitions are experimentally very well understood [51, 54–58].

For our purpose, the interest lies in quasiparticle excitations of the Andreev bound state, which can be smoothly tuned from being electron-like to hole-like without crossing any degeneracy point. Diagonalizing equation (2.18), the eigenvalues of the singlet and doublet states are:

$$E_S = (\mu + U/2) \pm \sqrt{(\mu + U/2)^2 + \Gamma_S^2} \qquad E_D = \mu \pm E_z \tag{2.19}$$

and the coherence factors of the singlet state $|S\rangle = u|0\rangle - v|2\rangle$ are:

$$u^2 = \frac{1}{2}\left(1 + \frac{\mu + U/2}{\sqrt{(\mu + U/2)^2 + \Gamma_{\mathrm{S}}^2}}\right), \qquad v^2 = 1 - u^2 \tag{2.20}$$

When $u = 1$, the ground state is the empty state and transport into the ABS is dominated by electrons. In the opposite limit where $v = 1$, the ground-state is the double occupied state and transport is dominated by holes. When $u = v$, hole-transport and electron-transport are equally likely and the Andreev bound state is said to be charge-neutral. As we will show below, this tunability is central to understanding how proximitized dots mediate CAR and ECT.

2.2.3 TRANSPORT IN A QD-ABS-QD JUNCTION

We now revisit the ECT and CAR transport processes introduced in section 2.2.1, this time replacing the bulk superconductor with a strongly proximitized quantum dot as described above. In the limit $\Gamma_{\mathrm{S}} > U$, the ground-state of the proximitized dot is the BCS-type singlet, given by equation (2.19) and equation (2.20). We want to find the possibility of transferring electrons via CAR and ECT between two quantum dots tunnel-coupled to either side of the proximitized quantum dot. The full Hamiltonian of the system is:

$$H = H_{\mathrm{QD}}^{l} + H_{\mathrm{ABS}}^{m} + H_{\mathrm{QD}}^{r} + \hat{V} \tag{2.21}$$

where $\hat{V}$ is the tunneling term coupling the left and right quantum dots to the proximitized dot in the middle. Assuming for now that spin is conserved when tunnelling from the left to the middle site (t_L), and from the middle to the right site (t_R), the coupling term is given by:

$$\hat{V} = t_L(c_{\mathrm{m},\downarrow}^{\dagger} c_{\mathrm{l},\downarrow} + c_{m,\uparrow}^{\dagger} c_{l,\uparrow}) + t_R(c_{m,\downarrow}^{\dagger} c_{r,\downarrow} + c_{m,\uparrow}^{\dagger} c_{r,\uparrow}) + h.c. \tag{2.22}$$

Direct tunnelling into the proximitized quantum dot requires matching the excitation energy $E_{\mathrm{ABS}} = E_{\mathrm{D}} - E_{\mathrm{S}}$ (equation (2.19)). When the energy of the quantum dots (μ_{QD}) is lower than E_{ABS}, instead a virtual excitation can take place, and the process must be completed by a second tunneling event returning the system to its ground state. The rates for both ECT and CAR can then be calculated by invoking Fermi's golden rule, for going from an initial state $|i\rangle$ to an equal energy final state $|f\rangle$ via a higher energy intermediate state $|m\rangle$:

$$W_{i\to f} = \frac{2\pi}{\hbar}\sum_{m}\left|\frac{\langle f|\hat{V}|m\rangle\langle m|\hat{V}|i\rangle}{E_m - E_i}\right|^2 \delta(E_i - E_f) \tag{2.23}$$

where E_i, E_m and E_f are the energies of the initial, intermediate and final states. Since the ground state of the strongly proximitized QD is always the singlet $|S\rangle$, the sum over the intermediate state only needs to account for the two possible excited doublet states ($|m\rangle$=$|\downarrow\rangle$,$|\uparrow\rangle$). The difference between CAR and ECT lies then in the initial and final states. For CAR, the quantum dots are each initially occupied with an opposite spin electron and end in the empty state, having created a Cooper pair (or reversed). For ECT, the left (or right) quantum dot is initialized with an electron, that ends on the opposite side. One of two possible transport cycles for each processes is illustrated in figure 2.9a,b.

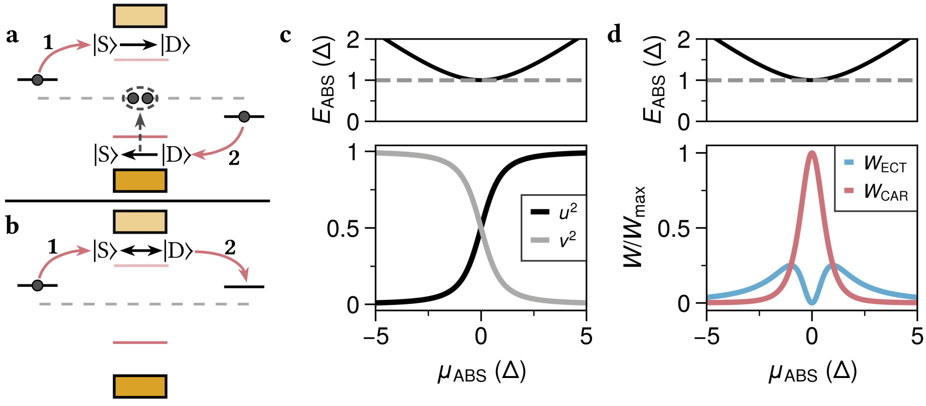

Figure 2.9: **Elastic co-tunneling and crossed Andreev reflection mediated by an Andreev bound state. (a)** Possible transport cycle for crossed Andreev reflection. **(b)** Possible transport cycle for elastic co-tunnelling. **(c)** Coherence factors of the $|S_{-}\rangle$ ground state $|u|^2$ and $|v|^2$, as a function of μ_{ABS}. The $\mu_{\mathrm{ABS}} = 0$ is taken as the point where E_{ABS} reaches its minimum. **(d)** Rates of CAR and ECT as a function of μ_{ABS} (equation (2.24)).

Plugging in equation (2.23) yields the key result of this section: the rates of CAR and ECT mediated by a proximitized quantum dot[5]:

$$W_{\mathrm{CAR}} \propto t_L^2 t_R^2 \left| \frac{2uv}{E_{\mathrm{ABS}}} \right|^2 \qquad W_{\mathrm{ECT}} \propto t_L^2 t_R^2 \left| \frac{u^2 - v^2}{E_{\mathrm{ABS}}} \right|^2 \tag{2.24}$$

The important thing to note, is that the rates of CAR and ECT depend differently on the coherence factors u and v of the Andreev bound state [25]. Both processes have two possible transport paths, either starting from a hole-like excitation of the Andreev bound state or an electron-like excitation. For CAR, these two paths interfere constructively such that its rate is proportional to $uv + uv$. For ECT on the other hand, its two possible transport paths interfere destructively, resulting in the proportionality to $u^2 - v^2$. The rates of the two processes as a function of μ_{ABS} are plotted in figure 2.9d, where u, v and E_{ABS} are inserted into equation (2.24) from equation (2.20) and (2.19). When $u = v$, W_{ECT} drops to zero while W_{CAR} reaches a maximum. On the other hand, when $u \ll v$ or $u \gg v$, W_{ECT} is always larger than the W_{CAR}. This behaviour guarantees that a point exists along μ_{ABS} where $W_{\mathrm{CAR}} = W_{\mathrm{ECT}}$, bringing us a step closer to the Kitaev chain sweet spot condition.

This connection between rates of CAR and ECT and the energy/charge of an Andreev bound state has been studied extensively and an extremely close correspondence was obtained between the theoretical behaviour in figure 2.9d and experiment [60]. For the purposes of the Kitaev chain, however, we have neglected a crucial detail. Since spin is conserved in $\hat{V}$, CAR only couples quantum dots with opposite spin while ECT couples quantum dots with the same spin. Thus, while the ABS provides a natural mediator of CAR and ECT, the spin selectivity currently imposed by $\hat{V}$ means that additional ingredients are required to realize the spinless effective Kitaev chain.

---

[5] See [25, 59] for full details of the calculation.

Adding spin-orbit coupling and magnetic field

In semiconductors with large atomic numbers, electrons experience a strong electric field generated by the heavy nuclei. For a moving electron, this is equivalent to a magnetic field $\vec{B}_{\mathrm{SO}}$ that lies perpendicular to the electric field and the momentum of the electron ($\vec{k}\times\vec{E}$). This magnetic field interacts with the electron's spin in a process known as spin-orbit coupling (SOC) [61–63]. Under spatially symmetric circumstances, the net effect averages out and does not produce significant spin-precession. Hence, symmetry must be broken to see the effect. Two distinct types are typically relevant in conventional semiconductor quantum wells (i.e. InAs, InSb, GaAs). In Dresselhaul SOC [64, 65], the effective field arises from intrinsic asymmetry of the crystal lattice (bulk-inversion asymmetry). In Rashba SOC, captured by a coefficient α_{SO}, symmetry is broken by structural factors, such as an applied external electric field [66]. In two-dimensional electron gases the external electric fields are generally applied perpendicular to the 2D quantum wells, so that the Rashba field lies in-plane. This will be the most relevant to the devices studied in this thesis.

In the context of the QD-ABS-QD system, SOC can affect transport in two distinct ways. Firstly, the eigenstates of the QDs themselves are affected, as SOC can couple spin-states from different orbitals in the QDs [67–70]. Secondly, an electron tunneling between different sites can experience spin-precession due to its motion in the effective Rashba field. Since we only include a single orbital in the analysis, we will not consider the former effect here. Regarding the latter, we consider the progression of the spin expectation value for an electron travelling in the xy-plane (perpendicular to the external electric field). The evolution of a spin aligned with angle ϕ_s with respect to the x-axis, and travelling at an angle θ over a distance r, is given by [71]:

$$\langle\vec{S}\rangle_r = \begin{pmatrix}\langle S_x\rangle_r\\ \langle S_y\rangle_r\end{pmatrix} = \begin{pmatrix}\cos\phi_s\cos^2(\Delta\theta/2)-\cos(2\theta-\phi_s)\sin^2(\Delta\theta/2)\\ \sin\phi_s\cos^2(\Delta\theta/2)-\sin(2\theta-\phi_s)\sin^2(\Delta\theta/2)\end{pmatrix} \tag{2.25}$$

Here $\Delta\theta(r)$ captures the angle of precession over a distance r. For Rashba spin orbit coupling, this is given by $\Delta\theta(r) = 2m^*\alpha_{\mathrm{SO}}r/\hbar^2$ [72], generally giving rise to a 'windshield wiper' spin precession shown in figure 2.10. The amount of precession with respect to the original spin alignment $\hat{n}$ can be projected to a 'spin-preserving' probability t_{n} and a 'spin-flipping' probability t_{so}:

$$|t_n|^2 = \left(\frac{1+\langle\vec{S}\rangle_r\cdot\hat{n}}{2}\right) \qquad |t_{\mathrm{so}}|^2 = \left(\frac{1-\langle\vec{S}\rangle_r\cdot\hat{n}}{2}\right) \tag{2.26}$$

This effect can be directly included in the calculations of CAR and ECT rates, by adapting the tunnelling term $\hat{V}$ in equation (2.22). Assuming that we can enforce a specific spin-orientation in the QDs, by applying an external magnetic field B_{ext}, an electron tunneling between sites now has a possibility of undergoing a spin-preserving process or a spin-flipping process:

$$\begin{aligned}\hat{V} = {} & t_{\mathrm{n}}(c^\dagger_{\mathrm{m},\downarrow}c_{\mathrm{l},\downarrow} + c^\dagger_{m,\uparrow}c_{l,\uparrow}) + t_n(c^\dagger_{m,\downarrow}c_{r,\downarrow} + c^\dagger_{m,\uparrow}c_{r,\uparrow}) + h.c.\\ & + t_{\mathrm{so}}(c^\dagger_{\mathrm{m},\downarrow}c_{\mathrm{l},\uparrow} + c^\dagger_{m,\uparrow}c_{l,\downarrow}) + t_{\mathrm{so}}(c^\dagger_{m,\downarrow}c_{r,\uparrow} + c^\dagger_{m,\uparrow}c_{r,\downarrow}) + h.c.\end{aligned} \tag{2.27}$$

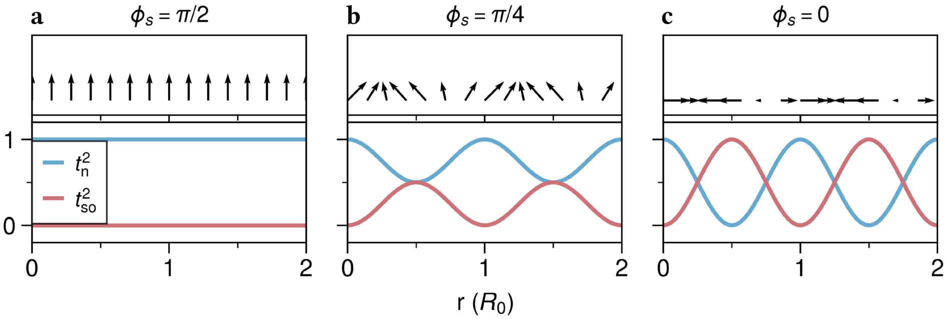

Figure 2.10: **Spin-precession in a Rashba spin-orbit field.** The precession of a spin moving in the xy-plane depends on the alignment of the spin with respect to its motion and the distance travelled. Top panels show the spin-orientation at selected points for travelling over a distance r along the x-axis in units $R_0 = m^* \alpha_{\mathrm{SO}}/h$, bottom panels show the probabilities in equation (2.26). **(a)** A spin aligned with $\vec{B}_{\mathrm{SO}}$ will not experience any precession. **(b)** Aligning the spin 45° to its motion precesses in a 'windshield wiper' motion. **(c)** A spin aligned at 90° to its motion allows a full rotation to occur.

A magnetic field additionally lifts the spin-degeneracy of the proximitized QD (see equation (2.19)), changing the weights of the $|\downarrow\rangle$ and $|\uparrow\rangle$ intermediate paths. We therefore distinguish $E_{\mathrm{ABS}}^{\uparrow(\downarrow)} = E_S - E_{D_{\uparrow(\downarrow)}}$. The spin-dependent rates of CAR and ECT, again utilising Fermi's golden rule in equation (2.23), can then be calculated for every spin combination of the QDs:

$$\begin{aligned}
W_{\mathrm{CAR}}^{\uparrow\downarrow} = W_{\mathrm{CAR}}^{\downarrow\uparrow} &\propto \left| \frac{(t_n^2 - t_{so}^2)uv}{E_{\mathrm{ABS}}^{\uparrow}} + \frac{(t_n^2 - t_{so}^2)uv}{E_{\mathrm{ABS}}^{\downarrow}} \right|^2 \\
W_{\mathrm{ECT}}^{\downarrow\uparrow} = W_{\mathrm{ECT}}^{\uparrow\downarrow} &\propto \left| \frac{(t_{\mathrm{n}} t_{\mathrm{so}})(u^2 - v^2)}{E_{\mathrm{ABS}}^{\uparrow}} + \frac{(t_{\mathrm{n}} t_{\mathrm{so}})(u^2 - v^2)}{E_{\mathrm{ABS}}^{\downarrow}} \right|^2 \\
W_{\mathrm{CAR}}^{\uparrow\uparrow} = W_{\mathrm{CAR}}^{\downarrow\downarrow} &\propto \left| \frac{2(t_n t_{so})uv}{E_{\mathrm{ABS}}^{\uparrow}} + \frac{2(t_n t_{so})uv}{E_{\mathrm{ABS}}^{\downarrow}} \right|^2 \qquad (2.28) \\
W_{\mathrm{ECT}}^{\uparrow\uparrow} &\propto \left| \frac{-t_n^2 v^2 - t_{so}^2 u^2}{E_{\mathrm{ABS}}^{\downarrow}} + \frac{t_{\mathrm{n}}^2 u^2 + t_{\mathrm{so}}^2 v^2}{E_{\mathrm{ABS}}^{\uparrow}} \right|^2 \\
W_{\mathrm{ECT}}^{\downarrow\downarrow} &\propto \left| \frac{-t_n^2 v^2 - t_{so}^2 u^2}{E_{\mathrm{ABS}}^{\uparrow}} + \frac{t_{\mathrm{n}}^2 u^2 + t_{\mathrm{so}}^2 v^2}{E_{\mathrm{ABS}}^{\downarrow}} \right|^2
\end{aligned}$$

These expressions encode all possible spin-dependent tunneling paths and interference effects via the mediating ABS. The interference of different paths again yields different behaviours for CAR and ECT, the amount of spin-precession in the tunneling process in addition to the coherence factors of the ABS. We include these equations here explicitly, as they capture the core essence of creating the Kitaev chain - the combination of magnetic field, spin-orbit coupling and a tunable Andreev bound state gives extensive control over ECT and CAR amplitudes for any possible spin-combination in the QDs.

The spin-specific rates of CAR and ECT are shown in figure 2.11a,b, as a function of the angle ϕ of $\vec{B}_{\text{ext}}$ with respect to the x-axis. When $\vec{B}_{\text{ext}}$ is aligned or anti-aligned with $\vec{B}_{\text{so}}$, no spin-precession can occur and $W^{\text{CAR}}_{\uparrow\uparrow}$, $W^{\text{CAR}}_{\downarrow\downarrow}$ are fully suppressed. Rotating $\vec{B}_{\text{ext}}$ immediately revives these previously forbidden processes. In combination with μ_{ABS}, this introduces two independent control parameters to achieve our goal: finding $W_{\text{CAR}}=W_{\text{ECT}}$ for a specific spin-polarisation. As shown in figure 2.11c, both tuning knobs allow for reaching this condition, regardless of whether the QDs are polarised to the same or opposing spins.

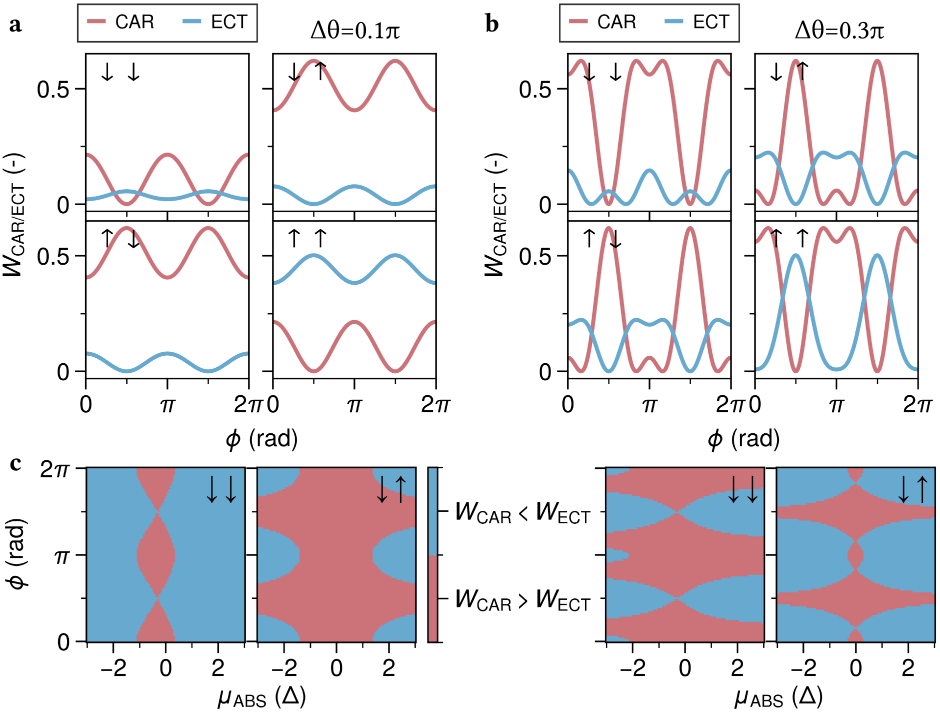

Figure 2.11: **Rates of CAR and ECT as a function of magnetic field angle and μ_{ABS}. (a)** For a small amount of spin-precession ($\Delta\theta = 0.1\pi$), the rates of CAR and ECT are roughly sinusoidal as a function of the external field angle. When $\phi = \pi/2$, the processes requiring spin-precession are fully suppressed. **(b)** As the maximum spin-precession approaches a half-rotation ($\Delta\theta = 0.3\pi$), higher harmonics start to appear in the angle dependence, increasing the likelihood of a crossover $W_{\text{ECT}} = W_{\text{CAR}}$. **(c)** The dependence on both μ_{ABS} and ϕ results in a large set of parameters where the sweet-spot condition $W_{\text{CAR}} = W_{\text{ECT}}$ can be achieved.

This concludes the quest for engineering a Kitaev chain - at least on the theory side. By spin-polarizing two QDs and coupling them via a proximitized QD in the Andreev bound state limit, all the parameters in the two-site Kitaev chain (equation (2.11)) can be controlled. The main focus of the experiments in this thesis are the demonstration of spin-selective ECT and CAR in Chapter 4, using this to make a two-site Kitaev chain in Chapter 5 and extending this technique to three sites in Chapter 6. Circling back, the goal of these investigations is the demonstration of creating unpaired Majorana bound states in a physical system. As a final part of this section, we point to the approximations used in modelling our system and possible consequences for generating Majoranas in more realistic, imperfect systems.

2.2.4 APPROXIMATING THE KITAEV CHAIN

The goal of section 2.2 has been to lay out the ingredients that will be used experimentally to engineer a Kitaev chain. In doing so, multiple approximations are made in order to simplify the discussion and highlight the key results. Since the eventual aim is the experimental creation of unpaired Majorana modes, by creating conditions that effectively map to the Kitaev chain, it is important to be aware how more realistic circumstances can affect this goal. The schematics below provide a more complete overview of the relevant energy scales and interactions to consider.

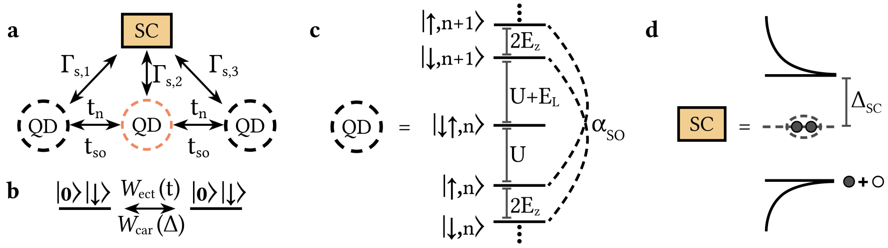

Figure 2.12: **A more complete model of the experimental system.** **(a)** The experimental two-site Kitaev chain consists of three QDs and a superconductor. Typically, the middle QD is strongly coupled to the superconductor, whereas the outer QDs are weakly coupled. A spin-conserving hopping t_n and spin-flipping hopping t_{so} transfers electrons between the QDs. **(b)** Under ideal conditions, the system is equivalent to a single spin-degenerate level in each QD, coupled via the effective CAR and ECT processes introduced in section 2.2.3 [36]. **(c)** In reality, each QD will consist of a ladder of spinful orbitals with charging energy U, separated by an additional 'level-spacing' E_L. Spin-orbit coupling can mix spin states from different orbitals. **(c)** The superconductor features a finite energy gap Δ_{SC}, a condensate of Cooper pairs as ground-state and a quasi-particle density of states that diverges near the gap-edge.

The experimental unit-cell will consist of three QDs and a superconductor (figure 2.12a). Ideally, the central QD is strongly coupled to the superconductor, while the outer QDs are only coupled to the central QD. In practice, the outer QDs may also interact directly with the superconductor as well. Furthermore, rather than being described by a single spin-polarised orbital, each QD contains a ladder of orbitals with potentially orbital-dependent charging energies, level spacings, and Zeeman splittings (figure 2.12c) [67]. Typical charging energies of the QDs studied in this thesis are on the order of 1- 2 mV (see Chapter 3), by far the largest relevant energy scale in the system. The assumption that only a single orbital participates in transport is therefore generally well-founded. The Zeeman energy, on the other hand, depends on material-specific properties and the applied magnetic field, and is often limited in magnitude. Spin therefore cannot be fully ignored. Similarly, the superconductor used experimentally has a relatively small energy gap of only $\Delta_{SC} = 220\,\mu V$. The induced gap of any sub-gap states is equal or smaller, meaning that their contribution can also not be fully neglected. A more realistic description of the system, taking these constraints into account, has been developed in the context of Kitaev chains in various levels of detail [35, 73]. Below, we address two refinements and their relation to the approximations used in section 2.2.

DESCRIBING THE SUPERCONDUCTOR

To describe a proximitized quantum dot in section 2.2.2, superconductivity was only included as an effective pairing term in the quantum dot. For a full description of a superconductor, typically BCS-theory is invoked [39, 74], which starts from the core assumption that a superconductor scatters pairs of electrons with opposite spin and opposite momenta:

$$H_{\text{BCS}} = \sum_{k\sigma} \xi_k c^\dagger_{k\sigma} c_{k\sigma} + \sum_{kk'} V_{kk'} c^\dagger_{k\uparrow} c^\dagger_{-k\downarrow} c_{-k'\downarrow} c_{k'\uparrow} \tag{2.29}$$

Here $c^\dagger_{k\sigma}$, $c_{k\sigma}$ are creation and annihilation operators for an electron with momentum k and spin $\sigma \in \{\uparrow, \downarrow\}$, and ξ_k is the single-electron energy with respect to the Fermi energy. In order to solve this model, two approximations used. The first assumption is that scattering will predominantly occur near the Fermi energy with $V_{kk'} = -V$ approximately constant. The second assumption is each pair of electrons only feels the average effect of all other pairs, neglecting fluctuations. This allows replacing the sum over k' by an order parameter $\Delta_{\text{SC}} = V \sum_k \langle c_{-k'\downarrow} c_{k'\uparrow} \rangle$. This is known as a *mean field approximation*. Implementing this, equation (2.29) can be written:

$$H^{\text{mf}}_{\text{BCS}} = \sum_{k\sigma} \xi_k c^\dagger_{k\sigma} c_{k\sigma} - \sum_{k} (\Delta_{\text{SC}} c^\dagger_{k\uparrow} c^\dagger_{-k\downarrow} + \text{h.c.}) \tag{2.30}$$

In this form, the model can be solved exactly. The ground-state is a condensate of Cooper pairs with $E_k = 0$, qualitatively introduced in section 2.2.1. The natural excitations in the model are superpositions of particles and holes known as Bogoliubov quasiparticles: $\gamma^\dagger_{k\uparrow} = u_k c^\dagger_{k\uparrow} - v_k c_{-k\downarrow}$. The pre-factors u_k, v_k are called BCS-coherence factors, capturing the electron-like and hole-like nature of the excitations. Their energy dispersion E_k and the density of states N^{sc}_k are given by:

$$E_k = \sqrt{\Delta^2_{\text{SC}} + \xi^2} \qquad N^{sc}_k = \frac{1}{N^{\text{n}}} \left| \frac{E_k}{\sqrt{E^2_k - \Delta^2_{\text{SC}}}} \right| \tag{2.31}$$

where N^{n} is the normal density of states (taken to be a constant). This reveals the following: most quasiparticles reside at $E_k = \Delta_{\text{SC}}$, where the density of states diverges. These lowest-energy excitations are equal electron-hole superpositions ($u^2_k, v^2_k = \frac{1}{2}$). For any sub-gap interactions with the superconductor, these excitations will dominate, motivating a further approximation. Rather than including the entire continuum of states, a single pair of particles at Δ_{SC} is included to represent any tunneling exchange with high-energy quasiparticles. This brings us to the *zero-bandwidth limit*:

$$H^{\text{zbw}}_{\text{BCS}} = \Delta_{\text{SC}} c^\dagger_\uparrow c^\dagger_\downarrow + \text{h.c.} \tag{2.32}$$

A single quantum dot level near the Fermi energy is assumed to predominantly interact with quasi-particles near the superconducting gap, represented by the single pair of particles. The final step is to remove the superconductor from the picture completely by setting $\Delta_{\text{SC}} \to \infty$, leading to the coupling between the $|0\rangle$ and $|2\rangle$ states of the quantum dot as an effective term Γ_{S} in the superconducting atomic limit (as we used in equation (2.17)).

In principle, the superconducting limit is sufficient to capture much of the relevant low-energy physics in the QD-ABS-QD system.

Weakly and strongly coupled quantum dots

A second assumption in modelling a proximitized quantum dot (in section 2.2.2) is that charging effects in the QD are small compared to the coupling to the superconductor. For a confined system in close proximity to a superconductor charging effects may be efficiently screened by the superconductor, making this a reasonable assumption. On the other hand, for a QD that is weakly coupled to the superconductor and covered with a metal, the charging effects are generally non-negligible. For instance, the outer QDs in figure 2.12a can couple to both the proximitized QD and the superconductor, so that superconducting correlations should be considered to some extent. In this case, an opposite limit can be considered: a system with an infinitely large charging energy, in the presence of a finite-sized gap superconductor. This situation can be treated as a magnetic impurity inside a superconductor, treated in Refs. [75–77], which leads to the formation of so-called Yu-Shiba-Rusinov (YSR) states.

In the YSR-limit, QD-SC interaction takes place by exchanging an electron in the quantum dot with a quasi-particle excitation in the superconductor, which is not possible in the superconducting atomic limit where $\Delta_{\mathrm{SC}} \to \infty$. When the quantum-dot is not coupled to the superconductor, the ground-state of the QD is either $|\uparrow\rangle$ or $|\downarrow\rangle$, while the ground-state of the superconductor is the BCS-singlet $|S\rangle$. Increasing the coupling to the superconductor Γ_{S} enables an exchange interaction, which swaps an electron in the quantum dot with an opposite spin quasi-particle excitation in the superconductor. This creates an effective coupling between the $|\uparrow,\downarrow\rangle$ and $|\downarrow,\uparrow\rangle$ states. A transition thus takes place as a function of Γ_{S}, between the following to ground states:

$$|\mathrm{gs}_{\mathrm{odd}}\rangle = |\downarrow, S\rangle, |\uparrow, S\rangle \qquad\qquad |\mathrm{gs}_{\mathrm{even}}\rangle = \frac{1}{\sqrt{2}}|\downarrow,\uparrow\rangle - |\uparrow,\downarrow\rangle \tag{2.33}$$

The even ground-state in this case is a YSR-singlet, markedly different from the BCS-singlet in the low U ‘ABS-regime’. In reality, each of the QDs in figure 2.12a will have both a finite charging energy and a finite coupling to the superconductor, with will have a finite Δ_{SC}. The intermediate regime is extensively covered in Ref. [78], showing a smooth crossover from the ABS-regime to the YSR-regime depending on U, Γ_{S} and Δ_{SC}.

The effect of treating the outer QDs in a YSR-description, in the context of the Kitaev chain, is detailed in Refs. [79, 80]; we borrow similar terminology in our description of the two-site Kitaev chain in Chapter 5. In the end, the question boils down to how well an experimental system resembling figure 2.12a can approach the ideal system of figure 2.12b, and more importantly: how this affects the prospect of creating and using Majoranas. To capture this, it can be useful to introduce a metric called the *Majorana polarisation.*

The Majorana polarisation

At the core of the above question lies the following: the introduction of Majorana operators remains a basis transformation, such that any excitation of an odd-even degeneracy can be described as a Majoranas excitation. A parity degeneracy can also be created in the proximitized QD studied in section 2.2.2, which can just as well be described by decoupled Majorana operators. This is, however, only useful when there is no spatial overlap between their wavefunctions. This existence of these ‘trivial’ zero-energy modes similarly hinders the ability to distinguish Andreev bound states and Majorana bound states in bulk semiconductor-superconductor systems [81].

It is thus useful to introduce some notion of 'Majorana-ness', that captures how well isolated Majorana modes in a system are. For general interacting, multi-orbital systems this is not straightforward [82], but several approaches have been proposed. A possible diagnostic is the Majorana polarisation M [35, 83, 84]. This quantity can be defined at the level of a given site j as:

$$M = \frac{\sum_\sigma (w_\sigma^2 - z_\sigma^2)}{\sum_\sigma (w_\sigma^2 + z_\sigma^2)} \qquad w_\sigma, z_\sigma = \langle O| d_{j\sigma} \pm d_{j\sigma}^\dagger |E\rangle \tag{2.34}$$

where $|O\rangle$ and $|E\rangle$ denote the even- and odd-parity eigenstates. The metric captures how well a particle-hole symmetric operator maps between two parity ground-states at a given site j. The Majorana polarisation is 1 for an ideal system. For a general realistic system, the quantity will only be close to 1. Although it is not straightforward to measure this quantity directly, it can have indirect observable consequences [85, 86]. A common proposal relies on coupling an additional quantum dot to a system that hosts Majoranas and measure the energy splitting of the zero-bias excitations [87–89], which has recently been tested as a viable technique [90]. As an alternative, in Chapter 5, we study how the Majorana polarisation can be estimated from the excitation spectrum of the system. Ultimately, the overlap between Majoranas/low Majorana polarisation will show up through decoherence of Majorana based qubits and imperfections in Majorana braiding experiments, which will be further discussed in Chapter 9.

2.3 MAJORANA KRAMERS PAIRS AND PARAFERMIONS

The presence of unpaired Majoranas is directly related to the presence of a two-fold degenerate ground state, as we saw in section 2.1.1 in the Kitaev chain. Large Zeeman energies and charging energies ($E_Z, U \gg t, \Delta$) are critical for realizing this condition in the experimental setting throughout this thesis. In Chapter 5, we will experimentally push these limits and study the system at zero magnetic field, so that there is no induced Zeeman splitting in the QDs. In this $E_Z = 0$ limit, the odd parity subspace will always be two-fold degenerate due to Kramers degeneracy, as a consequence of time-reversal symmetry. If a degeneracy can then be created between the odd and even parity ground states, this automatically results in a *three-fold* degeneracy. Interestingly, this higher-dimensional degeneracy warrants the introduction of two different types of zero-energy excitations:

- *Majorana Kramers pairs* - a set of four operators satisfying the Majorana algebra $(\gamma_{1,2}^\sigma)^2 = 1, \{\gamma_i, \gamma_j\} = 2\delta_{ij}$, each mapping between the even ground-state and either of the two odd ground-states (distinguished here by their net spin $\sigma \in \{\uparrow, \downarrow\}$). The four operators form two Kramers pairs, connected by time reversal symmetry.

- $\mathbb{Z}_3$*-parafermions* - operators $\hat{\chi}$ which satisfy the algebra $\chi^3 = 1$, $\chi^2 = \chi^\dagger$, $\chi_i\chi_j = \chi_j\chi_i e^{-i\frac{2\pi}{3}}$. Such operators 'cycle through' the three degenerate ground-states, returning to the initial state after three applications.

The action of these operators can be visualised by their respective effect on the many-body ground state degeneracies of interest, illustrated in figure 2.13.

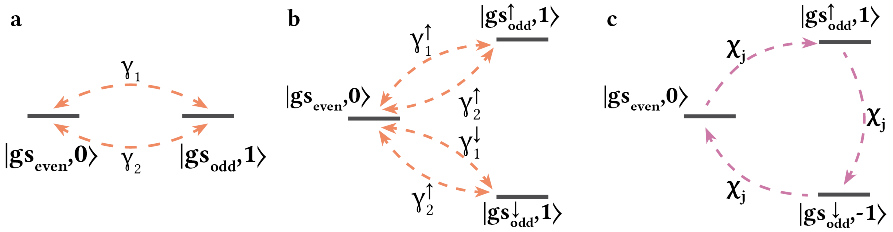
a
γ_1
γ_2
$|\mathbf{gs}_{\mathbf{even}},\mathbf{0}\rangle$
$|\mathbf{gs}_{\mathbf{odd}},\mathbf{1}\rangle$
b
$|\mathbf{gs}^{\uparrow}_{\mathbf{odd}},\mathbf{1}\rangle$
$\gamma_1^{\uparrow}$
$|\mathbf{gs}_{\mathbf{even}},\mathbf{0}\rangle$
$\gamma_2^{\uparrow}$
$\gamma_1^{\downarrow}$
$\gamma_2^{\uparrow}$
$|\mathbf{gs}^{\downarrow}_{\mathbf{odd}},\mathbf{1}\rangle$
c
$|\mathbf{gs}^{\uparrow}_{\mathbf{odd}},\mathbf{1}\rangle$
χ_j
$|\mathbf{gs}_{\mathbf{even}},\mathbf{0}\rangle$
χ_j
χ_j
$|\mathbf{gs}^{\downarrow}_{\mathbf{odd}},\mathbf{-1}\rangle$

Figure 2.13: **Action on a ground state degeneracy of Majoranas, Majorana Kramers Pairs en $\mathbb{Z}_3$ Parafermions.** Diagrams showing the relation between groundstate degeneracies and Majorana/Parafermion operators. Drawn states are at equal energy (drawn at different height for illustration purposes). **(a)** Majorana operators map between even and odd ground states, flipping fermion parity. **(b)** With time-reversal symmetry, the odd subspace is itself degenerate; Majorana Kramers pairs map the even state to either odd state, preserving spin sectors. **(c)** If each of three ground states carries a distinct quantum number, parafermions can be defined which cyclically permute the states.

Like Majoranas, both Majorana Kramers pairs [91–93] and parafermions [94, 95] are of interest in the context of topological quantum computing. The former, because they do not require breaking time reversal symmetry, which provides additional protection to certain perturbations and may ease experimental requirements. The latter, because the more general algebra spanned by these operators extends the possible quantum gates that can be implemented through exchange of the operators[6]. Experimental realizations of these systems generally require more exotic circumstances, compared to Majoranas [98–106].

Concepts related to parafermions will tie in with the experimental work in Chapter 7. To contextualize these experiments, we briefly describe the connection between the Kitaev chain and the transverse-field Ising spin chain in section 2.3.1. This serves as a stepping stone for understanding parafermions as a generalization of Majorana fermions (section 2.3.2), allowing for reintroducing properties of Majoranas in a more general fashion. Next, we introduce the model that underlies the experiments in Chapter 7 (section 2.3.3). To conclude, we discuss constructing $\mathbb{Z}_3$-parafermion toy models in section 2.3.4.

2.3.1 DUALITY OF THE KITAEV CHAIN AND THE ISING SPIN CHAIN

Before the advent of topological classifications, the study of phases of matter relied on symmetries and spontaneous symmetry breaking. A canonical example is the one-dimensional transverse-field Ising model, which describes a lattice of spins subjected to a magnetic field [107]:

$$H_{\text{Ising}} = -Jg\sum_j \sigma_j^x - J\sum_{\langle ij\rangle}\sigma_i^z\sigma_j^z \tag{2.35}$$

where $\sigma_j^{\mathrm{x,z}}$ are Pauli matrices acting on site j. The first term favours alignment of spins in the x-direction (→), where g can be seen as the strength of an external magnetic field.

---

[6] Exchange of Majoranas can only be used to implement Clifford gates, while $\mathbb{Z}_3$ parafermions can, potentially, allow for universal quantum computations [94, 96, 97].

The second term favours alignment of neighbouring spins (↑↑, ↓↓). The Hamiltonian is invariant under flipping all spins in the z-direction, and hence has $\mathbb{Z}_2$ symmetry. A quantum phase transition takes place between a paramagnetic phase (high g) and a ferromagnetic phase (low g). When $g \gg 1$, all spins align in the x-direction, such that there is a unique ground state that respects the $\mathbb{Z}_2$ symmetry: $|{\rightarrow}{\rightarrow}{\rightarrow}\cdots\rangle$. In the opposite limit where $g \to 0$, the spins instead align along z, which results in two degenerate states: $|{\uparrow}{\uparrow}{\uparrow}\cdots\rangle$ and $|{\downarrow}{\downarrow}{\downarrow}\cdots\rangle$. To respect the spin-flip symmetry, the true ground-state must be an equal superposition of these two states. However, in the limit of $N \to \infty$, any small perturbation forces the system to choose either of the aligned states, spontaneously breaking $\mathbb{Z}_2$ symmetry. The phase transition from the disordered phase to this ordered phase occurs at $g = 1$.

Under a Jordan-Wigner transformation [108] the Ising Hamiltonian (equation (2.35)) can be rewritten in terms of fermionic operators [109–111]:

$$H^{\mathrm{JW}}_{\mathrm{Ising}} = 2Jg\sum_{j=1}^{N}(c_j^\dagger c_j + 1) + J\sum_{j=1}^{N-1}(c_j^\dagger c_{j+1} + c_j^\dagger c_{j+1}^\dagger + \text{h.c.}) \tag{2.36}$$

Comparing equation (2.36) and equation (2.2), it is easy to see that this model is equivalent to the Kitaev chain for the parameters $t = \Delta = J$, $\mu = 2gJ$. This raises an interesting connection: the phase-transition at $g = 1$ in the spin language, corresponds exactly to the topological phase boundary $\mu = 2t$ in the fermionic language (see section 2.1.2). The spontaneously broken $\mathbb{Z}_2$ symmetry ties to an odd-even ground state degeneracy, in turn giving rise to Majoranas. Ref. [112] treats this connection in further detail. For this section the important concept is that local order in the spin language heralds non-local topological order in the fermionic system.

A direct link to Majoranas arises through Kramers-Wanniers duality [113], which poses a symmetry between the ordered and disordered phases of the Ising chain. Instead of the spin lattice, one can look at a dual system defined on the boundaries between spins, with sites $\tilde{j} = j + \frac{1}{2}$. In this description, 'disorder' operators are introduced, that concern the presence of domain walls in the spin lattice. The operator $\xi^{\mathrm{x}}_{\tilde{j}} = \sigma^{\mathrm{z}}_j\sigma^{\mathrm{z}}_{j+1}$ checks whether there is a domain wall at site $\tilde{j}$; $\xi^{\mathrm{z}}_{\tilde{j}}{=}\prod_{k<\tilde{j}}\sigma^{\mathrm{x}}_k$ creates a domain wall by flipping all spins to the left of $\tilde{j}$. Combined with spin operators, they can be used to define two operators that satisfy fermionic commutation relations [114]:

$$a_j = \xi^{\mathrm{x}}_j\sigma^{\mathrm{z}}_j \qquad\qquad b_j = i\xi^x_j\sigma^z_j\sigma^x_j \tag{2.37}$$

These operators additionally satisfy $(a_j)^2 = (b_j)^2 = 1$: they fit the definition of Majorana operators! Using these, equation (2.35) can be rewritten as:

$$H^{\mathrm{maj}}_{\mathrm{Ising}} = igJ\sum_{j}^{N} a_j b_j + iJ\sum_{j=1}^{N-1} b_j a_{j+1} \tag{2.38}$$

In this interpretation it is again easy to see that at $g = 0$, two unpaired Majorana operators arise (a_1, b_N), as in section 2.1.1. To head back to a fermionic description one takes $c^\dagger = a_j + ib_j$, $c_j = a_j - ib_j$ as before (section 2.1.1). The Majorana operators, which are highly non-local in terms of spin variables, can be written locally in terms of fermionic operators.

2.3.2 The $\mathbb{Z}_\mathrm{n}$ clock model

The above connection makes it more natural to bring up the more general question: given the topology arising from order in a $\mathbb{Z}_2$ symmetric spin chain, how does order in a general $\mathbb{Z}_n$ symmetric spin chain translate to a fermionic description? This question is treated in detail in Ref. [112], we summarize the relevant concepts here. The general system consists of N 'spins' with n allowed states $s_j \in \{1, \omega, \omega^2, \cdots, \omega^{n-1}\}$, where $\omega = e^{2\pi i/n}$. A general coupling between two spins s_j,s_k can be written:

$$-J \sum_{m}^{N-1} \alpha_m (s_j^* s_k)^m \tag{2.39}$$

which is invariant under the transformation $s_j \to \omega s_j$, satisfying $\mathbb{Z}_n$ symmetry. By constructing general Pauli operators for the n-dimensional case ($\sigma^\mathrm{x} \to \sigma$,$\sigma^\mathrm{z} \to \tau$), an extension of the 1D Ising model can be written for any n.
For the $n = 3$ case the most general form is:

$$H = -gJ \sum_{j=1}^{N} \left(\tau_j^\dagger e^{-i\phi} + \tau_j e^{i\phi} \right) - J \sum_{j=1}^{N-1} \left(\sigma_j^\dagger \sigma_{j+1} e^{-i\theta} + \sigma_j \sigma_{j+1}^\dagger e^{i\theta} \right) \tag{2.40}$$

Allowing ϕ, θ to be non-zero breaks spatial-parity symmetry; this is referred to as a *chiral* clock model. Like the Ising chain, the system displays phase transitions from a disordered phase to an ordered phase where $\mathbb{Z}_3$ symmetry is spontaneously broken. The order-disorder duality for the Ising chain is generalizable to any $\mathbb{Z}_n$ symmetric spin chain [115, 116], and the transformation that gives rise to Majoranas was shown to be applicable to the general case [114]. This allows for the introduction of two new operators by mixing disorder and spin operators, in the same fashion as equation (2.37), to obtain *parafermionic operators*[7]:

$$\chi_{2j-1} = \left(\prod_{k=1}^{j-1} \tau_k \right) \sigma_j \qquad\qquad \chi_{2j} = \omega^{(n-1)/2} \left(\prod_{k=1}^{j-1} \tau_k \right) \sigma_j \tau_j \tag{2.41}$$

These operators satisfy the general property of reaching identity after n applications ($(\chi_j)^n = 1$), and having an inverse operator that amounts to 'cycling backwards' ($\chi_j^\dagger = (\chi_j)^{n-1}$). Such operators no longer satisfy fermionic commutation relations (except for $n = 2$), instead:

$$\chi_j \chi_k = \omega \chi_k \chi_j \quad (j < k) \tag{2.42}$$

For $n = 2$ these properties reduce to the familiar Majorana relations, which can be considered to be $\mathbb{Z}_2$-parafermions. Similar to equation (2.38), the $n = 3$ spin chain (equation (2.40)) can be rewritten in terms of $\mathbb{Z}_3$-parafermions:

$$H = -Jg \sum_{j=1}^{N} \left(\chi_{2j-1}^\dagger \chi_{2j} \omega + \text{h.c.} \right) - J \sum_{j=1}^{N-1} \left(\chi_{2j}^\dagger \chi_{2j+1} \omega + \text{h.c.} \right) \tag{2.43}$$

---

[7] This naming is a historical link to work by Green [117], who demonstrated that general 'parastatistics', beyond bosonic and fermionic statistics, can satisfy valid relativistic field theories describing spin-1/2 particles.

The form of equation (2.43) is very similar to that of the Kitaev chain in the Majorana basis and suggests the possibility of unpaired parafermions at $g = 0$, but the analysis is significantly complicated by the non-fermionic commutation relations of the parafermions. Unlike the Ising chain, there is no simple free fermionic description, or a simple mapping between parafermions and local fermionic variables [118, 119], which we address further in section 2.3.4. One can, however, describe the conditions that should be desired of $\mathbb{Z}_3$ parafermionic modes.

In the Ising model, $\mathbb{Z}_2$ symmetry gives rise to parity conservation, paving the way for Majoranas that map different parity sectors. Similarly, $\mathbb{Z}_3$ symmetry gives rise to a conserved 'generalized parity' $\omega^{\hat{P}}$ in a fermionic description that takes 3 distinct values, with $\hat{P}$ a generalized parity operator[8]. Since it connects to a conserved quantity, we have $\left[H, \hat{P}\right] = 0$. Any parafermionic operator $\hat{\Phi}$ will be a zero-energy excitation that changes the generalized parity, so that the following properties should hold [112]:

$$\hat{\Phi}\hat{P} = \omega\hat{P}\hat{\Phi} \qquad\qquad \left[H, \hat{\Phi}\right] = 0 \tag{2.44}$$

The first property is the requirement that measuring the generalized parity after applying $\hat{\Phi}$ should introduce an additional ω compared to measuring parity before applying $\hat{\Phi}$, since $\hat{\Phi}$ changes the general parity by ω. The second property requires that *any* eigenstate of H is mapped to a new eigenstate by $\hat{\Phi}$ with the same energy. The latter imposes a major condition on the eigenvalues of H: the entire spectrum should be split into at-least three-fold degenerate sectors, consisting of three eigenstates with different generalized parity. Such a system is called *strongly degenerate* and $\hat{\Phi}$ is called a *strong zero mode*. We note again that these exact same statements can be made for the Majoranas in the Kitaev chain. The key difference is the fact that Majoranas map easily to local fermionic operators, allowing the connection to a experimentally realisable system of electrons, which is not generally the case here. Below we start instead from a fermionic Hamiltonian and show how it can be connected to a parafermionic description.

2.3.3 Poor man's Majorana Kramers pairs

The above sections served to introduce the notions of parafermions and Majorana Kramers pairs. The reason for going through all this trouble, is to build a foundation for interpreting the experimental system in Chapter 7. To emulate the spinless Kitaev chain experimentally in Chapters 4-6, an external magnetic field is applied that lifts Kramers degeneracy. The ECT and CAR interactions in a quantum-dot - superconductor array, however, do not require the magnetic field in order to couple the quantum dots [120]. We can therefore study the same system without a magnetic field, which drastically changes the description. A complete treatment of the two site system without magnetic field is covered in Ref. [121]; we highlight the key details here. To start, we consider a general chain of N spinful fermionic sites, with ECT and CAR coupling terms. Since spin can no longer be neglected, each site is described by a pair of operators $c^\dagger_{j,\sigma}, c_{j,\sigma}$ which annihilate or create an electron with spin $\sigma \in \{\uparrow, \downarrow\}$. The general chain is described by the Hamiltonian:

---

[8] As a reminder, for Majoranas the conserved quantity is the regular parity $(-1)^{\hat{N}}$, with $\hat{N}$ the total number operator (section 2.1.1).

$$\begin{aligned} H = &\sum_{j}^{N} \mu_j (c^\dagger_{j,\uparrow} c_{j,\uparrow} + c^\dagger_{j,\downarrow} c_{j,\downarrow}) + \sum_{j}^{N} U_j c^\dagger_{j,\downarrow} c^\dagger_{j,\uparrow} c_{j,\downarrow} c_{j,\uparrow} \\ &+ \sum_{j}^{N-1} \Delta_j e^{-i\phi_j} (c^\dagger_{j,\downarrow} c^\dagger_{j+1,\uparrow} - c^\dagger_{j,\uparrow} c^\dagger_{j+1,\downarrow}) + \sum_{j}^{N-1} t_j (c^\dagger_{j,\downarrow} c_{j+1,\downarrow} + c^\dagger_{j,\uparrow} c_{j+1,\uparrow}) + \text{h.c.} \end{aligned} \tag{2.45}$$

Here μ_j is the chemical potential energy and U_j a charging energy penalizing double occupancy of each site. The ECT-type coupling (t) is now included as a spin-preserving hopping, while the CAR-type coupling (Δ) manifests as an s-wave superconducting pairing between neighbouring sites, respecting time reversal symmetry. We restrict $\phi_j = 0$ for the purpose of this section.

In the experimental regime of interest, the charging energy U is typically much larger than the t, Δ interactions, so that we can opt to treat the $U \to \infty$ limit and simplify the analysis. To emulate this, we restrict the Fock-space basis to exclude any states with a doubly occupied site[9]. For just two sites, this leaves the Hamiltonian:

$$\begin{aligned} H_{\text{PMMKP}} = \sum_{\sigma \in \{\uparrow,\downarrow\}} &\mu_1 c^\dagger_{1,\sigma} c_{1,\sigma} + \mu_2 c^\dagger_{2,\sigma} c_{2,\sigma} + t_1 (c^\dagger_{1,\sigma} c_{2,\sigma} + c^\dagger_{2,\sigma} c_{1,\sigma}) \\ &+ \Delta_1 (c^\dagger_{1,\downarrow} c^\dagger_{2,\uparrow} - c^\dagger_{2,\uparrow} c^\dagger_{1,\downarrow} + \text{h.c.}) \end{aligned} \tag{2.46}$$

For this small system the Hamiltonian can again be diagonalized exactly, to obtain the odd and even parity ground states. In the same fashion as for the Kitaev chain, an odd-even parity degeneracy arises when tuning the t, Δ parameters. In this case, the degeneracy arises when $t = \sqrt{2}\Delta$, $\mu = 0$, a fact already noted in an earlier works [123] studying a closely related system. The ground-state is three-fold degenerate due to the additional Kramers degeneracy in the odd sector and consists of the following three eigenstates:

$$|\text{gs}_{\text{even}}\rangle = \frac{1}{\sqrt{2}}|0,0\rangle - \frac{1}{2}|\uparrow,\downarrow\rangle + \frac{1}{2}|\downarrow,\uparrow\rangle \qquad |\text{gs}_{\text{odd},\sigma}\rangle = \frac{1}{\sqrt{2}}(|0,\sigma\rangle - |\sigma,0\rangle) \tag{2.47}$$

Having obtained these ground states, one can try to enforce the construction of operators that map between them, in the two ways illustrated in figure 2.13b,c. Reproducing the results from Ref. [121], it is possible to construct Majorana Kramers pairs mapping the even ground state to either odd ground state:

$$\begin{aligned} \gamma_{2,\sigma} &= \eta_\sigma (1 - \hat{n}_1) c_{2,\sigma} - \frac{1}{\sqrt{2}} (n_{1,\sigma} c_{2,\sigma} - c^\dagger_{1,\sigma} c_{1,\bar{\sigma}} c_{2,\sigma}) + \text{h.c} \\ \gamma_{1,\sigma} &= i\eta_\sigma (1 - \hat{n}_2) c_{1,\sigma} + \frac{1}{\sqrt{2}} (n_{2,\sigma} c_{1,\sigma} - c^\dagger_{2,\sigma} c_{2,\bar{\sigma}} c_{1,\sigma}) + \text{h.c} \end{aligned} \tag{2.48}$$

Similarly, it is possible to construct parafermionic operators that cycle between each of the three ground states, that can be labelled by the generalized parity $\hat{P} = \omega^{\sum_j n_{j,\uparrow} + 2n_{j,\downarrow}}$ [124], which effectively conveys the net spin polarisation of each state:

---

[9] The proper discussion in [121] instead uses constrained fermions [122] that naturally disconnect the doubly occupied states, which we omit here for brevity. We incorporate constrained fermions in section 2.3.4.

$$\begin{aligned}\chi_2 &= (1-\hat{n}_1)\left(c_{2,\uparrow} - c^\dagger_{2,\downarrow}\right) + (c^\dagger_{2,\downarrow} c_{2,\uparrow} + \frac{1}{\sqrt{2}}(c^\dagger_{2,\uparrow} + c_{2,\downarrow}))c^\dagger_{1,\downarrow} c_{1,\uparrow} \\ &- \frac{1}{\sqrt{2}}(\hat{n}_{1\uparrow} c^\dagger_{2,\downarrow} + n_{1,\downarrow} c_{2,\uparrow}) - (1 - \frac{1+\ \sqrt{2}}{\sqrt{2}}\hat{n}_1)c^\dagger_{2,\uparrow} c_{2,\downarrow} - (1 - \frac{1+\ \sqrt{2}}{\sqrt{2}}\hat{n}_2)c^\dagger_{1,\uparrow} c_{1,\downarrow} \\ \chi_1 &= (1-\hat{n}_2)\left(c_{1,\uparrow} + c^\dagger_{1,\downarrow}\right) + (c^\dagger_{1,\downarrow} c_{1,\uparrow} + \frac{1}{\sqrt{2}}(c^\dagger_{1,\uparrow} - c_{1,\downarrow}))c^\dagger_{2,\downarrow} c_{2,\uparrow} \\ &- \frac{1}{\sqrt{2}}(\hat{n}_{2\uparrow} c^\dagger_{1,\downarrow} - n_{2,\downarrow} c_{1,\uparrow}) + (1 + \frac{1-\ \sqrt{2}}{\sqrt{2}}\hat{n}_1)c^\dagger_{2,\uparrow} c_{2,\downarrow} + (1 + \frac{1-\ \sqrt{2}}{\sqrt{2}}\hat{n}_2)c^\dagger_{1,\uparrow} c_{1,\downarrow}\end{aligned} \tag{2.49}$$

We reproduce these operators here explicitly, to highlight these operators do not appear as a local description in terms of fermions. Each is a combination of fermionic operators from both sites and both spins. The surprising observation is that the underlying degeneracy is nevertheless robust against perturbing the on-site energies of a single quantum dot μ_j, shown in figure 2.14. This is interesting, since for Majoranas in the Kitaev chain the protection against perturbations in μ could be understood by looking at their localisation (section 2.1.2). Unpaired Majoranas, described in terms of local fermionic operators, are not coupled by local perturbations due to their spatial separation. Furthermore, an overlap between Majoranas results in an immediate splitting of the zero energy modes when perturbing μ_j.

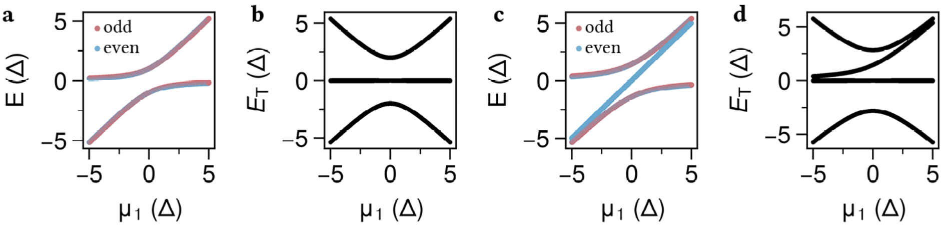

Figure 2.14: **Eigenvalues and excitation spectra of the Kitaev chain and the PMMKP chain**. Comparison of the eigenvalue spectrum at the sweet spot of the two-site Kitaev chain (equation (2.2)) and the zero-field equivalent (equation (2.46)), as a function of detuning μ_1. **(a)** Eigenvalues of the Kitaev chain. Each sector remains two-fold degenerate as μ_1 is perturbed. **(b)** This is reflected in the excitation spectrum as a persistent excitation at zero energy (repetition of figure 2.5c). **(c)** Eigenvalues of the PMMKP chain. Analogous to (a), each sector now consists of three eigenstates with a degenerate eigenvalue. **(d)** This leads to a very similar spectrum as (c), again resulting in a persistent zero bias excitation.

To understand the protection in this case, a more general principle needs to be introduced. Given that there is a parafermionic operator that commutes with the Hamiltonian, the energy spectrum will be strongly degenerate (equation (2.44)). For a perturbation V that commutes with Φ, we can expect for $H' = H + V$ that:

$$[V,\Phi] = 0 \Rightarrow [H',\Phi] = [H,\Phi] + [V,\Phi] = 0 \tag{2.50}$$

Any perturbation V that commutes with the parafermionic mode, will therefore preserve the symmetry that results in the strongly degenerate spectrum. Such a perturbation will therefore not lift the degeneracy, maintaining the zero energy excitations in the system.

In fact, the construction of the operators in equation (2.49) and equation (2.48) was guided by this principle, by enforcing a priori that they should commute with the number operators of the QDs. Notably, the above principle can be directly used to predict which other types of perturbations will maintain the ground-state degeneracy. Of particular interest to Chapter 7 is the scalability of the system at zero field. We can for example see for a two-site Kitaev chain, the Majoranas will commute with the addition of any new site via the t and Δ couplings. For the states in equation (2.49), this is definitely not the case.

In conclusion, the two-site system of coupled quantum dots with superconducting pairing has interesting properties both in the presence and absence of a magnetic field. The high field system is studied in Chapter 5, where we vary the magnetic field to study the Majorana polarisation introduced in section 2.2.4. This leads to the observation that stable zero energy modes can persist without any applied magnetic field, motivating the in-depth zero-field study in Chapter 7. As a final note, the Kitaev chain was of interest in particular because of its topological phase in the $N \to \infty$ limit, discussed in section 2.1.1. A similar analysis can be done for the zero field Hamiltonian studied here. While there is no $\mathbb{Z}_2$ topological phase transition expected in this system, studying short chain reveals a very similar behaviour of parity-degeneracies compared to the Kitaev chain phase diagram, shown in figure 2.15.

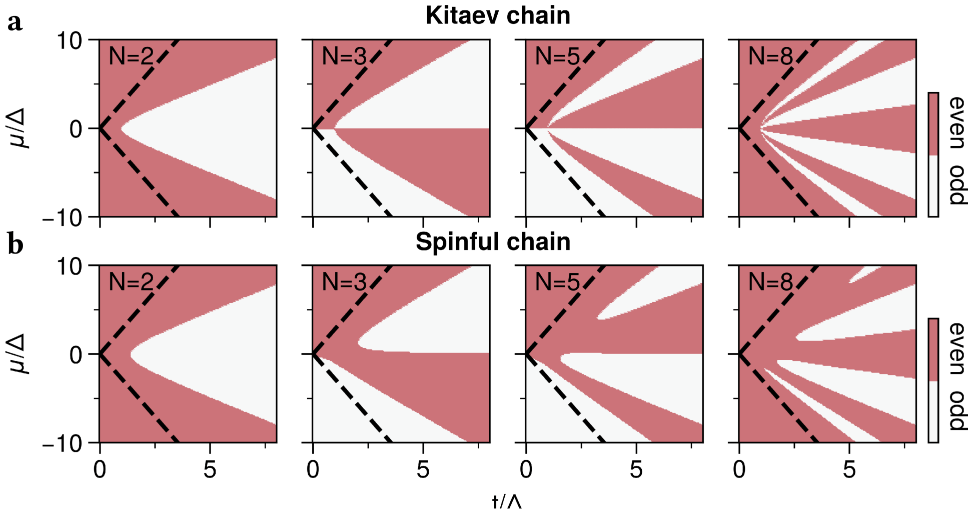

Figure 2.15: **Scaling behaviour of the Kitaev chain and the spinful counterpart.** **(a)** Phase diagram of the Kitaev chain for varying N. The lines where the ground-state parity switches correspond exactly to the zero-energy solutions plotted in figure 2.3 **(b)** Phase diagram of the zero-field equivalent (equation (2.45)). At N=2, the diagrams are very comparable, only differing in the location of the apex of the parity degeneracy line ($t = \Delta$ for the Kitaev chain, $t = \sqrt{2}\Delta$ for the zero-field system). As N is increased, there is no longer a degeneracy at $t = \sqrt{2}\Delta$, but the number of degeneracies nevertheless scales in a very comparable manner.

2.3.4 Building a $\mathbb{Z}_3$-parafermion chain

As the very final section of this theory chapter, we tie up loose ends and build an understanding of what it *would* take to construct a 'well behaved' $\mathbb{Z}_3$-parafermionic system. In the previous section, we summarized Ref. [121] where it was shown that it is possible to decompose the fermionic Hamiltonian of interest to Chapter 7:

$$\begin{aligned} H_{\mathrm{PMMKP}} = \sum_{\sigma\in\{\uparrow,\downarrow\}} & \mu_1 c^\dagger_{1,\sigma} c_{1,\sigma} + \mu_2 c^\dagger_{2,\sigma} c_{2,\sigma} + t_1 (c^\dagger_{1,\sigma} c_{2,\sigma} + c^\dagger_{2,\sigma} c_{1,\sigma}) \\ & + \Delta_1 (c^\dagger_{1,\downarrow} c^\dagger_{2,\uparrow} - c^\dagger_{2,\uparrow} c^\dagger_{1,\downarrow} + \mathrm{h.c.}) \end{aligned} \tag{2.51}$$

into a parafermionic Hamiltonian:

$$H = -\frac{(t+\sqrt{2}\Delta)}{2}\mathbb{I} + \frac{(t-\sqrt{2}\Delta)}{2}(\chi_1^\dagger \chi_2 + \chi_2^\dagger \chi_1) \tag{2.52}$$

where χ_1 and χ_2 are $\mathbb{Z}_3$-parafermion operators (equation (2.49)) satisfying $\chi_1^3, \chi_2^3 = 1$ and $\chi_2\chi_1 - \omega\chi_1\chi_2 = 0$ ($\omega = e^{i2\pi/3}$). This description helps to explain why a protected three-fold degenerate ground-state arises in equation (2.51), but the system does not scale trivially beyond $N = 2$, as we will study further in Chapter 7. Since the construction of χ_1, χ_2 required knowing a priori that the system has a threefold degenerate ground-state, this decomposition does not give any information for studying the general N-site case. This leaves a few open questions that are interesting to study, both for better understanding the experimental system and for better understanding $\mathbb{Z}_3$-parafermions in general:

1. Can χ_1, χ_2 be implemented in braiding or fusion schemes, given that they are not local objects in their fermionic description? Or, given that their construction is not unique, is there a choice where they are actually local?

2. Is it possible to map the general fermionic Hamiltonian to a parafermionic description, to see any hidden $\mathbb{Z}_3$ structure without prior knowledge of the groundstate degeneracies?

As a step toward answering this, we will address here a third, reverse question:

3. Can we map from a parafermionic Hamiltonian (with desirable $\mathbb{Z}_3$ structure) to a physically realizable fermionic Hamiltonian?

Understanding this may help to see how to fit the Hamiltonian equation (2.51) in the larger picture. We will use the tools introduced in section 2.3.2 and follow the commonly used sequence [125]:

$$\mathrm{Clock\ operators} \rightarrow \mathrm{Fradkin-Kadanoff\ parafermions} \rightarrow \mathrm{Fermions} \tag{2.53}$$

where we will try to express the clock-operators in terms of local fermionic operators, so that we hope to produce a local fermionic system via the parafermionic mapping [126]. Below we first address why this is necessary.

The issue with local parafermions

To start, we should define what we mean by the desire that the system should be 'local' and 'physically reasonable'. We raise here the following criteria:

- The parafermionic description should be local in the sense that $\mathbb{Z}_3$-edge modes of interest exist regardless of N, such as in equation (2.43).
- The mapped fermionic description should be local and physically reasonable in the sense that the Hamiltonian is Hermitian, conserves parity or particle number and only involves nearest neighbour/next-nearest neighbour interactions.

The simplest (naive) route to a fermionic parafermion chain, would be to follow the same procedure that leads to the Kitaev chain: construct parafermions in terms of strictly local fermionic operators and then couple them in pairs, with the aim of creating the reasonable fermionic system. A first question to address is therefore the following: is it possible *to begin with* to obtain parafermionic operators that are purely local in terms of fermionic operator. The short answer is: no, unless the number of sites $N = 1$. The reasoning is as follows: given two parafermionic operators χ_i and χ_j acting solely on site i and j in their fermionic construction, they must satisfy (for $j > i$) the commutation:

$$\chi_j \chi_i = \omega \chi_i \chi_j \tag{2.54}$$

When χ_i and χ_j act on different sites, solutions only exist for this equation when $\omega = 1$ or $\omega = -1$, while $\mathbb{Z}_3$ parafermions require $\omega = e^{i2\pi/3}$ [125]. Notably, this is why Majoranas (i.e. $\mathbb{Z}_2$ parafermions), which require $\omega = -1$, do not suffer this issue and *can* be readily expressed in terms of local fermionic operators.

The Fradkin-Kadanoff construction

The solution to the above problem involves the generalization of the Jordan-Wigner transformation (section 2.3.2), which allows to map from a spin system to a fermion system. The strategy is the same: strings need to be introduced in order to implement the correct bookkeeping for maintaining the parafermionic commutation relations. The construction starts by associating so-called *clock-operators* σ_i, τ_i to each site i, which satisfy *locally*:

$$\sigma_i^3, \tau_i^3 = 1 \qquad \sigma_i^\dagger = \sigma_i^2 \qquad \tau_i^\dagger = \tau_i^2 \qquad \sigma_i \tau_i = \omega \tau_i \sigma_i \tag{2.55}$$

while commuting across sites. As explicit representation, the commonly used matrices are:

$$\sigma_i = \begin{pmatrix} 0 & 1 & 0 \\ 0 & 0 & 1 \\ 1 & 0 & 0 \end{pmatrix} \qquad \tau_i = \begin{pmatrix} 1 & 0 & 0 \\ 0 & \omega & 0 \\ 0 & 0 & \omega^2 \end{pmatrix} \tag{2.56}$$

From here, one can construct the $2N$ *Fradkin-Kadanoff* parafermions [114]:

$$\chi_{2j-1} = \left(\prod_{k=1}^{j-1} \tau_k \right) \sigma_j \qquad \chi_{2j} = \omega \chi_{2j-1} \tau_j \tag{2.57}$$

which now satisfy the proper relations across the entire chain:

$$\chi_i^3 = 1 \qquad \chi_i^\dagger = \chi_i^2 \qquad \chi_j \chi_i = \omega \chi_i \chi_j \quad (i < j) \tag{2.58}$$

at the cost of the non-local strings extending across the chain.

Building a fermionic Hamiltonian

With a recipe for building parafermions in hand, we now consider how to construct a fermionic Hamiltonian from these objects. When doing so, we have the following desires:

1. The fermionic description should be local (i.e. involves at most nearest neighbour/next nearest neighbour interactions).

2. The fermionic description should be physically realizable (e.g. conserves parity).

In order to implement this, a possible strategy is to find a local fermionic description for the *clock operators* and then form combinations of parafermionic operators such that the non-local strings cancel, yielding a fermionic Hamiltonian that acts locally. Plugging in equation (2.57), possible 'legal' combinations of parafermionic operators are for instance:

$$\begin{aligned} \chi_{2j-1}^{\dagger}\chi_{2j} &= \chi_{2j-1}^{\dagger}\omega\chi_{2j-1}\tau_j = \omega\tau_j \\ \chi_{2j}^{\dagger}\chi_{2j+1} &= \omega^{*}\omega^{2}\chi_{2j-1}^{\dagger}\chi_{2j-1}\tau_j^{\dagger}\tau_j\sigma_j^{\dagger}\sigma_{j+1} = \omega\sigma_j^{\dagger}\sigma_{j+1} \end{aligned} \tag{2.59}$$

which are thus local in the clock operator description. If we then construct the clock operators in terms of local fermionic operators, the parafermionic Hamiltonian build from these terms will also remain local in the fermionic description. Notably, these terms are precisely the terms appearing in well-studied clock-models with interesting phase transitions (see section 2.3.2).

For a possible explicit implementation, we can start by working in a subspace where we can apply the matrix representation of the clock operators (equation (2.56)). A possible subspace is the $U \to \infty$ limit, where each site j is restricted to the basis $\{|0\rangle, |\uparrow\rangle, |\downarrow\rangle\}$. The allowed fermionic operators for creating the clock-operators then consists of the restricted subspace of *constrained fermions*, where each operator $\hat{o}$ is projected to $\hat{P}_j\hat{o}\hat{P}_j$ with $\hat{P}_j = 1 - n_{\uparrow,j}n_{\downarrow,j}$. This leaves 9 possible operator sequences that act locally in the constrained subspace. Namely:

$$\begin{aligned} &\widetilde{\mathbb{I}}_{\mathbb{j}} = \hat{P}_j \quad \widetilde{c}_{j,\downarrow} = \hat{P}_j c_{j,\downarrow}\hat{P}_j \quad \widetilde{c}_{j,\uparrow} = \hat{P}_j c_{j,\uparrow}\hat{P}_j \quad \widetilde{c}^{\dagger}_{j,\downarrow} = \hat{P}_j c^{\dagger}_{j,\downarrow}\hat{P}_j \quad \widetilde{c}^{\dagger}_{j,\uparrow} = \hat{P}_j c^{\dagger}_{j,\uparrow}\hat{P}_j \\ &\widetilde{n}_{\downarrow,j} = \widetilde{c}^{\dagger}_{j,\downarrow}\widetilde{c}_{j,\downarrow} \quad \widetilde{n}_{j,\uparrow} = \widetilde{c}^{\dagger}_{j,\uparrow}\widetilde{c}_{j,\uparrow} \quad \widetilde{c}^{\dagger}_{j,\uparrow}\widetilde{c}_{j,\downarrow} = c^{\dagger}_{j,\uparrow}c_{j,\downarrow} \quad \widetilde{c}^{j,\dagger}_{j,\downarrow}\widetilde{c}_{j,\uparrow} = c^{\dagger}_{j,\downarrow}c_{j,\uparrow} \end{aligned} \tag{2.60}$$

Using this, we can take the clock matrices equation (2.56) and directly build a fermionic representation of the clock operators (mapping the matrix elements to operators):

$$\begin{aligned} \sigma_j &= \widetilde{c}_{j,\downarrow} + \widetilde{c}^{\dagger}_{j,\uparrow} + \widetilde{c}^{\dagger}_{j,\downarrow}\widetilde{c}_{j,\uparrow} \\ &= c^{\dagger}_{j,\uparrow}c_{j,\downarrow}c_{j,\uparrow} + c_{j,\downarrow} + c^{\dagger}_{j,\downarrow}c_{j,\uparrow} + c^{\dagger}_{j,\downarrow}c^{\dagger}_{j,\uparrow}c_{j,\downarrow} + c^{\dagger}_{j,\uparrow} \\ \tau_j &= \widetilde{\mathbb{I}} + \omega\widetilde{n}_{j,\downarrow} + \omega^{2}\widetilde{n}_{j,\uparrow} \\ &= -2\,c^{\dagger}_{j,\downarrow}c^{\dagger}_{j,\uparrow}c_{j,\downarrow}c_{j,\uparrow} - \left(\frac{3}{2} + \frac{\sqrt{3}i}{2}\right)c^{\dagger}_{j,\uparrow}c_{j,\uparrow} - \left(\frac{3}{2} - \frac{\sqrt{3}i}{2}\right)c^{\dagger}_{j,\downarrow}c_{j,\downarrow} + 1 \end{aligned} \tag{2.61}$$

Through which we can construct a parafermionic system via equation (2.57) and equation (2.59):

$$
\begin{aligned}
H_{\mathbb{Z}_3} &= \sum_{j}^{N} \chi^{\dagger}_{2j-1}\chi_{2j} + \sum_{j}^{N-1} \chi^{\dagger}_{2j}\chi_{2j+1} + \text{h.c.} \\
&= \sum_{j}^{N} (\omega^{*}\tau_j^{\dagger} + \omega\tau_j) + \sum_{j}^{N-1} (\omega\sigma_j^{\dagger}\sigma_{j+1} + \omega^{*}\sigma_{j+1}^{\dagger}\sigma_j)
\end{aligned} \tag{2.62}
$$

where we can plug in the fermionic expressions for σ_j, τ_j As a first attempt this does not yield a correct system for the following two reasons:

1. The commutator $\left[\sigma_i, \sigma_j\right] = 0$ does not hold due to σ_j consisting of mixed odd and even terms.
2. The product $\sigma_j^{\dagger}\sigma_{j+1}$ in turn does not preserve parity.

The choice of clock operators, however, is not unique: a unitary transformation W on σ_i and τ_i, maintains the correct properties. Taking $\sigma_i' = W\sigma_i W^{\dagger}$ and $\tau_i' = W\tau W^{\dagger}$ one has:

$$
\begin{gathered}
(\tau')^3 = W\tau^3 W^{\dagger} = 1 \quad (\sigma')^3 = W\sigma^3 W^{\dagger} = 1 \\
\sigma'\tau' - \omega\tau'\sigma' = W\sigma\tau W^{\dagger} - \omega W\tau\sigma W^{\dagger} = 0 \quad (\sigma')^2 = W\sigma^2 W^{\dagger} = \sigma'^{\dagger}
\end{gathered} \tag{2.63}
$$

In addition, we can regain the required commutation across sites, by introducing yet another set of strings (this time the regular Jordan-Wigner construction, preserving the local algebra):

$$
\tau_j' = \tau'_{j,\text{(even)}} + \widetilde{S}_j \tau'_{\text{(j,odd)}} \qquad \sigma_j' = \sigma'_{\text{(j,even)}} + \widetilde{S}_j \sigma'_{\text{(j,odd)}} \tag{2.64}
$$

with $\widetilde{S}_j = \prod_{i=1}^{i<j}(1-2\widetilde{n}_{i,\downarrow,})(1-2\widetilde{n}_{i,\uparrow})$. Given this freedom, the question becomes whether there is a transformation W on σ_j,τ_j that results in a parity preserving fermionic Hamiltonian, when we interpret σ_j', τ_j' in the rotated basis $\{|0'\rangle, |{\uparrow}'\rangle, |{\downarrow}'\rangle\}$.

To analyse this, we note that this requires τ_j to be even in its fermionic description, while σ_j can in principle be either even or odd to ensure $\sigma_j^{\dagger}\sigma_{j+1}$ is even. For σ_j', as first attempt we can try to rotate to a basis where it is has either of the following forms:

$$
\sigma_j' = \begin{pmatrix} 0 & \cdot & \cdot \\ \cdot & 0 & 0 \\ \cdot & 0 & 0 \end{pmatrix} \qquad \text{or} \qquad \sigma_j' = \begin{pmatrix} \cdot & 0 & 0 \\ 0 & \cdot & \cdot \\ 0 & \cdot & \cdot \end{pmatrix} \tag{2.65}
$$

The left case can be immediately ruled out, since the form has an eigenvalue $\lambda = 0$, while the eigenvalues of σ_j are $1, \omega, \omega^2$. This leaves only the rightmost option, where σ_j' is even in fermionic operators. Interestingly, this also allows to conclude that it is not possible to have both the τ_j and σ_j terms simultaneously parity preserving through this method: writing both τ_j and σ_j in the rightmost form implies that they share an eigenvector (1,0,0), which is forbidden by their commutation relation. Any rotation W on σ_j that puts it on the even fermionic form, is therefore bound to mix even and odd terms in τ_j.

Through this approach, this leaves the option to generate a system from σ_j's that are even in their fermionic description. The general form of W that performs this mapping is:

$$W = \begin{pmatrix} \frac{1}{\sqrt{3}} & \frac{1}{\sqrt{2}} & \frac{1}{\sqrt{6}} \\ \frac{1}{\sqrt{3}} & -\frac{1}{\sqrt{2}} & \frac{1}{\sqrt{6}} \\ \frac{1}{\sqrt{3}} & 0 & -\frac{2}{\sqrt{6}} \end{pmatrix} \begin{pmatrix} e^{i\alpha} & 0 \\ 0 & U(2) \end{pmatrix} \tag{2.66}$$

with α a phase and $U(2)$ a unitary transformation. This yields for the case $\alpha = 1$, $U(2) = \mathbb{I}$:

$$\sigma_j' = W^\dagger \sigma_j W = \begin{pmatrix} 1 & 0 & 0 \\ 0 & -\frac{1}{2} & \frac{\sqrt{3}}{2} \\ 0 & -\frac{\sqrt{3}}{2} & \frac{1}{2} \end{pmatrix} \to \sigma_j' = \widetilde{\mathbb{I}} - \frac{1}{2}\widetilde{n}_{j,\downarrow} + \frac{1}{2}\widetilde{n}_{j,\uparrow} + \frac{\sqrt{3}}{2}\widetilde{c}^\dagger_{j,\downarrow}\widetilde{c}_{j,\uparrow} - \frac{\sqrt{3}}{2}\widetilde{c}^\dagger_{j,\uparrow}\widetilde{c}_{j,\downarrow} \tag{2.67}$$

Lastly, we need to map $\tau_j' = W^\dagger \tau_j W$ and add the required strings via equation (2.64). This makes τ_j' non-local in their fermionic description, which we set out to avoid. Fortunately we can choose to neglect the terms containing τ_j': we hide all the necessary fermionic and parafermionic ingredients in τ_j' and remain with desirable σ_j's. The following would then yield a fermionic Hamiltonian with both $\mathbb{Z}_3$ and $\mathbb{Z}_2$ symmetry:

$$H = \sum_j^{N-1} \chi_{2j}'\chi_{2j+1}' + h.c = \sum_j^{N-1} \omega\sigma_j'^\dagger \sigma_{j+1}' + \omega^* \sigma_{j+1}'^\dagger \sigma_j' \tag{2.68}$$

By construction, this Hamiltonian commutes with the $\mathbb{Z}_3$-symmetry operator $\hat{Q} = \Pi_i \tau_i'$, and has two $\mathbb{Z}_3$-edge modes (χ_1, χ_{2N}) that satisfy the two key properties:

1. $[H, \chi_1] = [H, \chi_{2N}] = 0$
2. $\chi_1 \hat{Q} = \omega \hat{Q} \chi_1$ and $\chi_{2N} \hat{Q} = \omega \hat{Q} \chi_{2N}$

As discussed in section 2.3.2, these properties ensure that the entire spectrum of the Hamiltonian is three-fold degenerate. This serves as a demonstration that a parity preserving, scalable fermionic Hamiltonian with built-in $\mathbb{Z}_3$ symmetry can in principle be created. What remains is to understand how a reverse mapping can be used to understand the $\mathbb{Z}_3$-structure of a given fermionic Hamiltonian (e.g. equation (2.45)).

3

EXPERIMENTAL METHODS

At the core of the experiments in this thesis lies an intricate setup that enables the interrogation of nanoscale, ultracold devices. Throughout the experimental chapters we are interested in probing electronic excitations of superconductor-quantum dot devices, to reveal the structure of even and odd parity subsectors. In particular, we aim to create a system that hosts Majorana zero modes, which manifest as peaks in device conductance at zero applied voltage bias. As main probe, we use tunneling spectroscopy techniques to measure currents and conductances, supplemented by radio frequency lead reflectometry techniques for fast device characterization. In section 3.1 we detail the relevant experimental techniques and the platform on which the devices are fabricated. The fabrication techniques specific to the material platform and the devices themselves have been excellently described in Refs. [127, 128]. Here, in section 3.2 we will instead focus in more detail on the typical tune-up procedures that precede the results presented in the experimental chapter and the device design considerations that affect the core building blocks of the experiments.

> *"Experimental physics is really, really so much fun"*
>
> - Dr. David van Driel

3.1 THE EXPERIMENTAL SETUP

THE experimental setup can be divided into three components. Firstly, we study nanoscale structures fabricated on indium–antimonide–arsenide (InSbAs) two dimensional electron gases (2DEGs) with epitaxially grown aluminium. Secondly, there are the quantum-mechanical building blocks: quantum dots, superconductivity and Andreev bound states. Although these are interesting in their own right, in this thesis they predominantly serve as foundation for constructing the Kitaev chain. Nevertheless, they are deserving of some extra attention. Finally, we have the electronical instruments that connect to the devices inside a dilution refrigerator. This allows to apply voltages and measure currents to observe the behaviour of the system when it is cooled down to 20 mK temperatures, a prerequisite for observing the physics of interest. We describe the material properties and experimental setup below, and dive deeper into the tune-up procedures in section 3.2.

3.1.1 PROPERTIES OF INSBAS WITH EPITAXIAL ALUMINIUM

The particular material stack used in this thesis was developed specifically for Majorana-related experiments [129], by combining the properties of two closely related 2DEG substrates. Indium arsenide (InAs) is known to interface well with aluminium [130, 131], being the first semiconductor where induced superconductivity was demonstrated [132, 133]. The good interface enables a strong proximity effect, which induces a robust superconducting gap in the semiconductor and has made InAs a well-established platform for hybrid experiments [130, 134, 135]. In contrast, indium antimonide (InSb) is less efficiently proximitized due to a band offset at the InSb-Al interface [136], but offers a larger effective g-factor and spin-orbit coupling strength. The material stack of the InSbAs-Al wafers is shown in figure 3.1. The quantum well is formed at the very top of the InSbAs lattice, near to the in-situ grown alunimum interface. The ratio of antimonide/arsenide has been varied in

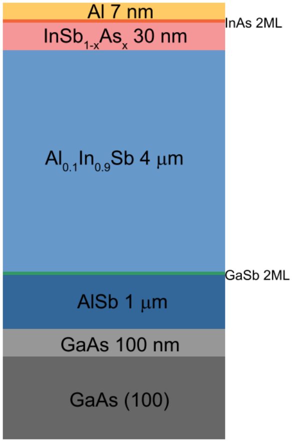

Figure 3.1: **Material stack of MBE-grown InSbAs-Al wafers.** Adapted from [129].

Electron density	$1 \times 10^{12}\,\mathrm{cm}^{-2}$
Electron mobility	$20\,000\,\mathrm{cm}^2/\mathrm{Vs}$
Effective mass m_e^*	$0.016 m_0$
Rashba spin-orbit α_{SO}	200-400 meV Å
InSbAs Landé g-factor	55
Al film thickness	7 nm
Induced SC gap Δ_{ind}	250 μeV*

Table 3.1: **Relevant Properties of the InSbAs-Al 2DEG stack.** Asterisk marks property extracted from devices in this thesis. Otherwise taken from [129].

the course of development of the material stack. The specific wafers used to fabricate the devices in this thesis contained a 13 % antimonide component.

Table 3.1 summarizes the properties of the material stack that are relevant to the experimental work. We note that other InSbAs platforms have been developed [137, 138]. The listed properties tie directly to the required elements for emulating a Kitaev chain treated in section 2.2:

- **Induced superconductivity** - the in-situ grown aluminium induces a hard superconducting gap in the quantum well, meaning there are no electronic states available at energies below Δ_{SC} in proximity to the superconductor. The superconducting correlations may extend into InSbAs over microns due the long coherence length of the semiconductor [137, 139].

- **Strong spin-orbit coupling** - a prerequisite for simultaneous crossed Andreev reflection and elastic co-tunneling between spin-polarised quantum dots [25].

- **Low effective mass and high mobility** - required for creating quantum dots with a sufficiently large level spacing between orbitals (see section 3.2).

- **High effective g-factor** - crucial for spin-polarising the quantum dots with an external magnetic field, such that effectively a single spin-species partakes in transport. The Zeeman energy of the quantum dots should ideally be larger than Δ_{ind}, at a magnetic field that is significantly lower than the critical field of the superconducting film.

An interesting aspect to note is that the spin-orbit coupling strength of InSbAs is larger than that of either InAs or InSb [140]. This is speculated to be a consequence of electrical fields accumulating at the interface with a dielectric material [129], which is introduced to isolate the conducting 2DEG layer from deposited gate electrodes.

For the dielectric material, a 20 nm layer of aluminium oxide (AlOx) is grown at 40 °C through atomic layer deposition. The choice for the low temperature deposition (compared to conventional >100 °C depositions) is a consequence of the rate of aluminium diffusing into the InSbAs layer becoming enhanced at higher temperatures, limiting the fabrication to below ≈50 °C. This poses additional limitations on the fabrication process: lithographically defined gates similarly cannot use a hot-baked PMMA mask. Instead, hardening of the mask has to occur in a room temperature vacuum, which can limit the resolution, adhesion and reproducibility that can be achieved through electron beam lithography techniques. Depending on the requirements, multiple dielectric layers and lithography-defined gate layers were used in order to minimize the possible spacing between neighbouring electrodes.

3.1.2 Multi-terminal DC and AC measurements

To study the properties of artificial Kitaev chain devices, we will be obtaining electronic transport measurements. A *device* in this context consists of a small region of conducting InSbAs 2DEG with aluminium, where the electrostatic landscape can be influenced by nanoscale gate electrodes (see section 3.2). In particular, we will be studying the differential conductance $G(V) = \mathrm{d}I(V)/\mathrm{d}V$ - the change in current through a devices with respect to a change in applied voltage bias. As a general principle, when the rate of tunneling of electrons from an external reservoir to a quantum mechanical system is low, such measurements can be directly related to the density of states of the system [141]. To perform these measurements, each device is contacted by normal metallic leads, in combination with gate electrodes that can alter the tunnelling rates of electrons. *Normal* here refers to a metal with a linear (ohmic) IV-characteristic (see figure 3.4), which at low temperatures can be modelled as an electronic reservoir following a Fermi-Dirac distribution. The aluminium superconducting segments in each device are electrically connected to ground, completing the circuit. The typical resistance of the devices in the regime of interest will be between $h/e^2 \approx 25\,\mathrm{k\Omega}$ (perfect resonant tunneling) and $>10\,\mathrm{M\Omega}$ (transport blockaded). Since we are interested in the low-energy behaviour of these devices, we will be applying small voltage biases between $-250\,\mu\mathrm{V}$ and $250\,\mu\mathrm{V}$ to the metallic leads (the typical size of the induced superconducting gap). For a $1\,\mu\mathrm{V}$ step size, the electrical circuitry should thus be able to resolve changes in currents on the order of a few pA.

The experimental setup used for obtaining DC and AC transport measurements is sketched in figure 3.2a. The connections are shown for a typical device with two normal contacts and one grounded superconductor. The resistance of the wiring down to the printed circuit board (PCB) is intentionally kept low such that applied voltage biases drop mainly over the larger device resistance. The device is brought in good thermal contact with the PCB via a heat-conducting adhesive (*GE varnish*) and electrically connected with aluminium bond-wires. In addition, each line passes through two low-pass RC-filters in series with a combined cut-off frequency around 100 Hz. Typical combined resistance of the wiring down to the device is on the order of $2\,\mathrm{k\Omega}$, mainly due to these filters.

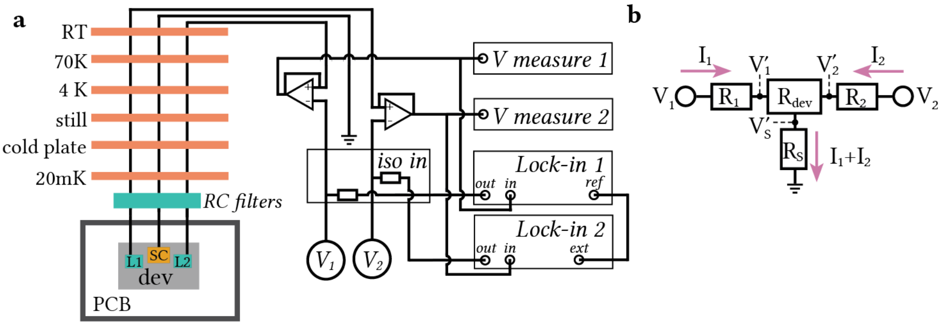

Figure 3.2: **Experimental setup for three-terminal AC/DC conductance measurements. (a)** Schematic overview of electronical components for a three-terminal conductance measurement. Voltage measurements are recorded with Keithleys, lock-ins are Keysight. **(b)** Simplified circuit diagram of voltages and currents in a three-terminal setup.

In this setup, the DC voltages V_1 and V_2 can be applied to leads L1 and L2 independently, resulting in currents I_1 and I_2 flowing through each respective path. Operational amplifiers convert the small currents flowing in the circuit to voltages on the order of ≈ 1 mV via a large resistance $R_{\text{op-amp}}$ of 10 MΩ, such that these can be easily resolved by the voltage measure instruments. The recorded voltages are interpreted as currents via $I_i = V_{i,\text{measure}}/R_{\text{op-amp}}$. To improve the measurements further, lock-in amplifiers are used that add a small (≈5 μV RMS) AC voltage on top of the DC voltages. In this way, a lock-in can measure the change $\mathrm{d}I_i$ directly by integrating over multiple oscillations $\mathrm{d}V_i$ supplied by the AC signal. The response outside of the input AC frequency is digitally filtered, bringing the additional benefit of filtering noise outside of a window around the source frequency ($f \pm \tau^{-1}$, where τ is the integration time). The AC signal is added via an isolated voltage divider, to suppress interference from external sources, such as the 50 Hz main line or transformers in equipment power supplies. By passing the output voltages arising from both I_1 and I_2 to each lock-in, we record the conductance matrix G_{ij} capturing the conductance of all transport paths in the device:

$$G_{ij} = \frac{\mathrm{d}I_i}{\mathrm{d}V_j} \tag{3.1}$$

In these setups it is common to distinguish *local transport* - currents between the lead and the superconducting ground, and *non-local transport* - currents running between two leads.

Care should be taken in interpreting lock-in measurements for various reasons, discussed in detail in Ref. [142]. First, for the response of any finite-frequency signal, the full complex impedance of all device components should be considered. In a fully resistive circuit, the AC input signal and resulting alternating output signal will always be in phase. Due to finite capacitances in the op-amp and between wiring, however, out-of-phase components will appear, increasing with higher frequencies. Additionally, the low-pass RC-filters at the 20 mK stage will diminish the amplitude of the input signal for higher frequencies closer to the cut-off requency. Generally, the higher the lock-in frequency, the larger the discrepancy between a conductance amplitude obtained via a lock-in and the amplitude derived from numerical derivative of the DC signal. The second effect to consider, is that the three-terminal setup results in a non-trivial voltage divider effect that arises from finite resistances of the filters and wiring leading up to the device. A model of the relevant currents, voltages and impedances in a three-terminal setup is sketched in figure 3.2b. The electrical wires have a typical resistance of 2 kΩ. The applied voltage V_1 will not correspond accurately to the voltage drop over the device $V_1' - V_S'$, if the device resistance is on the same order as the resistances R_1, R_s. These effects can be accounted for and corrected [143]. In general, we aim to keep the device resistance as high as possible (order of 100 kΩ) by pinching off the tunneling barriers as much as possible, such that these effects have a minimal impact.

3.1.3 RADIO FREQUENCY LEAD REFLECTOMETRY

The DC and AC measurement techniques discussed above are well suited for accurately measuring small currents and differential conductances. However, major down-sides of the techniques are the overhead of obtaining data point-by-point over a large parameter space and the relatively long integration times of the voltage measure modules and the lock-in amplifier. In most cases, we will be studying the differential conductance as a function of one or more gate voltages or applied voltage biases. Each voltage set-point adds ≈10 ms just from communication between the instruments and setting the voltages. For an accurate reading of the lock-in, the typical integration time is a few 100 ms or more. These factors add significant delay to the measurement time when exploring a large parameter space. For device characterization, we are generally not interested in determining a precise reading of the conductance, but rather in seeing for what parameters any finite conductance appears. During the course of the experimental work, faster methods for obtaining this information were gradually implemented. This is achieved via the technique of radio frequency (RF) lead reflectometry. For an extensive review of this technique, we refer to Refs. [144, 145].

In RF reflectometry, a resistive device with variable resistance R_{dev} is embedded in an LC resonator circuit, with resonance frequency $2\pi f_r = \frac{1}{\sqrt{LC}}$. A simple schematic overview of such a circuit is shown in figure 3.3a. The circuit is connected to a high-frequency voltage source via a transmission line, with standard characteristic impedance $Z_0 \approx 50\,\Omega$. If the impedance of the combined system Z_{load} is close to Z_0, most signal will be transmitted, whereas if $Z_{\mathrm{load}} \gg Z_0$ most signal will be reflected. The key to the technique is to choose L and C_{P} such that Z_{load} is close to Z_0 for typical values of R_{dev}, guaranteeing maximal sensitivity of the reflected or transmitted signals to changes in R_{dev}. This is known as *impedance matching*. Ideally, the resistances R_{L} should be as small as possible and R_{C} as large as possible. In this limit the matching condition is $R_{\mathrm{match}} = \frac{L}{Z_0 C}$, where R_{match} is the typical device resistance of interest, which guides the resonator design.

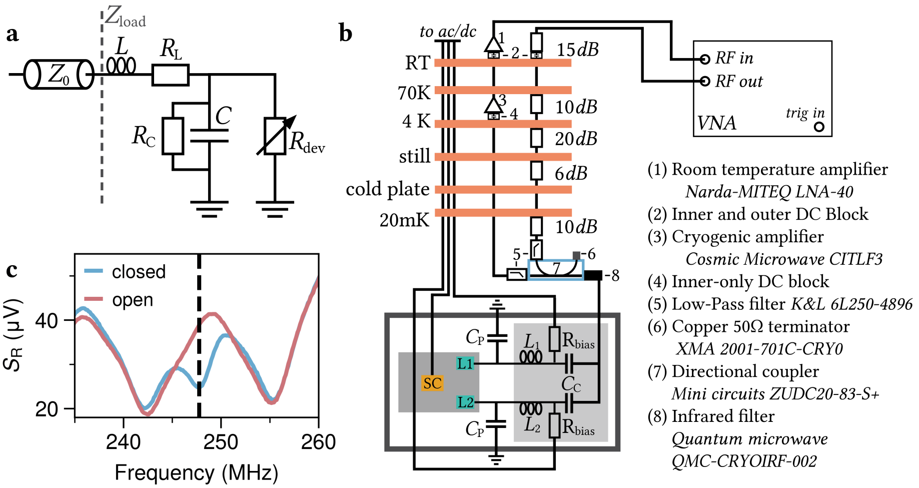
a
Z_{load}
Z_0
L
R_{L}
R_{C}
C
R_{dev}
b
to ac/dc
RT
70K
4 K
still
cold plate
20mK
1
2
3
4
5
6
7
8
15dB
10dB
20dB
6dB
10dB
RF in
RF out
VNA
trig in
C_{P}
L_1
R_{bias}
L1
SC
L2
C_{C}
L_2
R_{bias}
C_{P}
(1) Room temperature amplifier
Narda-MITEQ LNA-40
(2) Inner and outer DC Block
(3) Cryogenic amplifier
Cosmic Microwave CITLF3
(4) Inner-only DC block
(5) Low-Pass filter K&L 6L250-4896
(6) Copper 50Ω terminator
XMA 2001-701C-CRY0
(7) Directional coupler
Mini circuits ZUDC20-83-S+
(8) Infrared filter
Quantum microwave
QMC-CRYOIRF-002
c
closed
open
S_{R} (μV)
40
20
240
250
260
Frequency (MHz)

Figure 3.3: **Experimental setup for multiplexed radio frequency lead reflectometry. (a)** Circuit components for an LC resonator connected to variable resistance R_{dev}. **(b)** Schematic overview of electronical components for RF lead reflectometry. Each lead is connected to an LC matching circuit, fabricated on an additional silicon substrate. Schematic adapted from [127]. **(c)** Example of reflected RF signal S_{R} as a function of frequency for a device in the closed regime ($R > 10\,\mathrm{M\Omega}$) versus the same device in the open, resistive regime ($R \approx 50\,\mathrm{k\Omega}$).

Implementing this technique in the experimental setup requires combining the DC setup from section 3.1.2 with a suitable resonator circuit. The circuitry specific to the work in this thesis is shown in figure 3.3b. The InSbAs substrate is known to be lossy for high-frequency signals, so that we opt to fabricate the resonator circuit on a separate silicon substrate[1]. A bond-wire connects each ohmic lead in the InSbAS device to an inductor, which forms the LC resonator cavities via the combination with the capacitance to ground of the bond-wire (C_P). This is typically referred to as a parasitic capacitance and can generally not be accurately controlled. Different inductances are chosen such that different resonators have a sufficiently separated resonance frequency. The DC and AC signals enter via a resistor R_{load} ($\approx$10 kΩ), which blocks the high-frequency signals. Similarly, a capacitance C_C blocks the DC currents and voltages, effectively separating the RF and DC signals. The input RF signals are heavily attenuated on the path down to the device, such that the effective photon temperature matches the millikelvin environment. A directional coupler guides the reflected signals back down a separate path with minimal attenuation, where a cryogenic amplifier at 4 K and an amplifier at room temperature enhance the small reflected signals so that they can be recorded by the VNA. The response of multiple leads can be measured simultaneously by *multiplexing*, by sending different frequency signals and demodulating the reflected signal accordingly.

A demonstration of the technique is shown in figure 3.3c. We obtain the reflected signal of a resonator connected to an ohmic contact of a device, as a function of frequency. Gate voltages allow to open or close the path to ground, to compare the response when we have an open (resistive) device or a closed (pinched off) device. When the device is pinched off, the reflected signal dips around the LC resonator frequency f_R. When the device is open, the dip disappears as Z_{load} approaches Z_0 and the high frequency signal is transmitted. To infer the device's conductance, we apply a constant frequency pulse around f_R, where the response in reflected signal is maximal as a function of R_{dev}. Ideally, there is a linear mapping between this response and the device conductance. Due to the short integration time of this technique (on the order of microseconds), a major speed-up can be achieved in characterising devices. A practical example of this is highlighted in section 3.2.4.

3.2 Characterising a QD-ABS-QD system

In order to study the interactions of quantum dots coupled via Andreev bound states, each of these components needs to be characterised individually. Their properties should be in correspondence with the assumptions discussed in section 2.2.4. The quantum dots require large Zeeman energies and well separated orbitals and the Andreev bound state should be extended, discrete levels within a hard superconducting gap. We discuss these characterisations here, which apply in principle to all the experimental chapters. The presented experimental data are selected from measurements obtained over multiple devices. For pedagogical reasons, this skews the selection in this chapter towards the clearest datasets.

An SEM image of a typical device, used in this thesis to study crossed Andreev reflection and elastic co-tunneling in Chapter 4, is shown in figure 3.4a. Initially, each chip starts as a 5 mm by 5 mm surface of conducting 2DEG substrate, fully covered with 7 nm of alumunium. For each device, a small segment of InSbAs 2DEG is electrically isolated through chemical

---

[1] For the development of the RF measurement setup and resonator chips I am grateful to Christian, Ivan, Qing and Yining.

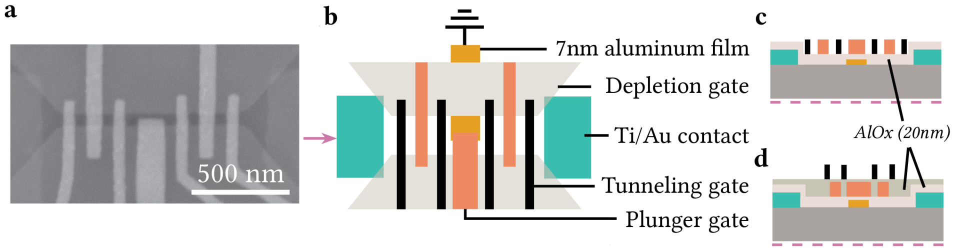

Figure 3.4: **Overview of an exemplar two-site Kitaev chain device. (a)** Scanning electron microscope image of an exemplar device used to study the coupling of quantum dots via Andreev bound states. A thin aluminium strip extends below the large top depletion gate into the channel between the two depletion gates (not visible in this SEM). **(b)** Schematic overview of the main components of a device. **(c)** Side-view of components for a cut along the channel, in between the depletion gates (not to scale). Grey layers represent 20 nm AlOx. **(d)** Side-view of a device design with an extra dielectric layer to separate the plunger gates and tunneling gates to decrease the spacing between neighbouring gates.

etching of unneeded aluminium and InSbAs, by etching sufficiently deep into the InSbAs layer. Next, a thin superconducting strip is created with a lithographically defined PMMA mask, again removing excess aluminium via chemical etching with *Transene D*. Contacts and gates are deposited via standard electron beam lithography and metal evaporation techniques. To create a proper galvanic connection to each device, argon milling is used to remove any unwanted oxides before depositing the titanium/gold contacts.

3.2.1 Forming a one-dimensional channel

As first characterisation for each device, a narrow conductance channel needs to be isolated to ensure that current can only pass to the superconductor via the channel where quantum dots and Andreev bound states will be located. The InSbAs 2DEG is conducting at low temperatures and needs to be selectively depleted. To do so, we apply voltages to the two large depletion gates that fully cover the regions where a conductance path to ground is undesired. Each depletion gate has a threshold voltage below which current is prevented from flowing underneath the region covered by the gate. In order to calibrate the threshold voltages, we apply an equal voltage bias to the left and right ohmic contacts (V_1, V_2) and monitor the currents I_1, I_2 to the superconductor, which remains as the only path for currents to ground. A typical measurement for a functional device is shown in figure 3.5a.

In these measurements five distinct regimes can be identified, illustrated in figure 3.5b:

① - Neither depletion gate is below threshold, so that current paths are available below both depletion gates

② and ③ - Full depletion below only one of the depletion gates, current flow remains below the non-depleted gate.

④ - The desired regime: both depletion gates below threshold, remaining current must flow via the channel between the gates.

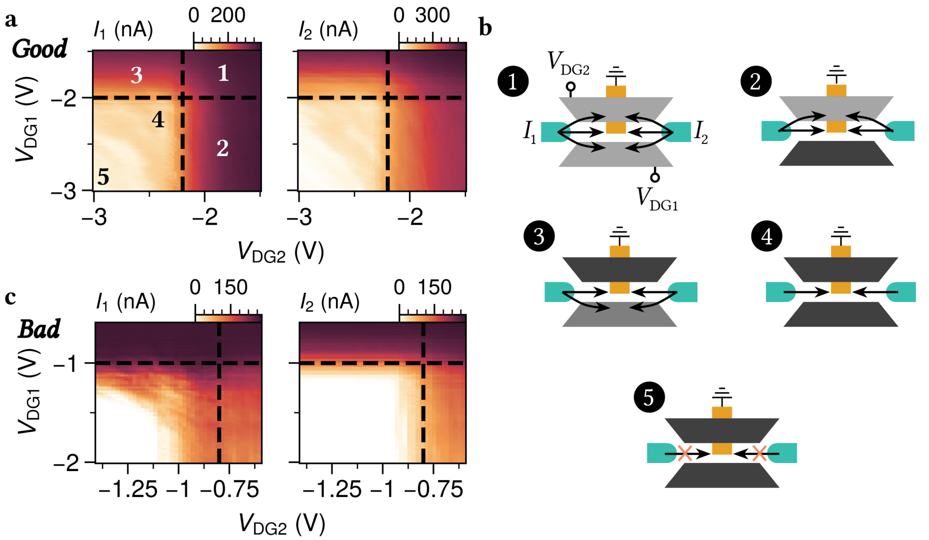

Figure 3.5: **Tuning the depletion gates to form a 1D channel. (a)** Example of a depletion gate characterisation measurement. Currents I_L and I_R are measured while varying V_{DG1} and V_{DG2}, with equal applied voltage biases V_L, V_R (1 mV). In a functional device, five distinct regimes can be identified, described below. **(b)** Schematic illustration of current flow in the five regimes of depletion gate settings indicated in (a). **(c)** Example of a poorly functional device. An asymmetry is clearly visible between I_1 and I_2, indicating that the right side of the channel closes much quicker than the left side of the channel. Applied voltage bias is 2 mV to both contacts.

> ⑤ - Fringing fields in the channel between the depletion gates start to pinch-off the channel, ultimately cutting of current flow completely.

The size of the functional region ④ is ideally as large as possible, which will be affected by the separation between the depletion gates and the electrostatics in the dielectric layer. Placing the depletion gates closer together generally should result in the channel closing more rapidly. Placing them too far apart, however, negatively impacts the size of the quantum dots that will be formed inside the channel, lowering their level spacing. Additionally, the region where current flows through the channel in the I_1 measurement should be equal to the region observed in the I_2 measurement. Imperfections in the design may result in one side of the channel pinching off more quickly than the other side, as shown in figure 3.5c.

It should be noted that the choice of large depletion gates used here is not a common design for quantum dot devices studied in InSb, InAs and GaAs structures, which often use a single layer of thin gates for confinement of charges [146]. The choice of using the large structures here comes from two goals beyond the contents of this thesis. The first goal is the desire to scale these types of devices to larger systems with more than three quantum dots, with channels running in two dimensions. The large gates are economical in isolating currents to the desired regions, reducing the number of gates per additional quantum dot compared to a single gate-layer design. A second goal is the use of a technique called *gate reflectometry* [145], which allows to probe the charge of a system that is not electrically connected to an ohmic reservoir. In this technique, similar to lead reflectometry discussed above, radio-frequency voltages are applied to tunneling or plunger gates via a resonator circuit. The reflected signal from such a circuit becomes sensitive to a capacitive coupling to charges within the channel. Without the large depletion gates, these signals can leak to ground via a capacitive coupling to non-depleted 2DEG regions that are in connection with the ohmic contacts (which have a low resistance to ground for aforementioned reasons). By ensuring the gates are only capacitively coupled to the depletion gates, this leakage signal can be avoided by the addition of a large resistance in this path to ground. This technique, in a similar device architecture, is discussed in Refs. [147, 148].

3.2.2 Forming quantum dots

Once a conductance channel is isolated via tuning of the depletion gates, we can start to form the building blocks of the Kitaev chain. First we introduce the experimental properties of quantum dots, which we want to use as (effectively) spinless fermionic sites. In the theoretical discussion, we treated quantum dots as zero-dimensional objects hosting a single spin-polarised orbital. Experimentally, they are realized by electrostatically isolating a small segment of semiconductor. To capture the physics of such a structure, both classical and quantum mechanical effects must be considered. On the classical side, there is Coulomb repulsion arising from bringing negatively charged electrons close together. On the quantum side, the allowed electron energies on the island become discrete, similar to a “particle in a box”, once its dimensions are comparable to the Fermi wavelength in the quantum well.

A circuit diagram of a typical quantum dot setup is sketched in figure 3.6a. In this picture, the quantum dot is modelled as a small island with a well-defined number of electrons N, connected to a source and a drain through parallel resistive and capacitive elements. For N to remain well defined[2], the resistance to source and drain should satisfy $R_S, R_D \gg h/e^2$. The source-drain potential difference is set by the bias voltage V_{SD}=V_{S}-V_{D} and a voltage V_{G} can be applied to a nearby gate with capacitive coupling to the quantum dot C_{G}. We are interested in the conditions on V_{G} and V_{SD} under which a finite current flows through the quantum dot. A simple way to describe this is provided by the *constant interaction model*, which relies on two assumptions. The first, is that the Coulomb interactions are fully captured by the total, constant capacitance of the quantum dot to its surroundings $C = C_{\mathrm{G}} + C_{\mathrm{S}} + C_{\mathrm{D}}$. The second, is that the energy difference of consecutive quantized levels $\Delta E = E_{i+1} - E_i$ is independent of these interactions and taken to be constant. The electrostatic energy of the island as a function of N is then given by [67, 149, 150]:

$$E(N) = \frac{(-eN + C_S V_S + C_D V_D + C_G V_G)^2}{2C} + \sum_n^N E_n \tag{3.2}$$

up to an omitted constant that is independent of N. The energies E_n are the assumed solutions to the ‘particle in a box’ Schrödinger equation, which depend on the specifics of the confinement potential. Given that there are $N-1$ electrons on the island, we want to know the energy cost of adding the Nth electron. This is the electrochemical potential

---

[2] This condition arises from the uncertainty relation $\Delta E \Delta t \gtrsim h$, inputting for ΔE the typical charging energy e^2/C and for Δt the characteristic time of charging a capacitor RC.

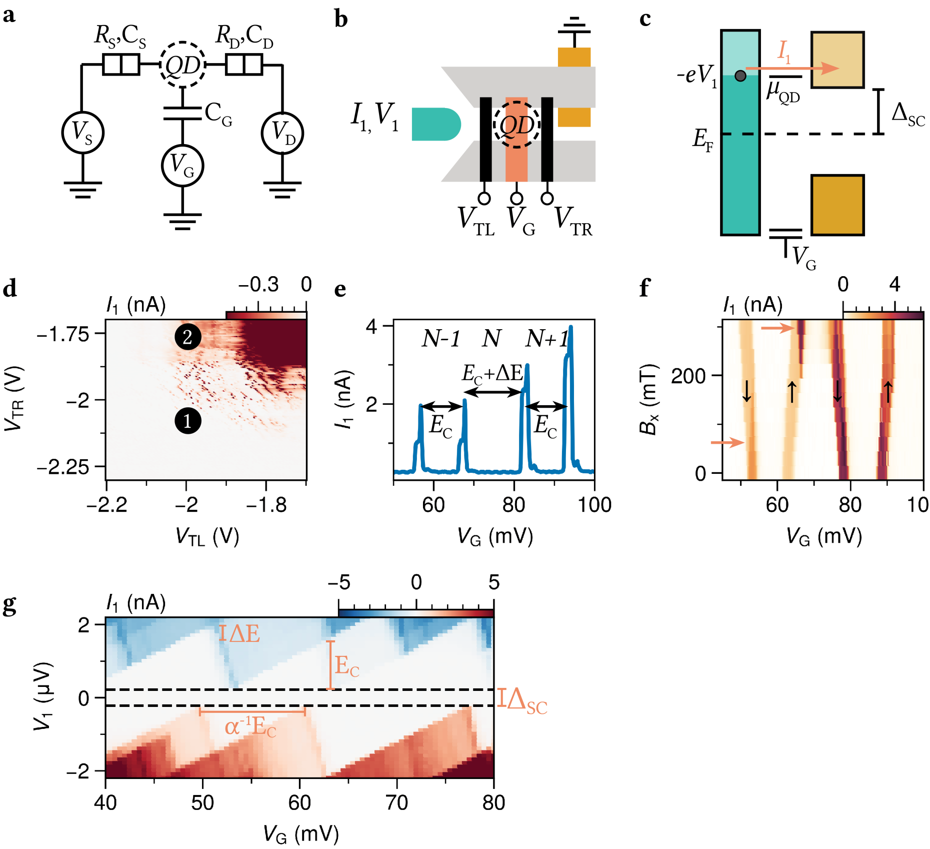

Figure 3.6: **Characterising the quantum dots.(a)** Circuit model of a quantum dot setup. **(b)** Schematic of relevant voltages and currents used for characterising a quantum dot in the experimental device. **(c)** Semiconductor picture of transport through a QD from a normal lead to a superconducting lead. **(d)** Initial characterisation measurement of the tunnelling gates V_{TL} and V_{TR}. **(e)** Coulomb resonances in current measured as a function of the plunger gate voltage V_{G}. The spacings are proportional to the charging energy E_C and the level spacing ΔE. **(f)** Coulomb resonances as a function of external magnetic field, showing the effects of Zeeman splitting. Pink arrows highlight additional features arising from spin-states becoming available or unavailable for transport, reflected in the current amplitude. **(g)** Current measured as a function of V_1 and V_{G}, showing Coulomb diamond features within which current is blockaded.

energy $\mu(N)$, defined as:

$$\mu(N) = E(N) - E(N-1) = \frac{e^2}{C}(N - \frac{1}{2}) - \frac{e}{C}\sum_i C_i V_i + E_N \tag{3.3}$$

Finally, this lets us derive the addition energy, or the energy difference between two consecutive electron occupations:

$$E_{\mathrm{add}}(N) = \mu(N) - \mu(N-1) = \frac{e^2}{C} + \Delta E \tag{3.4}$$

From this expression we see that the typical cost of adding an electron to the system is $E_C = \frac{e^2}{C}$, called the charging energy, plus the quantized level spacing ΔE. Experimentally, we desire energy scales to be as large as possible. For the charging energy, this means reducing the total capacitance, which can be achieved by decreasing the size of the QD, increasing the distance to the gates or changing the dielectric to a lower κ material. The level spacing ΔE is experimentally not a constant factor as assumed here, and depends on the microscopic potentials in the system as well as the dimensionality. As a simple guide, for an electron with effective mass m^* in an n-dimensional box of dimension L, the following holds for the level spacing at the Fermi energy [150]:

$$\text{(1D)} \quad \Delta E \propto \frac{N}{m^* L^2} \qquad\qquad \text{(2D)} \quad \Delta E \propto \frac{1}{m^* L^2} \tag{3.5}$$

The relevant device components for controlling and characterising a quantum dot in the experimental setting are illustrated in figure 3.6b. Two voltages V_{TL},V_{TR} applied to tunneling barriers control the effective resistance of each junction. The voltage V_{G} controls the gate voltage, typically called a plunger gate. The potential difference between source and drain is controlled by V_1 and the current I_1 is monitored. A subtle difference arises due to the drain in the setup being a superconducting lead, rather than a normal metal. The effect of this is best understood by considering electron transport through the quantum dot in the semiconductor picture, shown in figure 3.6c. The voltage V_1 raises or lowers the available energies of electrons in the normal lead, while the grounded superconductor has an available density of states above the energy gap Δ_{SC}. The electrochemical potential of the quantum dot is directly controlled by V_{G}, as seen from equation (3.3):

$$\mu_{\mathrm{QD}} \propto \frac{eC_{\mathrm{G}}}{C} V_{\mathrm{G}} \tag{3.6}$$

The proportionality constant $\alpha = \frac{C_{\mathrm{G}}}{C}$ is called the *leverarm*. The working principle for understanding transport in the system is as follows: electron transport to the quantum dot is only possible when μ_{QD} lies at or below the potential of the lead, set by V_1. In turn, transport to the superconductor is possible when there is an available density of states in the superconducting lead aligned with the chemical potential, completing the transport cycle. The opposite principles hold for the reverse current direction.

To characterize the quantum dot's properties, we first sweep the tunnelling barriers V_{TL} and V_{TR} while applying a constant voltage bias ($> \Delta_{\mathrm{ind}}/e$), shown in figure 3.6d. In the low tunneling regime ①, current oscillations start to appear, signifying the formation of a quantum dot. Next, we measure the current as a function of the plunger gate voltage V_{G}, shown in figure 3.6e. Peaks in current arise periodically, when $-eV_1 > \mu_{QD} > \Delta_{\mathrm{SC}}$. In between these peaks transport is prohibited, known as Coulomb blockade, where the number of electrons on the quantum dot remains constant. Crucially, we observe here an alternating pattern of small and large spacings between consecutive peaks: each spin-degenerate orbital accepts two electrons, so that the effect of a finite ΔE is only visible every second peak. This is what allows for spin-polarising the Coulomb resonances, by applying an external magnetic field B. The magnetic field leads to a spin-dependent correction to the level-spacing due to the Zeeman energy:

$$E_z^{\uparrow,\downarrow} = \mp\frac{1}{2}\mu_\mathrm{B} g B \tag{3.7}$$

The constant g is a material-specific property called the *g-factor*. Figure 3.6f shows the response of the Coulomb resonances to a magnetic field, where resonances belonging to the same orbital are observed moving in opposite directions. Once sufficient magnetic field is applied, transport through each resonance is dominated by a single spin-species. It should be noted that the state lowering in gate voltage is denoted spin-↓ rather than the expected spin-↑, which is a consequence of the negative g-factor of electrons in InSbAs[3]. To convert this change in gate voltage to an energy scale, we need to measure the leverarm α. This can be obtained by measuring I_1 as a function of both V_1 and V_G, shown in figure 3.6g. This measurement maps out so-called *Coulomb diamonds*: regions in which transport is blockaded due to misalignment of μ_QD and eV_SD. The tilted shape of the Coulomb diamonds is a result of asymmetry between the capacitive couplings to source and drain C_S and C_D. From the slopes of the edges of the Coulomb diamonds, the leverarm can be accurately extracted.

3.2.3 Superconductivity and Andreev bound states

The next building blocks of the experimental Kitaev chain are discrete, extended Andreev bound states located in the InSbAs region in proximity to the superconductor. Ideally, we require control over a single discrete level, with no other sub-gap transport paths available. Since we intend to tunnel-couple a quantum dot to either side of this state, the spatial extend should allow for wavefunction overlap with both quantum dots. The relevant gates for characterising the hybrid region are sketched in figure 3.7a. The operating principles are similar to forming a quantum dot in the previous section. The voltages V_TL,V_TR applied to the tunnel gates adjacent to the superconducting segment are used to create a small confined region surrounding the superconductor, with low tunneling rates to the normal leads on either side. In the low-tunneling regime, the induced hard-superconducting gap manifests as a blockade of current for applied voltages within eV_1=$\pm\Delta_\mathrm{SC}$ (figure 3.7b). This can be converted to differential conductance directly via numerical derivative (figure 3.7c), revealing sharp coherence peaks.

Next, we search for discrete sub-gap states that allow for transport to occur at energies below Δ_ind. Such states will disperse as a function of the voltage V_ABS applied to the gate covering the hybrid segment. A typical measurement is shown in figure 3.7d, recording the local conductance G_{11} and non-local conductance G_{21} when voltage biasing the left contact. A similar measurement is performed from the opposite contact (figure 3.7e), to obtain G_{22} and G_{12}. A discrete excitation is observed in each of these four measurements. From these measurements, we extract three important pieces of information. First, the dispersion reaches a minimum and does not cross V_1=0, indicating the ground state remains the BCS singlet $|S\rangle$=$u|0\rangle$-$v|2\rangle$ (section 2.2.2). Secondly, the appearance of the same feature in all four measurements shows that the underlying state enabling transport is extended across the

---

[3] The g-factor can be related to the band gap of a semiconductor via the Roth formula $g = g_e - \frac{2}{3}\frac{\alpha_\mathrm{SO}}{E_\mathrm{g}(\alpha_\mathrm{SO}+E_\mathrm{g})}E_\mathrm{P}$[151], where $g_e \approx 2$ is the normal electron g-factor, α_SO the spin-orbit strength and E_g the band-gap.

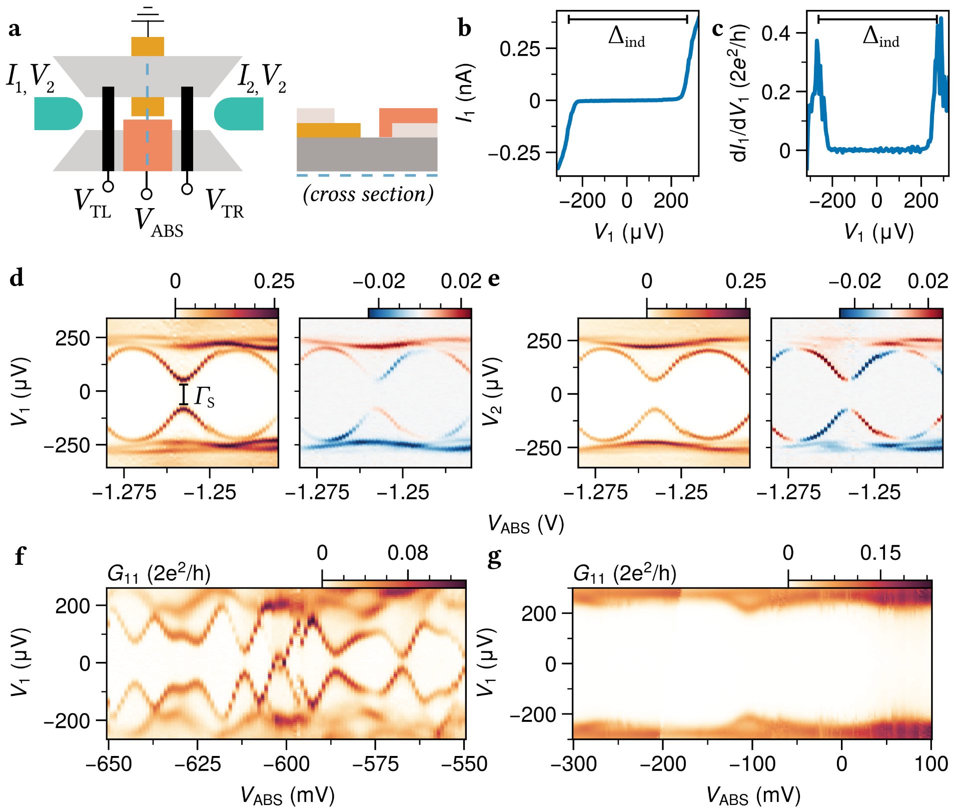

Figure 3.7: **Characterising the hybrid segment.** **(a)** Schematic overview of relevant voltages and currents used for characterising a hybrid segment. Cross section on the right shows relative position of the different layers on top of the 2DEG substrate (omitting the dielectric layers). **(b)** Exemplar IV trace, with voltages V_{TL} and V_{TR} tuned to a low-tunneling rate into the hybrid from both sides. A clear plateau is observed where I_{L}=0. **(c)** Direct numerical derivative of the measurement. The numerical derivative is an accurate way to probe conductance, but typically less successful at filtering noise compared to using a lock-in amplifier. **(d)** Measurement of G_{11} and G_{21} as a function of V_{ABS}, for a range showing the dispersion of a single Andreev bound state. **(e)** Measurement in the same range of V_{ABS}, from the opposite lead, showing the same discrete state in G_{22} and G_{12}. The sub-gap density of states in the hybrid segment can strongly vary depending on device design, shown here by larger range V_{ABS} scans **(f)** and **(g)** for two different devices.

entire hybrid segment. Lastly, the non-local measurements G_{12} and G_{21} can be directly related to the charge of the singlet state, as both are proportional to the BCS coherence factors $|u^2| - |v^2|$. The change in sign of these non-local conductances show that the charge character of the excitation can be smoothly controlled, which is a crucial prerequisite for controlling the relative amplitudes of virtual ECT and CAR processes.

In the theory section 2.2.2, we modelled the hybrid section as a quantum dot with superconducting correlations. In the limit of large Γ_S and small U, the ground state is expected to be a BCS singlet and we call the sub-gap state in such regime an Andreev bound states (ABS). While the observed behaviour qualitatively fits this description, it should be noted that the depletion gates are unable to deplete the semiconducting region underneath the superconductor. In the semiconducting layer, there is therefore no actual confinement in the direction underneath the superconductor, as seen in the cross section in figure 3.7a. Nevertheless, the observation of well-separated Andreev bound states suggests the spatial extend of the states is comparable to the neighbouring quantum dots. As a possible explanation, we suspect that the confinement arises from the strong induced superconductivity directly below the aluminium. This can induce a mismatch in the Fermi velocity between the InSbAs directly below the aluminium and the non-covered regions, leading to a scattering off of this interface [152]. We further note that we observe the density of states in the hybrid segment to be affected by confinement in a similar fashion as expected for quantum dots. We compare two measurements in figure 3.7f,g obtained on two separate devices. The size of the hybrid segment was reduced in the design of the device where the measurement in (g) was obtained, which we suspect results in the significantly lower density of sub-gap states and decreased charging energy.

3.2.4 RF CHARGE-STABILITY DIAGRAMS

Once the quantum dots and Andreev bound states are electrostatically defined, the main objective of this thesis will be to study how an Andreev bound state facilitates transport that couples the separated quantum dots. To characterise the interaction between two quantum dots, or between a quantum dot and an Andreev bound state, we obtain so called charge-stability diagrams. In such a measurement, the gate voltages controlling the relevant chemical potential energies are varied, while attached Ohmic leads are kept at zero voltage bias. By recording either current or conductance, this maps out the conditions under which electrons can enter the system, which can only occur when there is a ground state degeneracy. The underlying physics is discussed in more detail in Chapter 5. Here we show the technique used for speeding up these measurements with RF lead reflectometry.

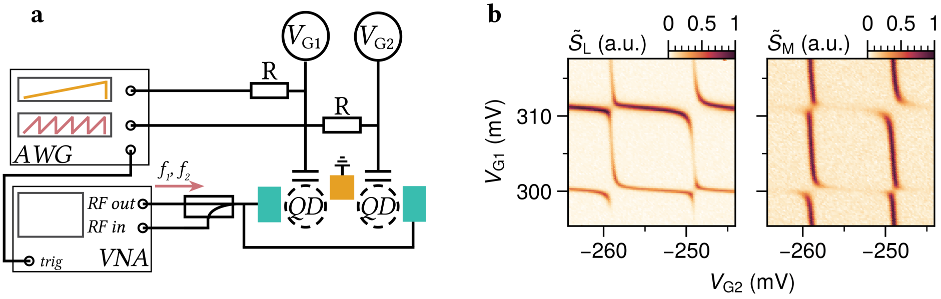

Figure 3.8: **Measuring fast charge stability diagrams with lead reflectometry. (a)** Schematic of setup for rasterized charge stability diagram measurements, using sawtooth pulses on two AWG channels to drive the quantum dots. **(b)** Example of a multiplexed high-resolution charge stability diagram of two tunnel-coupled quantum dots, obtained with the method displayed in (a). The 100x100 datapoints were obtained at 10 Hz on the fast sawtooth, repeated 5 times and averaged, for a total measurement time of 50s compared to > 60 minutes required for an DC/AC equivalent.

The setup is shown in figure 3.8a (omitting the full DC and RF components discussed in section 3.1). An AWG is used to generate two sawtooth pulses, which are added to the DC gate voltages V_{G1}, V_{G2} controlling the quantum dot potentials via a 20 Ω resistor. A slow pulse is applied to one QD, while N pulses are applied to the other. The VNA is triggered to record continuously the reflected signal of two multiplexed frequencies, corresponding to the resonators attached to either lead. A typical measurement is shown in figure 3.8, which are used to characterize the interdot couplings throughout this thesis.

3.2.5 Calibrating the QD-ABS coupling

An important consideration in the full QD-ABS-QD system is the tunnel coupling between each QD and the hybrid segment. The goal is to use the Andreev bound states to mediate the virtual ECT and CAR processes between the QDs. The amplitudes of these processes depend on the charge and energy of the Andreev bound state, but are also proportional to the tunneling amplitudes of the left and right QD into the hybrid section. For this purpose, the tunneling rates between each QD and the hybrid segment should be kept as high as possible (Regime ② in figure 3.6), which can be directly controlled by the tunneling gates located in between each QD and the ABS.
There are, however, two caveats:

1. A high tunneling rate increases the overlap of the QD states within the hybrid segment, decreasing the Majorana polarisation [79].
2. Coupling a normal QD too strongly to a proximitized QD can drive a doublet-singlet transition in the normal QD.

An experimental setup considering just a single QD and the hybrid segment is illustrated in figure 3.9a. This subsystem can be treated as two quantum dots, with one coupled to a normal contact and the other coupled to a superconducting contact (figure 3.9b). This system is treated in detail in Refs. [153, 154]. To model this, we borrow the building blocks developed in section 2.2 and extract the ground-state parity of a normal quantum dot with a finite charging energy U, coupled to a strongly proximitized quantum dot with zero charging energy and finite superconducting pairing Γ_S.

The ground-state phase diagram as a function of μ_{QD} and μ_{ABS} are plotted in figure 3.9c-e, for varying tunnel coupling t between the two subsystems. For large coupling t, the When t approaches Γ_S, the energy of the ABS drives a transition of the doublet QD ground-state to a YSR-singlet in a significant parameter space. Such a regime is not operational for creating a Kitaev chain, as the condition $\mu_{QD} = 0$ cannot be met for a large range of μ_{ABS}. Experimentally, these interactions can be studied by measuring charge stability diagrams as a function of V_{QD} and V_{ABS}. Varying V_T can be used to calibrate the coupling. Notably, the coupling will also vary orbital to orbital due to specifics of the quantum dot wavefunctions. A great demonstration of this is provided by the measurement shown in figure 3.9f[4].

---

[4] Measurements were obtained with an equivalent nanowire device [80], kindly provided by Francesco Zatelli and David van Driel.

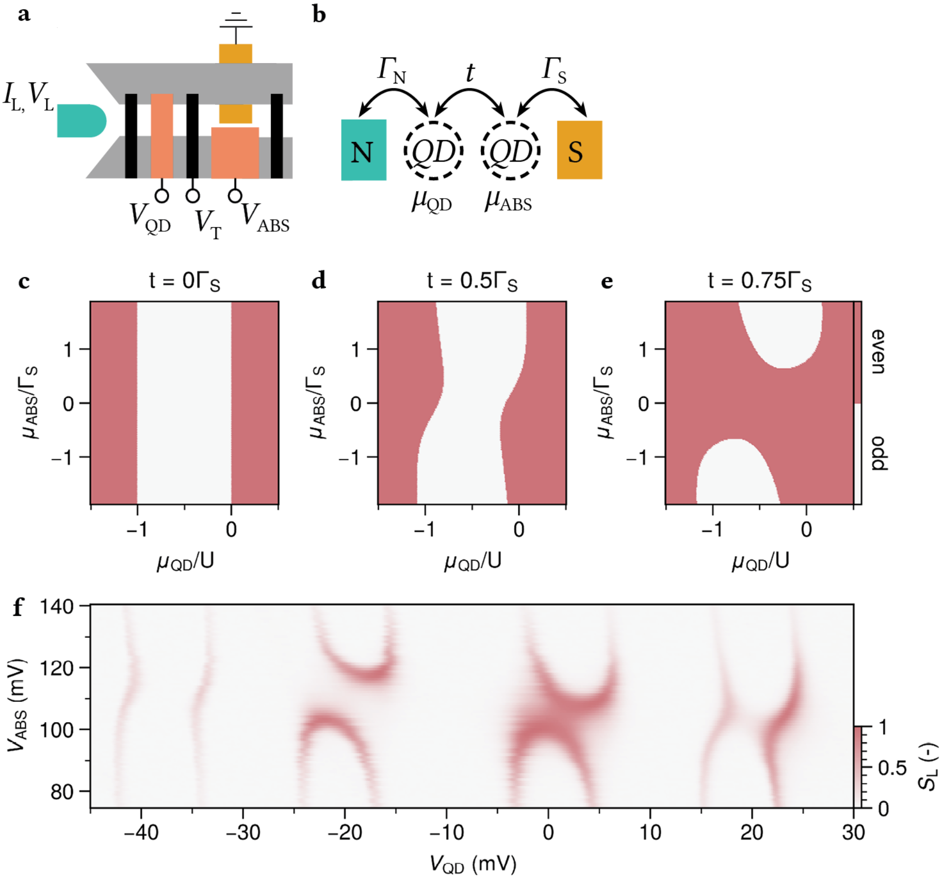

Figure 3.9: **Characterizing the tunneling rate between a normal quantum dot coupled to a proximitized quantum dot. (a)** Schematic overview of relevant voltages and currents for characterising the tunneling rate between a quantum dot and a hybrid segment. **(b)** Relevant parameters capturing the interaction between a quantum and an Andreev bound state. **(c)** Without any coupling ($t = 0$), the ground-state parity of the quantum dot is solely decided by μ_{QD}. **(d)** As the coupling is increased, the charge degeneracy point of the QD is renormalized as a function of μ_{ABS}. **(e)** Beyond a critical coupling, μ_{ABS} can generate a region where the QD remains in the singlet ground state for all μ_{QD}. **(f)** Exemplar measurement of a QD-ABS phase diagram obtained through lead reflectometry, showing four neighbouring orbitals either weakly coupled or strongly coupled to an Andreev bound state. This measurement serves to demonstrate the existence of the different regimes (d),(e), but also shows that the coupling t is orbital dependent.

4

PROBING ELASTIC CO-TUNNELING AND CROSSED ANDREEV REFLECTION

So far we have established the theoretical and experimental tools required to engineer a Kitaev chain. As the first step of the experimental investigation, we present a study of the two virtual subgap tunneling processes required for implementing a Kitaev chain: elastic co-tunneling (ECT) and crossed Andreev reflection (CAR). By coupling two quantum dots to a semiconductor–superconductor hybrid segment, we gain precise control over the energy and spin of electrons injected into the hybrid system. This enables us to extract information about CAR and ECT rates as a function of various system parameters. In particular, we investigate the role of spin–orbit coupling, by rotating the alignment of an external magnetic field. We observe that strong spin-orbit interactions allow for significant crossed Andreev reflection between two quantum dots with an equal spin-alignment, effectively implementing the p-wave superconducting pairing required for constructing a Kitaev chain.

Zeiden alle and're spinnen:
O, Sebastiaan, nee, Sebastiaan,
kom, Sebastiaan, laat dat nou,
wou je aan een web beginnen
in die vreselijke kou?

- Annie M.G. Schmidt

The work in this chapter has been published as: *Triplet correlations in Cooper pair splitters realized in a two-dimensional electron gas*, Qingzhen Wang†, **Sebastiaan L. D. ten Haaf**†, I. Kulesh, Di Xiao, Candice Thomas, Michael J. Manfra and Srijit Goswami, *Nature Communications* **14**, 4876 (2023) [155].
Personal contribution includes device fabrication, obtaining measurements and writing of the manuscript.
†Authors contributed equally

4.1 INTRODUCTION

Cooper pairs occupy the ground state of superconductors and are composed of maximally entangled electrons with opposite spin. Coupling two normal leads to a superconductor gives rise to non-local transport processes directly involving both leads. For instance, two opposite-spin electrons from a Cooper pair in the superconductor can be split into the leads via a process known as Cooper pair splitting (CPS). The dominant transport mechanism that gives rise to CPS is crossed Andreev reflection (CAR), whereby a higher order process allows two electrons to be injected simultaneously into the superconductor to form a Cooper pair. Additionally, a single electron can tunnel through the superconductor from one lead to the other through a process known as elastic co-tunnelling (ECT). The ability to control these processes has important implications for two distinct fields. Firstly, CAR and ECT are crucial ingredients required to implement a Kitaev chain [14] using quantum dot-superconductor hybrids [33, 37], which is the main focus of this thesis. Secondly, efficient CPS can be used to generate spatially separated entangled electrons, that could be used to perform a Bell test [156–161].

Cooper pair splitting has been studied in various mesoscopic systems coupled to superconductors, such as semiconductor nanowires [45–47, 162], carbon nanotubes [48, 49], and graphene [163]. Generally in these experiments, quantum dots (QDs) are introduced between the leads and the superconductor to enhance the desired signals. The charging energy of the QDs ensures that electrons forming a Cooper pair preferentially split into separate dots, rather than occupying levels in the same dot. This results in correlated electrical currents at the two normal leads. It has thus far been challenging to independently measure the relevant virtual processes (i.e. ECT and CAR) and isolate them from local processes, such as normal Andreev reflection or direct tunnelling via sub-gap states. In a set of studies on hybrid nanowires, it was shown that these challenges could be overcome to create a highly efficient Cooper pair splitter [26] and to realize a minimal Kitaev chain [28]. A key idea is that the QDs can be coupled via extended Andreev bound states (ABSs) in the semiconductor-superconductor hybrid [25, 27, 35], rather than the continuum above the superconducting gap. Therefore, by controlling the ABS energy with electrostatic gates, it was possible to tune the relative amplitudes of ECT and CAR (see section 2.2.3). These developments pave the way for more advanced experiments, where the geometrical constraints of 1D systems will pose restrictions on the complexity of possible devices. This motivates the reproduction of the results in the InSbAs 2DEG platform, which offers flexibility in device design and can serve as a scalable platform to create and manipulate topologically Majorana bound states in artificial Kitaev chains.

We demonstrate in this chapter the observation of high efficiency CAR and ECT in the 2D semiconductor platform. This is achieved by coupling two quantum dots via a hybrid proximitized section in an InSbAs 2DEG. By applying an external magnetic field, we polarise the spins of the QDs, allowing us to use them as spin-filters. This, in combination with highly efficient CPS, allows us to accurately resolve the spin of the electrons involved in CAR and ECT. The large spin-orbit coupling in our 2DEGs, in combination with the device dimensions, results in significant spin precession for the electrons. Importantly, we show that this leads to strong equal-spin CAR currents that are of similar amplitude to the conventional opposite-spin processes. Through rotation of the magnetic field angle relative to the spin-orbit field, we show that the ECT and CAR processes can be tuned to equal amplitudes, satisfying a key requirement for realizing a Kitaev chain in semiconductor-superconductor hybrids.

4.2 DEVICE AND EXPERIMENTAL SET-UP

We study two devices fabricated on an InSbAs 2DEG with epitaxial aluminum, as described in section 3.1. The material has a low effective mass, large g-factor and large spin-orbit coupling strength[129, 164]. Figure 4.1a,b illustrate the device structure together with the three-terminal measurement circuit. The two depletion gates (pink) define a quasi-1D channel of about 150 nm, contacted on each side with normal leads. The middle of the channel is proximitized via a 150 nm-wide aluminium strip (green), which is kept electrically grounded. Quantum dots on the left and right are created using the finger gates (blue) and the ABS energy is controlled by the central ABS gate (purple).

The biases V_L and V_R applied to the left and right leads can be varied independently. The currents I_L and I_R in the left and right leads are measured simultaneously. We define in this chapter a positive current as the flow of electron charge from the leads to the superconductor. First, the two innermost finger gates are used to define tunneling barriers on either side of the hybrid region.

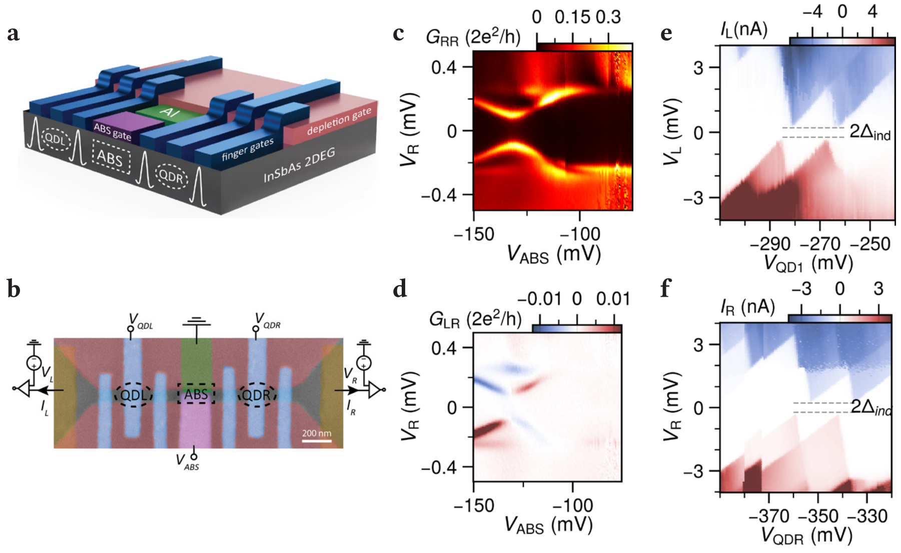

Figure 4.1: **Basic device characterization.** **(a)** A 3D illustration of the device. The two quantum dots (QDL and QDR), and the region hosting ABSs are indicated. For clarity, the gate-dielectric layers are not shown. **(b)** False-color scanning electron micrograph of Device 1, including a schematic of the circuit diagram for three-terminal measurements. Tunneling spectroscopy measurements showing **(c)** local conductance G_{RR} and **(d)** non-local conductance G_{LR} as a function of the ABS gate voltage V_{ABS} and right bias voltage V_R. Coulomb diamonds of the QDs are measured for **(e)** QDL and **(f)** QDR.

Figure 4.1c,d show the measured local conductance $G_{RR} = \frac{dI_R}{dV_R}$ and non-local conductance $G_{LR} = \frac{dI_L}{dV_R}$ as a function of the ABS gate voltage V_{ABS}. The induced gap in the hybrid section is found to be $\Delta_{ind} \approx 220\,\mu eV$. The correspondence between G_{RR} and G_{LR} shows the presence of an extended discrete ABS in the proximitized section. The observed sign-switching in the non-local signal is typical for an extended ABS probed in a three-terminal measurement [55, 165, 166]. Next, two quantum dots are created on either side of the proximitized section. Their electro-chemical potentials are controlled by applied voltages V_{QDL} and V_{QDR}. The charge stability diagrams of both QDs (Figure 4.1e,f) show Coulomb diamonds with clear even-odd spacing. The pair of Coulomb peaks show linear splitting as a function of magnetic field, indicative of a spin-degenerate single orbital level (figure 4.5). The superconducting gap Δ_{ind} is clearly visible at the charge degeneracy points, indicative of a weak coupling to the proximitized region [167, 168]. Charging energies of QDL and QDR are 1.9 meV and 1.4 meV respectively, much larger than the induced superconducting gap.

4.3 RESULTS

4.3.1 SIGNATURES OF ECT AND CAR

For CAR, an electron from each of the two leads is simultaneously transferred to the superconductor via an extended ABS to form a Cooper pair (Figure 4.2a). This should therefore result in positively correlated currents in the leads ($I_L = I_R$). For ECT (Figure 4.2b), an electron from the left or right lead tunnels to the opposite lead via the hybrid section, which should thus give rise to negatively correlated currents ($I_L = -I_R$). As we will show below, by controlling the QD levels and voltage biases, it is possible to distinguish currents arising from ECT and CAR. Such measurements are shown in Figure 4.2c,d. Here V_{QDL} and V_{QDR} are each tuned close to a selected charge degeneracy point and the currents I_L and I_R are simultaneously measured. The large charging energies of the dots ensure that each lead strongly prefers accepting or donating a single electron. We further ensure that the applied biases are lower in energy than any sub-gap states in the hybridized region, such that local transport is suppressed. To demonstrate CAR, we set $V_L = V_R = -120\,\mu V$ and sweep V_{QDL} and V_{QDR}. A finite current is observed only along a line with negative slope, for both I_L and I_R (Figure 4.2c). Furthermore, the currents are equal both in magnitude and sign (Figure 4.2e). Converting the gate voltages to electro-chemical potentials (μ_L, μ_R), we confirm that CAR mediated transport occurs when $\mu_L = -\mu_R$ (figure 4.8c). This is consistent with the requirement that the energies of the electrons forming the Cooper pair must be equal and opposite. To demonstrate ECT, we apply biases with opposite polarity ($V_L = -V_R = -120\,\mu V$). Unlike CAR, a finite current is observed only along a line with positive slope (Figure 4.2d). This is consistent with energy conservation during ECT, which demands that $\mu_L = \mu_R$. Furthermore, the currents are now equal in magnitude, but opposite in sign (Figure 4.2f). Note that when biasing only V_L or V_R and grounding the other lead, both ECT and CAR become visible in the charge stability diagram (figure 4.6).

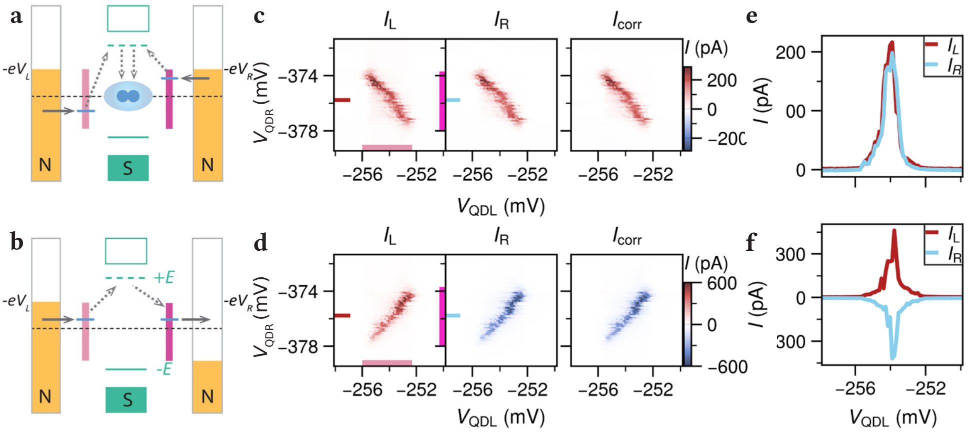

Figure 4.2: **Correlated CAR and ECT signals.** Diagrams of the transport cycles for **(a)** CAR and **(b)** ECT. Blue lines indicate the energies of the QD levels required for transport via the ABS at energy $\pm E$. Purple bars mark the energy window in which transport is allowed, corresponding to the marked regions in the measurement panels (**c** and **d**). **(c)** Charge stability measurement of QDL and QDR with $V_L = V_R = -120\,\mu\mathrm{V}$ taken at $V_{ABS} = -245\,\mathrm{mV}$. Equal currents with the same sign are observed at the left (I_L) and right (I_R) leads only when the QD energy levels are anti-aligned, as expected for CAR. **(d)** Repeated measurement, but with $V_L = -V_R = -120\,\mu\mathrm{V}$. Equal currents with opposite sign are observed only when the QDs are aligned in energy, as expected for ECT. The correlated currents I_{corr} are calculated from I_L and I_R as described in the main text. Exemplary line traces at $V_{QDR} = -375\,\mathrm{mV}$ for CAR and ECT are plotted in **(e)** and **(f)** respectively.

Importantly, for both CAR and ECT we observe no notable current when the bias and energy conditions are not met, indicating that unwanted local processes are strongly suppressed. In combination with strongly correlated currents, this suggests a relatively large signal-to-noise ratio of the CPS process. To characterize this, we calculate the CPS efficiency and visibility (figure 4.8). Following[26, 49], we obtain a combined CPS efficiency above 90 %, on par with the highest previously reported values [26, 49]. Applying a larger bias that exceeds the sub-gap state energy (but is still below Δ_{ind}) results in additional local, non-correlated signals which only depend on a single QD (figure 4.7) and significantly reduce the CPS efficiency. To systematically characterize the CAR and ECT measurements, we calculate the correlated current $I_{corr} \equiv \mathrm{sgn}(I_L I_R)\cdot\sqrt{|I_L||I_R|}$ (Figure 4.2c,d) [26]. It is non-zero only when I_L and I_R are both non-zero and thus highlights features arising from ECT or CAR. Furthermore the sign of I_{corr} clearly distinguishes CAR (always positive) from ECT (always negative).

4.3.2 ZERO FIELD SPIN BLOCKADE

In the absence of a magnetic field, the orbital levels of the QDs are spin-degenerate. Therefore, if the dot has an even number of electrons, the first electron to occupy the next orbital (a transition denoted as 0 ↔ 1) can be either spin-up or spin-down. However, to add the second electron (1 ↔ 2), the Pauli exclusion principle requires it to have an opposite spin. The effect of this spin-filling rule leads to a blockade of transport, which depends on the nature of the underlying process.

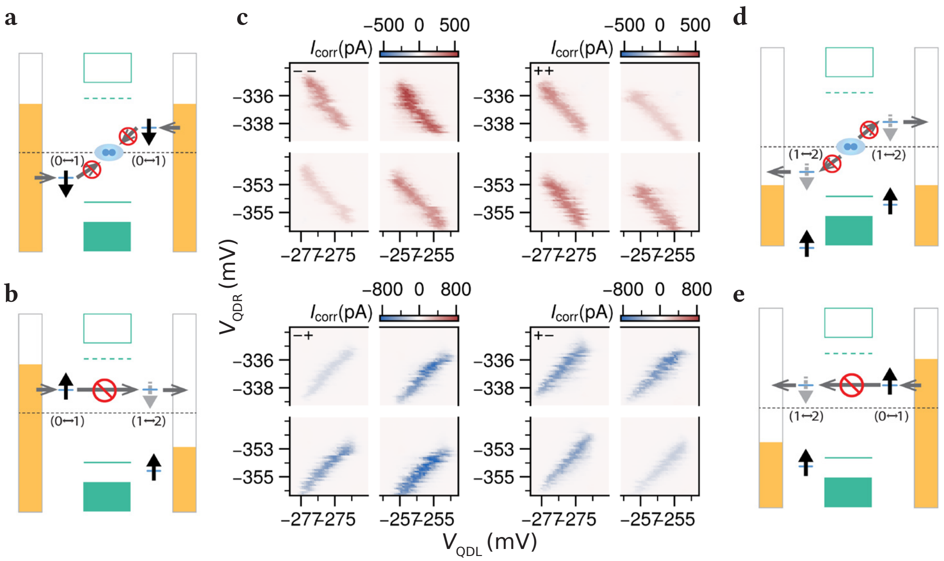

Figure 4.3: **Spin blockade at zero magnetic field.** Charge stability diagrams are obtained for all four bias polarity combinations, to measure either CAR ($V_L = V_R$) or ECT ($V_L = -V_R$). **(a),(b),(d)** and **(e)** show energy diagrams illustrating situations expected to lead to transport blockades. Arrows within the dots either represent an already occupied spin state (black), or a state available to be occupied by an incoming electron (grey). **(c)** The corresponding measurements of I_{corr} plotted against V_{QDL} and V_{QDR}, with applied biases $|V_L| = |V_R| = 120\,\mu V$ and $V_{ABS} = -220$ mV. The used bias polarity for each set of measurements is noted in the top left corner. For each bias configuration a specific transition is suppressed (dashed circles) as a consequence of the blockade depicted alongside the measurement. Gate voltage ranges are interrupted to zoom-in on the relevant ECT and CAR features.

We first focus on ECT in the (−,+) bias configuration, denoting that a negative bias is applied to the left lead and a positive bias is applied to the right lead (Figure 4.3b). When the QDs are tuned to the (0 ↔ 1, 1 ↔ 2) transition, a situation can arise where the left QD is occupied with e.g. a spin-up electron (coming from the left lead), whereas the right QD can only accept a spin-down electron (since the spin-up state has already been occupied). At this point transport from left to right is blocked, analogous to the well-known Pauli blockade in double quantum dots [169]. This spin blockade is clearly seen when the QDs are tuned over successive charge transitions. In Figure 4.3c we see that the ECT current is suppressed for the (0 ↔ 1, 1 ↔ 2) transition. Reversing the bias polarities to (+,−), a similar blockade is observed for the (1 ↔ 2, 0 ↔ 1) transition, as expected (see Figure 4.3e).

In the (−,−) configuration, only CAR mediated transport can occur and we find a suppression in CAR current for the (0 ↔ 1, 0 ↔ 1) transition. This is a direct consequence of the Cooper pairs in an s-wave superconductor having a singlet pairing. Thus, for transport to occur, each QD must donate an electron of *opposite* spin in order to create a singlet Cooper pair in the superconductor. Transport is therefore blocked when both dots are occupied by electrons with the same spin (Figure 4.3a). Finally, in the (+,+) configuration a blockade is expected for the (1 ↔ 2, 1 ↔ 2) transition (Figure 4.3d), as observed in the measurements. Qualitatively similar measurements of spin blockade for CAR and ECT are presented for another device (figure 4.12). We note that a finite amount of current remains for each blockaded transition, indicating the presence of a spin-relaxation mechanism in our system. The hyperfine interaction is one such mechanism that can lift the Pauli blockade [170, 171]. We confirm this by applying a magnetic field to suppress the spin-mixing due to the hyperfine interaction, and find that 35 mT is sufficient to fully suppress the remaining current (figure 4.9).

4.3.3 SINGLET AND TRIPLET ECT/CAR

The spin degeneracy of the QD levels is lifted by applying a magnetic field, allowing us to operate them as spin-filters (figure 4.5). When the Zeeman splitting exceeds $|eV_\mathrm{L}|, |eV_\mathrm{R}|$, only spin-down (↓) electrons are involved in transport at a $(0 \leftrightarrow 1)$ transition and only spin-up (↑) electrons at a $(1 \leftrightarrow 2)$ transition. In the absence of spin-orbit coupling, CAR is only expected to occur when both QDs are tuned to host electrons with opposite spin. The opposite applies to ECT, where a current is only expected when the QDs are tuned to receive electrons with equal spin.

As shown in Figure 4.4b, when an in-plane field of 150 mT is applied along B_y (i.e. perpendicular to the channel), CAR current is only present in the quadrants where the electrons have opposite spins (↓↑ and ↑↓) and completely suppressed for the equal-spin (↓↓ and ↑↑) configuration. Similarly, no current is detected for opposite-spin ECT, while transport is allowed for equal-spin ECT. This spin-dependent transport indicates that the direction of the spin-orbit field $\mathbf{B}_\mathrm{SO}$ is along B_y, making spin a good quantum number. This is also consistent with the expected Rashba spin-orbit interaction in a quasi-1D channel with momentum along the z-direction and electric field perpendicular to the 2DEG plane. Applying the magnetic field perpendicular to $\mathbf{B}_\mathrm{SO}$ (i.e. along B_z), a spin-up electron may acquire a finite spin-down component due to the spin-orbit interaction, or vice versa. The consequence of this can be seen in Figure 4.4c, where we now observe sizeable currents for equal-spin CAR and opposite-spin ECT. The full evolution of the spin-specific ECT and CAR currents can be obtained by performing an in-plane rotation of the magnetic field (Figure 4.4d). The averaged amplitudes of equal-spin CAR and opposite-spin ECT currents $\langle I_\mathrm{corr}\rangle$ are found to oscillate smoothly between full suppression at $\theta \approx 90^\circ$ and 270° ($\mathbf{B} \parallel \mathbf{B}_\mathrm{SO}$), and their maximum strength at $\theta \approx 0^\circ$ and 180° ($\mathbf{B} \perp \mathbf{B}_\mathrm{SO}$). This result does not depend on a specific choice of orbitals in the QDs (figure 4.10).

The ability to accurately resolve the spin of the electrons in CPS is particularly relevant in the context of entanglement witnessing. An important metric capturing this, is the spin cross-correlation [158, 159]. As described in [172], we calculate the spin cross-correlation from the measured currents as:

$$C = \frac{(I^{\uparrow\uparrow} + I^{\downarrow\downarrow} - I^{\uparrow\downarrow} - I^{\downarrow\uparrow})}{(I^{\uparrow\uparrow} + I^{\downarrow\downarrow} + I^{\uparrow\downarrow} + I^{\downarrow\uparrow})} \tag{4.1}$$

and plot it for both CAR and ECT as a function of θ (Figure 4.4e). I^{ij} corresponds to the average correlated current $\langle I_\mathrm{corr}\rangle$ associated with each spin configuration, where $i, j \in \{\uparrow, \downarrow\}$. $C = \pm 1$ when there is a perfect correlation or anti-correlation between the spins of electrons

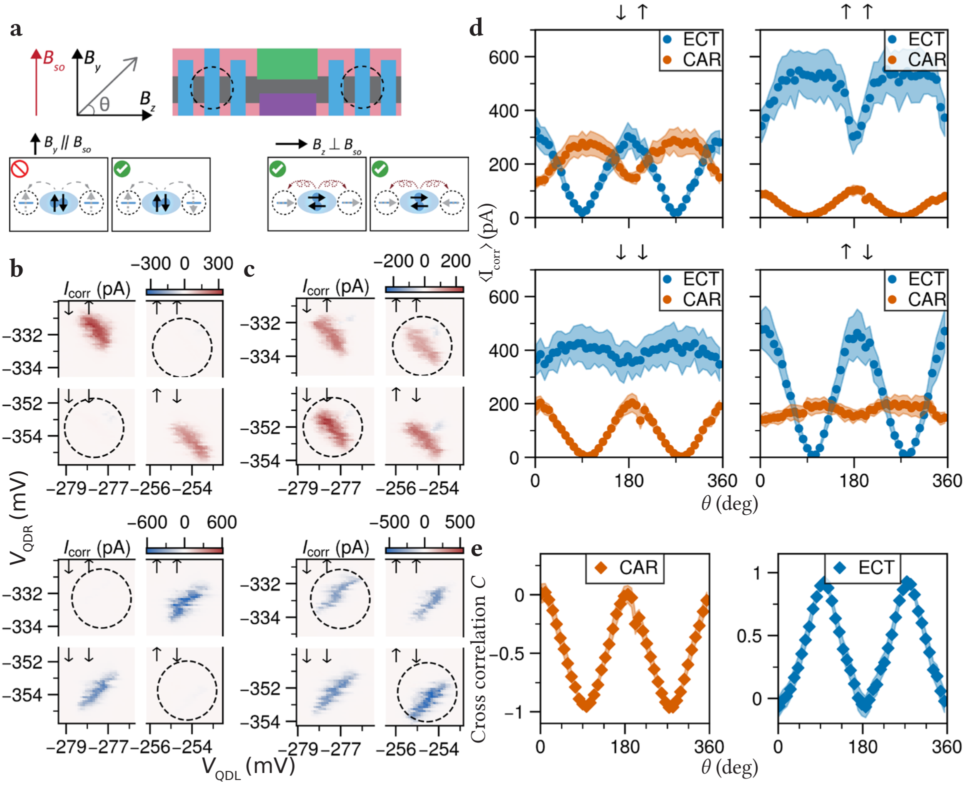

Figure 4.4: **CAR and ECT at finite magnetic field**. **(a)** A schematic showing the coordinate system of the applied magnetic field with respect to the device. **(b)** Measurement of I_{corr} for CAR (top) and ECT (bottom) with $\mathbf{B} \parallel B_y = 150\,\mathrm{mT}$ and $V_{\mathrm{ABS}} = -220\,\mathrm{mV}$. Lower biases ($|V_{\mathrm{L}}|, |V_{\mathrm{R}}| = 70\,\mu\mathrm{V}$) are applied to keep the bias window below any sub-gap states, whose energies are pulled down by the finite magnetic field (figure 4.5). Equal-spin CAR and opposite-spin ECT are fully suppressed (circled). **(c)** Measurement of I_{corr} with $\mathbf{B} \parallel B_z = 150\,\mathrm{mT}$. The blockades in **(b)** have been clearly lifted. **(d)** Angle-dependence of $\langle I_{\mathrm{corr}} \rangle$ for the different spin channels for a full rotation of the magnetic field in the y-z plane. The (−,+) and (+,+) bias configurations are used for ECT and CAR respectively. Each data point represents a single charge stability diagram for a specific spin channel. The data extraction procedure is described in figure 4.11. **(e)** The calculated spin cross-correlation (as defined in the text) of CAR and ECT, derived from (**d**).

entering the QDs. In contrast, $C = 0$ when the probabilities of equal-spin and opposite-spin transport become equal. When $\mathbf{B} \parallel \mathbf{B}_{\mathrm{SO}}$ we obtain a value of $C = -0.96$ for CAR, demonstrating a nearly perfect singlet pairing between the QDs. Similarly, for ECT $C = +0.93$ is obtained. When $\mathbf{B} \perp \mathbf{B}_{\mathrm{SO}}$, C reaches close to 0 for both CAR and ECT, stressing that the triplet component can be tuned to be of similar magnitude to the conventional singlet pairing.

4.4 SUMMARY

In summary, we have used quantum dot-superconductor hybrids to demonstrate highly efficient Cooper pair splitting in a two-dimensional semiconductor platform. Using spin-polarised quantum dots, we performed spin-selective measurements of ECT and CAR and showed that the strong spin-orbit interaction in ternary 2DEGs results in comparable strengths of singlet and triplet correlations between the quantum dots. Finally, through magnetic field rotations, we showed that it is possible to obtain equal amplitudes of ECT and CAR, establishing 2DEGs as a suitable platform to study Majorana bound states in artificial Kitaev chains.

4.5 DISCUSSION

The demonstration of singlet and triplet correlations with Cooper pair splitters in 2DEGs paves the way for more advanced experiments to study entanglement and topological superconductivity. An interesting open question relates to the underlying mechanism that allows for strong triplet CAR in these devices. One possibility is for two equal-spin electrons to form a normal s-wave Cooper pair, due to spin precession in the tunnel barriers. Another path is that an induced p-wave superconducting pairing arises in the hybrid section, such that two equal-spin electrons form a Cooper pair. In order to distinguish these possibilities, we propose to create quasi-1D channels that are bent (rather than straight), resulting in different spin-orbit directions in each arm of the Cooper pair splitter[158, 173]. We discuss this in more detail in Chapter 9. Such devices are easily implemented in 2DEGs where any arbitrary shape of the channel can be realized simply by altering the design of the depletion gates. Given the high fidelity spin correlation we have demonstrated here, such devices could also be used to detect entanglement by performing a Bell test with electrons from a Cooper pair [158].

The main motivation for the experiments in this chapter was the realization of a minimal Kitaev chain in an InSb nanowire [28], which opens up several possibilities to systematically study Majorana bound states (MBSs). In this regard the 2DEG platform is particularly suitable, since it readily allows for extending these measurements to multi-site QD chains. Additionally the flexibility of the 2DEG allows for the simultaneous measurement of density of states at the edges and in the bulk. Such investigations are continued in Chapter 5 and Chapter 6. As a future goal, one could use these chains to perform tests of non-Abelian exchange statistics via braiding experiments [19, 174], which necessarily require a 2D platform, discussed further in Chapter 9.

DATA AVAILABILITY

Raw data and analysis scripts for all presented figures are available on Zenodo [175].

4.6 METHODS

FABRICATION

Device 1 (main text) and Device 2 (supplementary) were fabricated using techniques described in detail in [176]. A narrow aluminum strip is defined in an InSbAs-Al chip by wet etching, followed by the deposition of two normal Ti/Pd contacts. After deposition of 20 nm AlOx via atomic layer deposition (ALD), the two depletion gates are evaporated. Following a second ALD (20 nm AlOx) Ti/Au gates are evaporated in order to define the QDs and tune the ABS energy.

MEASUREMENTS

All measurements are performed in a dilution refrigerator with a base temperature of 20 mK. Magnetic fields are applied using a 3D vector magnet. The alignment of the magnetic field with respect to the device is expected to be accurate within $\pm 5^\circ$. Transport measurements are performed in DC using a three-terminal set-up, where the aluminum is electrically grounded (Figure 4.1b). Current amplifier offsets are determined by the average measured current when both dots are in Coulomb blockade. CAR and ECT processes can be observed over a wide range of V_{ABS} voltages. Once a V_{ABS} setting was found with both strong CAR and ECT currents, it was kept at a constant value throughout the rest of the measurements. Further care was taken to implement the same orbitals in both QDs for all presented measurements in the main text. The mismatch between exact V_{QDR} and V_{QDL} values at which ECT and CAR are observed is due to gate instabilities, causing a drift of charge degeneracy points over a period of time. Therefore, the field rotation measurement in Figure 4.4e was performed multiple times. No quantitative difference was observed between measurements. Presented data was selected due to high stability of the QDs over the course of the measurements.

4.7 Extended Data

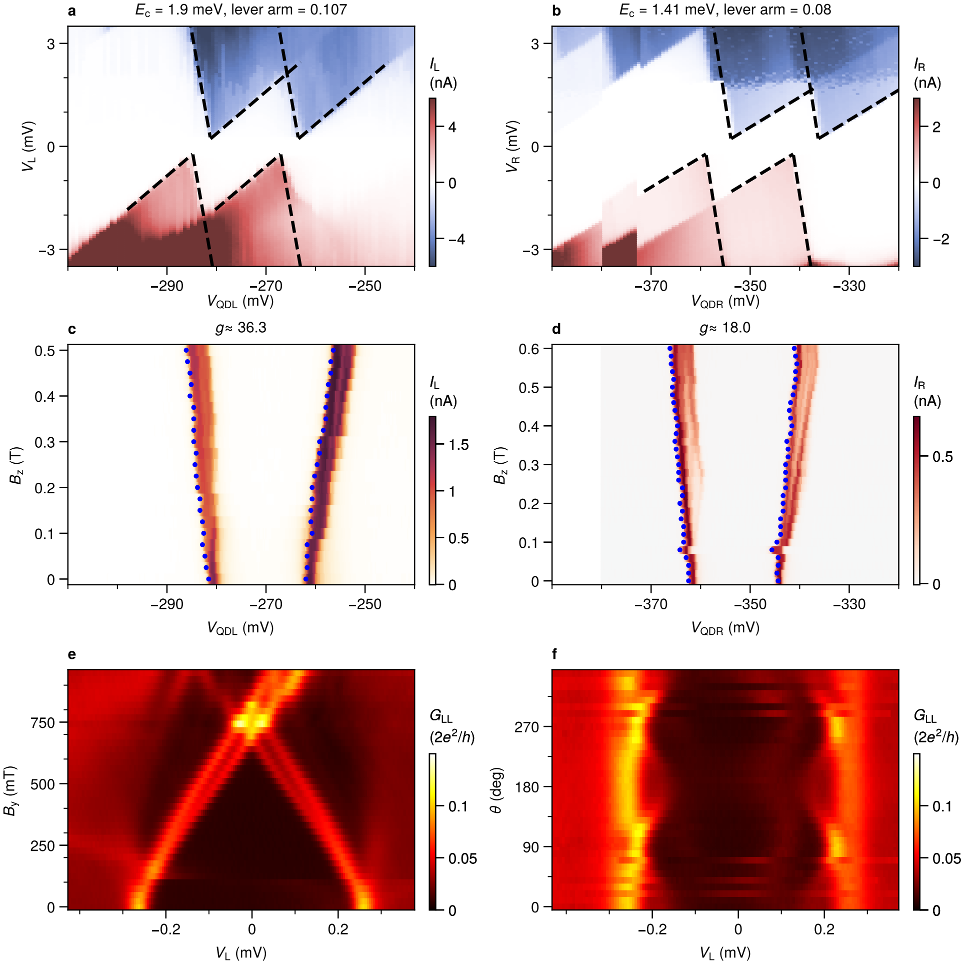

Figure 4.5: **Quantum dot and ABS characterization.** Extraction of charging energy E_c and lever arm for (**a**) QDL and (**b**) QDR from Coulomb diamonds shown in Fig 1 of the main text. Evolution of Coulomb peaks with B_z for (**c**) QDL and (**d**) QDR shows Zeeman splitting causing the separation between the resonances to increase. Bias voltages are $(V_L, V_R) = (-450\,\mu V, 0)$ for the left measurement, and $(0, -350\,\mu V)$ for the right measurement. g-factors of -36 and -18 are derived for the QDL and QDR respectively. **(e)** Measured local conductance G_{LL} of the hybrid section with increasing magnetic field $B \parallel B_y$ at $V_{ABS} = -245$ mV. **(f)** Field rotation in the y-z plane with a fiedld magnitude of 100 mT, showing a slight anisotropy of the ABS energy.

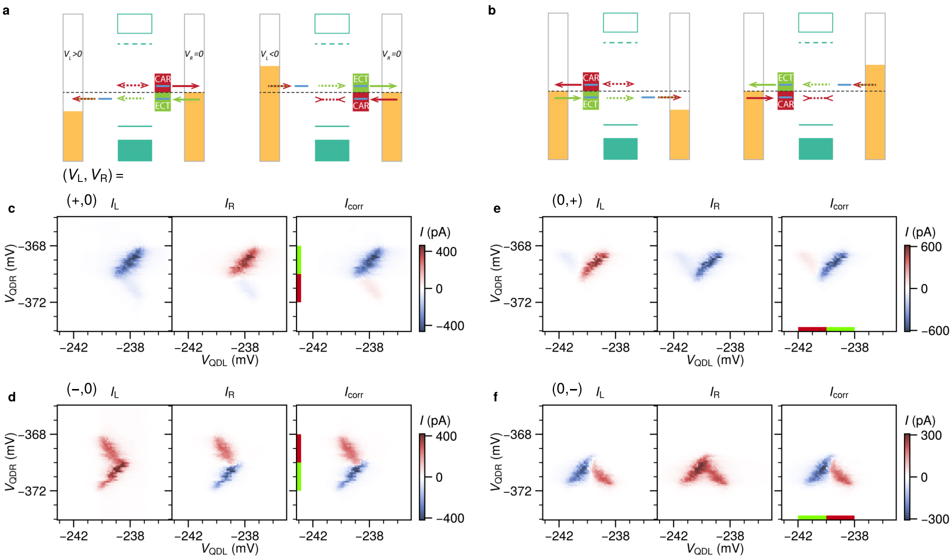

Figure 4.6: **Simultaneous measurement of ECT and CAR**. Energy diagrams for the expected transport when biasing only the **(a)** left or **(b)** right side of the device. **(c)-(f)** Corresponding measurements with the bias polarities labelled in the top left corners. Two distinct features with opposite slope appear in each charge stability diagram. This is because both ECT and CAR can now occur, depending on the position of the QD levels with respect to the grounded side. Red (CAR) and green (ECT) bars indicate the corresponding gate voltage ranges in which each process is allowed.

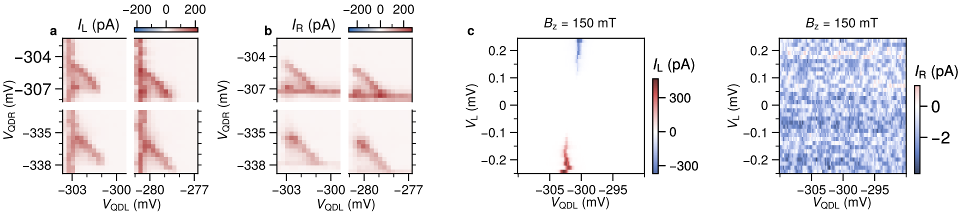

Figure 4.7: **Filtering local transport processes.** A key requirement for isolating CAR and ECT is the ability to filter out local processes. For the measurements presented in the main text it was ensured that the applied biases remained below the energy of any subgap states. With applied biases of −120 μV on both sides and an external magnetic field B_z = 150 mT, additional currents appear in **(a)** I_L and **(b)** I_R on top of the currents arising through CAR. Fixing V_{QDR} at −320 mV (i.e., putting the right dot off-resonance), I_L and I_R are measured as a function of the left bias V_L and left plunger gate V_{QDL}. **(c)** Current arising through local processes appears once the applied bias exceeds the ABS energy. No current is detected in I_R.

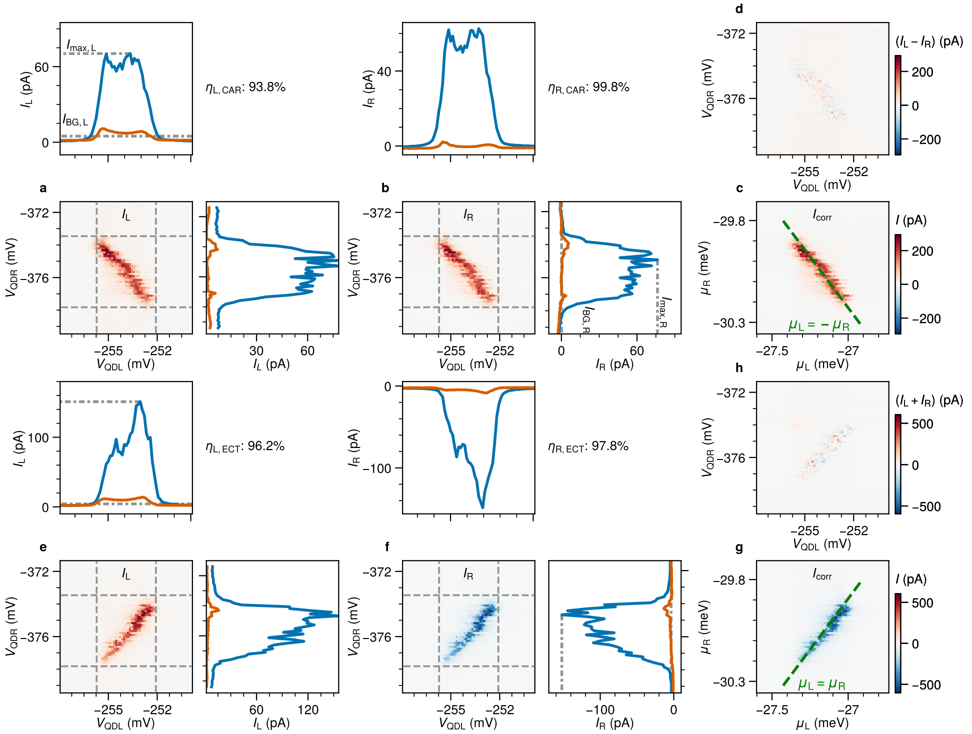

Figure 4.8: **Cooper pair splitting efficiency.** Analysis of the data presented in Fig. 2. **(a,b)** Measured currents I_{L} and I_{R} arising from CAR. The top panel shows I_{L} averaged over the V_{QDR} range indicated by the horizontal grey lines (blue) and the background trace averaged outside the horizontal grey lines (orange). The right panel shows I_{L} averaged over the V_{QDL} range indicated by the vertical grey lines and the background trace averaged outside the vertical grey lines. The efficiency of each junction is defined as $\eta_j = 1 - \frac{I_{BG,j}}{I_{max,j}}$ where the $I_{BG,j}$ is the average value of the background trace and $I_{max,j}$ is the maximum of the averaged I_j. We extract an η of about 94% for the left junction and 99% for the right junction. Taking the product this gives a combined efficiency of $\eta_L \eta_R$ of about 93%. Using the lever arms extracted from the Coulomb diamonds (Fig. S1), the correlated current I_{corr} is plotted as a function of μ_{L} and μ_{R} in **(c)**. The dashed line corresponds to $\mu_{\mathrm{L}} = -\mu_{\mathrm{R}}$, confirming that transport occurs when the dot levels are anti-aligned. Calculating $I_{\mathrm{L}} - I_{\mathrm{R}}$ shows very small remaining current, verifying $I_{\mathrm{L}} = I_{\mathrm{R}}$ **(d)**. **(e,f)** Similar analysis of I_{L}, I_{R} and averaged currents for ECT. The combined efficiency is again found to be about 93%. **(g)** I_{corr} in μ_{L}- μ_{R} space, together with the line where $\mu_{\mathrm{L}} = \mu_{\mathrm{R}}$, showing that transport takes place when the QD levels are aligned. **(h)** Plotting $I_{\mathrm{L}} + I_{\mathrm{R}}$ shows again that little signal remains, highlighting that $I_{\mathrm{L}} = -I_{\mathrm{R}}$ for ECT.

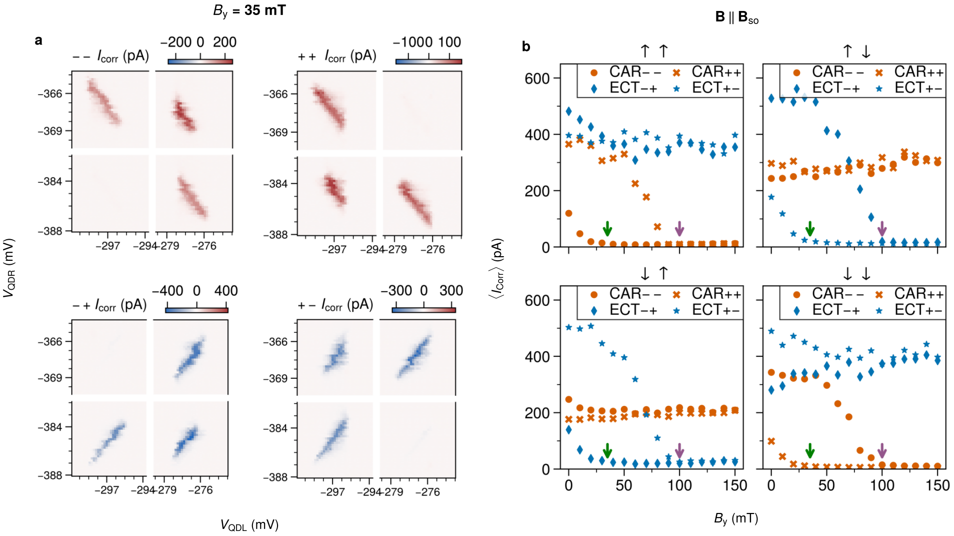

Figure 4.9: **Field evolution of ECT and CAR.** **(a)** The charge stability diagrams at B_y = 35 mT, of the same resonances used in the main text, show that the weakened transitions in each bias configuration (circled in Fig. 2c) are now completely blocked. This is interpreted as a result of the magnetic field overcoming the hyperfine interaction in the QDs. **(b)** Spin-filtered measurements of $\langle I_{\mathrm{corr}} \rangle$ for ECT and CAR as a function of magnetic field $B_y \parallel \mathbf{B}_{\mathrm{SO}}$, for each bias configuration. Two transitions are present in each quadrant. Above roughly 35 mT (green arrows) the Pauli-blockaded process in each quadrant becomes fully suppressed. Above 100 mT (purple arrows) the Zeeman splitting exceeds the applied biases (|100 μV|) such that only the spin-preserving processes remain (i.e. opposite-spin CAR and equal-spin ECT).

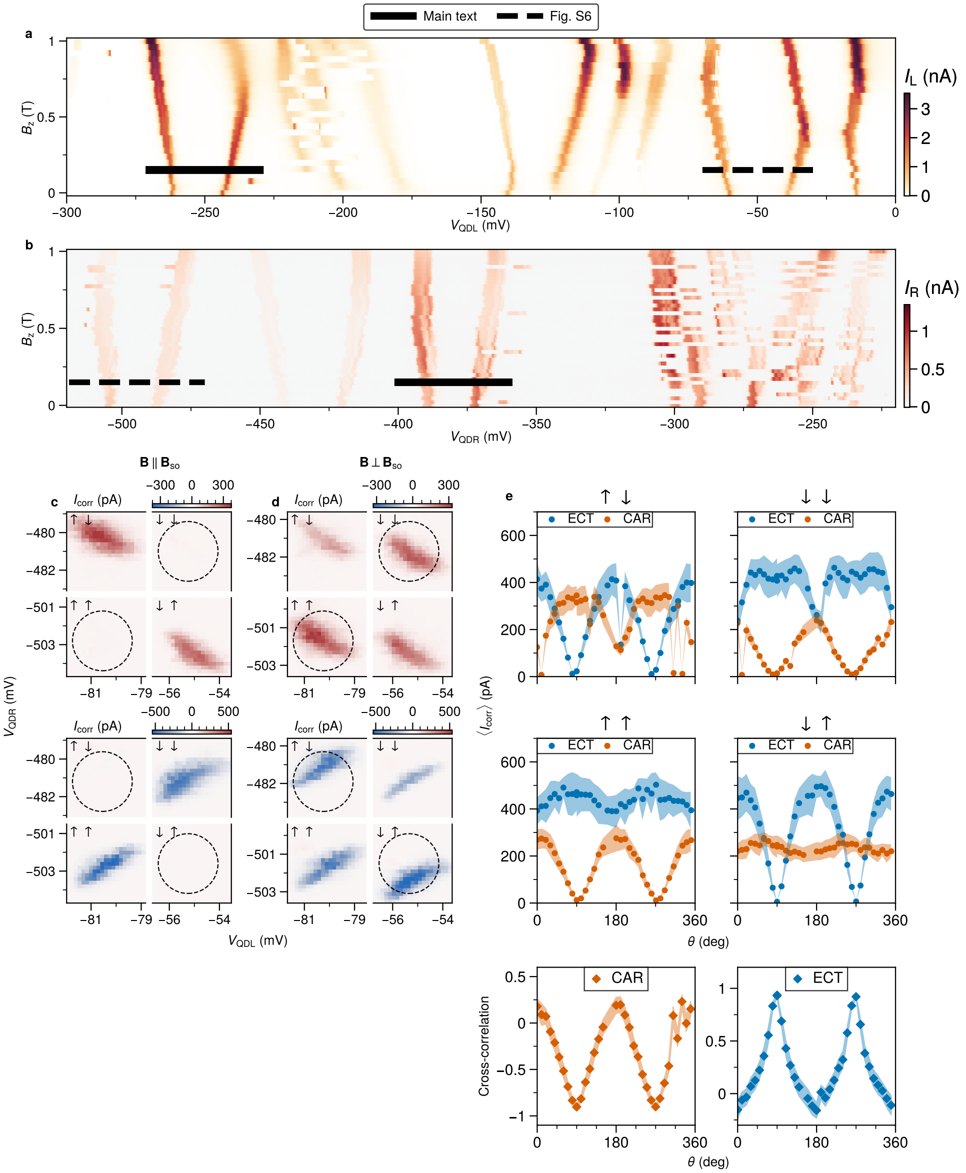

Figure 4.10: **Field angle dependence with another pair of QD resonances. (a,b)** Field evolution of Coulomb resonances in the QDs over an extended range of V_{QDL} and V_{QDR}. The effect of Zeeman splitting is observed for multiple orbitals in each QD. Solid black lines indicate the orbitals used in the main text, while the dashed lines indicate different orbitals used for data presented here. **(c,d)** Repetition of measurements presented in Fig. 4(c,d) for the second pair of resonances. Unconventional processes (equal-spin CAR and opposite-spin ECT) are fully suppressed at $B \parallel B_{SO}$ and recovered at $B \perp B_{SO}$. A full field rotation **(e)** yields similar behaviours of $\langle I_{corr} \rangle$ and cross-correlation to the dependence shown in Fig. 4f.

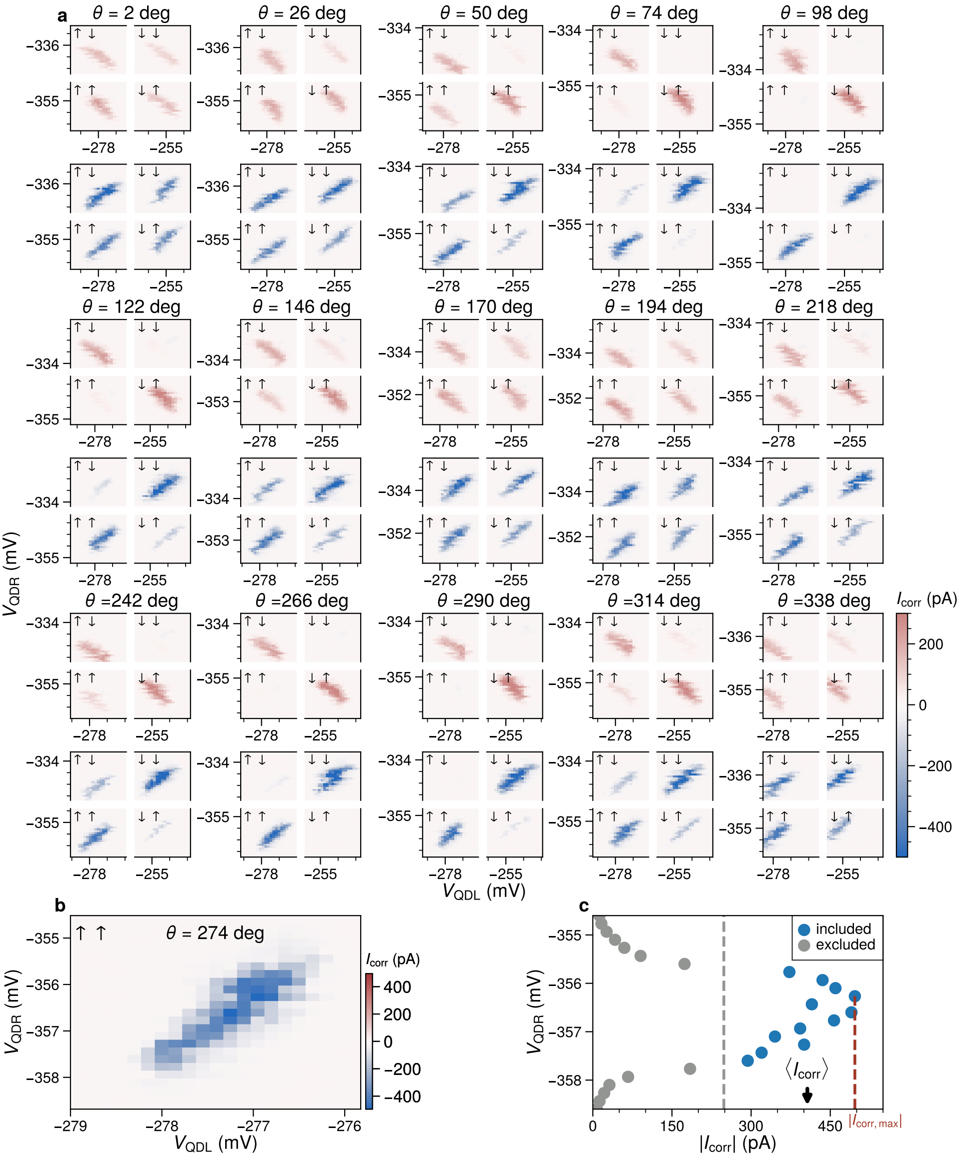

Figure 4.11: **Raw data from Fig 4f and data extraction. (a)** Selection of raw data used for extracting the field angle dependence of CAR and ECT rates presented in Fig. 4f. For each angle the four quadrants with different spin configurations of I_{corr} are plotted for CAR (top panels) and ECT (bottom panels). A single quadrant is converted to a single data point to quantify the spin-selective rate of CAR and ECT at a specific angle of the magnetic field. The data extraction process is detailed in panel **(c)** for the measurement of ↑↑-ECT at $\theta = 274^\circ$ (plotted again in **(b)**). The maximum value of $|I_{\mathrm{corr}}|$ for each horizontal line-cut is extracted and plotted as a function of V_{QDR}. To exclude data at the edge of the bias window, a threshold is set at half of the maximally recorded $|I_{\mathrm{corr,max}}|$. The included values are labeled in blue, from which the average $\langle I_{\mathrm{corr}} \rangle$ and standard deviation is derived.

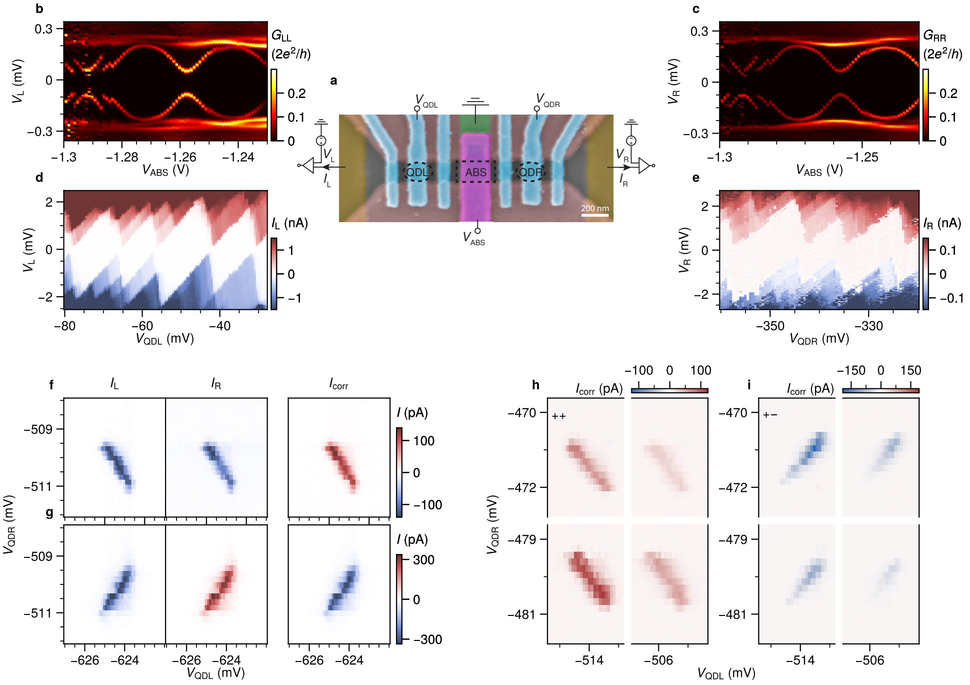

Figure 4.12: **Measurements on additional device (Device 2). (a)** False-color scanning electron micrograph of Device 2, with the circuit diagram used for three-terminal measurements. Scale bar is 200 nm. The distance between the centers of the QDs is about 800 nm (in contrast to 600 nm for Device 1 presented in the main text). Tunneling spectroscopy measurements of the **(b)** local conductance G_{LL} and **(c)** G_{RR} as a function of V_{ABS} show correlated states, indicating the presence of an extended ABSs. Measured Coulomb diamonds for **(d)** QDL and **(e)** QDR. The extracted charging energy is about 1.2 meV for both dots. **(f)**,**(g)** Similar to Fig. 2, measured left current I_L, right current I_R and the calculated correlated current I_{corr}, for CAR ($V_L = V_R = 100\,\mu V$) and ECT ($V_L = 100\,\mu V$ and $V_R = -100\,\mu V$). Measurements over successive charge transitions reveal the expected spin blockade for **(h)** CAR (+,+) and **(i)** ECT (+,−) at zero magnetic field.

5

ENGINEERING A TWO-SITE KITAEV CHAIN

The previous chapter demonstrates that Andreev bound states can facilitate crossed Andreev reflection and elastic co-tunnelling between two-spin polarised quantum dots in an InSbAs 2DEG platform. In this chapter, we build upon these observations by studying an identical setup, but in a regime where the tunnel coupling between the quantum dots and the Andreev bound state is increased. In this regime, the system is expected to behave as an artificial Kitaev chain hosting Majorana bound states (MBSs) [28, 33, 37, 38]. We demonstrate systematic control over the inter-dot couplings through in-plane rotations of the magnetic field and via electrostatic gating of the proximitized region. This allows us to tune the system to sweet spots in parameter space, where robust correlated zero bias conductance peaks are observed in tunnelling spectroscopy. We interpret these signals as arising from two MBSs localized on either of the quantum dots. To study the extent of hybridization between the localized MBSs, we probe the evolution of the energy spectrum with magnetic field and estimate the Majorana polarization, an important metric for Majorana-based qubits [35, 177]. This implementation of a Kitaev chain on a scalable and flexible 2D platform provides a realistic path towards more advanced experiments that require manipulation and readout of multiple MBSs.

> *“Wat is mijn kathedraal? Ik werk aan een kathedraal die ik niet ken en als hij voltooid is, zal ik er niet meer zijn en niemand zal weten dat ik eraan heb gewerkt”*
>
> - Willem Frederik Hermans, *Nooit meer slapen*

The work in this chapter has been published as: *A two-site Kitaev chain in a two-dimensional electron gas*, **Sebastiaan L. D. ten Haaf**†, Qingzhen Wang†, A. Mert Bozkurt, Chun-Xiao Liu, Ivan Kulesh, Philip Kim, Di Xiao, Candice Thomas, Michael J. Manfra, Tom Dvir, Michael Wimmer and Srijit Goswami.
Nature **630**, 329–334 (2024) [178].
Personal contribution includes device fabrication, obtaining measurements, contributing to numerical analysis and writing of the manuscript.
†Authors contributed equally.

5.1 Introduction

Superconductor-semiconductor hybrid systems have been intensively investigated as a potential platform to engineer topologically protected Majorana bound states (MBSs). In particular, significant efforts have been dedicated to studying one-dimensional systems coupled to s-wave superconductors [16, 17, 81]. However, uncontrolled microscopic variations in hybrid devices have complicated the study of MBSs [21–23]. A potential way to mitigate the effects of disorder, is to create a Kitaev chain [14] using an array of quantum dots (QDs) with controllable couplings [33, 37, 38]. In fact, a chain consisting of only two QDs, while not topologically protected, is sufficient to create localized MBSs [33]. These so-called "oor man's Majorana" were realized in nanowires [28], which has led to proposals [177, 179–181] to study non-Abelian statistics by fusing or braiding MBSs in multiple two-site chains. However, in order to perform these studies, and move towards a Majorana-based qubit with integrated readout and control, it is vital to have a scalable and flexible 2D architecture.

In this chapter we realize a two-site Kitaev chain by coupling two spin-polarised QDs in an InSbAs two-dimensional electron gas (2DEG). By tuning the couplings between the QDs to so-called "sweet spot", we demonstrate correlated zero-bias conductance peaks (ZBPs) that are resilient to local perturbations. In addition to electrostatic control, we show that the planar 2DEG geometry allows one to reach such sweet spots through an in-plane rotation of the magnetic field. An important prerequisite to produce localized MBSs, is that the Zeeman splitting in the QDs is sufficiently large [35]. Surprisingly, however, we find that several features used to identify "sweet spot" (such as correlated ZBPs) actually persist down to zero magnetic field. We show that the evolution of the energy spectrum with magnetic field provides complementary information, which allows us to estimate the Majorana polarisation (section 2.2.4), a metric quantifying the extent of hybridization between MBSs [35, 83, 177].

5.2 The Kitaev chain with strongly coupled dots

The Kitaev model [14] can be implemented by coupling spin-polarised QDs via Andreev bound states (ABSs) in a semiconductor-superconductor hybrid [28]. Coupling between the QDs is mediated by the two types of coherent tunneling processes, which we introduced in section 2.2.1. The hopping interaction arises through elastic co-tunnelling (ECT) and a pairing interaction arises via the creation or breaking of a Cooper pair in the superconductor through crossed Andreev reflection (CAR). To emulate a Kitaev chain, the relative amplitudes of these processes must be controlled [25–27]. Furthermore, large inter-dot couplings are desired in order to isolate zero-energy MBSs from higher-energy excitations [33]. This can be achieved by increasing tunnelling rates between the QDs and the proximitized region, additionally inducing superconducting correlations in the QDs [79, 80]. In this regime the QDs can be described as Yu-Shiba-Rusinov (YSR) states [53, 54, 153, 154, 182, 183].

An energy level diagram of the system is shown in figure 5.1b, where, at finite magnetic field, the ground state of each proximitized QD is either a doublet state $|\downarrow\rangle$ or a singlet state $|S\rangle$. The electro-chemical potential of the QDs are denoted μ_L and μ_R. We consider the combined state of the QDs $|\sigma_L,\sigma_R\rangle$, where $\sigma_L, \sigma_R \in (|S\rangle, |\downarrow\rangle)$.

In this description, ECT and CAR processes give rise to two types of effective couplings. States with total odd-parity ($|\mathrm{S},\downarrow\rangle$ and $|\downarrow,\mathrm{S}\rangle$) have the same total spin ($\frac{1}{2}$) and therefore couple through a spin-conserving term Γ_o. States with total even-parity ($|\mathrm{S},\mathrm{S}\rangle$ and $|\downarrow,\downarrow\rangle$) have different total spin (0 or 1) and couple through a spin non-conserving term Γ_e. Similar to a system with non-proximitized QDs [33, 37], MBSs should arise when these couplings are equal (Γ_o=Γ_e) [79], further detailed in section 5.7. Figure 5.1c shows the numerically obtained conductance G, considering the local transport, as a function of μ_L and μ_R (details of the model can be found in section 5.7). This charge stability diagram (CSD) reveals avoided crossings at the charge degeneracy points, indicative of strong inter-dot coupling. In the absence of spin-orbit interaction only the spin-conserving coupling Γ_o is relevant, thus strongly hybridizing the odd-parity states. Horizontal and vertical conductance features are visible between avoided crossings as a result of local Andreev reflection, typical for YSR-states.

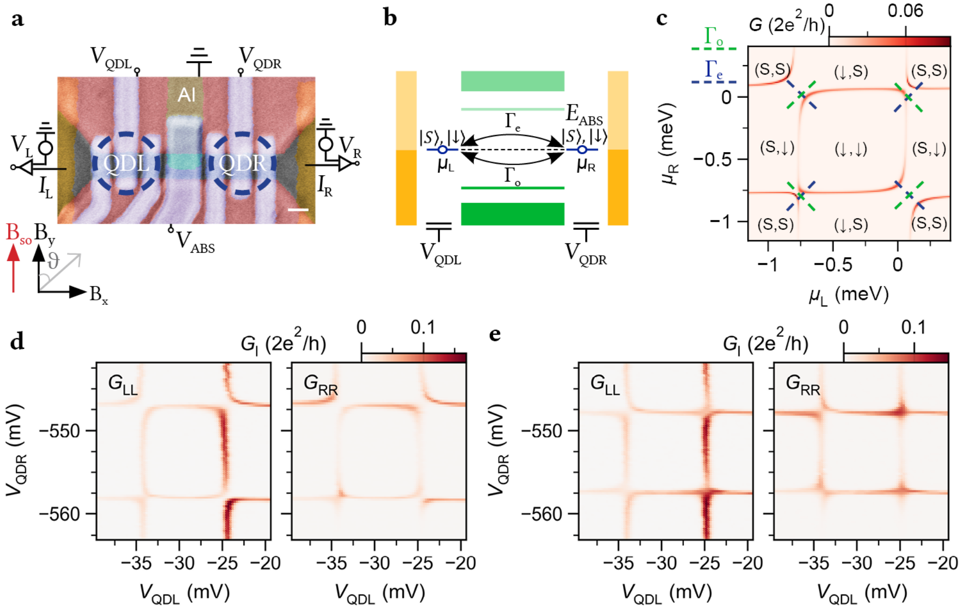

Figure 5.1: **Device, model and CSDs (a)** False-colored scanning electron micrograph of device A. Inset axis shows coordinates of the external magnetic field and the expected spin-orbit field direction w.r.t. the device orientation. The gate-defined QDs (QDL and QDR) are indicated. Scale bar is 100 nm. **(b)** Energy level diagram showing two spin-polarised YSR-states in two QDs that are coupled through a hybrid section. An Andreev bound state (at energy E_ABS) mediates two types of virtual tunnel couplings between the QDs, denoted by Γ_e and Γ_o. **(c)** Numerically calculated CSD of two coupled QDs, in the absence of spin-orbit coupling. Dashed lines indicate which states are expected to be hybridized through each type of coupling. **(d)** Measured CSD across two charge degeneracy points in QDL and QDR with $\theta = 0°$ ($B \parallel B_\mathrm{SO}$), corresponding to numerical conductance in (c). **(e)** Measured CSD with $\theta = 75°$. Data in (d) and (e) are taken at V_ABS =−624 mV and $B = 100$ mT.

5.3 DEVICE AND MEASUREMENT SET-UP

A scanning electron micrograph of a typical device (device A) is shown in figure 5.1a. Gate-defined QDs are created on the left and right of a region proximitized by aluminium (green). The QDs are strongly coupled to the superconductor, resulting in the formation of sub-gap YSR states (detailed in figure 5.5). Biases applied to the left and right leads (V_L and V_R) can be varied and the currents in the left and right leads (I_L and I_R) can be measured simultaneously. Using standard lock-in techniques, we measure local conductances G_LL ($\frac{\mathrm{d}I_\mathrm{L}}{\mathrm{d}V_\mathrm{L}}$) and G_RR ($\frac{\mathrm{d}I_\mathrm{R}}{\mathrm{d}V_\mathrm{R}}$), denoted G_l, and non-local conductances G_LR ($\frac{\mathrm{d}I_\mathrm{L}}{\mathrm{d}V_\mathrm{R}}$) and G_RL ($\frac{\mathrm{d}I_\mathrm{R}}{\mathrm{d}V_\mathrm{L}}$), denoted G_nl. We report on two similar devices. Device A was used for measurements in figure 5.1, figure 5.3 and figure 5.4. Device B (image shown in figure 5.6) was used to obtain the measurements in figure 5.2. All measurements are performed in a dilution refrigerator, with a base temperature of 20 mK.

By applying a magnetic field along the spin-orbit field, the effect of the spin-orbit interaction is suppressed (see figure 5.6), as previously observed in similar devices [155]. We measure G_l, as V_QDL and V_QDR are swept across two charge degeneracy points in each QD, resulting in the CSDs shown in figure 5.1d. Similar to the simulations (figure 5.1c), we find avoided crossings that indicate a strong coupling between odd parity states, i.e., $\Gamma_\mathrm{o}>\Gamma_\mathrm{e}$. Next, we rotate the external magnetic field away from the spin-orbit field, allowing spin non-conserving processes to occur. This is reflected in the avoided crossings in the CSDs (figure 5.1e), where we indeed see that even-parity states can now hybridize, indicating a sizeable Γ_e. In particular, the top left and bottom left avoided crossings have changed direction, indicating an even parity ground state at these charge degeneracy points. The evolution from figure 5.1d to figure 5.1e suggests that the field angle can be used to tune the system into the sweet spot ($\Gamma_\mathrm{o}=\Gamma_\mathrm{e}$) where MBSs emerge.

5.4 RESULTS

5.4.1 TUNING TO THE MAJORANA SWEET SPOT

We demonstrate the field-angle control over ECT and CAR in figure 5.2. Figure 5.2a shows a CSD obtained with $B \perp B_\mathrm{SO}$, around the charge transition corresponding to the lower left corner of figure 5.1c. The diagonal avoided crossing indicates that $\Gamma_\mathrm{e}>\Gamma_\mathrm{o}$. Rotating the field to align with B_SO results in an anti-diagonal avoided crossing, as now $\Gamma_\mathrm{o}>\Gamma_\mathrm{e}$ (figure 5.2c). The separation between the branches of the avoided crossing is proportional to $\sqrt{|\Gamma_\mathrm{o}^2-\Gamma_\mathrm{e}^2|}$ (detailed in section 5.7), which can be used to quantify the relative strength of the couplings. Measuring this quantity for several angles (figure 5.2d) shows a smooth evolution of the coupling strength as a function of the field angle. Importantly, at an intermediate angle the avoided crossing disappears (figure 5.2b), indicating $\Gamma_\mathrm{e}=\Gamma_\mathrm{o}$. Under these conditions, the odd and even parity ground states are degenerate at the charge degeneracy point, i.e., $\delta\mu_\mathrm{L} = \delta\mu_\mathrm{R} = 0$, leading to localized MBSs on each QD [79]. We refer to this point in parameter space as the Majorana sweet spot. At the sweet spot, simultaneous tunneling spectroscopy on the left and right QD demonstrates correlated ZBPs (figure 5.2e). Higher energy excitations are visible at ± 40 µV, providing an estimate of the effective couplings at the sweet spot to be $\Gamma_\mathrm{e}= \Gamma_\mathrm{o}\approx$ 20 µeV. These ZBPs are expected to persist when only

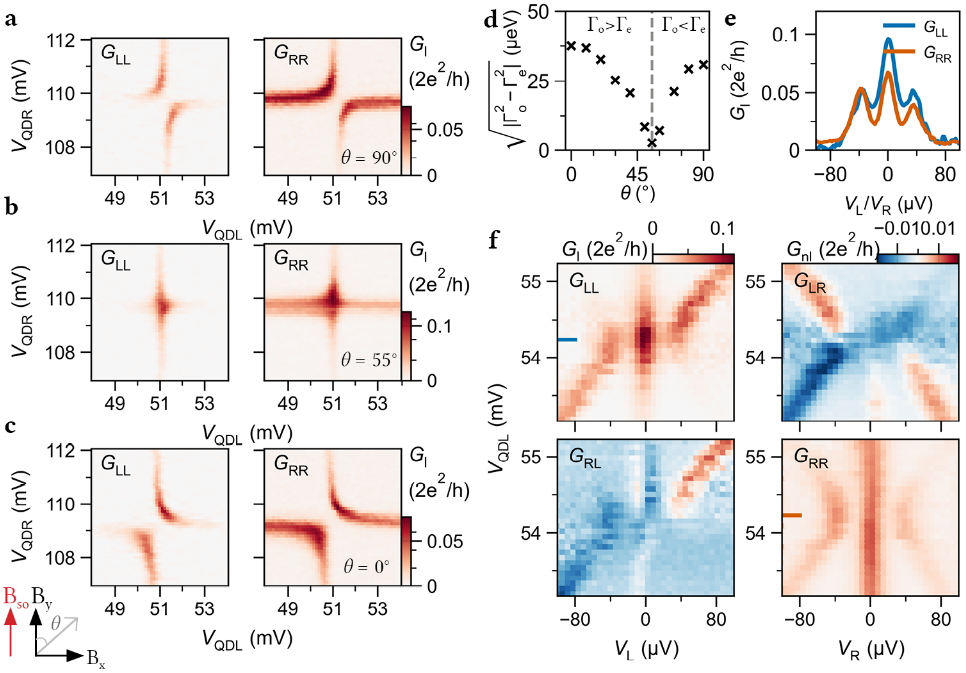

Figure 5.2: **Tuning Γ_e and Γ_o with magnetic field angle.** Measurements obtained for device B, characterized in figure 5.6. **(a)** CSD showing a diagonal avoided crossing (Γ_e>Γ_o), obtained with $B \perp B_{SO}$. **(c)** Rotating the field such that $B \parallel B_{SO}$, the avoided crossing changes direction ($\Gamma_e \approx < \Gamma_o$). **(b)** At 55° the the avoided crossing disappears ($\Gamma_e = \Gamma_o$). **(d)** Extraction of $\sqrt{|\Gamma_o^2 - \Gamma_e^2|}$ from CSDs measured at various magnetic field angles. **(e)** G_l measured at the centre of the CSD in (b), showing correlated zero-bias peaks. **(f)** G_l and G_{nl} measured upon detuning V_{QDL}, while keeping V_{QDR} on resonance. Correlated zero-bias peaks persist across a large voltage range. Raw data and the extraction procedure is presented in figure 5.7. Measurements are taken at B =80 mT.

a single QD is perturbed, as they result from MBSs localized on each of the QDs. To confirm this, we measure G_l and G_{nl} upon detuning V_{QDL}, while keeping V_{QDR} constant (figure 5.2f). The ZBPs indeed persist in G_l, while higher energy excitations are observed to disperse when QDL is detuned. Further, in G_{nl} only the higher energy excitations are visible while the ZBPs themselves do not appear, a signature of the localized nature of these zero-energy states. These observations are consistent with experiments on nanowires [28] and theoretical predictions [33].

The above procedure for tuning to the sweet spot is guaranteed to work if one starts with a field angle where Γ_e>Γ_o, since Γ_e can always be decreased by rotating the field towards B_{SO}. If a field rotation reveals that such an angle cannot be found, one can reach the sweet spot via electrostatic control over the hybrid section [28], since Γ_e and Γ_o are affected by the charge and energy of the ABSs [25, 27]. Here, the ABS energies are controlled via the voltage V_{ABS}, applied to the gate above the proximitized region. With the magnetic field directed away from the spin-orbit field (as in figure 5.1e), we study the evolution of the CSDs with V_{ABS}. Figure 5.3a shows a diagonal avoided crossing, signifying Γ_o>Γ_e.

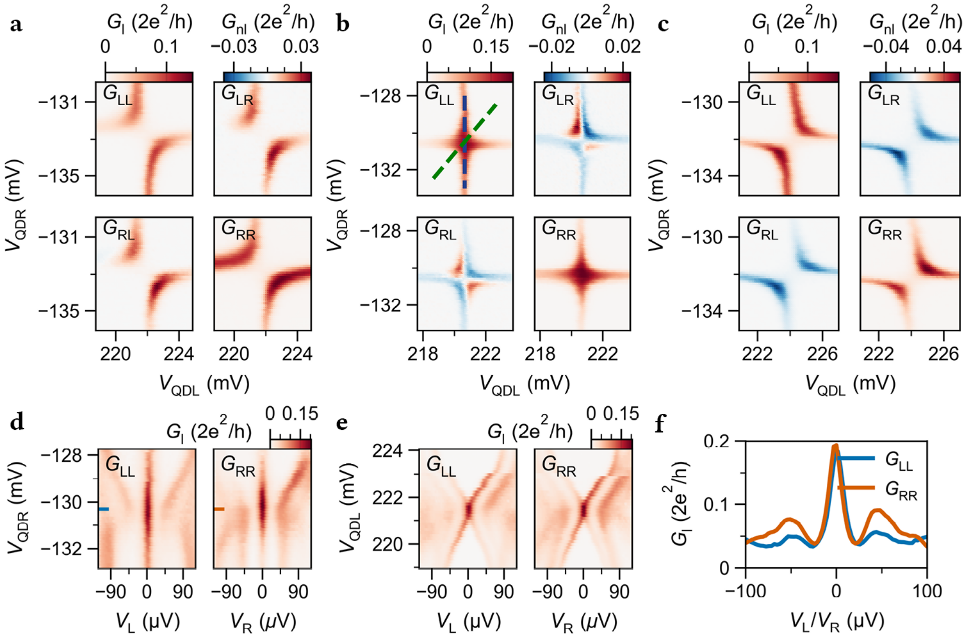

Figure 5.3: **Electrostatically tuning to the Majorana sweet spot.** **(a)**, **(b)** and **(c)** show CSDs taken at three different applied voltages V_{ABS}, in device A. The system is smoothly tuned from the $\Gamma_o > \Gamma_e$ regime in (a) to the $\Gamma_o < \Gamma_e$ regime in (c). In between, the $\Gamma_o = \Gamma_e$ condition is satisfied (b). A more extensive range is highlighted in figure 5.10. **(d)** Tunneling spectroscopy measurements at the sweet spot. V_{QDR} is tuned along the blue path shown in (b), while QDL is kept on resonance. **(e)** Tunneling spectroscopy as V_{QDL} and V_{QDR} are tuned simultaneously along the green path shown in (b). **(f)** Line-trace from (d) with V_{QDL} and V_{QDR} tuned to the sweet spot in (b) (corresponding to $\delta\mu_L = \delta\mu_R = 0$). Data is taken with $B = 150\,\mathrm{mT}$.

By tuning V_{ABS}, the avoided crossing changes direction, indicating $\Gamma_e > \Gamma_o$ (figure 5.3c). At an intermediate V_{ABS} the avoided crossing disappears (figure 5.3b), satisfying the sweet spot condition ($\Gamma_e = \Gamma_o$). Similar to figure 5.2, we now detune V_{QDR} along the blue dashed line in figure 5.3b and measure G_l, again finding correlated, persisting ZBPs (figure 5.3d). Line-cuts from figure 5.3d are shown in figure 5.3, giving an estimate of $\Gamma_e = \Gamma_o = 25\,\mu\mathrm{eV}$. When both QDs are detuned simultaneously, along the green dashed line in figure 5.3b, the correlated ZBPs disperse quadratically (figure 5.3e). This is expected for a two-site Kitaev chain, where the ZBPs are only protected from local perturbations [33]. An extended dataset and a comparison with numerical results is shown in figure 5.9.

In addition to G_l, the non-local measurements in figure 5.3a-c can provide further information about underlying transport mechanisms. For example, it has been shown that for CAR, local and non-local signals have the same sign, while for ECT their sign should be opposite [26]. Since charge is ill-defined for YSR-states, there is no one-to-one correspondence between the dominant inter-dot coupling (i.e., Γ_e, Γ_o) and the dominant underlying transport mechanism (i.e., CAR, ECT). Nevertheless we find a qualitatively similar behaviour, whereby for $\Gamma_o > \Gamma_e$ the non-local conductance is positive, whereas for $\Gamma_e > \Gamma_o$ it is negative. We show that this is indeed expected (see figure 5.11), and that the sign of G_L is dictated by the positions of the QDs w.r.t. their charge degeneracy.

5.4.2 ESTIMATING THE MAJORANA POLARISATION

The ideal Kitaev chain is based on a spinless model. Thus, emulating this system with spinful QDs, as presented here, requires the Zeeman energies of the QDs to be sufficiently large compared to the effective coupling between the QDs [33, 37, 38, 79, 177]. In addition, MBSs on either QD should be isolated from each other. A parameter capturing these factors is the so-called Majorana polarisation (MP) [83], which has recently been investigated theoretically in the context of Kitaev chains [35]. The MP is a metric (denoted $|M|$) that quantifies the extent to which localized MBSs hybridize, and is relevant for experiments that require controlled manipulation of multiple MBSs, such as braiding [177, 180] and parity-based qubits [33, 179, 184, 185]. The MP ranges from 0 (lowest polarisation) to 1 (highest polarisation), and in experiments it is desirable to have a high value of MP. It was shown that both "low" and "high" MP can result in similar transport signatures [35], raising an important question about how one could experimentally distinguish between these regimes.

In order to investigate this, we track the evolution of the system from 300 mT to 0 mT (along B_z). At each field, we find similar crossings in the CSDs (figure 5.4a-c). Simultaneous tunneling spectroscopy of the QDs at these crossing points reveal correlated ZBPs, down to zero magnetic field (figure 5.4j). Furthermore, the behaviour of non-local conductance around the centre of each crossing [35] also shows no discernible differences as the field is reduced. At first instance, these observations are surprising, since MBSs require time reversal symmetry to be broken. However, we note that the combination of time-reversal symmetry and Coulomb interactions can result in robust zero energy modes associated with Kramers pairs of Majorana zero modes, as discussed in [121]. While further investigation is needed to confirm this interpretation, we can conclude that experimentally it is difficult to extract information about the MP from such measurements.

On the other hand, we find that the dispersion of higher energy excitations in tunnelling spectroscopy has a distinctly different behaviour at each magnetic field, and allows us to obtain information about the MP. While the ZBPs themselves persist upon detuning QDR for all values of B, the excited states show a markedly different behaviour (figure 5.4d–f). For example, at large detuning of QDR, excited states are visible at $\pm 100\,\mu$V in figure 5.4d, while reaching only $\pm 60\,\mu$V in figure 5.4e. We denote this energy difference between the first excited states and the ZBPs as E_{gap} at the sweet spot and as E_{det} at large negative detuning, and extract these energies over an extensive range in B (figure 5.4k). Both E_{det} and E_{gap} are found to increase monotonically with increasing magnetic field. For these sets of measurements, E_{gap} starts to saturate at $30\,\mu$V at higher fields, while E_{det} increases linearly until saturating at $80\,\mu$V. The latter can be expected, since the excitation energy of the hybrid system approaches the excitation energy, i.e., the Zeeman energy of an isolated QD, when either of the QDs is detuned.

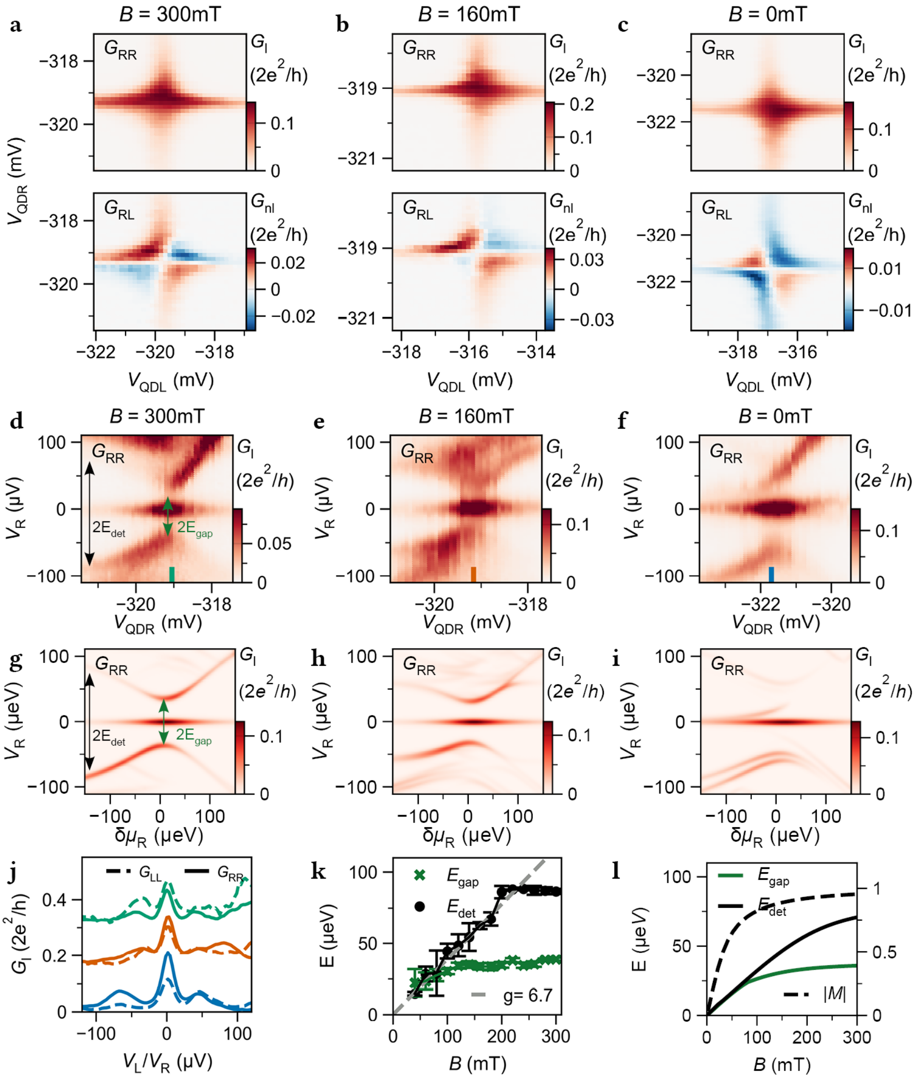

Figure 5.4: **Majorana sweet spots in varying magnetic field. (a)**, **(b)** and **(c)** CSDs at "Majorana sweet spots" measured at applied fields of 300 mT, 160 mT and 0 mT respectively. At each field, V_{ABS} is adjusted to tune to the "sweet spot", following the procedure from figure 5.3. **(d-f)** Measured G_{RR} upon detuning QDR, while keeping QDL on resonance. Data is saturated for visibility of the excited states. Energies of interest (E_{gap} and E_{det}) are highlighted in (d). **(g-i)** Numerically calculated conductance, for qualitative comparison with (e-g). **(j)** G_{RR} (solid) and G_{LL} (dashed) line-cuts at the centre of each CSD, from indicated positions in (d-f), highlighting the presence of correlated ZBPs. Offsets of 0.15 and 0.3 are applied for 160 mT and 300 mT respectively. **(k)** Extraction of the energies E_{gap} and E_{det} from measurements between 300 mT and 0 mT (full dataset in figure 5.13). Dashed line shows a linear fit of E_{det}, providing an estimate for the g-factor of QDL. **(l)** Numerically extracted evolution of E_{gap} and E_{det} (solid) and corresponding Majorana polarisation $|M|$ (dashed) as a function of the magnetic field.

We compare these measurements with numerical simulations of the system, with input from experimental parameters, and find that indeed E_{det} provides a lower bound estimate of E_z of the QDs (figure 5.12). This allows to approximate a g-factor from figure 5.4k. Using this, the simulated spectra demonstrate a qualitatively similar behaviour in the dispersion of the excited states (figure 5.4g-i). Furthermore, we find that the evolution of both E_{gap} and E_{det} compare well to the experimental results (figure 5.4l). These results allow us to numerically estimate the Majorana polarisation for the system, as a function of magnetic field (figure 5.4l). We find that as B increases, the MP increases quickly from 0 and then starts to approach 1 around 100 mT, where E_{gap} begins to saturate. The comparison here yields $M \approx 0.96$ at around $B = 300\,\mathrm{mT}$. A similar analysis is performed for measurements using the sweet spot shown in figure 5.3, where E_{gap} reaches 50 μV, from which we extract a lower MP estimate of $M \approx 0.9$ (figure 5.14). Whether these estimates can be considered a "high" MP is dependent on the operations one intends to perform. For example, specific braiding protocols have been shown to be reliable for $M \approx 0.98$ [177]. It should be noted that these experiments do not constitute a direct measurement of the MP. One way to achieve this is to introduce an additional QD on either side with a tunneling coupling to either MBS [87–89], which has recently been demonstrated experimentally [90]. Regardless, the presented measurements show that the evolution of the system from zero magnetic field to high magnetic field can be well understood within the framework of the Kitaev model.

5.5 DISCUSSION

The results in this chapter first and foremost reproduce the findings on InSb nanowires [28], where the experimental implementation of a two-site Kitaev chain was first demonstrated. The reproducibility of these results demonstrate that the underlying physics is platform independent and marks a promising path forward in the study of Majoranas. We chose to develop the InSbAs platform for this purpose, due to the flexibility of the 2D top-down fabrication. While more complicated experiments on more sites will require finetuned control over many gate voltages, many experiments may now be within reach that were previously inaccessible, which we address in Chapter 9.

The purpose of section 5.4.2 is to provide a partial assessment of whether we can expect the system to be suitably described by the Kitaev chain model, in order to perform the next generations of experiments relying on the presence of unpaired Majoranas. A surprising finding is that many of the key Majorana signatures in the two-site Kitaev chain can be reproduced in the absence of a magnetic field. This has spurred a deeper theoretical study, presented in Ref. [121]. We stress, however, that we can expect these features to be reliable indicators when the Zeeman energies in the quantum dots are known. While in the meantime more general metrics have been explored [82], we expect that the Majorana polarisation estimate used here gives at-least a rough indication that we can get close to the ideal case. A study on InSb nanowires has used a more direct measurement to infer this information [90], which agrees with this assessment. An interesting aspect of the investigation shown here, is that the effective g-factor of the system in figure 5.4 was found to be only 6.8, while the non-proximitized QDs in Chapter 5 have a g-factor that is 3-7 times higher. While on one hand this means that strongly coupling the QDs can come at quite a cost to the Zeeman energy, we nevertheless find that there is sufficient wiggle-room in the parameter space to sufficiently spin-polarise the system. We therefore expect that it should be possible to create devices with the high Majorana polarisations required for e.g. braiding experiments.

5.6 Summary

In summary, we have implemented a two-site Kitaev chain in a two-dimensional electron gas by coupling two QDs via ABSs in a superconductor-semiconductor hybrid region. We demonstrate a smooth control over the inter-dot couplings, both by rotations of the magnetic field and by tuning the energy of Andreev bound states in the hybrid section. At specific points in the parameter space, zero energy excitations arise that are stable against local perturbations of either QD. We show that these “sweet spots” (accompanied by correlated ZBPs) appear in the system even at zero magnetic field, and are by themselves insufficient to gain information about the polarisation of MBSs. Rather, we find that the magnetic field dependence of the finite-bias energy spectrum allows us to distinguish between high and low polarisation regimes. The presence of stable zero-energy modes at zero magnetic field warrants further investigation, to be continued in Chapter 7.

Data availability

Raw data and analysis scripts for all presented figures are available on Zenodo [186].

5.7 Methods

Device fabrication and yield

All devices were fabricated using techniques described in detail in [176]. A narrow aluminium strip is defined in an InSbAs-Al chip by wet etching, followed by the deposition of two normal Ti/Pd contacts. After deposition of 20 nm AlOx via atomic layer deposition (ALD), two Ti/Pd depletion gates are evaporated. Following a second ALD layer (20 nm AlOx), seven Ti/Pd finger gates are evaporated in order to define the QDs and tune the ABSs energy. The two depletion gates define a quasi-1D channel with a width of about 160 nm, contacted on each side by a normal lead. The aluminium strip induces superconductivity in the middle section of each device, with an induced gap on the order of 200 μeV. The presence of extended ABSs is confirmed through tunnelling spectroscopy. ABSs are found to be present over a large range of V_{ABS}, the voltage applied to the gate covering the hybrid region. Finger gates on the left and right of the aluminium define QDs with charging energies above 1 mV (figure 5.5a,b).

Two devices were used to obtain the data presented in this chapter. Both showed strong hybridization between the QDs, as presented here. Device A was used to study the field evolution of Majorana sweet spots and to obtain the measurements presented in figure 5.1, figure 5.3 and figure 5.4. Device B was used to demonstrate the role of spin-orbit coupling on the interdot interactions, and the control over interactions through magnetic field as presented in figure 5.2. Regarding device yield, 12 devices were measured for the purpose of studying hybridized QDs. Of these, 8 devices could be tuned to regimes with strongly coupled QDs that showed the tunability displayed in figure 5.3. Of the non-functional devices, 2 failed due to trivial reasons (e.g. losing electronic connection due to missing bond-wires after cooling). The remaining 2 devices failed at the stage of forming the 1-D channel, where we found some optimization is needed to discover the optimal separation between the top and bottom depletion gate.

Transport measurements and data processing

Transport measurements are performed in AC and DC using a three-terminal set-up, where the aluminum is electrically grounded. Each Ohmic lead is connected to a current-to-voltage converter and biased through a digital-to-analogue converter that applies both DC and AC biases. Offsets of the applied voltage-bias on each side are corrected via independently calibrating the Coulomb peaks in the QDs on each side. The voltage outputs of the current meters are recorded with two digital multimeters and two lock-in amplifiers. When applying a DC voltage to the left Ohmic (V_L) the right lead (V_R) is kept grounded and vice versa. AC excitations are applied on each side with amplitudes around 5 μV RMS and frequencies of 19 Hz (left) and 29 Hz (right). In this way, we measure the full conductance matrix G by first measuring the response of I_L and I_R to V_L and then to V_R. We account for the voltage-divider effect by correcting the conductances using known fridge line resistances (3.6 kΩ in device A, 3.3 kΩ in device B), as detailed in [143]. This correction was done for all presented spectroscopy data, except for the data shown in figure 5.3d-f. Magnetic fields were applied using a 3D vector magnet. The alignment of the magnetic field of device A is expected to be accurate within ±10° and calibrated through performing tunneling spectroscopy of the hybrid section as a function of field angle. The alignment of device B is expected to be accurate within ±5°.

Due to device instabilities or charge jumps, electrostatics of the QDs experience small drifts over the course of the measurements. Investigated orbitals were tracked while collecting the presented datasets. For each tunnelling spectroscopy measurements at a sweet spot, where V_QDL and/or V_QDR were detuned, a CSD was obtained directly before and directly after to ensure that no drifts occurred during such a measurement. If such a drift occurred, the measurement was discarded and repeated. Such drifts are the cause of small discrepancies in gate voltages between highlighted paths in figure 5.3b and the measurements shown in figure 5.3d,e. The highlighted paths represents the corrected path taken w.r.t. the CSD shown in figure 5.3b, based on the CSDs obtained before and after the measurements.

Extracting QD parameters

In order to compare energy scales between experiments and numerical calculations, the gate voltages V_QDL and V_QDR are converted to electro-chemical potential energies μ_L and μ_R. For this purpose we extract the dimensionless lever arms α. When forming sub-gap YSR states in the QDs, the effective lever arm of each QD around a zero-bias charge degeneracy can differ from the lever arm of the uncoupled QD, depending e.g. on hybridization with the hybrid region (figure 5.8), extensively addressed in [80]. For analysis we therefore estimate both the normal-state lever arm (denoted α_N) and the lever arm of the sub-gap YSR-states (denoted α_YSR), at the specific V_ABS regimes of interest. Device B was operated in a regime without significant difference between α_N and α_YSR, such that the analysis in figure 5.2d uses the lever arms extracted in figure 5.6. With the orbitals in figure 5.4, sweet spots were investigated at magnetic field values between 0 mT and 300 mT, where the energy of excited states E_{det} was extracted at a fixed detuning of V_{QDR}. A g-factor is extracted from this data, by a linear fit of E_{det} up to 180mT (before saturation). For this dataset α_{YSR} was only obtained at 0 mT (figure 5.5), such that any change in α_{YSR} as a function of magnetic field can not be accounted for in the analysis in figure 5.4l and figure 5.4. When extracting E_{det} at constant detuning of V_{QDR} at each field, μ_{R} may not be constant but rather is expected to decrease (figure 5.8). We note that the lack of this correction may lead to slightly underestimating the g-factor in figure 5.4h, which in turn will lead to a lowered estimation of the Majorana polarization. For the extractions of E_{det} and E_{gap}, G_{LL} and G_{RR} line-traces are obtained at the sweet spot and at a detuning of V_{QDR} of -2mV, corresponding to a detuning of $\mu_{\mathrm{R}} \approx 100\mu eV$. From each line-trace, the separation between the ZBPs and the first higher energy excitation is extracted by fitting Gaussian peaks symmetrically around zero-bias. Error-bars are given by the uncertainty in these fits.

NUMERICAL TRANSPORT CALCULATIONS

For all presented numerical results, a description of the system incorporating both the two QDs and the middle hybrid section was used, recently introduced in [35]. We employ the same model and highlight key points and used numerical parameter below. The model considers tunneling between two normal QDs (L,R) and a central QD (M), which is in proximity to a superconductor. Each site j has electrochemical potential energy μ_j. A spin-conserving hopping t allows transport between the outer QDs and central QD. The effect of spin-orbit interactions is included through a spin-flip hopping term t_{SO} between the outer QDs and central QD. The presence of the SC is included by attributing a superconducting pairing term Δ_i in each QD. To match the experimental geometry, $\Delta_{\mathrm{L,R}}, < \Delta_{\mathrm{M}}$ Lastly, the left and right sites are assigned a large on-site charging energy U and a Zeeman splitting E_z between the $|\downarrow\rangle$ and $|\uparrow\rangle$ occupation. The Hamiltonian is constructed as follows:

$$
\begin{aligned}
H = &\sum_{j,\sigma} \mu_j n_{j\sigma} + \sum_{j} U_j n_{j\uparrow} n_{j\downarrow} + \sum_{j} E_{Z\,j}(n_{j\downarrow} - n_{j\uparrow}) \\
&+ \sum_{j\neq \mathrm{M},\sigma} [t_j d^{\dagger}_{j\sigma} d_{C\sigma} + h.c.] \\
&+ \sum_{j\neq \mathrm{M}} [t^{\mathrm{SO}}_j d^{\dagger}_{j\downarrow} d_{C\uparrow} - t^{\mathrm{SO}}_j d^{\dagger}_{j\uparrow} d_{C\downarrow} + h.c.] \\
&+ \sum_{j} [\Delta_{\mathrm{j}} d^{\dagger}_{j\uparrow} d^{\dagger}_{j\downarrow} + h.c.]
\end{aligned}
$$

where $d_{j\sigma}, d^{\dagger}_{j\sigma}$ and $n_{j\sigma}$ are the annihilation, creation, and number operators respectively for each site. The sum j runs over the sites (L,M,R) and σ over the spin degree of freedom $(\uparrow, \downarrow)$. For simplicity, a left and right symmetry is assumed, such that a Majorana sweet spot lies along $\mu_{\mathrm{L}} = \mu_{\mathrm{R}}$. Sweet spots are obtained by scanning the parameter space spanned by $\mu_{\mathrm{L}} = \mu_{\mathrm{R}}$ and μ_{M} and finding degeneracies between lowest odd and even eigenstates. All transport calculations are obtained using the rate equation detailed in [35]. Similar to [35], we calculate the quantity of Majorana polarization (MP) (originally introduced in [83] and briefly covered in section 2.2.4). This quantity, denoted M_j, is defined per site j as:

$$\begin{aligned} M_j &= \frac{\sum_\sigma (w_\sigma^2 - z_\sigma^2)}{\sum_\sigma (w_\sigma^2 + z_\sigma^2)} \\ w_\sigma &= \langle O|(d_{j\sigma} + d_{j\sigma}^\dagger)|E\rangle \\ z_\sigma &= \langle O|(d_{j\sigma} - d_{j\sigma}^\dagger)|E\rangle \end{aligned}$$

where $|O\rangle$ and $|E\rangle$ are the lowest-energy odd and even states respectively. Due to symmetrically chosen parameters $|M_\mathrm{L}| = |M_\mathrm{R}| = |M|$, such that a single MP value can be extracted for a specific set of parameters. To provide an experimental observable that reflects a high or low $|M|$, we investigate the behavior of two transition energies, denoted in the main text as E_gap and E_det. Numerically these are obtained from the Hamiltonian as the energy difference between the lowest even state and the second-lowest odd state, at specific values of μ_L and μ_R. E_gap is obtained with μ_L and μ_R set to corresponding to their sweet spot value. E_det is obtained with μ_R detuned by $\approx \Delta_\mathrm{M}$. In the absence of the Zeeman term, both E_gap and E_det are zero by definition, due to the degeneracy of the odd states in the presence of time reversal symmetry. The dependence of M, E_gap and E_det on E_z is demonstrated in figure 5.14.

In order to compare to experiments, parameters are selected to match realistic values. We set Δ_M = 100 μeV and $\Delta_\mathrm{L,R} = 0.5\Delta_\mathrm{M}$. The charging energy U is fixed in both dots to be $10\Delta_\mathrm{M}$, except for figure 5.1d where a value of $7\Delta_\mathrm{M}$ is used to better highlight the behaviour of all four avoided crossings in the large CSD. For the analysis in figure 5.4, tunneling terms t and t_SO are fine-tuned such that at large E_z the sweet spot gap of 30 μeV is obtained, to match the experimental result. This gives $t_\mathrm{SO} = 0.4t = 0.7\Delta_\mathrm{M}$. Similarly, to compare to the experimental results in figure 5.9 and figure 5.14, t and t_SO are fine-tuned to obtain a sweet spot gap of 50 μeV at large E_z. This results in $t_\mathrm{SO} = 0.4t = 0.85\Delta_\mathrm{M}$.

EFFECTIVE MODEL IN THE STRONG COUPLING REGIME

The above description is used for all presented calculations. To provide an intuitive understanding of these results, we invoke a description of the system through an effective model, introduced in detail in [79]. Here we provide a brief summary of the relevant findings. When the energy E_ABS of the sub-gap state in the middle site is large compared to tunnel couplings between the QDs, the middle site can be integrated out. This leaves a description of the system including only effective couplings between YSR states in the left and right QD sites. Additionally, it is assumed that E_z is sufficiently large such that only the $|\downarrow|$ occupation of each QD partakes in transport. In this description, a Hamiltonian can be constructed in a singlet-doublet basis. The ground state of each QD is either the $|\downarrow\rangle$ doublet or a singlet $|S\rangle$ of the form $|S\rangle = u_\mathrm{L,R}|0\rangle - v_{\mathrm{L,R}|}|\downarrow\uparrow\rangle$. Here the u, v components depend on the chemical potential energies μ_L and μ_R of the left and right dot: ($u_\mathrm{L,R}^2 = 1 - v_\mathrm{L,R}^2 = \frac{1}{2} + \frac{\mu_{L,R}+U}{\sqrt{U^2+E_\mathrm{ABS}^2}}$). The effective Hamiltonian is obtained:

$$H_\mathrm{coupling}^\mathrm{eff} = \sum_{\sigma,\eta=\uparrow,\downarrow} (t_{\sigma\eta} c_{L\sigma}^\dagger c_{R\eta} + \Delta_{\sigma\eta} c_{L\sigma}^\dagger c_{R\eta}^\dagger) + h.c., \tag{5.1}$$

where $c_{\mathrm{L,R}}$ and $c^{\dagger}_{\mathrm{L,R}}$ are annihilation and creation operators for the left and right sites. Further, $t_{\sigma\eta}$ specifies the amplitude of an electron with spin σ from left site tunneling to occupy a state with spin η in the right side, or vice versa. $\Delta_{\sigma\mu}$ specifies the amplitude of the creating or breaking of a Cooper pair through electrons with spins σ and η in the left and right QDs ($\sigma, \eta \in [\uparrow, \downarrow]$). Due to the spin-orbit interaction two equal-spin electrons can also be coupled via the Δ-term. Importantly, this description is equivalent to the weakly coupled model discussed in [33], when changing from a charge occupation basis to a YSR-state basis. Now, two types of coupling arise between the total even-parity states (denoted Γ_{E}) and between total-odd parity states (Γ_{O}). Each are combination of ECT and CAR amplitudes:

$$\begin{aligned}
\Gamma_{\mathrm{E}} = \langle SS|H^{\mathrm{eff}}_{\mathrm{coupling}}|\downarrow\downarrow\rangle \quad &= -\Delta_{\uparrow\uparrow} v_L v_R + \Delta_{\downarrow\downarrow} u_L u_R + t_{\uparrow\downarrow} v_L u_R - t_{\downarrow\uparrow} u_L v_R, \\
\Gamma_{\mathrm{O}} = \langle S\downarrow|H^{\mathrm{eff}}_{\mathrm{coupling}}|\downarrow S\rangle \quad &= -t_{\uparrow\uparrow} v_L v_R + t_{\downarrow\downarrow} u_L u_R + \Delta_{\uparrow\downarrow} v_L u_R - \Delta_{\downarrow\uparrow} u_L v_R,
\end{aligned}$$

The coupling Γ_{O} results in bonding and anti-bonding states of the form $u|\mathrm{S},\downarrow\rangle \pm v|\downarrow,\mathrm{S}\rangle$. Γ_{E} forms bonding and anti-bonding states of the form $\alpha|\mathrm{S},\mathrm{S}\rangle \pm \beta|\downarrow,\downarrow\rangle$. When $\Gamma_{\mathrm{E}} = \Gamma_{\mathrm{O}}$ the even and odd ground states become degenerate at $\mu_{\mathrm{L}} = \mu_{\mathrm{R}}$, equivalent to the $t = \Delta$ condition in the "poor Man's Majorana" description [33]. In figure 5.2d, we extract the distance between the branches of the avoided crossing in the experimentally obtained CSDs, after converting the gate voltages to the YSR energies of each QD. In the effective description this distance corresponds to analysing where the line $\mu_L = \mu_R$ or $\mu_L = -\mu_R$ intersects a degeneracy between the even and odd ground state energies. This gives two points, separated by $\sqrt{8|\Gamma_{\mathrm{O}}^2 - \Gamma_{\mathrm{E}}^2|}$.

5.8 Extended Data

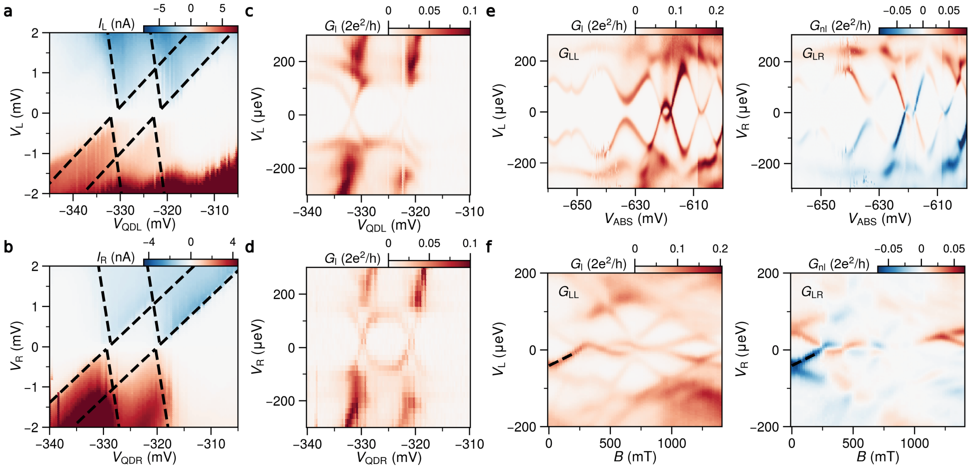

Figure 5.5: **Characterization of QDs and ABS spectroscopy for device A. (a-b)** Coulomb diamond measurements of the left and right QDs, in the regime used for measurements presented in figure 5.4. Charging energies are estimated to be 1.1 meV in each QD. The lever arm of the left and right dot is estimated to be $\alpha \approx 0.11$. **(c-d)** Zoomed in views of figures (a) and (b) in a smaller energy range. Due to a large tunnel coupling between the QDs and the hybrid section, YSR-states form in the sub-gap spectrum of the QDs. Tunneling spectroscopy around the charge degeneracy points in (a-b) reveal clear sup-gap features within the Coulomb diamonds. As V_{QDL} and V_{QDR} are tuned, the sub-gap features form an eye-shape feature enclosing the doublet charge occupation. This behavior is typical for YSR-states with large charging energies [154]. **(e)** Crossed Andreev reflection and elastic co-tunneling require the presence of extended ABSs. Local G_{l} and non-local conductance G_{nl} of the hybrid region are measured via tunnelling spectroscopy and their identical energy dependence as a function of V_{ABS} highlights that ABSs extend across the entire hybrid section. Comparable behavior was observed in a wide V_{ABS} range from 0 to −1 V. The measurement presented in figure 5.1 is taken at the V_{ABS} with the eye-shaped crossing. **(f)** ABS spectroscopy as a function external magnetic field at $V_{\mathrm{ABS}} = -623$ mV. The effect of splitting of the doublet state can be observed at low fields. A g-factor of 5.5 is extracted by linear fitting of the lowest sub-gap states (dashed line) in figure 5.5d.

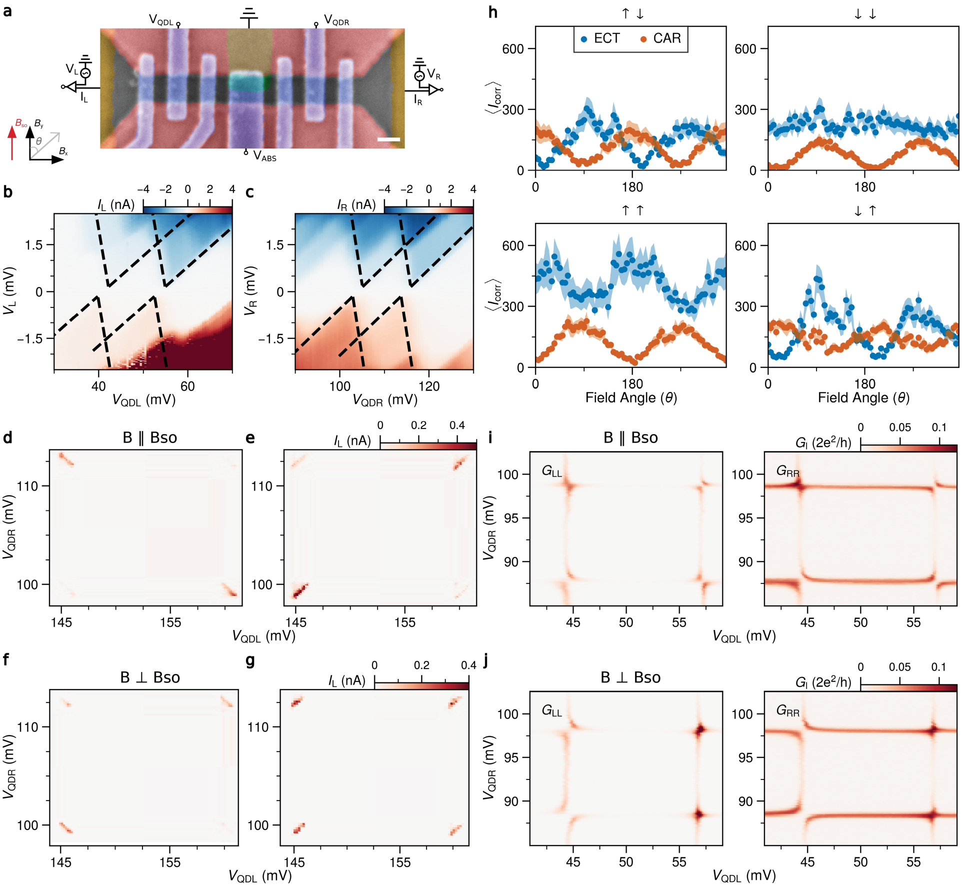

Figure 5.6: **Characterization of device B. (a)** Scanning electron micro-graph of device B, used to obtain the measurements presented in figure 5.2. Scale bar shown is 100 nm. **(b-c)** Coulomb diamond measurements of the left and right QDs. Charging energies are extracted to be 1.4 meV. The lever arm α_N is extracted to be about 0.11 for each QD. This lever arm is used for the extraction in figure 5.2d. (**d-e**) To validate the direction of B_{SO} and to show the connection between interactions in strongly coupled QDs and underlying ECT and CAR processes, we first measure ECT and CAR currents in the weakly coupled dots, as detailed in [155]. With $B \perp B_{SO}$, measurements of CAR (d) and ECT (e) show the typical blockades for same-spin and opposite-spin charge configurations respectively. In (**f-g**), with $B \parallel B_{SO}$, the spin non-conserving ECT and CAR processes are observed to be revived. **(h)** Measuring CAR and ECT rates as a function of magnetic field angle θ shows the currents for the spin non-conserving processes are indeed smoothly controlled and become suppressed when $\theta = 0$. This supports the interpretation that $B \parallel B_{SO}$ when B is perpendicular to the 1-D channel. **(i-j)** Next, the QDs are operated with higher tunnelling rates between the QDs and the SC, to enable strong couplings. Similar to figure 5.1e-f, CSDs are obtained in the strongly interacting regime, taken with the verified $B \parallel B_{SO}$ and $B \perp B_{SO}$ respectively.

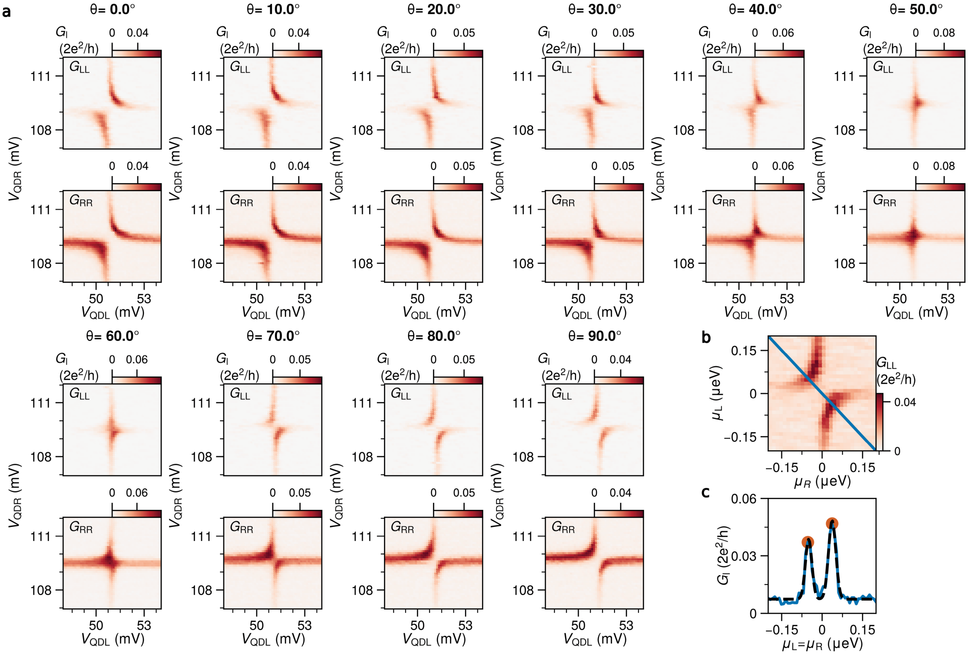

Figure 5.7: **Extended dataset of Figure 2**. **(a)** CSDs measured at various magnetic field angles θ between 0° and 90°, used to extract the data shown in figure 5.2d. **(b)** Example of the extraction process. For each obtained CSD, V_{QDL} and V_{QDR} are converted to energies μ_{L} and μ_{R} using lever arms obtained in figure 5.6. Next, the conductance is extracted along a $\mu_{\mathrm{L}} = -\mu_{\mathrm{R}}$ or $\mu_{\mathrm{L}} = \mu_{\mathrm{R}}$ line. **(c)** Two Gaussian peaks are fitted to extract the separation between the two avoided crossings, from which the quantity $\sqrt{|\Gamma_{\mathrm{o}} - \Gamma_{\mathrm{e}}|}$ is obtained (plotted in figure 5.2d).

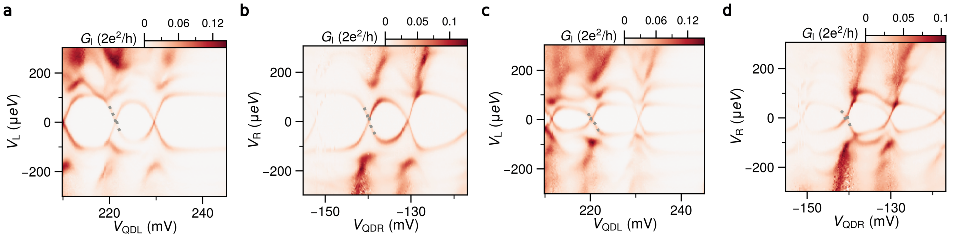

Figure 5.8: **Characterisation of YSR-states in QDs of Figure 3.** To complement the data in figure 5.3, figure 5.9 and figure 5.14, we measure the sub-gap states in QDL and QDR (see figure 5.5). Using this, we obtain the lever arms of V_{QDL} and V_{QDR} on the YSR-state energies (denoted α_{YSR}) (see section 5.7). **(a-b)** Sub-gap spectroscopy of QDL and QDR at B_z=0 mT. From the slopes of the states upon crossing $V_{\mathrm{L}}, V_{\mathrm{R}} = 0$, we estimate $\alpha_{\mathrm{YSR}} \approx 0.045$. Applying an external magnetic field lowers the energy of ABSs in the hybrid region, as a result of Zeeman splitting, This in turn will affect the YSR-spectrum of the QDs, due to increased hybridization between the QDs and the ABS. **(c-d)** Measuring sub-gap spectroscopy of QDL and QDR at B_z=225 mT for the same settings as in (a-b) shows indeed the effective lever arm here decreases to $\alpha_{\mathrm{YSR}} \approx 0.028$.

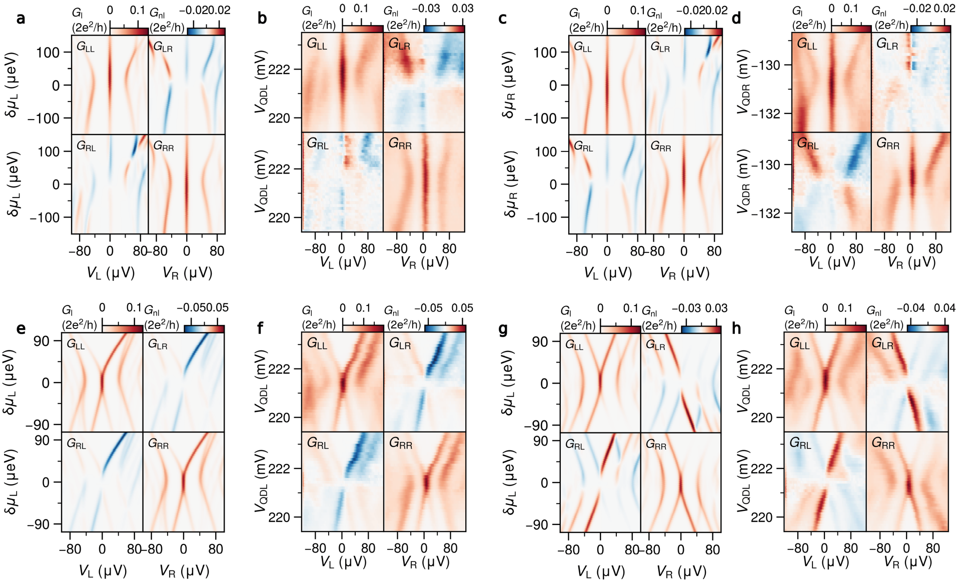

Figure 5.9: **Full conductance spectra at the sweet spot upon detuning V_{QDL} and V_{QDR}.** A comparison between numerically calculated conductance and measured conductance in support of Figure 3, measured at $B = 225\,\mathrm{mT}$. Presented results show the evolution of G_l and G_nl for four different cases: **(a-b)** detuning V_{QDL}, **(c-d)** detuning V_{QDR}, **(e-f)** detuning both V_{QDL} and V_{QDR} simultaneously along a diagonal path and **(g-h)** detuning both anti-diagonally. For each case, we find the behavior of both G_l and G_nl is well described by the numerical results.

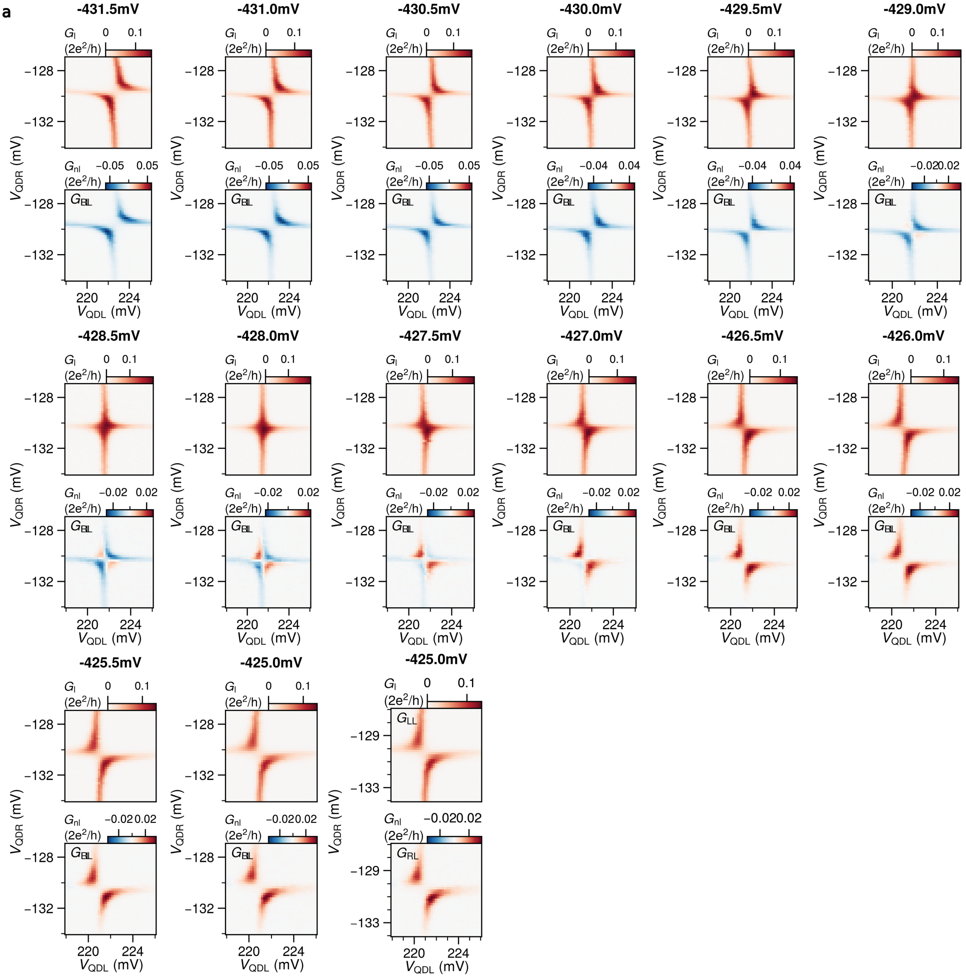

Figure 5.10: **Extended dataset for Figure 3. (a)** Sets of CSDs obtained while varying V_{ABS} in the range presented in figure 5.3. The range of V_{QDL} and V_{QDR} is constant for each measurement. The slight drift of the avoided crossing upon varying V_{ABS} is owed to cross-capacitance between V_{ABS} and the potential of the QDs.

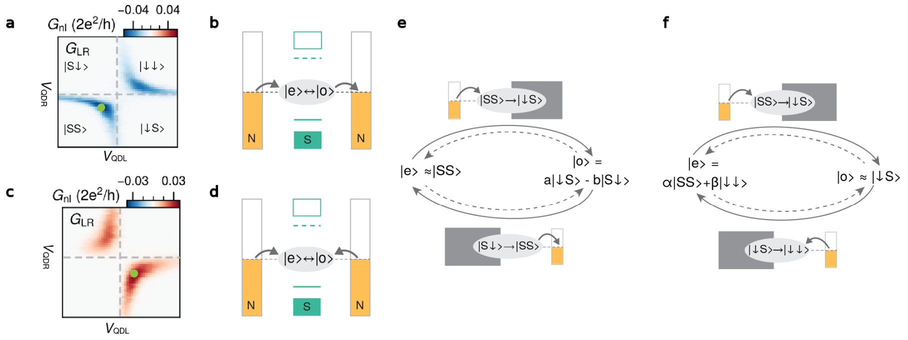

Figure 5.11: **Energy diagrams detailing non-local transport.** In CSDs presented in figure 5.3, a clear sign change is observed when changing from the $\Gamma_O > \Gamma_E$ regime to the $\Gamma_O < \Gamma_E$ regime. This can be understood by considering the possible transport cycles that underlie the measured non-local conductance. **(a)** When $\Gamma_O > \Gamma_E$, G_{nl} is observed to be negative in the measured CSDs (see figure 5.3c). **(c)** When $\Gamma_O < \Gamma_E$, the same measurements yield a positive G_{nl} (see figure 5.3a). Horizontal and vertical dashed lines indicate $\mu_R = 0$ and $\mu_L = 0$ respectively. The state of the uncoupled system is labelled in each quadrant. **(b,d)** In such CSD measurements, zero-bias transport can take place when the odd and even ground states are degenerate. For non-local transport to occur, the system can accept a hole/electron from one lead, and relax non-locally to its original state by either (b) donating a hole/electron to the opposite lead, giving rise to negative G_{nl}, or (d) accept a hole/electron from the opposite lead, giving rise to positive G_{nl}. The preferred path is dictated by the quadrant in μ_L, μ_R space where the odd-even degeneracy occurs. **(e)** When $\mu_L, \mu_R > 0$ or $\mu_L,\mu_R < 0$, the former path is expected to dominate and the resulting G_{nl} will be negative. **(f)** When $\mu_L > 0$ and $\mu_R < 0$ or vice versa, the latter path is expected to dominate and resulting G_{nl} will be positive.

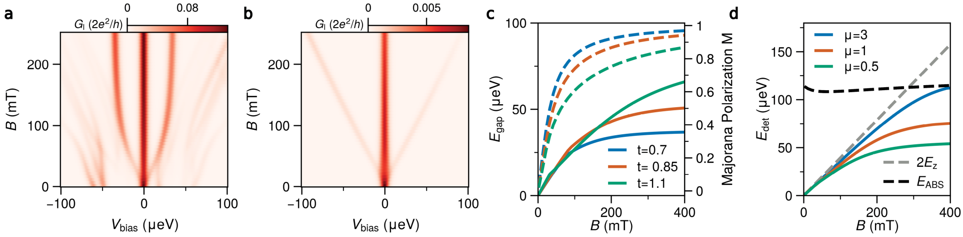

Figure 5.12: **Numerical analysis of E_{gap} and E_{det}** Numerical calculations supporting the results presented in Figure 4. Through the procedure detailed in section 5.7, Majorana sweet spots are obtained and analysed for fields between 0 mT and 300 mT. **(a)** Field evolution of G_{RR} line-traces at each sweet spot, showing the excitations above the ZBPs gradually increasing in energy and then saturating at ±30 μeV. **(b)** Field evolution of G_{RR} line-traces when QDR detuned by $3\Delta_{ind}$, showing the excited states increase linearly in energy. From calculations in (a) and (b), E_{gap} and E_{det} are obtained, given by the energy between the lowest even-parity state and second-lowest odd-parity state. **(c)** Extraction of E_{gap} (solid) and the Majorana polarization (dashed), for different values of the tunneling parameter t. In each case $t_{so} = 0.4t$. Larger tunnel coupling results in larger hybridization between ABSs, in turn lowering the MP at a specific magnetic field. **(d)** Extraction of E_{det} for various values of detuning μ_R. In each case the slope at low fields corresponds to $2E_z$ (dashed grey line). The larger the detuning of μ_R, the longer this holds. The dashed black line shows the energy of the ABS E_{ABS}. At large detuning E_{det} will increase linearly with $2E_z$, until becoming of comparable E_{ABS} becomes the lowest energy scale.

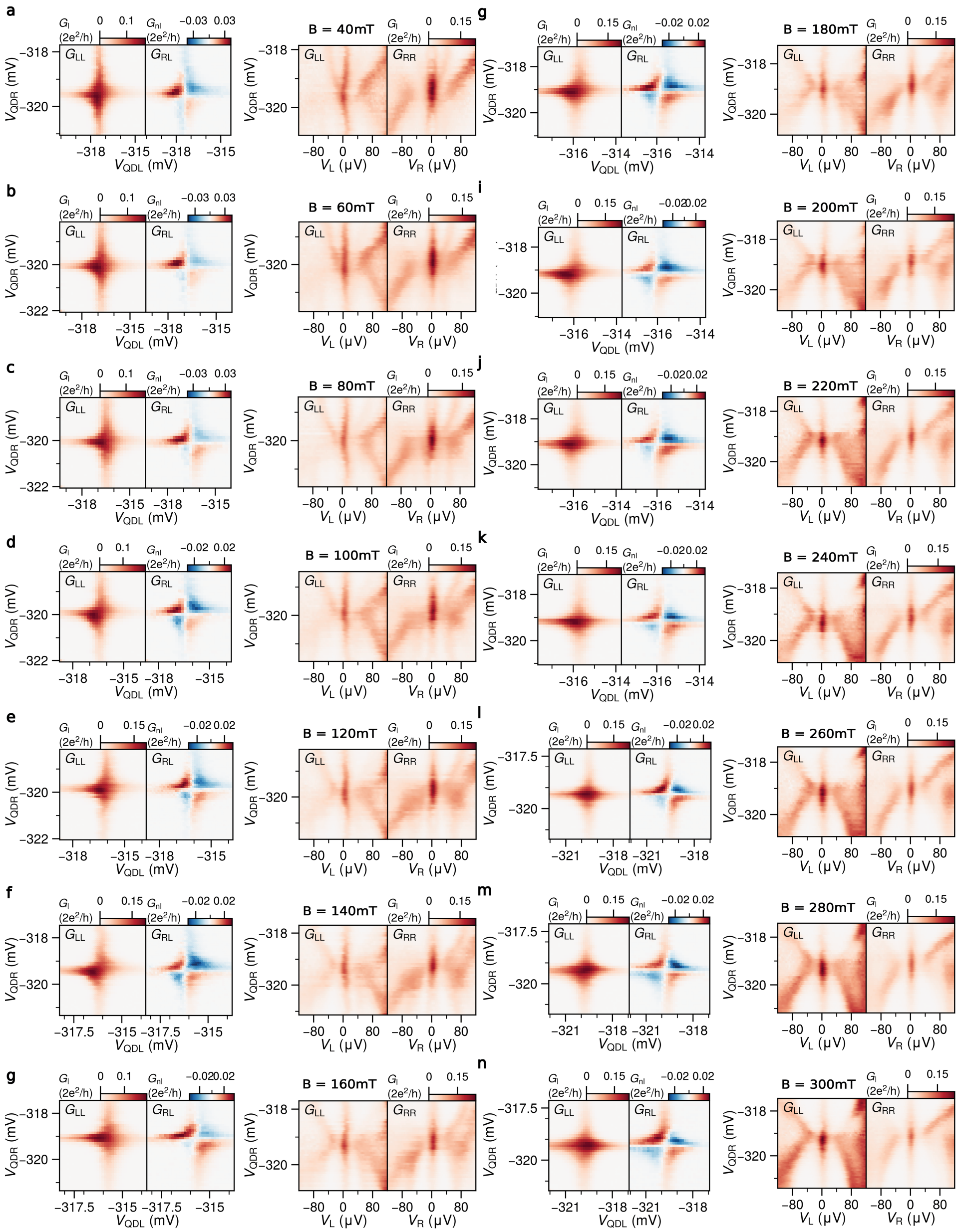

Figure 5.13: **Raw datasets for Figure 4k.** Obtained 'sweet spots' at magnetic fields between 0 mT and 300 mT. **(a-i)** CSDs and tunnelling spectroscopy are measured at each sweet spot, where V_{QDR} is detuned. From these measurements E_{det} and E_{gap} are extracted, as described in the main text and in section 5.7.

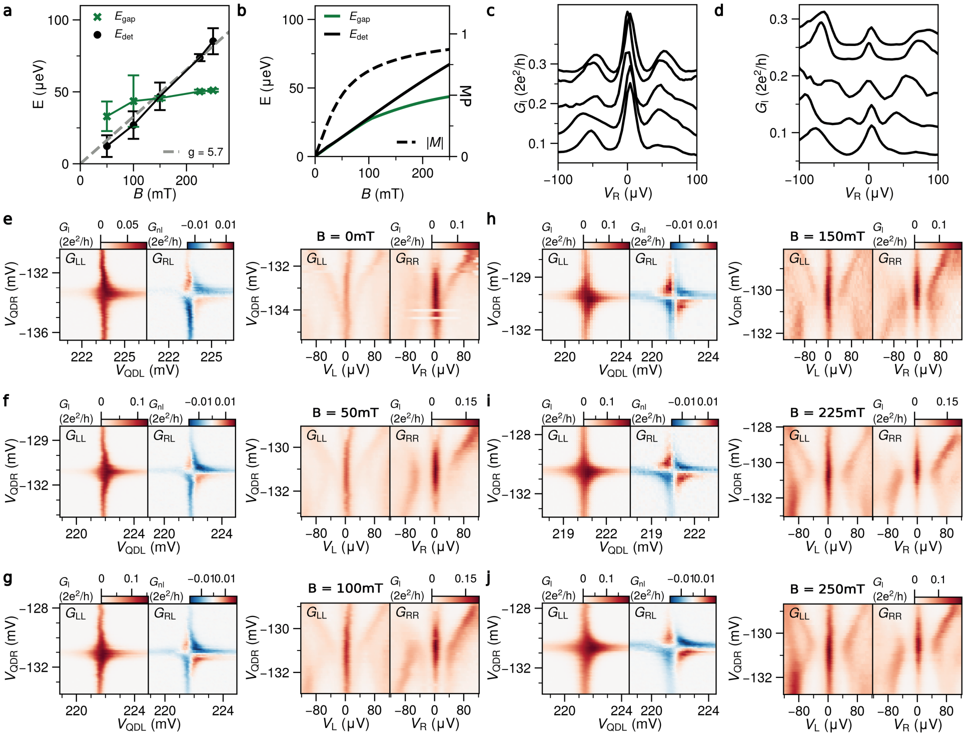

Figure 5.14: **Extended datasets supporting Figure 4k.** Reproduction of the main results from figure 5.4, using the orbitals shown in figure 5.3. Data was obtained at 6 different field values B between 0 and 250 mT. At each field V_{ABS} is adjusted to tune to the sweet spot. **a** Extraction of E_{det} and E_{gap}, similar to the analysis presented in figure 5.4k. From a linear for of E_{det} a g-factor of 5.7 is estimated. **(b)** Numerically obtained E_{det} and E_{gap}, using parameters tuned to compare to (a). At 250mT, an estimate of $M \approx 0.9$ is obtained. Extrapolation for comparison to figure 5.4l yields $M \approx 0.92$ at 300mT. **(c)** and **(d)** Waterfall plots highlighting the line-traces used to extract the data in (a). **(e-j)** Raw datasets of CSDs and tunnelling spectroscopy measurements, from which (a-d) is extracted. Datasets at 150 mT and 225 mT datasets are repeated from figure 5.3 and figure 5.9 respectively.

6

MAJORANAS AT THE EDGES OF A THREE-SITE KITAEV CHAIN

In Chapter 5, we show that two quantum dots (QDs) coupled via a semiconductor - superconductor hybrid segment can form an artificial two-site Kitaev chain hosting Majorana bound states (MBSs). In longer chains, these zero-energy states should appear localised on the edges of the chain [14], on the outermost QDs. The remaining QDs, comprising the ‘bulk’, are then expected to host an excitation gap that protects the MBSs at the edges from local on-site perturbations. In this chapter we study the connection between the bulk and edges in a minimal system, by extending the method used to make a two-site system in order to realize a three-site Kitaev chain. Through direct tunneling spectroscopy on each site, we show that the appearance of stable zero-bias conductance peaks at the outer QDs is correlated with the presence of an excitation gap in the middle QD. Furthermore, we show that this gap can be controlled by applying a superconducting phase difference between the two hybrid segments and that the MBSs are robust only when the excitation gap is present. We find a close agreement between experiments and the original Kitaev model, confirming key predictions for MBSs in a three-site chain.

> *Two can be as bad as one.*
> *It’s the loneliest number since the number one.*
>
> - Harry Nilsson

The work in this chapter has been published as: *Observation of edge and bulk states in a three-site Kitaev chain*, **Sebastiaan L. D. ten Haaf**, Yining Zhang, Qingzhen Wang, Alberto Bordin, Chun-Xiao Liu, Ivan Kulesh, Vincent P.M. Sietses, Christian G. Prosko, Di Xiao, Candice Thomas, Michael J. Manfra, Michael Wimmer and Srijit Goswami.
Nature **641**, 890–895 (2025) [187].
Personal contribution includes device design, obtaining measurements and writing of the manuscript.

6.1 Introduction

The study of topology in condensed matter has generated interest in engineering quantum phases hosting modes that are robust to external perturbations [18, 188–190]. In particular, realisations of 1-D topological superconductors [16, 17] are expected to host robust edge modes known as Majorana bound states (MBSs), first predicted by the Kitaev chain model [14]. Such states are separated by a bulk region with an excitation gap that prevents local perturbations from affecting the zero-energy modes at the edges, a consequence of the so-called bulk-edge correspondence [191, 192]. Experimentally, much effort has gone towards top-down approaches to engineer such systems by coupling semiconductors to superconductors [81]. However, microscopic disorder in these systems complicates the study of MBSs [20, 23, 193–196]. Alternatively, bottom-up approaches aim to mitigate this, e.g. by constructing a Kitaev chain atom-by-atom [197, 198] or by engineering arrays of quantum dots (QDs) in semiconductor-superconductor hybrids [37, 38]. An implementation of the latter approach with two QDs [33] was recently demonstrated in nanowires [28], leading to the experimental study in Chapter 5. However, in a two-site chain neither QD site can be associated with a bulk. In contrast, a chain with three QDs constitutes a minimal system where one could distinguish distinct edges hosting MBSs (the outer QDs) and a bulk (the middle QD). Recent work demonstrated stable zero-energy modes in such a system [34], but was unable to investigate the density of states of the middle QD.

In this chapter, we study a three-site Kitaev chain in an InSbAs 2DEG and perform a detailed study of the bulk and edge states in the system. Crucially, ohmic contacts attached to each QD allow us to directly probe the density of states at all three sites. By controlling the interdot couplings and the superconducting phase difference, we can tune the system such that robust zero-bias conductance peaks (ZBPs) arise on the outer QDs. We demonstrate that these correlated ZBPs at the edges are accompanied by an excitation gap in the middle QD. This gap can be controlled by tuning the phase difference between the superconductors, allowing us to establish a clear correlation between the presence of isolated zero-energy edge modes and their robustness against on-site perturbations. In particular, access to every QD allows us to track how the weight of the Majorana wavefunction evolves across each site as the device parameters are varied. Finally, we construct a phase diagram of a finite Kitaev chain by identifying regions in parameter space where ZBPs are observed. Through continuous control over the interdot couplings and the QD electrochemical potential energies, we show that this region grows when extending from a two-site chain to a three-site chain. These findings are in close agreement with the original Kitaev model, and provide important insights for more advanced experiments with MBSs.

6.2 The Kitaev model for a three-site QD chain

Implementing a Kitaev chain on a QD array requires control over the electrochemical potential energy of each site, and the amplitudes of couplings between neighbouring sites. This can be engineered by coupling spin-polarised QDs via Andreev bound states in semiconductor-superconductor hybrids [28]. Here, a hopping interaction (t) occurs through elastic co-tunneling (ECT). Crossed Andreev reflection (CAR) provides a pairing interaction (Δ) via the creation or breaking of Cooper pairs in the superconductor [25, 27, 60, 199].

Intrinsic spin-orbit coupling allows for CAR between neighbouring sites with the same spin, or ECT between neighbours with opposite spin, otherwise forbidden due to spin-conservation [26]. When the Zeeman energy in each QD is large ($E_z \gg t, \Delta$), a single spin-species dominates transport at charge degeneracy points, thus emulating the Kitaev model [35, 73]. To distinguish different charge configurations for the three QDs, the spin configuration is used as a label. The energy level diagram for a chain with three QDs is shown in figure 6.1a. Electrochemical potential energies are denoted μ_i, where $i \in \{\mathrm{L,M,R}\}$ refers to the left, middle or right QD respectively. The effective couplings between the left and middle QD, t_1 and Δ_1, and between the middle and right QD, t_2 and Δ_2, are indicated. Uncoupled MBSs arise on the outer QDs at a so-called 'sweet spot' in parameter space, when all three QDs are aligned with the Fermi level of the superconductor ($\mu_\mathrm{i} = 0$) and the interdot couplings are equal in amplitude pairwise ($|t_1| = |\Delta_1|$, $|t_2| = |\Delta_2|$). Notably, the coupling amplitudes are not necessarily purely real in a system with more than two QDs [34, 38, 200]. A gauge degree of freedom allows one to take t_1, t_2 and Δ_1 to be real and assign a complex phase only to Δ_2, denoted ϕ_Δ. The Hamiltonian of the system can then be written as:

$$H = \mu_\mathrm{L} c_\mathrm{L}^\dagger c_\mathrm{L} + \mu_\mathrm{M} c_\mathrm{M}^\dagger c_\mathrm{M} + \mu_\mathrm{R} c_\mathrm{R}^\dagger c_\mathrm{R} + (t_1 c_\mathrm{M}^\dagger c_\mathrm{L} + t_2 c_\mathrm{R}^\dagger c_\mathrm{M} + \Delta_1 c_\mathrm{M} c_\mathrm{L} + \Delta_2 e^{i\phi_\Delta} c_\mathrm{R} c_\mathrm{M} + h.c.) \tag{6.1}$$

We compare our experimental results to this three-site Kitaev model. Numerical simulations of the conductance are performed using a scattering matrix approach with experimentally extracted parameters. A more detailed description is included in section 6.6.

6.3 Device and experimental set-up

A scanning electron micrograph of the measured device is shown in figure 6.1b. Large gates (red) define a quasi-1D channel across two thin aluminium strips that are connected by a continuous loop. An external magnetic field B_z applied perpendicular to the loop controls the superconducting phase difference ϕ_SC between the two strips, with a flux period of 28 µT (figure 6.5). The energy of the ABSs in the left and right hybrid regions can be tuned by voltages $V_\mathrm{ABS}^{(1)}$ and $V_\mathrm{ABS}^{(2)}$ respectively. Narrow gates define three QDs in the channel. Their electrochemical potentials are controlled by voltages V_QDL, V_QDM and V_QDR respectively. Voltages applied to a left, middle and right lead (V_L, V_M and V_R) can be varied and the currents in each lead (I_L, I_M and I_R) can be measured independently. Lock-in amplifiers allow for direct measurements of the local conductance at each probe ($G_{ii} = \frac{dI_i}{dV_i}$, $i \in \{\mathrm{L,M,R}\}$). To capture features appearing simultaneously on multiple sites, the correlated conductance $G_\mathrm{corr}^{i,j} = \sqrt{G_{ii} \cdot G_{jj}}$ is extracted when relevant. Results in the main text are obtained using a single orbital in each QD, characterised in figure 6.6 and figure 6.7. All measurements are performed at $B_x = 200$ mT, applied perpendicular to the spin-orbit field in these systems [155].

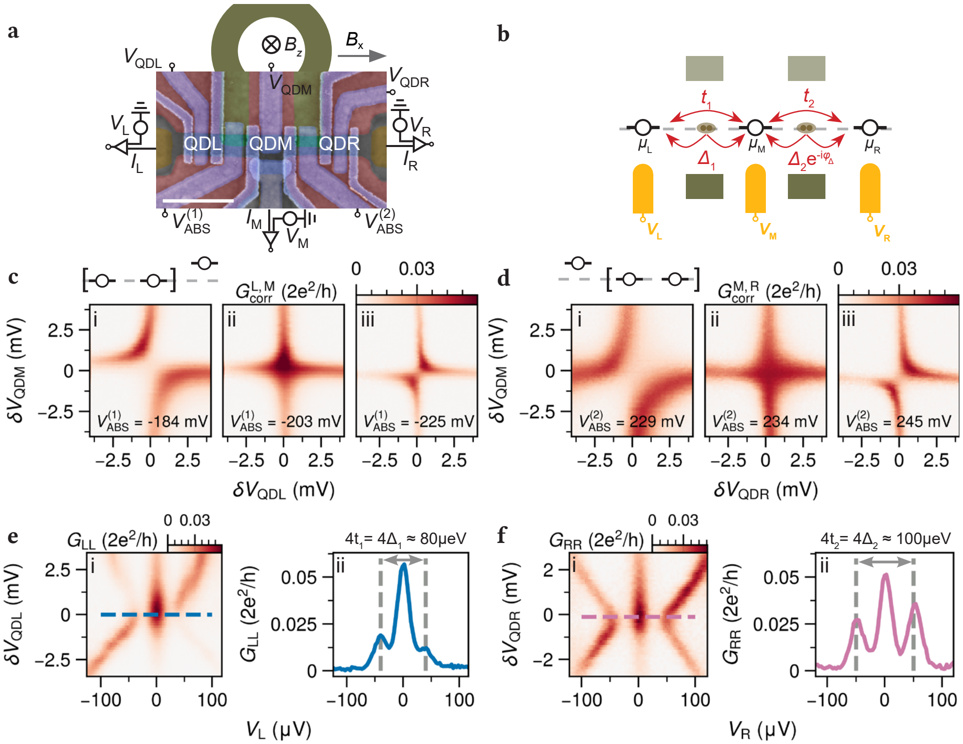

Figure 6.1: **Device, model and characterisation of two-site pairs. (a)** Energy level diagram of the three-site Kitaev chain model, indicating the different interdot couplings in the system. **(b)** Scanning electron micrograph of the device. The scale bar is 500 nm. Positions of gate-defined QDs are indicated. Two superconducting strips are connected in a loop with a diameter of 10 μm and kept grounded (not drawn to scale). The DC circuit diagram shows a four-terminal measurement set-up (a full circuit diagram, including resonators for reflectometry measurements, is shown in figure 6.5). **(c)** Measured correlated conductance $G_{\text{corr}}^{\text{L,M}} = \sqrt{G_{\text{LL}} \cdot G_{\text{MM}}}$ as a function of V_{QDL} and V_{QDM}, upon varying $V_{\text{ABS}}^{(1)}$. The notation δV_{QDi} refers to the voltage set with respect to the nearest charge degeneracy point. **(d)** Measured correlated conductance $G_{\text{corr}}^{\text{M,R}} = \sqrt{G_{\text{MM}} \cdot G_{\text{RR}}}$ as a function of V_{QDR} and V_{QDM}, upon varying $V_{\text{ABS}}^{(2)}$. The disappearance of the avoided crossing in panels (c.ii) and (d.ii) signifies satisfying the two-site sweet spot conditions. **(e)** Finite bias spectroscopy measurement of G_{LL} at the left QD pair sweet spot, while varying V_{QDL}. **(f)** Finite bias spectroscopy of G_{RR} at the right QD pair sweet spot, while varying V_{QDR}. Line-traces taken at the minima of the higher energy excitations allow for estimating the experimental coupling amplitudes at the sweet spots (panels e,f.ii). Results presented use the ↓↑↑ spin-configuration. Further characterisation of the two-site pairs is presented in figure 6.8.

6.4 RESULTS

6.4.1 TUNING THE TWO-SITE PAIRS

Tuning a three-site Kitaev chain amounts to pairwise tuning of the two-site sweet spots ($t_i = \Delta_i$) [37]. These conditions can be inferred from zero-bias charge stability diagrams (CSDs) for the two pairs of QD resonances [33], using the methods employed for two-site Kitaev chains (see Chapter 5) [28, 80, 178]. First, we obtain CSDs for the left and middle QDs, while keeping the right QD in Coulomb blockade (figure 6.1c). The measurement is repeated as $V_{\mathrm{ABS}}^{(1)}$ is varied, to locate when the avoided crossing in the CSD changes direction. A diagonal avoided crossing indicates $\Delta_1 > t_1$ (figure 6.1c.i), whereas an antidiagonal avoided crossing results from $t_1 > \Delta_1$ (figure 6.1c.iii). At an intermediate value of $V_{\mathrm{ABS}}^{(1)}$, the desired $t_1 = \Delta_1$ condition is satisfied, where the avoided crossing disappears (panel c.ii). This procedure is repeated for the middle and right QDs, now varying $V_{\mathrm{ABS}}^{(2)}$. This is seen in figure 6.1d, where $t_2 = \Delta_2$ is satisfied in panel d.ii.

It has been shown that robust, correlated ZBPs arise at these two-site sweet spots [28, 80, 178]. These are manifestations of localised MBSs, in the two-site case referred to as “Poor Man’s Majoranas" as their stability is limited to single QD perturbations [33]. We demonstrate this stability of the ZBPs for each pair of QDs. In figure 6.1e we measure G_{LL} as QDL is detuned, for the configuration in figure 6.1c.ii. Similarly, G_{RR} is measured for the configuration in figure 6.1d.ii upon varying V_{QDR} (figure 6.1f). In both cases we find robust zero energy states. At the charge degeneracy point, the higher-energy excitations provide an estimate [33] for $t_1 = \Delta_1 \approx 20\,\mu\mathrm{eV}$ (figure 6.1e.ii) and $t_2 = \Delta_2 \approx 25\,\mu\mathrm{eV}$ (figure 6.1f.ii). These measurements are in good agreement with the theoretical spectrum for well-polarised QDs [35, 79, 121], signifying that the ingredients for a full three-site Kitaev chain are present.

6.4.2 PHASE CONTROL AND PROBING THE BULK EXCITATION GAP

With t and Δ balanced for each QD pair, the full three-site chain can be investigated. Now the phase difference between the superconductors becomes a relevant parameter since it can affect the relative phase between the interdot couplings [34, 37, 38]. To investigate this, we set $V_{\mathrm{ABS}}^{(1)}$ and $V_{\mathrm{ABS}}^{(2)}$ to the sweet spot values obtained in figure 6.1 and set the QDs to their charge degeneracy points. The conductance spectrum of each QD is then measured as a function of B_z (figure 6.2a). ZBPs are continuously observed on the outer QDs (G_{LL} and G_{RR}), while the middle QD (G_{MM}) hosts higher energy excitations that move down to zero energy periodically. This period in B_z is equal to the period of ϕ_{SC} (28 µT) measured for the bare superconducting junction. We compare this behaviour to numerically calculated conductance spectra (figure 6.2b) of the three-site Kitaev chain as a function of ϕ_Δ, using the experimental coupling amplitudes estimated in figure 6.1. A clear correspondence to the experimental result is obtained. When the phase is 0 (modulo 2π), ZBPs are present in G_{LL} and G_{RR}, while an excitation gap is present in G_{MM}. As the phase is tuned towards π, finite-energy excitations lower in energy until the excitation gap is closed.

The observed behaviour can be understood when considering the Kitaev chain model in the Majorana basis (see section 6.6), visualised in figure 6.2c. Each QD site can be represented by two Majoranas. For $\phi_\Delta = 0$, an uncoupled Majorana arises only on the left and right sites, while the middle site is gapped. Experimental line-traces (figure 6.2d) at the corresponding magnetic field value are in agreement with this interpretation. A ZBP is present in G_{LL} and G_{RR} (panels i and iii), whereas G_{MM} only shows excitations at higher bias (panel ii). This is a direct indication of the localisation of the MBS wavefunctions on the outer QDs. In stark contrast, at a magnetic field that corresponds to $\phi_\Delta = \pi$, ZBPs are found on all three sites (figure 6.2e). Here, the coupling between neighbouring Majoranas is rearranged (see figure 6.2c), resulting in four uncoupled Majorana modes: one localised on

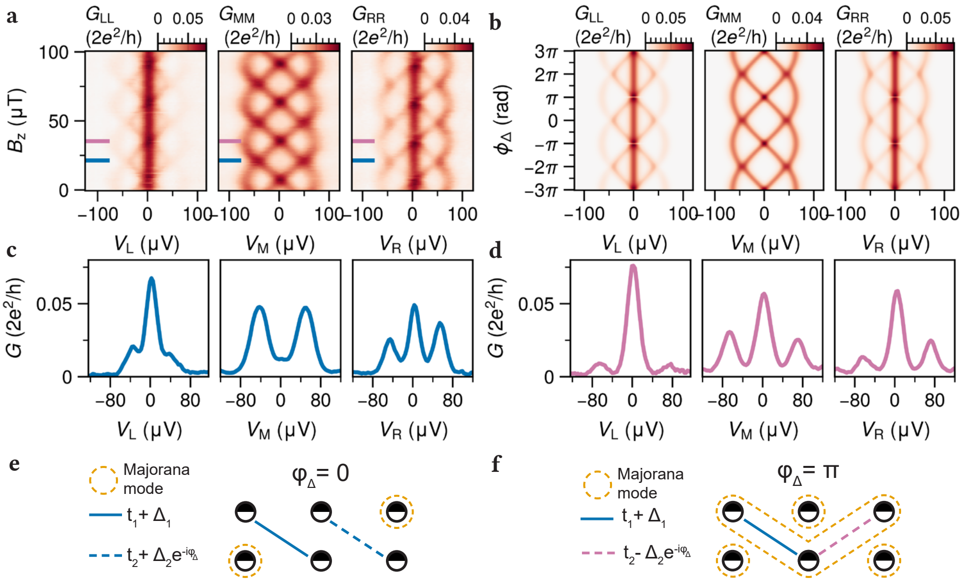

Figure 6.2: **Phase control at the three-site sweet spot.** **(a)** Measured conductances G_{LL}, G_{MM} and G_{RR} at the sweet spot configuration obtained in Fig 1, as a function of magnetic field B_z applied perpendicular to the superconducting loop. When either of the outer QDs is set off-resonance, B_z no longer affects the conductance spectra (shown in figure 6.8), indicating the observed behaviour here is an effect on the full three-site chain. **(b)** Evolution of numerically calculated conductances in a three-site Kitaev chain upon varying ϕ_Δ. Numerical parameters used are $\mu_L = \mu_M = \mu_R = 0$, $t_1 = \Delta_1 = 20\,\mu\text{eV}$ and $t_2 = \Delta_2 = 25\,\mu\text{eV}$ (matching estimations in figure 6.1e,f). **(c)** Visual representation of the three-site Kitaev chain Hamiltonian at $\phi_\Delta = 0$ and $\phi_\Delta = \pi$, in the Majorana basis. Connecting lines indicate non-zero coupling terms between Majoranas for each case. Dashed circles highlight the distribution of uncoupled Majorana modes (further detailed in section 6.6). **(d)** Line-traces taken from (a) at $B_z = 21.4\,\mu\text{T}$, corresponding to $\phi_\Delta = 0$. The finite conductance at zero bias in panel d.ii can be largely attributed to thermal broadening, investigated in figure 6.9. **(e)** Line-traces taken at $B_z = 35.4\,\mu\text{T}$, corresponding to $\phi_\Delta = \pi$.

each site, and an additional delocalized mode extending across all three sites. Consequently, every site has a finite density of states at zero bias, leading to the observed conductances.

6.4.3 Shifting the Majorana wavefunctions

The presence or absence of the excitation gap in the middle QD has direct consequences for the robustness of the ZBPs on the outer QDs. In an ideal system, the energy of each isolated MBS cannot be lifted due to particle-hole symmetry. Only an overlap between the two MBSs can achieve this, which is prevented by an excitation gap. As shown above, the excitation gap is affected by ϕ_Δ. The robustness of the ZBPs is therefore also expected to be phase-dependent. We compare the conductance spectra obtained at B_z values corresponding to $\phi_\Delta = 0$ and $\phi_\Delta = \pi$, where the excitation gap is either present or closed.

We first consider the spectra at $\phi_\Delta = 0$, upon detuning QDL (figure 6.3a). The ZBP in G_{LL} remains at zero bias, while a ZBP gradually appears in G_{MM}. The conductances at zero bias are expected to be proportional to the density of the Majorana wavefunction at each site (see figure 6.12). Figure 6.3b shows extracted line-traces at zero bias. As QDL is detuned, G_{LL} gradually reduces, while G_{MM} simultaneously increases. This happens because the weight of the Majorana wavefunction shifts from the left to the middle QD (illustrated in figure 6.3c) [201]. Finally, we see that the spectrum at QDR is hardly affected, a consequence of the isolation of the MBS on this site.

The spectra at $\phi_\Delta = \pi$, where the gap in QDM is closed, have a markedly different behaviour (figure 6.3d). The ZBP in G_{LL} now splits immediately in energy as QDL is detuned. This is indeed expected, since MBSs in the system now directly overlap, and are thus no longer robust to detuning. Line-traces at zero bias (figure 6.3e) show two important features. Firstly, G_{LL} now drops faster compared to figure 6.3b, due to the lack of protection. Secondly, the ZBPs in both G_{MM} and G_{RR} are now unaffected by the detuning of the left QD. This can again be understood in terms of the MBS wavefunctions (illustrated in figure 6.3f), whereby detuning the left QD now fuses the localised MBS on QDL with the delocalised MBS extending across the chain [200, 202, 203]. These observations, and conductance spectra obtained for additional combinations of QD detunings, again show a striking agreement with numerical simulations (figure 6.11 and figure 6.13).

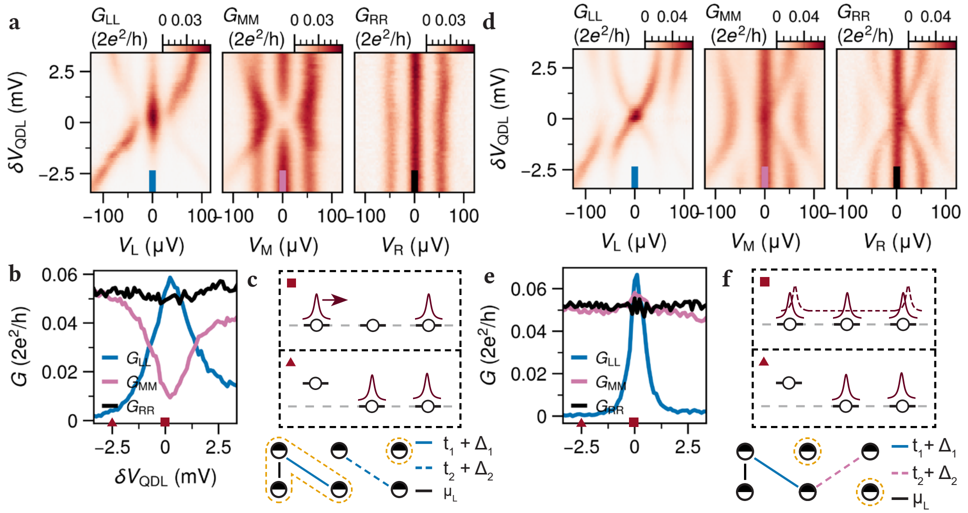

Figure 6.3: **Bulk protection of the MBS wavefunctions.** **(a)** Measured conductances with B_z = 21.4 μT (corresponding to ϕ_Δ= 0 in figure 6.2) when sweeping V_{QDL} around the charge degeneracy point. Measurements are performed with the same gate configuration as in figure 6.2. The ZBP in G_{LL} gradually decreases in height, whereas a ZBP in G_{MM} gradually appears. **(b)** Zero-bias line-traces of conductance along indicated paths in (a). **(c)** Visual representation of the measurements in (b), showing the MBS wavefunctions when V_{QDL} is on resonance (square symbol) or off-resonance (triangle symbol). Bottom schematic shows the effect of introducing the coupling term μ_{L}, in the picture introduced in figure 6.2. **(d)** Repetition of the measurement in (a) with B_z = 35.4 μT (corresponding to $\phi_\Delta = \pi$). The ZBP in G_{LL} now splits from zero energy as V_{QDL} is detuned. The ZBPs in G_{MM} and G_{RR} remain, as the system effectively becomes a two-site chain as V_{QDL} is detuned. **(e)** Zero-bias line-traces of conductance along indicated paths in (d). **(f)** Visual representation of the measurements in (e), detailed in text. The smooth control over ϕ_Δ through B_z allows for comparing these conductance spectra at any intermediate phase, shown in figure 6.10.

6.4.4 ZBPs outside the sweet spot

In previous sections the system was characterised at fine-tuned sweet spots where ZBPs appear on the outer QDs. It is expected that ZBPs should also be present away from these sweet spots. This follows from a key property of the Kitaev model, whereby the region in parameter space that hosts MBSs grows as the number of sites N is increased. For finite chains, MBSs are fully localised at the edges only at the $t_{\mathrm{i}} = \Delta_{\mathrm{i}}$ sweet spot [29]. However, ZBPs arising from delocalized MBSs are expected away from this point. To study this, it is instructive to extract zero-energy solutions of the Kitaev chain as a function of μ and t, for fixed Δ. An exact analytical expression for the zero-energy solutions exists for any N [29], shown in figure 6.4a. For $N = 2$, the solutions lie on a single hyperbola, with a vertex at $t = \Delta$, $\mu = 0$ (i.e. the two-site sweet spot). For each odd N, $\mu = 0$ is always a solution [204] (see $N = 3$). As N increases, the number of solutions increases and gradually fills the region where $|\mu| < 2t$. As $N \to \infty$, this region is filled with states exponentially close to zero energy, ultimately creating a topological phase within which the MBSs are always localised at the edges. The zero-energy solutions can be studied by measuring zero-bias conductances on each QD while varying both interdot couplings and the QD electrochemical potential energies. Figure 6.4b and figure 6.4c show numerical simulations, for $N = 2$ and $N = 3$ respectively.

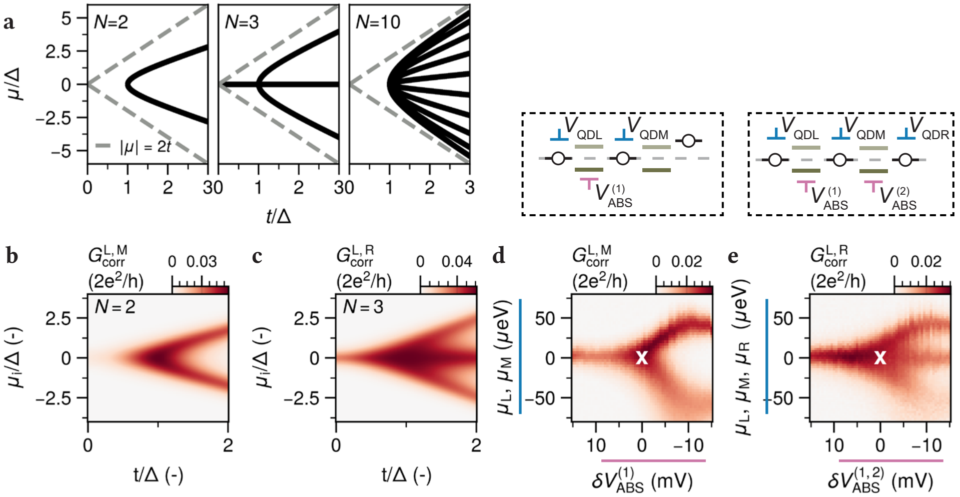

Figure 6.4: **The finite Kitaev chain's phase space. (a)** Analytical zero-energy solutions to the N-site Kitaev chain with fixed Δ, for different N (reproduced from [29]). The grey dashed line indicates the boundary of the topological phase formed at $N \to \infty$. Numerically calculated conductance is shown for **(b)** N = 2 and **(c)** N = 3. Here, $\Delta = 20\,\mu\mathrm{eV}$. **(d)** Measured correlated conductance when sweeping $V_{\mathrm{ABS}}^{(1)}$ against V_{QDL} and V_{QDM} (converted to μ_{L} and μ_{M} using QD leverarms). **(e)** Measured correlated conductance when sweeping both $V_{\mathrm{ABS}}^{(1)}$ and $V_{\mathrm{ABS}}^{(2)}$ against V_{QDL}, V_{QDM} and V_{QDR}. White 'x' marks the point in parameter space referred to as the sweet spot for the two and three site chain. In (d) and (e), x-axis are flipped to match numerical simulations. The ↑↑↑ spin-configuration is used. Measurements are reproduced in figure 6.15.

Experimentally this parameter space is only indirectly accessible, as t_i and Δ_i are not controlled independently. However, starting with the hybrid gates at their sweet spot value (denoted $\delta V_{\mathrm{ABS}}^{(\mathrm{i})} = 0$) and sweeping both simultaneously, the system can be smoothly tuned between $t_\mathrm{i} < \Delta_\mathrm{i}$ and $t_\mathrm{i} > \Delta_\mathrm{i}$ regimes (full procedure in figure 6.14). Figure 6.4d shows this for the left and middle QD pair. Here, the conductance features meeting at $\delta V_{\mathrm{ABS}}^{((\mathrm{i}))} = 0$ agree qualitatively with the behaviour expected from figure 6.4b. Instead of extending linearly as $t_1 > \Delta_1$, the feature saturates in μ_i, since t_1 does not increase independently of Δ_1 in these experiments. The finite conductance 'tail' at $\mu_\mathrm{i} = 0$ here is a consequence of both t and Δ decreasing in amplitude (see figure 6.14), which is not captured by the theory model.

Finally, the measurement is performed for the full three-site chain, sweeping simultaneously both hybrid gates against detuning all three QDs (figure 6.4e). The appearance of the additional conductance feature along $\mu_\mathrm{i} = 0$ marks the first step of the growth into a topological phase in this discrete system and agrees well with the Kitaev chain model in a large parameter space. These measurements allow us to qualitatively visualise the increase in stability of the MBSs as the chain is extended, which was experimentally studied in Ref. [34]. We find that conductance decays more slowly for the three-site chain compared to the two-site chain as one moves away from the sweet spot (marked by white 'x') in any direction.

6.5 SUMMARY

In summary, we have realised a three-site Kitaev chain by coupling three QDs via two semiconductor-superconductor regions. We find that the phase difference between the superconductors controls the relative phase between the interdot couplings, and thereby the energy spectrum of the system. This finding is particularly relevant for the study of zero energy modes in longer chains [82, 205], where control over these phases becomes crucial [37, 200]. By appropriately tuning the phase, we show that the appearance of ZBPs on the outer QDs is accompanied by an excitation gap in the middle QD, evidence of the zero-energy modes being localised at the edges. We further demonstrate that detuning of the QDs in the chain allows one to smoothly transfer the weight of the Majorana wavefunction between different sites. This kind of spatial manipulation of MBSs is a crucial requirement in gate-based braiding proposals for realising a Majorana qubit [174, 180]. Overall, these experiments agree well with the predictions of the Kitaev model in a wide parameter space and are an important step towards studies that require a reliable way to produce robust, localised Majorana bound states [177, 181, 206].

DATA AVAILABILITY

All raw data obtained in relation to this chapter and the scripts to produce the figures are available on Zenodo [207].

6.6 Methods

Fabrication and yield

The measured device was fabricated using the techniques described in detail in [129] and [128]. Aluminium loop structures are defined in an InSbAs-Al chip by wet etching, followed by the deposition of three ohmic Ti/Pd contacts. After deposition of 20 nm AlOx via 40 °C atomic layer deposition (ALD), three large Ti/Pd depletion gates are evaporated: one large top depletion gate and two bottom depletion gates each extending halfway. The bottom consists of two gates in order to independently form the left and right halves of the channel, separated by a thin channel where the middle lead is placed. This simplifies placing an additional gate in front of the middle ohmic contact, in order to have a well defined tunneling barrier for the middle probe. Additionally, it simplifies finding a suitable active region where the 2DEG is depleted below the gates, while a narrow conductance channel remains in between. The channel width is designed to be 200 nm. Following a second ALD layer (20 nm AlOx), a first layer of six Ti/Pd finger gates is evaporated. These are used for controlling the electrochemical potential energies of the QDs and hybrid regions and for defining the tunneling barrier for the middle contact. A third ALD layer (20 nm AlOx) is deposited, followed by evaporation of the remaining six Ti/Pd finger gates that define the three QDs. For RF-measurements, superconducting LC-resonator circuits are fabricated on a separate chip with a silicon substrate, by etching NbTiN. To apply DC voltages, bias tees are created by depositing 20 nm Cr structures with resistances of $\approx 5\,\mathrm{k\Omega}$.

For the investigation presented in this chapter, in total sixteen devices were fabricated, with small variations in device dimensions. Of these, twelve had no visible defects under optical/SEM inspection of the finished devices. Some challenges were faced with simultaneously connecting all 15 gates to the printed circuit board and connecting all 3 ohmic contacts via the resonator chip. In total six devices were bonded and cooled down, of which in five instances fridge wiring and bonding issues caused gate or ohmic connections to be absent once reaching milli-Kelvin temperatures. Once these issues were resolved, the final device was used for obtaining the measurements demonstrated in this manuscript. This device was cooled down twice over the course of five months, in which we were able to reproduce our findings when re-starting from a ‘reset’ device. The main text highlights results within a single cooldown, data from the other sets of experiments is included in this supplementary.

DC transport measurements

Measurements are performed in a dilution refrigerator with a base temperature of 20 mK. Transport measurements presented in the main text are performed in AC and DC using a four-terminal set-up (three ohmic contacts plus two aluminium strips connected in a loop). The aluminium strips induce a gap of $\approx 220\,\mu\mathrm{V}$ (figure 6.5) and are kept electrically grounded. Each ohmic lead is connected to a current meter and biased through a digital-to-analogue converter and both DC and AC voltages can be applied. Offsets of the applied voltage-bias on each lead are corrected via independently measuring the Coulomb peaks in the QDs and looking at the change in sign of the current. The voltage outputs of the current meters are recorded with three digital multimeters and three lock-in amplifiers. When applying a DC voltage to one lead (e.g., V_L), the other leads (i.e., V_M and V_R) are kept grounded. AC excitations are applied with amplitudes around 5 μV RMS and a frequency of 23 Hz. In this way, a full conductance matrix $G_{ij} = \frac{dI_i}{dV_j}$ is obtained by measuring the response of I_L, I_M and I_R, to V_L, V_M and V_R. Three separate measurements are required, as only a single lead is biased at a time. Small offsets in measured conductances arise using the lock-in amplifiers, due to capacitances to ground within the electronics. These offsets are calibrated using Coulomb blockaded measurements and corrected. It should be noted that voltage-divider effects arise when applying biases in a four-terminal set-up. For three-terminal set-ups, the measured conductances and applied biases are generally corrected [143]. For a four-terminal set-up, however, such a calculation gets cumbersome. Here, we focus on low tunneling regimes ($\mathrm{G} \ll 2\mathrm{e}^2/\mathrm{h}$) where the device resistance is large compared to the resistances of the fridge lines and the current meters, such that the multi-terminal effect is small. Nevertheless, this should be kept in mind when e.g. interpreting the non-local conductances in figure 6.13.

Magnetic fields are applied using a 3D vector magnet. The field perpendicular to the superconducting loop (B_z) is generated using a high-resolution current source, giving a B_z resolution below 0.1 μT (providing sufficient resolution for the flux period of 28 μT). A small (but significant) hysteresis on the order of 5 μT is observed when sweeping B_z in opposite directions. This is counteracted by setting B_z first to −100 μT and then sweeping this field back in the positive direction, such that consecutive experiments where B_z is varied are consistent. To spin-polarise the QDs, a magnetic field of 200 mT is applied parallel to the channel (B_x). Due to an imperfection in the alignment, this introduces a small B_z component as well, on the order of 80 flux quanta. It was not possible to accurately correct this offset for this work, and so we do not determine the B_x value that corresponds to precisely 0 flux through the loop.

RF-REFLECTOMETRY MEASUREMENTS

The experiments require the tuning of 15 gate voltages in order to create the three-site chain, which results in a large parameter space of gate voltages. To speed up the tuning process we employ radio-frequency (RF) lead reflectometry [145] in addition to the DC conductance measurements. Each Ohmic contact is connected to an inductor, designed with varying inductances $L_\mathrm{L,M,R} = 0.2, 0.5, 1.5$ μH. Together with a parasitic capacitance to ground via bond-wires, this results in resonators with frequencies of $f_\mathrm{L,M,R} = 723, 505, 248$ MHz. A complete circuit diagram including the fridge wiring and filters is provided in [139]. Using a directional coupler, we obtain the reflected signal of each lead. We denote with S_{21}^L, S_{21}^M and S_{21}^R the normalised reflected signals of the left, middle and right lead respectively, which correspond roughly linearly to conductance. All three signals can be measured simultaneously through multiplexing [208], using the circuit shown in figure 6.5. In combination with saw-tooth pulses on the QD plunger gates, generated by arbitrary waveform generators, this allows for scanning the parameter space many times faster than through DC measurements. For clarity, throughout this chapter the data obtained with RF reflectometry is displayed in a different colormap from the DC conductance data.

DEVICE TUNE-UP

Here, we detail how the device shown in figure 6.1 was tuned to reach the point of obtaining the measurements presented in this chapter. To start, a conductance channel has to be isolated, by tuning the three large depletion gates. A regime is obtained where the 2DEG is fully depleted below these gates, but a finite current remains in the channel. Next, we perform tunnel spectroscopy of the hybrid regions to verify the presence of gate-tunable sub-gap states (figure 6.5). Then, the remaining gates are activated to form the three QDs. We find a regime in which the QDs are stable and contain orbitals with a large level spacing, such that sufficient Zeeman energies can be induced through the external magnetic field without mixing states in neighbouring orbitals. The InSbAs hetero-structure investigated in this manuscript does not have a capping layer, such that the confinement layer is very close to the surface [129]. Thus the QDs can couple easily to disorder in the dielectric, resulting in regimes in parameter space that are unstable. This constitutes a challenge in tuning up all 3 QDs into stable regimes, further discussed in figure 6.7.

Once a stable regime is found, we tune the interdot couplings by studying charge stability diagrams of the QDs and the ABSs in the hybrid regions, following the protocols in [79, 80]. An important requirement is that the interdot coupling amplitudes should exceed the line-width of the conductance measurements, in order to clearly resolve the full density of states. However, if the middle QD is too strongly coupled to both hybrids, its chemical potential energy becomes dependent on the superconducting phase [209]. In this case, the interdot coupling amplitudes (t, Δ) themselves become phase dependent and additional modulations in the conductance spectra are observed (see figure 6.9e). We limited the coupling between the ABSs and the middle QD in order to stay away from this regime (as verified by figure 6.8d,h), in order to compare the conductance spectra as a function of B_z directly to the Kitaev chain model in figure 6.2. For the conductance spectra measurements shown in figure 6.2 and figure 6.3, it is crucial that the QDs remain on resonance throughout the measurements. The center of each resonance was determined by measuring independently the Coulomb resonances for each QD in RF-reflectometry and fitting a Lorentzian line-shape. This was done directly before and after each measurement, to verify that no gate jump or drift occurred. Additionally, CSDs for the left and right QD pairs were obtained before and after each set of measurements, to ensure that the interdot couplings had not changed. In case any gate-jumps occurred, the measurements were repeated.

KITAEV MODEL AND NUMERICAL CALCULATIONS OF CONDUCTANCE

The Hamiltonian of a three-site Kitaev chain is given by:

$$H = \mu_\mathrm{L} n_\mathrm{L} + \mu_\mathrm{M} n_\mathrm{M} + \mu_\mathrm{R} n_\mathrm{R} + (t_1 c_\mathrm{M}^\dagger c_\mathrm{L} + t_2 c_\mathrm{R}^\dagger c_\mathrm{M} + \Delta_1 c_\mathrm{M} c_\mathrm{L} + \Delta_2 e^{i\phi_\Delta} c_\mathrm{R} c_\mathrm{M} + h.c.), \qquad (6.2)$$

where c_i is the annihilation operator for the fermion on site $i \in [\mathrm{L}, \mathrm{M}, \mathrm{R}]$, $n_i = c_i^\dagger c_i$ is the number operator, μ_i is the onsite energy, t_i and Δ_i are the normal and superconducting tunneling amplitudes between neighbouring sites, and ϕ_Δ is the phase difference between the two superconducting leads which can be controlled by the magnetic flux threading through the loop. The corresponding Bogoliubov-de-Gennes Hamiltonian is:

$$h_{K3} = \begin{pmatrix} \mu_{\mathrm{L}} & t_1 & 0 & 0 & \Delta_1 & 0 \\ t_1 & \mu_{\mathrm{M}} & t_2 & -\Delta_1 & 0 & \Delta_2 e^{-i\phi_\Delta} \\ 0 & t_2 & \mu_{\mathrm{R}} & 0 & -\Delta_2 e^{-i\phi_\Delta} & 0 \\ 0 & -\Delta_1 & 0 & -\mu_{\mathrm{L}} & -t_1 & 0 \\ \Delta_1 & 0 & -\Delta_2 e^{i\phi_\Delta} & -t_1 & -\mu_{\mathrm{M}} & -t_2 \\ 0 & \Delta_2 e^{i\phi_\Delta} & 0 & 0 & -t_2 & -\mu_{\mathrm{R}} \end{pmatrix} \tag{6.3}$$

under the basis of $(c_{\mathrm{L}}^\dagger, c_{\mathrm{M}}^\dagger, c_{\mathrm{R}}^\dagger, c_{\mathrm{L}}, c_{\mathrm{M}}, c_{\mathrm{R}})$. To calculate the differential conductance through the system, we use the scattering matrix method, where the S matrix can be obtained from the Weidenmuller formula as below:

$$S(\omega) = \begin{pmatrix} S^{ee} & S^{eh} \\ S^{he} & S^{hh} \end{pmatrix} = \hat{1} - iW^\dagger(\omega - h_{K3} + \frac{i}{2}WW^\dagger)^{-1}W, \tag{6.4}$$

where $W = \mathrm{diag}(\sqrt{\Gamma_{\mathrm{L}}}, \sqrt{\Gamma_{\mathrm{M}}}, \ldots, -\sqrt{\Gamma_{\mathrm{L}}}, -\sqrt{\Gamma_{\mathrm{M}}}, \ldots)$ is the matrix describing the dot-lead couplings, with Γ_i being the coupling strength between QDi and lead-i. The zero-temperature conductance is thus:

$$G^{(0)}_{\alpha\beta}(\omega) = \delta_{\alpha\beta} - |S^{ee}_{\alpha\beta}(\omega)|^2 + |S^{he}_{\alpha\beta}(\omega)|^2 \tag{6.5}$$

in unit of e^2/h. The finite-temperature conductance is obtained by a convolution between the zero-temperature conductance and the derivative of the Fermi distribution:

$$G^T_{\alpha\beta}(\omega) = \int_{-\infty}^{+\infty} dE \frac{G^{(0)}_{\alpha\beta}(E)}{4k_B T \cosh^2[(E-\omega)/2k_B T]}. \tag{6.6}$$

In the numerical calculations shown in the current work, we use $t_1 = \Delta_1 = 20\,\mu\mathrm{eV}$, $t_2 = \Delta_2 = 25\,\mu\mathrm{eV}$, which are extracted from experimental data in figure 6.1. In addition, we set $\Gamma_{\mathrm{L}} = \Gamma_{\mathrm{M}} = \Gamma_{\mathrm{R}} = 0.7\,\mu\mathrm{eV}$, which does not affect the simulations qualitatively, but were selected to give the same order of magnitude of conductance. Lastly, we set $T = 50\,\mathrm{mK}$.

THE KITAEV CHAIN IN THE MAJORANA BASIS

To guide interpretation of the measurements, it is instructive to consider the three-site Kitaev chain Hamiltonian in terms of Majorana operators. This is done by introducing two Majorana operators for each fermionic site:

$$c_n = (\gamma_{na} + i\gamma_{nb})/\sqrt{2}, \quad c_n^\dagger = (\gamma_{na} - i\gamma_{nb})/\sqrt{2}, \quad \{\gamma_{ma}, \gamma_{nb}\} = \delta_{mn}\delta_{ab}. \tag{6.7}$$

As such, the Hamiltonian can be written as (relabelling L,M,R to 1,2,3 for convenience):

$$\begin{aligned} H = {} & i\mu_1\gamma_{1a}\gamma_{1b} + i\mu_2\gamma_{2a}\gamma_{2b} + i\mu_3\gamma_{3a}\gamma_{3b} + i(t_1+\Delta_1)\gamma_{2a}\gamma_{1b} + i(-t_1+\Delta_1)\gamma_{2b}\gamma_{1a} \\ & + it_2\gamma_{3a}\gamma_{2b} - it_2\gamma_{3b}\gamma_{2a} + i\Delta_2\cos\phi(\gamma_{3a}\gamma_{2b} + \gamma_{3b}\gamma_{2a}) + i\Delta_2\sin\phi(\gamma_{3a}\gamma_{2a} - \gamma_{3b}\gamma_{2b}). \end{aligned} \tag{6.8}$$

Therefore, at the sweet spot of a three-site Kitaev chain, i.e., $\mu_n = 0, t_1 = \Delta_1, t_2 = \Delta_2, \phi = 0$, we have:

$$H(\phi = 0) = i2t_1\gamma_{2a}\gamma_{1b} + i2t_2\gamma_{3a}\gamma_{2b}. \tag{6.9}$$

On the other hand, at $\mu_n = 0, t_1 = \Delta_1, t_2 = \Delta_2, \phi = \pi$, the Hamiltonian becomes:

$$H(\phi = \pi) = i2t_1\gamma_{2a}\gamma_{1b} - i2t_2\gamma_{3b}\gamma_{2a}. \tag{6.10}$$

A bilinear term of Majorana operators indicates a coupling between them. This is what is visualised through the schematics used in the main text (i.e. figure 6.2c).

MAJORANA ZERO MODES FOR A KITAEV CHAIN AT $\phi = 0$ AND $\phi = \pi$

We now calculate the wavefunctions of Majorana zero modes of the Kitaev chain. To distinguish it from the Majorana basis using γ's, we use χ_n to denote the Majorana zero modes. The definition of a Majorana zero-energy quasiparticle is:

$$[H, \chi_n] = 0, \quad \chi_n^\dagger = \chi_n. \tag{6.11}$$

For the Kitaev chain with $\phi = 0$ the solutions are easily obtained: since γ_{1a} and γ_{3b} do not appear in the Hamiltonian in Eq. (6.9), the wavefunctions of the two Majorana zero modes are:

$$\chi_1 = \gamma_{1a}, \quad \chi_2 = \gamma_{3b}, \tag{6.12}$$

i.e., one is completely localised at the left QD and the other at the right QD, separated in space by the middle QD. On the other hand, when $\phi = \pi$, there exist four Majorana zero modes, of which the first three are again easy to find as shown below:

$$\chi_1 = \gamma_{1a}, \quad \chi_2 = \gamma_{2b}, \quad \chi_3 = \gamma_{3a}. \tag{6.13}$$

They are localised at the left, middle and right QD respectively. The ansatz of the fourth Majorana zero mode is $\chi_4 = A\gamma_{1b} + B\gamma_{2a} + C\gamma_{3b}$, which yields:

$$\chi_4 = \frac{t_2}{\sqrt{t_1^2 + t_2^2}}\gamma_{1b} - \frac{t_1}{\sqrt{t_1^2 + t_2^2}}\gamma_{3b}. \tag{6.14}$$

That is, χ_4 is delocalised at the left and right QDs (no wavefunction weight in the middle dot), with the relative weights determined by the gap of the left and right pairs. One can note that once the left or right QD is detuned from resonance, i.e., a finite μ_1 or μ_3, χ_4 would couple with χ_1 or χ_3, giving an energy splitting. This explains the splitting of the zero-bias conductance peak observed in the π-phase Kitaev chain studied in the main text (figure 6.3d).

THE MAJORANA DENSITY

The main text focuses on conductance spectra of the three-site Kitaev chain at $\phi_\Delta = 0$, when the left QD is detuned. Here we show that an isolated zero-bias conductance peak reveals the Majorana wavefunction profiles. Assuming equal dot-lead coupling strengths $\Gamma_i = \Gamma$ and an isolated zero-energy state of h_{K3}, the S matrix can be simplified to:

$$S(\omega) \approx \hat{1} - i\frac{\Gamma}{\omega + i\frac{\Gamma}{2}}\begin{pmatrix} u_1u_1^* + v_1^*v_1, \dots \\ u_2u_1^* + v_2^*v_1, \dots \\ \vdots \\ -(v_1u_1^* + u_1^*v_1), \dots \\ -(v_2u_1^* + u_2^*v_1), \dots \\ \vdots \end{pmatrix} \tag{6.15}$$

where u_i and v_i are the electron and hole components of the zero-energy quasiparticle state on site-i. By definition $u^* = (\xi_A + i\xi_B)/\sqrt{2}, v = (\xi_A - i\xi_B)/\sqrt{2}$, where ξ_A and ξ_B are Majorana wavefunctions. We thus have $uu^* + v^*v = |\xi_A|^2 + |\xi_B|^2, -2u^*v = -(\xi_A^2 + \xi_B^2)$. Furthermore, h_{K3} is real at $\phi = 0$, giving real u and v. Thereby ξ_A is purely real and ξ_B is purely imaginary, giving $uu^* + v^*v = \rho_A + \rho_B, -2u^*v = -(\rho_A - \rho_B)$, where $\rho_{A/B} = |\xi_{A/B}|^2$ are the local Majorana densities. As a result, the local conductance in the zero-temperature limit is:

$$G_{ii}^{(0)}(\omega) = \frac{(\Gamma/2)^2}{\omega^2 + (\Gamma/2)^2} \cdot 4(\rho_{Ai} + \rho_{Bi} - 4\rho_{Ai}\rho_{Bi}). \tag{6.16}$$

Here, the profile of the zero-bias conductance peak has a Lorentzian shape with its broadening width being fixed by the dot-lead coupling strength. Although finite-temperature effects will change this prefactor, a key finding here is that the local zero-bias conductance of a multi-terminal junction is proportional to the Majorana densities.

For a three-site Kitaev chain at its sweet spot, as considered in the current work, the zero-energy eigenfunction is $\psi = \frac{1}{2}(\frac{1}{\sqrt{1+4a^2}}, \frac{-2a}{\sqrt{1+4a^2}}, 1, \frac{-1}{\sqrt{1+4a^2}}, \frac{2a}{\sqrt{1+4a^2}}, 1)^T$, giving $\rho_A = (0, 0, 1/2)$ and $\rho_B = \frac{1}{2}(\frac{1}{1+4a^2}, \frac{4a^2}{1+4a^2}, 0)$ where $a = \mu_1/4t$ is the dot detuning with respect to gap. Therefore, the profiles of local zero-bias conductances as a function of dot detuning are:

$$\begin{aligned}
G_{11}(V=0) &\propto 2\rho_B = \frac{1}{1+4a^2}, \\
G_{22}(V=0) &\propto 2\rho_B = \frac{4a^2}{1+4a^2}, \\
G_{33}(V=0) &\propto 2\rho_A = 1.
\end{aligned} \tag{6.17}$$

Thus, the local conductance profiles as a function of dot detuning indicate the moving of Majorana zero modes in a three-site chain. We compare these findings to the experimental data in figure 6.12.

LINE-SHAPE OF CONDUCTANCE TRACES

When probing the excitation gap in the middle QD at the three-site sweet spot (figure 6.2), a finite in-gap conductance remains. In part, this can be expected due to thermal-broadening effects on the higher energy excitations. We address here the expected line-shapes for the conductances at a three-site sweet spot. The conductance measurements are performed in the limit of low tunneling between the leads and the QDs, such that we can expect the QD-lead coupling $\Gamma \ll \mathrm{k_B}T$. In this limit, the line-shape of a single QD resonance as a function of applied V_bias is given by [210]:

$$G(V_{bias}) \propto A\cosh\left(\frac{V_\mathrm{bias}}{2k_\mathrm{B}T}\right)^{-2} \tag{6.18}$$

In conductance measurements of a three-site chain sweet-spot, the density of states depends on the site that is probed. For the left QD, three conductance peaks are expected: one at zero bias, and two at $\pm\, 2t_1$. We thus model the conductance G_LL as a function of V_L to be the sum of 3 contributions:

$$G_{\mathrm{LL}}(V_{\mathrm{L}}) = A_1 \cosh\left(\frac{V_{\mathrm{L}} - 2t_1}{\gamma}\right)^{-2} + A_2 \cosh\left(\frac{V_{\mathrm{L}}}{\gamma}\right)^{-2} + A_3 \cosh\left(\frac{V_{\mathrm{L}} + 2t_1}{\gamma}\right)^{-2} \tag{6.19}$$

Where we replace the factor of $2k_{\mathrm{B}}T$ with a general broadening factor γ. Similarly, the right QD has three conductance peaks: one at zero bias, and two at $\pm\, 2t_2$. We model the conductance G_{RR} as a function of V_{R} to be:

$$G_{\mathrm{RR}}(V_{\mathrm{R}}) = B_1 \cosh\left(\frac{V_{\mathrm{R}} - 2t_2}{\gamma}\right)^{-2} + B_2 \cosh\left(\frac{V_{\mathrm{R}}}{\gamma}\right)^{-2} + B_3 \cosh\left(\frac{V_{\mathrm{R}} + 2t_2}{\gamma}\right)^{-2} \tag{6.20}$$

From these fits, the values of t_1 and t_2 are determined. The conductance of the middle QD is then expected to have 4 peaks: at $\pm t_1$ and at $\pm t_2$, giving the sum of the following four contributions:

$$G_{\mathrm{MM}}(V_{\mathrm{M}}) = C_1 \cosh\left(\frac{V_{\mathrm{M}} - 2t_1}{\gamma}\right)^{-2} + C_2 \cosh\left(\frac{V_{\mathrm{M}} + 2t_1}{\gamma}\right)^{-2} \tag{6.21}$$

$$+ C_3 \cosh\left(\frac{V_{\mathrm{M}} - 2t_2}{\gamma}\right)^{-2} + C_4 \cosh\left(\frac{V_{\mathrm{M}} + 2t_2}{\gamma}\right)^{-2} \tag{6.22}$$

6

These analytical expressions are in agreement with the conductance traces obtained from the numerical simulations, in the parameter regime described above. We compare the expressions to experimental data in figure 6.9.

6.7 Extended Data

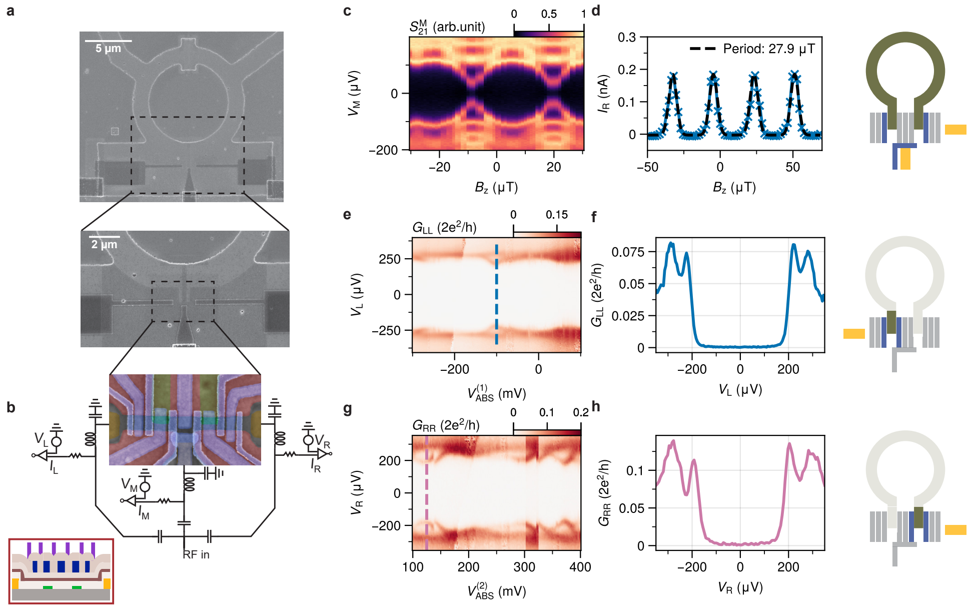

Figure 6.5: **Device description and characterisation of hybrid sections.** **(a)** Zoomed out SEMs of copies of the measured device obtained after deposition of Ohmic contacts, showing the full structure of the superconducting loop. **(b)** Close-up SEM of the finished device, including the full circuit diagram. Bottom left in-set shows a cross-sectional schematic of the device along the channel, adapted from [128], to visualise the order of the three gate layers. Resonators are formed by inductors in combination with a parasitic capacitances to ground, which allows for fast radio-frequency (RF) measurements, used in this work for tuning and characterisation of the system. Voltage sources and current meters are attached to each lead via ≈ 5 kΩ resistors, acting as bias tees, used to obtain the conductance measurements in the main text. Sub-figures (c-h) show characterisations of the three possible hybrid configurations, after a 1-D channel is formed with the large depletion gates. Schematics on the right display the activated tunneling gates and relevant Ohmic contacts for each row. **(c)** RF-spectroscopy of the Josephson junction formed by the two superconducting fingers at the ends of the loop, as a function of the magnetic field B_z perpendicular to the loop. **(d)** Measured current I_R with V_R=100 μV, in a wider range of B_z. Fitting the oscillations with a periodic Gaussian function provides an estimate for the flux periodicity (28 μT). **(e)** Tunneling spectroscopy of the left SC finger in isolation, as a function of $V_{ABS}^{((1))}$ applied to the gate covering the left hybrid region. **(f)** Line-trace from (e) at $V_{ABS}^{((1))}$=−100 mV, to show the presence of a sub-gap state in the left hybrid. **(g)** Tunneling spectroscopy of the right SC finger in isolation, as a function of the gate covering the right hybrid region ($V_{ABS}^{((2))}$). **(h)** Line-trace from (g) at $V_{ABS}^{((2))}$=125 mV to show the presence of a sub-gap state in the right hybrid.

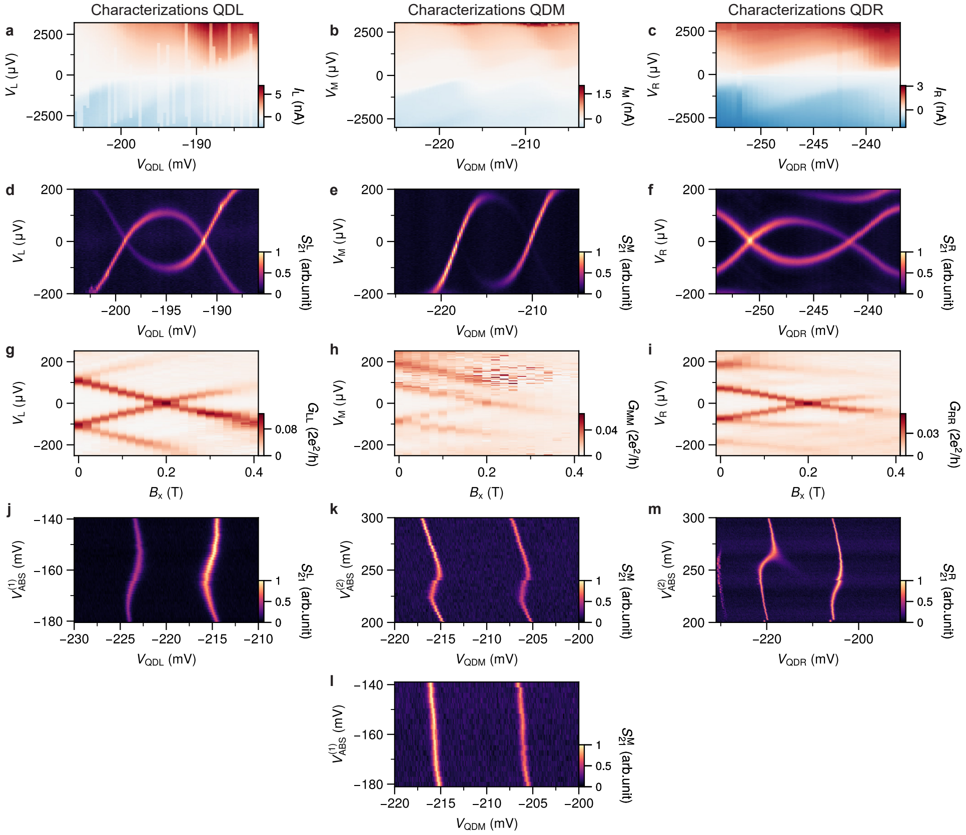

Figure 6.6: **Quantum dot characterisations.** Results presented in the main text are obtained using a single orbital in each QD. Characterisation measurements of each QD is shown here. Left, middle and right columns pertain to the left, middle and right QD respectively. **(a-c)** Coulomb diamonds measured at B_x=0 mT. To achieve strong interdot coupling, barriers between QD and neighbouring regions are kept relatively open, such that a finite current can be observed within each Coulomb diamond. The outline roughly indicates the charging energies to be >1 mV. **(d-f)** RF-Spectroscopy of each QD in the same regime as (a-c), for a smaller range of applied voltage biases. In this strong coupling regime, so-called Yu-Shiba-Rusinov states form at sub-SC gap energy scales whose energies are non-linearly dependent on the plunger gate voltages [211]. **(g-i)** Spectroscopy as a function of magnetic field B_x applied along the 1-D channel, with each plunger gate set close to the zero field charge degeneracy point based on (d-f). The slope of the splitting sub-gap states provides an estimate of the g-factors for these parameters to be 18.4, 14.8 and 13.7 respectively. **(j-m)** Examples of QD-ABS charge stability diagrams, used to calibrate the interdot interactions following the procedure detailed in [79, 80]. The discrepancies in the plunger gate voltages used for each orbital between (a-c) and (j-m) arise due to gate-jumps and cross-talk between neighbouring barrier gates.

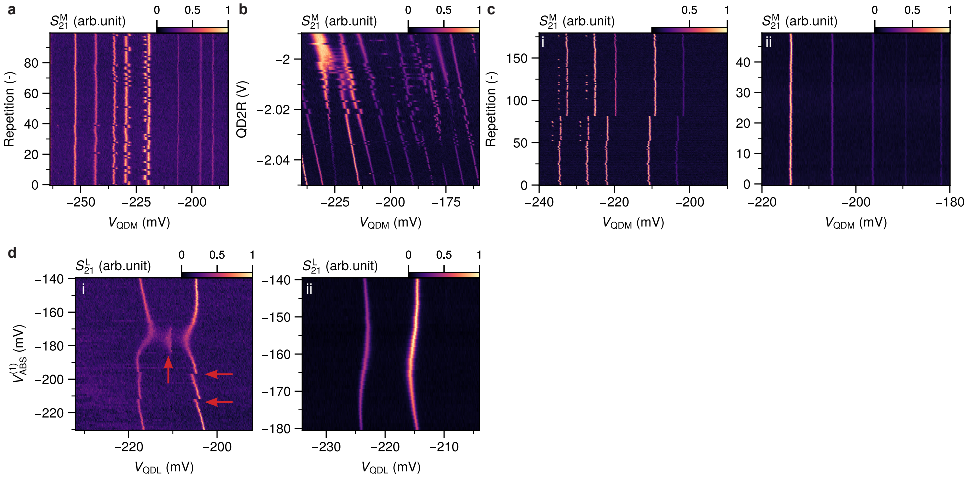

Figure 6.7: **QD stability. (a)** Example of repeated RF-measurements of the middle QD resonances. The same measurement was repeated 100 times, once every second. The plot shows a stack of all repetitions. The resonances at $-225\,\mathrm{mV}$ are observed to switch between two states during this time, which makes them unsuitable for slow DC measurements. **(b)** In order to find a stable regime, we observe the effect of varying the barrier gates forming the QDs. Here, for example, the middle QD resonances are found to be more stable when the right barrier gate is tuned below $-2.02\,\mathrm{V}$. **(c)** This becomes apparent when comparing repeated RF measurements for (i) unstable and (ii) stable regimes. **(d)** In addition, charge-jumps in the gate voltages can affect the charge-stability diagrams. Panel (i) shows an example of a CSD for QDL and the left hybrid gate, where charge jumps occur in both $V_{\mathrm{ABS}}^{(1)}$ and V_{QDL} (indicated by the red arrows). By fine-tuning the barrier gates forming QDL, we can reach a state where these jumps are avoided in the region of interest, shown in panel (ii).

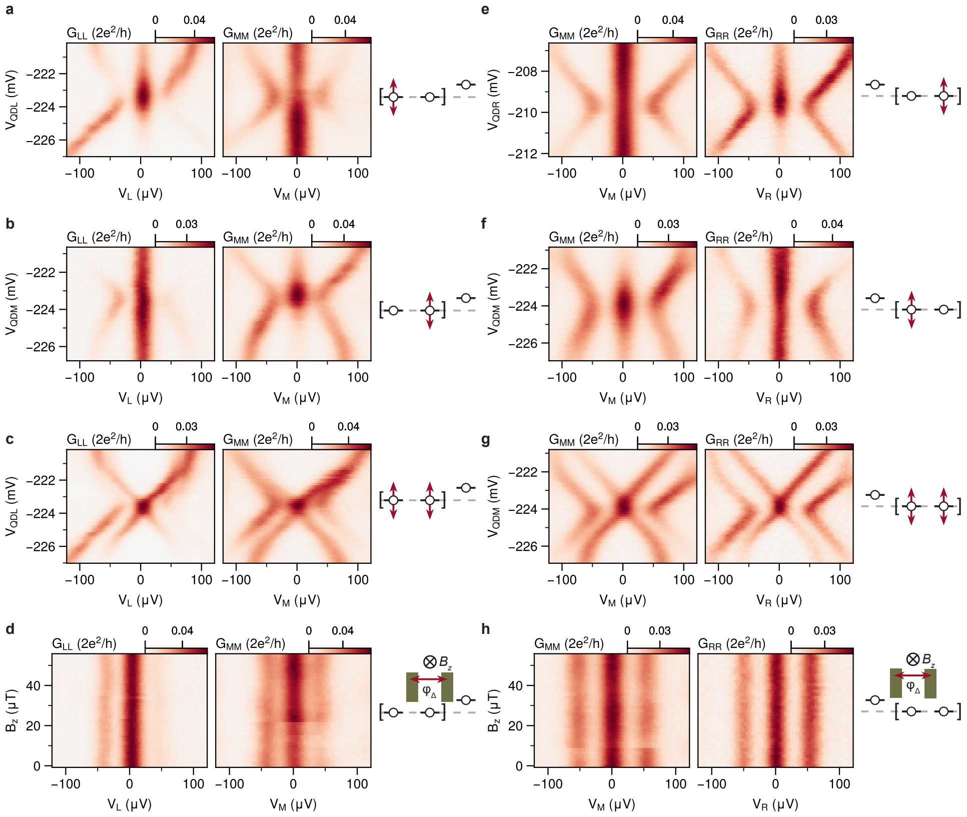

Figure 6.8: **Conductance spectra of two-site QD pairs.** Studying CSDs for pairs of QDs provides information about the interdot couplings and allows one to reach the sweet spot conditions shown in figure 6.1c,d. In addition, finite bias conductance spectra at the two-site sweet spots should be obtained [121] for all possible combinations of QD detunings. This is shown here for the charge configuration in figure 6.1. Adjacent schematics represent the configurations of the QDs and the parameters varied. Left column: tunneling spectroscopies of the left QD pair at a sweet spot (i.e. $t_1 = \Delta_1$), with the right QD kept in Coulomb blockade. G_{LL} and G_{MM} are measured as a function of **(a)** detuning V_{QDL}, **(b)** detuning V_{QDM}, **(c)** detuning both V_{QDL} and V_{QDM} simultaneously and **(d)** Applying a magnetic field B_z perpendicular to the superconducting loop. Right column: tunneling spectroscopy of the right pair of QDs at a sweet spot (i.e. $t_2 = \Delta_2$), with the left QD kept in Coulomb blockade. G_{MM} and G_{RR} are measured as a function of **(e)** detuning V_{QDR} **(f)** detuning V_{QDM}, **(g)** detuning both V_{QDM} and V_{QDR} and **(h)** Applying a magnetic field B_z perpendicular to the superconducting loop. It is important to note that (d) and (h) are obtained for the same configuration as the flux-dependence measurements in figure 6.2, with the only difference being that here the outer QD is kept in Coulomb blockade. The lack of response to B_z rules out more trivial origins of the flux dependence in figure 6.2, such as oscillations of the middle QDs electrochemical potential energy.

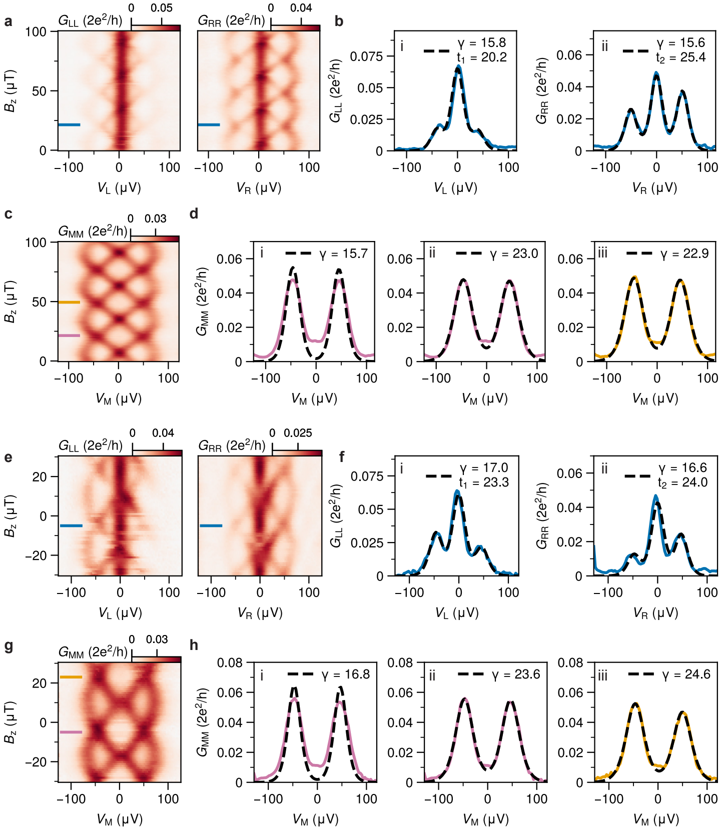

Figure 6.9: **Fitting of conductance line-traces.** The measurements in figure 6.2 show a finite in-gap conductance in G_{MM} when $\phi_\Delta = 0$. Possible origins for this include thermal broadening, and small deviations in the QD plunger gate voltages from being precisely at $\mu_i = 0$. Here we address the former, by comparing the conductance bias-traces with the theoretically expected shapes in the small lead-QD coupling limit ($\Gamma \ll k_B T$) described in section 6.6. **(a)** Repetitions of conductance spectra for G_{LL} and G_{RR} as a function of B_z, as shown in figure 6.2a. **(b)** Line-cuts taken from the indicated position in (a), at B_z corresponding to $\phi_\Delta = 0$. G_{LL} is fitted to equation (6.19) and G_{RR} is fitted to equation (6.20), yielding estimates for t_1 and t_2. We find the conductances are well described by the temperature-limited fits and find both are described by the same broadening parameter ($\gamma = 15.6$). **(c)** Repetition of conductance spectra for G_{MM} as a function of B_z from figure 6.2a. **(d)** Using the t_1 and t_2 values extracted in (b), we fit the indicated G_{MM} line-cut from (c) to equation (6.22). In (i), γ is fixed to be the same value as extracted in (b), while in (ii) γ is included as fitting parameter. (iii) uses the same fitting as (ii), for a line-cut taken at a different 2π period as indicated in (c). The conductance is again well-described by the temperature-limited fit. A larger broadening parameter is however required, which was found to be caused by the power supply of the cryogenic amplifier. In (ii) and (iii) the measured conductance at $V_{\mathrm{M}} = 0$ is $\approx 3\mathrm{mG}_0$ larger than explained by the fits. From equation (6.17), this remainder would correspond to offsets in $\mu_{\mathrm{L}}/\mu_{\mathrm{R}}$ on the order of ±5 μeV. The plunger gate voltages are set with a resolution of 60 μV, which combined with a QD leverarm of ≈0.05 would translate to potential offsets on the order of 3 μeV in μ_{L} and μ_{R}. **(e-h)** shows a repetition of the outlined procedure, for measurement using the charge configuration shown in figure 6.15. A similar behaviour is observed.

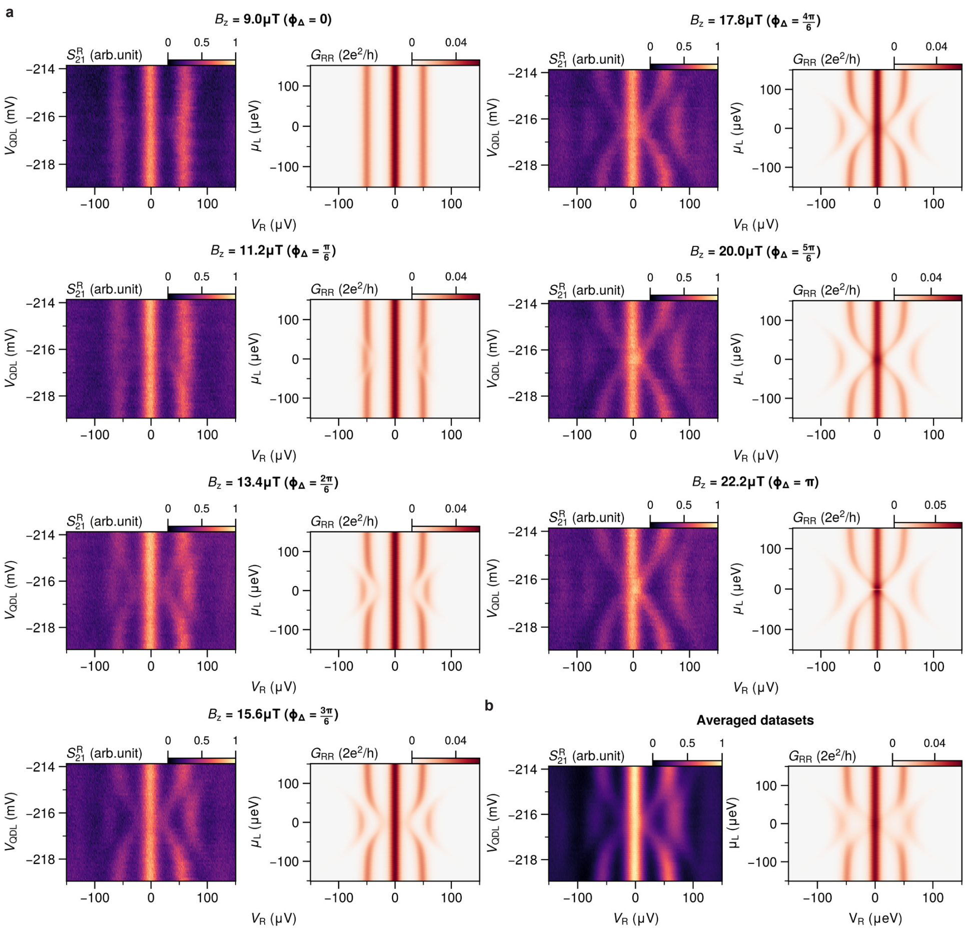

Figure 6.10: **Conductance spectra for ϕ_Δ between 0 and π.** In the main text, figure 6.3 shows measurements of conductance spectra at a three-site sweet spot, obtained at two B_z values corresponding to $\phi_\Delta = 0$ and $\phi_\Delta = \pi$. The ability to control the flux allows us to perform such measurements at any intermediate value of ϕ_Δ. **(a)** RF-spectroscopy measurements of S_{21}^R and corresponding numerical simulations, upon detuning V_{QDL}, for seven values of B_z corresponding to ϕ_Δ = 0 and $\phi_\Delta = \pi$. The experimental evolution corresponds well to the numerical simulation at each stage. Recent work on a three-site Kitaev chain with two separately grounded SCs [34] concludes that a small voltage difference between the SCs (on the order of μV), may give rise to rapid phase oscillations. Hence, it is assumed their (slow) measurements reflect an average over many periods of ϕ_Δ. **(b)** Shows averaged RF-spectroscopy for 25 measurements in the same range as (a), and the corresponding numerically averaged simulation, finding good agreement with the reported behaviour in [34].

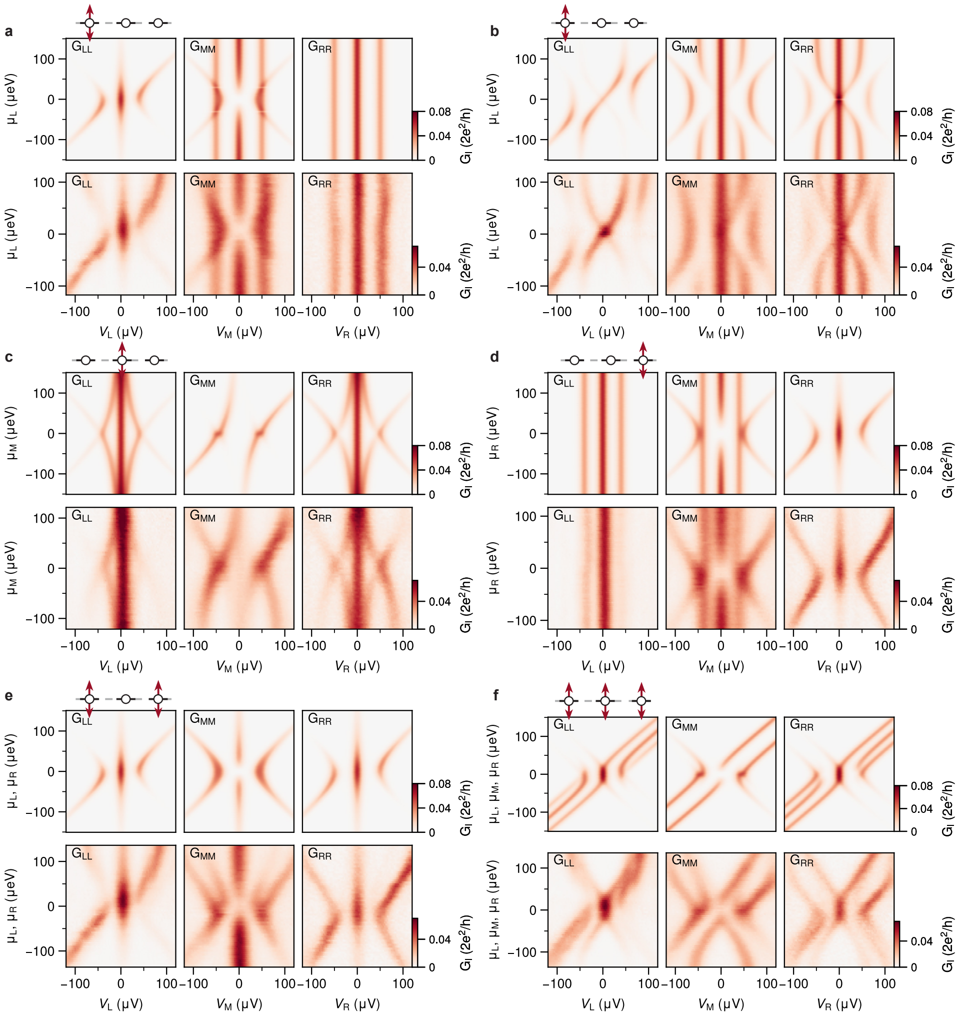

Figure 6.11: **Three-site conductance spectra for different QD detuning combinations**. In a three-site Kitaev chain, the ZBPs arising on the outer QDs are expected to persist when detuning either a single QD or pairs of QDs [34]. Fig. 3 only demonstrates the response to detuning V_{QDL}. Here, four other possible detuning combinations are highlighted, for the same device configuration. Accompanying numerical simulations use the same set of parameters as shown in the main text. Plunger gate voltages have been converted to chemical potential energies using the QD leverarms. **(a)** and **(b)** show repetitions of the conductance spectra shown in figure 6.3, where $\phi_\Delta = 0$ and $\phi_\Delta = \pi$ respectively, including a comparison to the numerical simulation. Furthermore, we show the response at $\phi_\Delta = 0$ to **(c)** Detuning V_{QDM} (μ_{M}), **(d)** detuning V_{QDR} (μ_{R}), **(e)** detuning both V_{QDL} and V_{QDR} and **(f)** detuning all three QDs simultaneously. When $\phi_\Delta = 0$, the ZBP measured in G_{LL} and G_{RR} only splits from zero-energy when all three QDs are detuned.

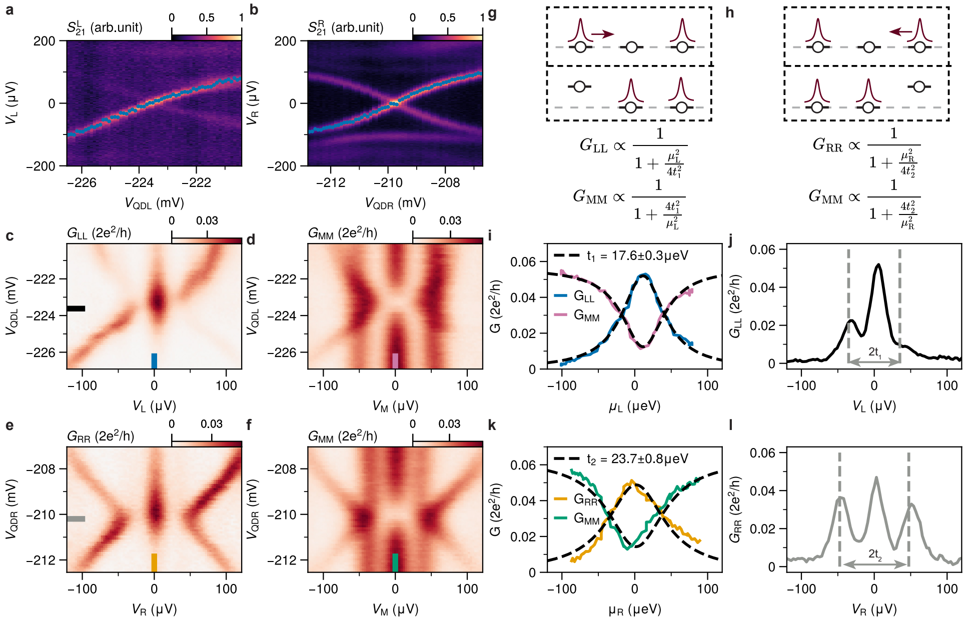

Figure 6.12: **Shifting the MBS wavefunction - comparison to analytical result.** At a three-site Kitaev chain sweet spot, with $\phi_\Delta = 0$, detuning either of the outer QDs shifts the MBS wave-function to the middle QD. In section 6.6, we derive that this reflects in the zero-bias conductance of each site and depends only on the coupling parameters t_1/t_2 (= Δ_1/Δ_2) (see equation (6.17)). To do this analysis experimentally, first the chemical-potential energies μ_L, μ_R of QDL and QDR are measured as a function of **(a)** $V_{\rm QDL}$ and **(b)** $V_{\rm QDR}$, by measuring each QD spectrum with the unused QDs in Coulomb blockade. With all parameters tuned to the sweet spot values, we detune $V_{\rm QDL}$ around charge degeneracy and measure **(c)** $G_{\rm LL}$ and **(d)** $G_{\rm MM}$, as shown in figure 6.3a. Additionally, we detune $V_{\rm QDR}$ and measure **(e)** $G_{\rm RR}$ and **(f)** $G_{\rm MM}$. As visualised in **(g)** and **(h)**, these experiments result in the shifting of the MBS wave-function from the outer QD to the inner QD. In (c,d), the conductances measured at $V_{\rm L}$,$V_{\rm M}$ = 0 depend only on $\mu_{\rm L}$ and t_1. Similarly for (e,f) they scale according to $\mu_{\rm R}$ and t_2. **(i)** We extract $G_{\rm LL}$ and $G_{\rm MM}$ along $V_{\rm L}$,$V_{\rm M}$ = 0 from (c) and (d) and convert $V_{\rm QDL}$ to $\mu_{\rm L}$ using (a). Fitting the analytical formulas shown in (g), with an additional scaling factor, an estimate for t_1 of 17.6 μeV is obtained. This can be compared to the width of the excitation gap at $\mu_{\rm L}$ = 0, which theory predicts to be $2t_1$. **(j)** shows the line-trace, with the dashed lines indicating the expected location of the excited states based on the extraction in (i). **(k)** We repeat this procedure for $G_{\rm RR}$ and $G_{\rm MM}$ along $V_{\rm R}$,$V_{\rm M}$ = 0 from (e) and (f), converting $V_{\rm QDL}$ to $\mu_{\rm R}$ using (b). Now fitting the formulates shown in (h), we can estimate t_2 of 23.7 μeV. **(l)** This again agrees with the excitation gap at $\mu_{\rm R}$ = 0.

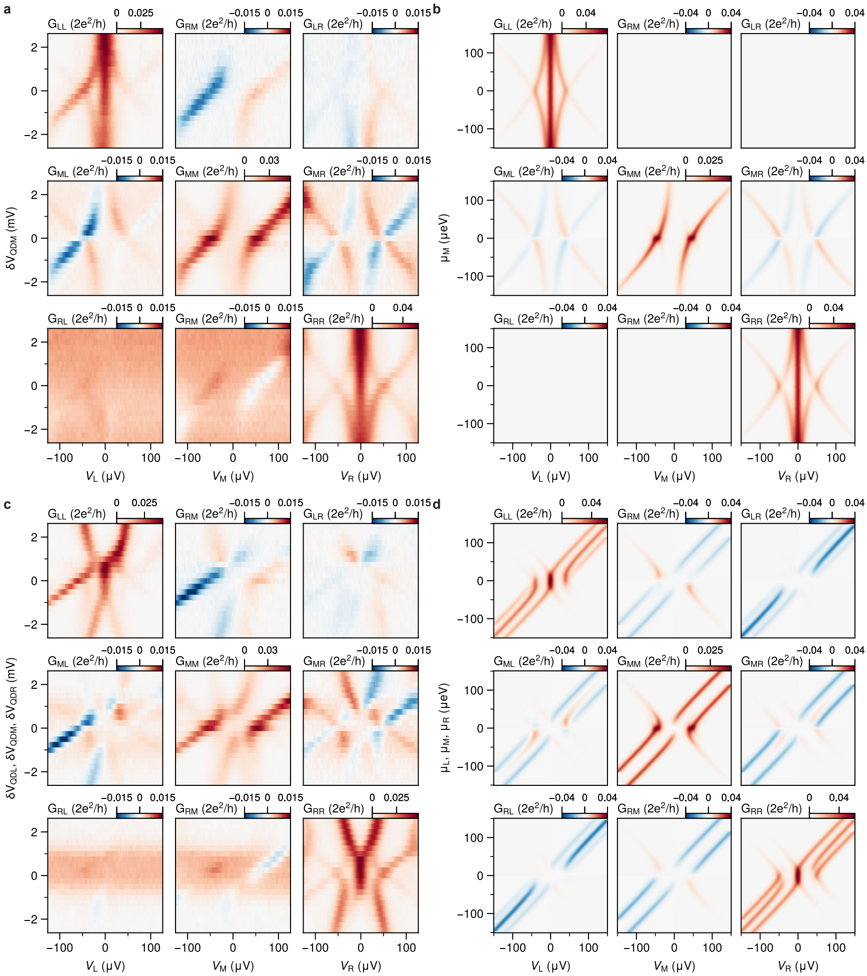

Figure 6.13: **Full local and non-local conductance matrix measurements**. The main text focuses on measurements of local conductances probed through each of the three normal contacts. For such measurements, the non-local responses are recorded in addition, not shown due to size constraints. Here two measurements are highlighted, for the charge configuration shown in Fig S4g. **(a)** Local and non-local conductances when detuning V_{QDM}, compared to **(b)** numerical simulations of detuning μ_{M}. Strikingly, the ZBPs do not appear in the non-local measurements, as expected due to arising from MBSs localised on the outer QDs. Additionally, the same patterns of positive and negative non-local conductance in G_{ML} and G_{LM} are observed, with the sign inverting at $\mu = 0$. Unlike the simulations, signals appear in G_{RM}, G_{LR}, G_{RL} and G_{RM} that are not captured by the effective model. We note that a more complete model incorporating explicitly the hybrid regions such as in [35] may be needed to fully describe all non-local effects. **(c)** Local and non-local conductances when simultaneously detuning V_{QDL}, V_{QDM} and V_{QDR}, compared to **(d)** numerical simulations of detuning all μ_{i}.

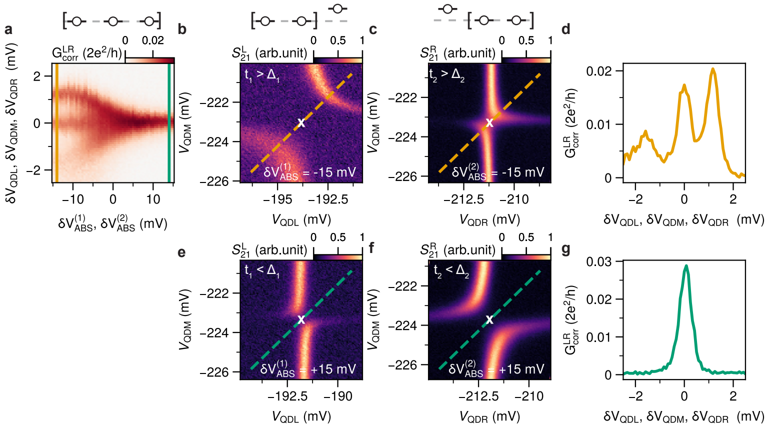

Figure 6.14: **Details of measurement procedure for figure 6.4** In the main text, figure 6.4 highlights zero-bias conductance measurements at a three-site sweet spot, when simultaneously varying V_{QDL}, V_{QDM} and V_{QDR} against simultaneously sweeping $V_{\mathrm{ABS}}^{((1))}$ and $V_{\mathrm{ABS}}^{((2))}$. Here, we detail how these measurements are performed. **(a)** shows a repetition of the data as shown in figure 6.4e. First, the sweet spot values for $V_{\mathrm{ABS}}^{((1))}$ and $V_{\mathrm{ABS}}^{((2))}$ were determined from measuring CSDs, through the process shown in figure 6.1. We denote these values $\delta V_{\mathrm{ABS}}^{((1))}$=0 and $\delta V_{\mathrm{ABS}}^{((2))}$=0 respectively. Next, we apply 15 mV to each, with respect to these sweep spot voltages, in the direction that results in an avoided crossing signifying $t > \Delta$. Due to cross-coupling, the resonance value for each QD needs to be re-determined. This is done by measuring the zero-bias Coulomb resonance for each QD, with the two other QDs set off resonance, and fitting a Lorentzian line-shape to determine the centre. **(b)** and **(c)** show CSDs measured at these V_{ABS} values for the left-middle and middle-right pairs respectively, taken for verification of the interdot coupling. Both sides show an antidiagonal avoided crossing signifying t_{i}>Δ_{i}. The centers as obtained by the centering procedure are marked by the crosses. After centering, all three QDs are brought on resonance and swept simultaneously, accounting for differences in leverarms (see figure 6.12). Here the orange line-trace in (a) is obtained, shown in **(d)**. The same procedure is repeated for every set-point, until reaching $V_{\mathrm{ABS}}^{((1))}$, $V_{\mathrm{ABS}}^{((2))}$ = +15 mV. Now both CSDs show a clear diagonal avoided crossing, shown in **(e)** and **(f)**. The new centers are marked, differing within a few mV from those in (b)/(c). The green dashed lines mark the paths taken by the simultaneous sweep for the green line in (a), plotted in **(g)**.

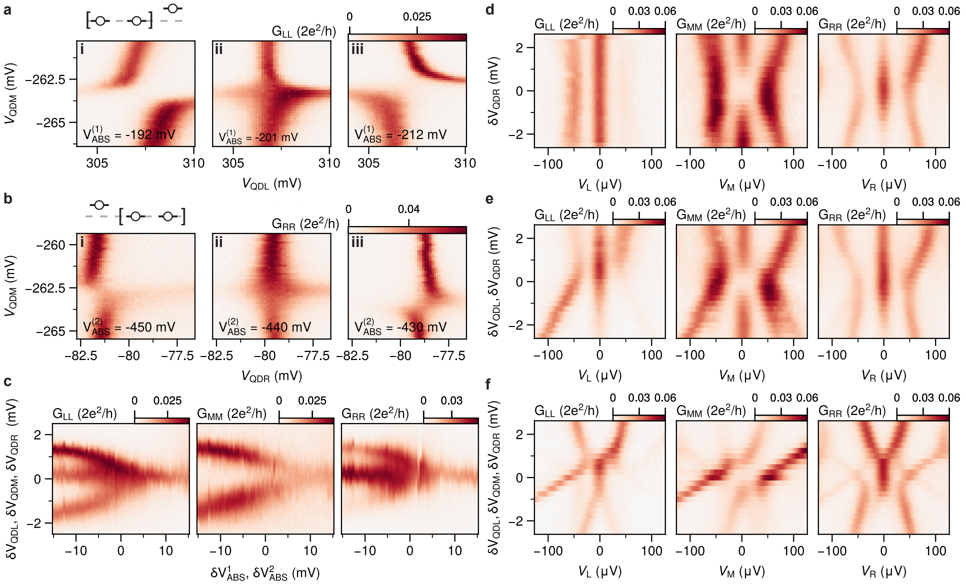

Figure 6.15: **Reproduction of main results in a separate cooldown.** The measurements in figure 6.4 were repeated for validation during a separate cooldown of the same device. First, two-site sweet spots were obtained for both two-site pairs, as in figure 6.1. **(a)** CSDs for resonances in the left and middle QD, varying $V^{(1)}_{\mathrm{ABS}}$ in a range where the avoided crossing changes direction to determine the sweet spot (panel ii). Similarly, a sweet spot was obtained for the middle and right QD, upon varying $V^{(2)}_{\mathrm{ABS}}$, shown in **(b)**. The magnetic field B_z corresponding to $\phi_\Delta = 0$ was determined from the spectroscopy measurements shown in figure 6.9g. **(c)** In this configuration, the measurement shown in figure 6.4 was repeated, using the same procedure as detailed in figure 6.14. Additionally, we reproduce here the conductance spectra at the sweet spot as a function of **(d)** detuning V_{QDR}, **(e)** detuning both V_{QDL} and V_{QDR} and **(f)** detuning simultaneously all 3 QDs.

7

THE SPINFUL KITAEV CHAIN

A critical requirement for creating isolated Majorana bound states is that time reversal symmetry must be broken. In Chapter 5, we tested the limits of this requirement by studying the two-site Kitaev chain as a function of the strength of the applied external magnetic field. To our surprise, signatures of the presence of Majoranas, such as stable zero-bias conductance peaks, persist even when removing the magnetic field altogether. In this chapter, we continue this investigation in order to understand the behaviour of the system at zero magnetic field, following the theoretical work in Ref. [121]. A threefold degenerate ground-state in the presence of time reversal symmetry allows to make a connection to Majorana Kramers pairs and $\mathbb{Z}_3$-parafermions, as introduced in section 2.3. We further investigate the scaling of the two-site system to three sites in the absence of a magnetic field. We find then that strongly degenerate ground states can be found only at finetuned points in parameter space, both theoretically and experimentally.

You say you're lookin' for someone
Never weak but always strong
To protect you an' defend you
Whether you are right or wrong
Someone to open each and every door
But it ain't me, babe
No, no, no, it ain't me, babe
It ain't me you're lookin' for

- Bob Dylan

The work in this chapter appears online as: *Probing ground-state degeneracies of a strongly interacting Fermi-Hubbard model with superconducting correlations* , **Sebastiaan L. D. ten Haaf**†, Sebastian Miles†, Qingzhen Wang, A. Mert Bozkurt, Ivan Kulesh, Yining Zhang, Christian G. Prosko, Di Xiao, Michael Wimmer and Srijit Goswami, arXiv:2512.13242 [212].

Personal contribution includes device fabrication, obtaining measurements, performing numerical and analytical analysis and writing of the manuscript.

†Authors contributed equally

7.1 Introduction

The Fermi-Hubbard model is a fundamental model for strongly correlated electron systems, capturing the competition between electron kinetic energy and on-site Coulomb repulsion [213, 214]. Despite its seeming simplicity, the model exhibits a rich phase diagram, including metallic, insulating, magnetic, and superconducting phases [214, 215]. This fundamental importance has motivated many experimental efforts to realize the Fermi-Hubbard model in controllable platforms such as ultra-cold atoms in optical lattices [216], trapped ions [217], and superconducting circuits [218, 219]. Semiconductor quantum dots are another natural platform, due to the intrinsic strong electron-electron interactions in the form of on-site Coulomb repulsion [220]. Recent experiments have studied different aspects of the Fermi-Hubbard model using small quantum dot arrays [221, 222]. Semiconductor quantum dots were also put forth as a platform to implement a non-interacting model exhibiting topological superconductivity - the Kitaev chain [14, 33, 37, 38]. Short Kitaev chain can be successfully implemented using small arrays of quantum dots coupled by superconducting hybrid segments [28, 34, 178, 187]. In addition to normal electron hopping between quantum dots, the hybrid superconducting segments mediate Cooper pair splitting processes, effectively implementing a p-wave pairing term between neighbouring quantum dots [25, 35]. Though the charging energy is still the largest energy scale in these devices [178], the effects of interactions are minimized by a finite Zeeman splitting on the dots, effectively suppressing interactions between different spin species. In this chapter, we combine these two research directions, and study a superconducting extension of the Fermi-Hubbard model using quantum dot arrays. To this end, we experimentally implement short chains of quantum dots coupled by superconducting hybrid segments, as used to implement Kitaev chains [28, 80, 178], but now in the absence of a magnetic field. In this regime, the effect of electron interactions on the quantum dots is restored. This effectively yields a one-dimensional Fermi-Hubbard model with an additional nearest-neighbour, spatially-odd pairing term [121]. This model was recently shown theoretically to feature peculiar ground state degeneracies due to the interplay between strong interactions and superconducting pairing. In particular, a two-site system was predicted to exhibit three-fold degenerate spectrum due to correlations [121], linked to the emergence of strong zero modes [94, 112] protected by a $\mathbb{Z}_3$-parity operator.

We implement devices with effectively two and three interacting sites on InSbAs 2DEGs with epitaxial aluminium and study their low energy spectra through conductance measurements. Our experiments reproduce the main results of the theoretical predictions in Ref. [121]: a stable ground state degeneracy is observed in the two-site chains, which is lifted when extending to three sites. Additionally, we find in both theory and experiment that introducing a superconducting phase difference between the hybrid QDs allows to tune also a three-site system to a strongly degenerate configuration. The striking agreement between experiment and theory suggests that the quantum dot platform is well suited to explore the interplay between strong correlations and superconductivity in extended Fermi-Hubbard type models.

7.2 The spinful QD chain model

A chain of QDs coupled via superconductors can be described by a Fermi-Hubbard Hamiltonian with an additional nearest-neighbour superconducting term:

$$H = H_{\mathrm{D}} + H_{\mathrm{U}} + H_{\mathrm{ECT}} + H_{\mathrm{CAR}}. \tag{7.1}$$

Here, $H_{\mathrm{D}} = \sum_i \mu_i (n_{i,\uparrow} + n_{i,\downarrow})$ models the QDs chemical potential μ_i, while $H_{\mathrm{U}} = \sum_i U_i n_{i,\uparrow} n_{i,\downarrow}$ models the on-site Coulomb repulsion. The superconducting segment hosts gate-tunable Andreev bound states, that generate two virtual transport processes coupling the neighbouring QDs [25–27, 60, 155]. Elastic co-tunneling (ECT) facilitates hopping of an electron between two sites. We model this process as:

$$H_{\mathrm{ECT}} = \sum_i t^{(i,i+1)} (c^\dagger_{i,\uparrow} c_{i+1,\uparrow} + c^\dagger_{i,\downarrow} c_{i+1,\downarrow}) + h.c. \tag{7.2}$$

between sites i and j.
Crossed Andreev reflection (CAR) facilitates a pairing interaction via the creation or breaking of Cooper pairs in a superconductor, modelled by:

$$H_{\mathrm{CAR}} = \sum_i \Delta^{(i,i+1)} (c^\dagger_{i,\uparrow} c^\dagger_{i+1,\downarrow} - c^\dagger_{i,\downarrow} c^\dagger_{i+1,\uparrow}) + h.c. \tag{7.3}$$

Notably, due to only including nearest-neighbour couplings, spin-orbit interactions can be gauged away (see section 7.6) and hence we only include spin-preserving processes.

In the devices of interest, typical interdot couplings are on the order of 20 µV, while typical charging energies are on the order of 1-2 mV, such that Coulomb repulsion is the largest energy scale in the system (figure 7.6). We therefore restrict ourselves to the $U = \infty$ limit to compare experiments and theory in the main text. To capture this, we project out the double occupancy restricting us to an effective basis $\{|0\rangle, |\uparrow\rangle, |\downarrow\rangle\}$ on each dot. A summary of more extensive modelling that includes the nearest neighbour processes can be found in section 7.6. For two QD sites, Refs. [123, 223] have shown that the system features a 'sweet spot' at $\mu_1 = \mu_2 = 0$ and $t^{(1,2)} = \sqrt{2}\Delta^{(1,2)}$. Here, the ground state of the system is threefold degenerate and hosts Majorana Kramers pairs [121], which are stable against detuning of individual QDs. Below, we start by characterising such 'sweet spots' in a two QD system experimentally and study the evolution of the low-energy spectrum when adding a third QD.

7.3 Device and experimental setup

The device used to obtain the results in the main text is shown in figure 7.1b, containing three quantum dots and two superconducting regions. The two SC strips (green) are connected in a continuous loop and kept grounded. An external magnetic field B_z controls the superconducting phase difference between the strips. Andreev bound states (ABSs) are induced in the regions proximitized by the SCs (figure 7.6). The energies of the ABSs in the left and right hybrid sections are controlled by the voltages denoted $V^{(1)}_{\mathrm{ABS}}$ and $V^{(2)}_{\mathrm{ABS}}$. Three large gates (red) are used to confine a quasi-1D channel.

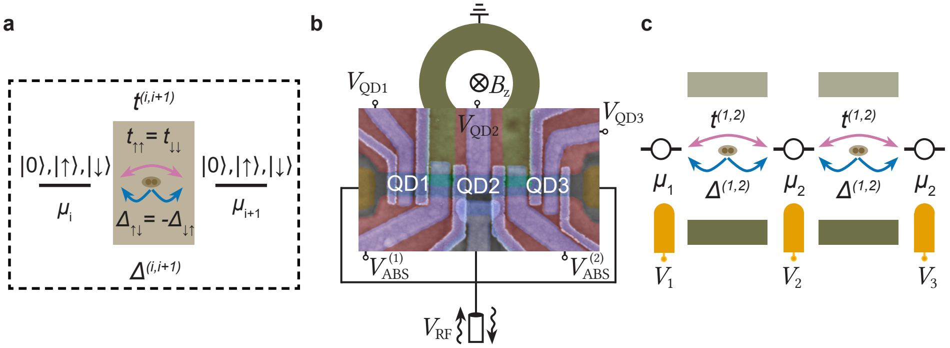
a
b
c
$t^{(i,i+1)}$
$t_{\uparrow\uparrow} = t_{\downarrow\downarrow}$
$|0\rangle, |\uparrow\rangle, |\downarrow\rangle$
μ_i
$\Delta_{\uparrow\downarrow} = -\Delta_{\downarrow\uparrow}$
$|0\rangle, |\uparrow\rangle, |\downarrow\rangle$
μ_{i+1}
$\Delta^{(i,i+1)}$
V_{QD1}
$\otimes B_z$
V_{QD2}
V_{QD3}
QD1
QD2
QD3
$V_{ABS}^{(1)}$
$V_{ABS}^{(2)}$
V_{RF}
$t^{(1,2)}$
$t^{(1,2)}$
μ_1
$\Delta^{(1,2)}$
μ_2
$\Delta^{(1,2)}$
μ_2
V_1
V_2
V_3

Figure 7.1: **Model and device schematics (a)** Schematic of the nearest-neighbour interactions for two spinful fermionic sites coupled via a superconductor. We assume equal tunneling rates for spin-up and spin-down such that $t^{(i,j)} = t^{(i,j)}_{\downarrow\downarrow} = t^{(i,j)}_{\uparrow\uparrow}$ and $\Delta^{(i,j)} = \Delta^{(i,j)}_{\uparrow\downarrow} = -\Delta^{(i,j)}_{\downarrow\uparrow}$, where the sign is due to time reversal symmetry. To implement the $U = \infty$ limit, the double occupied state is disallowed. **(b)** False colour scanning electron micrograph of a copy of device A. Two aluminium strips are connected via a continuous loop with a radius of 10 µm (not drawn to scale). Scale bar is 500 nm. **(c)** Schematic representation of the three site device, highlighting the parameters relevant for the theoretical simulations.

Narrow finger gates (blue), separated by a dielectric layer, are used to confine three QDs and control their electrochemical potentials (V_{QDi}). Each QD can be probed by an ohmic lead, which enable recording the device conductance in two separate ways. Applied voltages (V_1, V_2 and V_3) and measured currents (I_1, I_2 and I_3) are used to measure the local differential conductance in each lead ($G_{ii} = \frac{dI_i}{dV_i}$). In addition, each lead is connected to an off-chip resonator, which allows for measuring the RF-reflectometry response, denoted $\tilde{S}_{\mathrm{i}}$ (for details, see section 7.6 and figure 7.7). This signal is linearly proportional to the device conductance in the regime of interest [144, 224, 225], explicitly shown in Ref. [139] for this device.

7.4 Results

7.4.1 The two-site sweet spot at zero field

After forming three QDs through electrostatic tuning of the finger gates, we focus first on the coupling between QD1 and QD2, keeping QD3 away from Coulomb resonance. The key to generating stable zero-energy modes in this two-QD system, widely studied at finite magnetic fields [28, 33, 35, 80, 178], is that the simultaneous presence of ECT and CAR creates a competition between different parity ground-states. ECT couples states with the same total particle number, whereas CAR couples states whose particle number differs by two. Notably, this competition can be present also without an external magnetic field [120]. To observe this, we study charge stability diagrams (CSDs) across a single orbital in each QD through lead reflectometry. When ECT dominates, diagonal avoided crossings are expected, as shown in an exemplary measurement in figure 7.2a. Control over $V_{\mathrm{ABS}}^{(1)}$ affects the underlying CAR and ECT processes, which can drastically change the CSD. Changing $V_{\mathrm{ABS}}^{(1)}$ by $\approx 50\,\mathrm{mV}$, the connectivity in the entire CSD changes, showing now only antidiagonal avoided crossings (figure 7.2b), indicating CAR has become the dominant process. This continuous control over the connectivity ensures that, for each pair of resonances, a ‘sweet-spot’ exists where the avoided crossing disappears. There, zero-energy modes are expected to arise that are resilient against detuning individual QDs (local perturbations) and protected to at least second-order against joint detuning of all QDs (global perturbations, cf. [121]). Zooming in on the bottom-left pair of transitions and fine-tuning $V_{\mathrm{ABS}}^{(1)}$, we find such a ‘sweet spot’ at $V_{\mathrm{ABS}}^{(1)} = -180.3\,\mathrm{mV}$ (figure 7.2c).

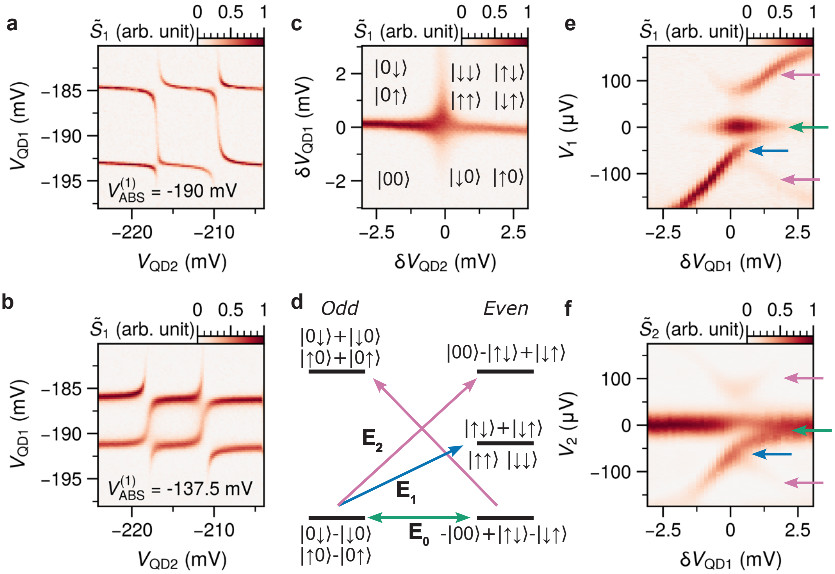

Figure 7.2: **The two-site sweet spot.** Tuning the coupling between QD1 and QD2, with QD3 tuned to a Coulomb blockaded regime. **(a)** Exemplar CSD in an ECT dominated regime ($V_{\mathrm{ABS}}^{(1)} = -190\,\mathrm{mV}$), showing four anti-diagonal avoided crossings. **(b)** Exemplar CSD in a CAR dominated regime ($V_{\mathrm{ABS}}^{(1)} = -137.5\,\mathrm{mV}$), showing four diagonal avoided crossings. Examples were chosen to showcase the change in connectivity can arise in all 4 quadrants of the CSDs. More general CSDs are shown in figure 7.8. **(c)** Close up CSD of the bottom left quadrant, at an intermediate value of $V_{\mathrm{ABS}}^{(1)} = -180.3\,\mathrm{mV}$. **(d)** Energy level diagram for the two parity sectors at the sweet spot (detailed in the main text). Coherence factors have been omitted for brevity. **(e)** Tunnelling spectroscopy measured when detuning V_{QD1}, with V_{QD2} set on resonance. Coloured arrows correspond to transitions indicated in (d). Reproduction of results in a separate device is shown in figure 7.10-figure 7.12.

To understand the density of states, we highlight an energy level diagram of the effective model at the sweet spot ($t^{(1,2)} = \sqrt{2}\Delta^{(1,2)}$, $\mu_{\mathrm{i}} = 0$) in figure 7.2d, following Ref. [121]. The spectrum is strongly degenerate, i.e. all energy manifolds feature a three-fold degeneracy. This structure results in single-electron transitions from the ground-states at three possible energies, labelled by the coloured arrows. We measure these transitions experimentally through lead-reflectometry of lead 1 and lead 2 and sweep V_{QD1}. The three expected transitions can be clearly identified (figure 7.2e). Most trivially, we observe excitations symmetrically around zero energy which disperse with V_{QD1}, denoted as E_2 (pink). Secondly, we see stable zero-bias conductance peaks (green) reflecting the zero-energy excitations (E_0) between the degenerate even and odd ground-states. These excitations can be understood as arising from Kramers pairs of Majorana modes, as detailed in [121]. It is important to note that they are not expected to be localized on either of the QDs, but are nevertheless robust against perturbing the chemical potential of a single QD (see also figure 7.9). Lastly, we find a transition appearing only at negative bias (blue). This transition, denoted E_1, is a signature of the presence of the triplet states in the even parity subspace [120], breaking particle hole symmetry in the conductance spectrum. Notably, this appears to be the only feature that distinguishes this system from the two-site system at finite magnetic field [28, 80, 178]. The particle or hole-like nature of the feature depends on the charge configuration of the QDs, which we demonstrate in figure 7.12. We note that an interesting phenomenon related to the triplet states, negative local differential conductance [120], is not observed in these measurements, but has been found to appear in a similar configuration, further explored in appendix C. The presence of the triplet states is expected to be a detrimental factor when scaling the system beyond two sites [121], which we study below.

7.4.2 Naive scaling from two to three sites

At finite magnetic fields, the conditions that give rise to stable zero modes in the two-site chain can be extended to obtain stable zero modes in longer chains [37]. By satisfying the 'sweet spot' condition between all pairs of neighbouring QDs and setting all QDs on resonance, stable ZBPs were expected on the outermost sites [200, 226], which was recently demonstrated experimentally in three-site systems [34, 187]. As shown in [227], this is not necessarily true for strong zero modes however: the additional states added to the Hilbert space can introduce couplings which split the required strong degeneracy of the levels. In [121], a crucial part for the strong degeneracy was that triplet states in the excited manifold exactly decouple from the rest of the spectrum. This breaks down when naively turning on the coupling to the third site despite tuning t, Δ to the same values. To demonstrate this, we first repeat the procedure demonstrated in figure 7.2 for QD2 and QD3, with QD1 off resonance, to obtain a $t^{(2,3)} = \sqrt{2}\Delta^{(2,3)}$ sweet spot for the right QD pair (figure 7.9). With either of the outer QDs off-resonance, the remaining two QDs thus host a pair of ZBPs. Next, we bring all three QDs on resonance and perform finite-bias spectroscopy measurements. Figure 7.3a shows RF-spectroscopy measurements of $\tilde{S}_1$ and $\tilde{S}_3$, when detuning V_{QD3}. We observe that the ZBPs split in energy as soon as δV_{QD3} approaches resonance. This is in stark contrast to the two-site systems in isolation, which are resilient against local perturbations (figure 7.2), as well as to the behaviour observed for three-site systems at finite magnetic fields [34, 187]. We find the behaviour closely matches the numerical simulations in figure 7.3b. The characteristic diamond shape of the splitting is reminiscent of the behaviour expected when coupling a quantum dot to an overlapping pair of Majoranas [87, 88, 90]. In that context, this measurements highlights the expected non-locality of the Majorana Kramers pairs in this system: even at the sweet-spot for two-sites, the zero-energy modes are not localized on either QD. We illustrate this interpretation in Figs. 3c,d: what were two delocalized but isolated Majorana Kramers pairs in the two-site system (c) begin hybridizing through processes involving the previously uncoupled triplet states (d).

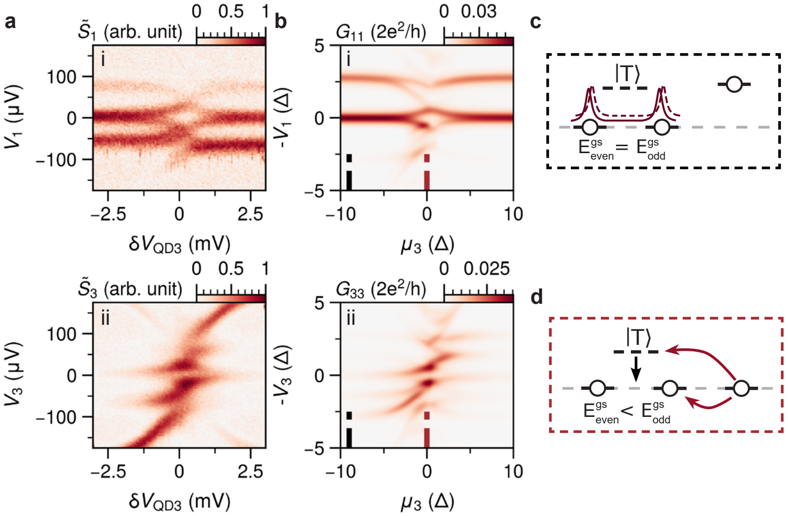

Figure 7.3: **Scaling from two to three sites.** Measurements obtained with both pairs of QDs individually tuned to a sweet spot configuration. **(a)** Spectroscopy of the left (S_1) and right (S_3) while sweeping V_{QD3}. Once QD3 is on resonance, the ZBP on both sides is observed to split. **(b)** Numerically calculated conductance with (settings), showing similar behaviour. To understand this, we consider schematically the situation when QD3 is **(c)** off and **(d)** on resonance. When QD3 is off resonance, the triplet subspace is uncoupled from the rest of the system and a pair of spatially overlapping Majorana Kramers pairs is present on both QDs. Adding the third QD couples to both zero energy modes and allows the triplet states to participate, favouring the even ground-state in energy (see Ref. [121] for further details).

7.4.3 SUPERCONDUCTING PHASE CONTROL

We turn our attention to the final tunable parameter: the phase difference between the superconductors. In a two-site system, this phase difference can be gauged away and therefore does not affect the energy spectra. This is no longer the case when a third site is added [37, 112, 228, 229]. Instead, the phase breaks time reversal and inversion symmetry. Sweeping the phase, it has been predicted to allow to rediscover the strong zero modes [112], albeit with reduced stability [227]. We look for ground-state degeneracies by measuring zero-bias conductance in the parameter space around the $V^{(1)}_{\mathrm{ABS}}$ and $V^{(2)}_{\mathrm{ABS}}$ values that corresponded to two-site sweet-spots. Sweeping all three QDs around their charge degeneracy points simultaneously and varying both $V^{(1)}_{\mathrm{ABS}}$ and $V^{(2)}_{\mathrm{ABS}}$, we map out the conditions that give rise to zero-bias conductance when $\phi = 0$, shown in figure 7.4a. The 'x' marks the point in parameter space where ZBPs originally arose in the isolated two-site systems (figure 7.2). In accordance with figure 7.3, there is now no zero-bias conductance at this point in the three-site system. We compare the measurement to calculated conductance from the effective model, when all μ_{i} are varied simultaneously versus $t^{(1,2)} = t^{(2,3)}$, for fixed $\Delta^{(1,2)} = \Delta^{(2,3)}$ (figure 7.4b). Next, we apply a small out-of-plane field B_z through the superconducting loop corresponding to a π-phase and repeat the measurement, shown in figure 7.4c. Interestingly, this results in a mirrored pattern that again matches well with the theory (figure 7.4d). While at π-phase we still do not yield a degeneracy at the two-site sweet spot parameters (marked by 'x'), the evolution from figure 7.4a implies this should

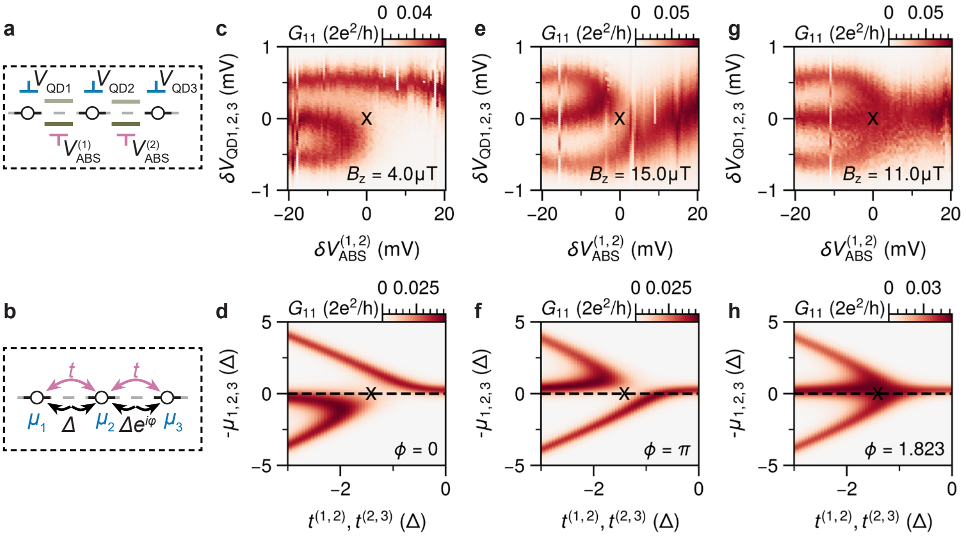

Figure 7.4: **Superconducting phase as tuning knob.** To understand where zero-energy modes arise in the full three-site system, a larger parameter space is explored (procedure detailed in figure 7.13). For each QD pair, sweet spot values are obtained, denoted as $\delta V_{\mathrm{ABS}}^{(\mathrm{i})} = 0$. Zero-bias conductance measurements are performed upon simultaneously varying δV_{QDi} versus sweeping $V_{\mathrm{ABS}}^{(\mathrm{i})}$ around their sweet-spots. **(a)** Measurement obtained for $B_z = 4\,\mu$T, corresponding roughly to $\phi = 0$. **(b)** We compare this to a numerical simulation, where all μ and all t parameters are swept together, for fixed Δ. **(c-f)** We repeat the measurements and simulations for $B_z = 15\,\mu$T (c), corresponding roughly to $\phi = \pi$ (d) and (e) $B_z = 11\,\mu$T corresponding to (f) $\phi = 1.86$.

be possible to achieve when fine-tuning the SC phase. By sweeping the phase for the degeneracy to cross $\mu_i = 0$ at $\delta V_{\mathrm{ABS}}^{(1,2)} = 0$, we arrive at the measurement shown in figure 7.4e. Theoretically, we find this corresponds to the exact phase of $\phi = \arccos(-1/4)$, shown in figure 7.4f (see section 7.6). At this angle, the system in fact exhibits a three-fold (strongly) degenerate spectrum at the point $\mu = 0$, $t = \sqrt{2}\Delta$. It should be noted that temperature broadening in the experiment results in zero-bias conductance in a larger region where theory predicts a single non-protected point in parameter space. Going further, we do find this point lies along a line in the $\phi - t$ parameter space, parametrized by:

$$t = \sqrt{-1/2\cos(\varphi)}\Delta \tag{7.4}$$

For each of these points the systems spectrum is strongly degenerate at $\mu = 0$. In the two site case studied in Ref. [121], this allowed decomposing the low energy subspace into Majorana Kramers pairs and $\mathbb{Z}_3$ parafermions.

7.4.4 Finetuned strong degeneracies

In figure 7.4 we have observed that tuning the superconducting phase difference yields configurations for which the degeneracy lines cross μ_i =0. When $t^{(i,j)} = \sqrt{2}\Delta^{(i,j)}$ = (the two-site sweet-spot), the phase at which this crossing occurs is $\pi = \arccos(-1/4)$, where the entire spectrum is found to be strongly degenerate. We find that by allowing $\Delta^{(i,j)} \neq t^{(i,j)}$,

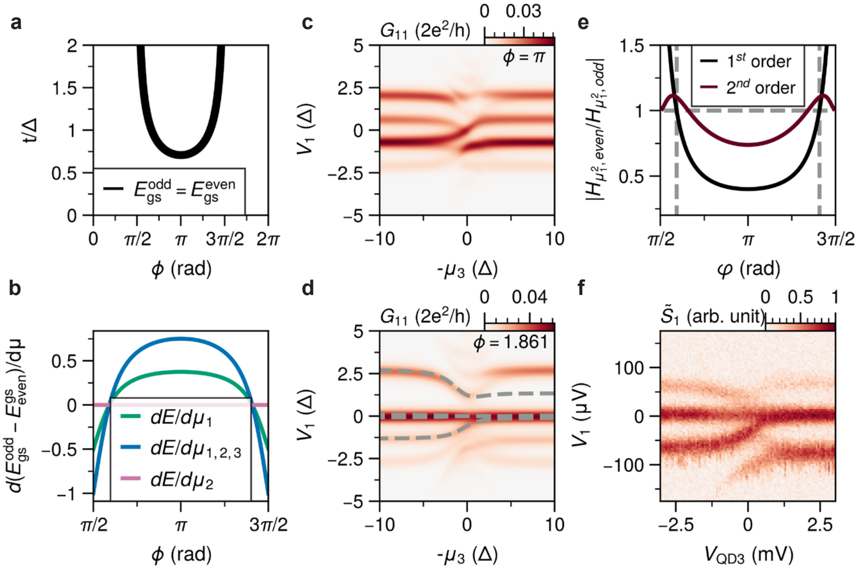

Figure 7.5: **Strongly degenerate ground states in the three-site chain.** **(a)** Analytical solution yielding $E_{\mathrm{gs}}^{\mathrm{odd}} = E_{\mathrm{gs}}^{\mathrm{even}}$ for the three-site chain when $\mu_i = 0$ (given by equation (7.5)), resulting in a strongly degenerate spectrum. **(b)** Derivative of the energy difference between the odd and even ground states with respect to detuning μ. The derivatives vanish at two specific points. The significance can be seen when comparing the conductance spectrum of detuning μ_3 at **(c)** $\phi = \pi$ and **(d)** $\phi = 1.861$. The numerical energy spectrum is overlaid in (d) to highlight that a small energy splitting still arises at larger detuning of μ_3. **(e)** Perturbative expansion of first order and second order derivatives, highlighting that the higher order derivative does not vanish at the same ϕ value as the first order. **(f)** Measurement of S_1 when detuning QDR, with the settings in figure 7.4c, in order to compare with the predicted spectrum (d). Repeated measurements for a range of B_{x} values is shown in figure 7.14.

there exists a whole line in parameter space for which the spectrum is strongly degenerate. Fixing $\mu_i = 0$ and calculating the spectrum analytically (see section 7.6), we find the condition for degeneracy to be:

$$t^{(i,j)} = \sqrt{-\frac{1}{2\cos(\varphi)}}\,\Delta^{(i,j)}, \tag{7.5}$$

where $\Delta^{(1,2)} = \Delta^{(2,3)}$ and $t^{(1,2)} = t^{(2,3)}$. Along this line (figure 7.5a), the Hamiltonian in Eq. (7.1) commutes with the total fermion parity operator $P_F = \prod_{i,\sigma}(1 - 2n_{i,\sigma})$, and a $\mathbb{Z}_3$-parity operator $P_3 = \exp\left[i\frac{2\pi}{3}\sum_i(n_{i,\uparrow} + 2n_{i,\downarrow})\right]$ [124]. The 27 levels contained in the low-energy subspace split into 7 distinct manifolds: 3 triply-degenerate levels with $E < 0$, 1 nine-fold degenerate manifold at $E = 0$, and another 3 triply-degenerate manifold with $E > 0$ (see section 7.6).

Ideally, a point can be found where the strongly degenerate spectrum again gives rise to Majorana Kramers Pairs or $\mathbb{Z}_3$ parafermions, as in [121]. To assess this, we numerically calculate the linear derivatives of the energy splitting between odd and even ground states with respect to the individual dot chemical potentials, $\partial_{\mu_i}(E_{\mathrm{even},0} - E_{\mathrm{odd},0})$ (figure 7.5b).

Doing so for all φ, we find that the ground state degeneracy is unaffected by changes of the chemical potential of the central dot, μ_2, in linear order. In contrast, the degeneracy splits linearly when varying the chemical potential of the outer dots, μ_1, μ_3, except for two points where the coupling in linear order of perturbation theory vanishes. Numerically these phases are found to be at $\varphi^* \in \{1.86, 4.42\}$ (cf. figure 7.5). To verify this, we numerically calculate a perturbative expansion for the ground state manifold when perturbed by any $\mu_i(n_{i\uparrow} + n_{i\downarrow})$[230], i.e. local perturbations to the chemical potential of one of the QDs. Since the perturbations neither break parity nor time-reversal symmetry, we can understand the system's response by considering the ratio $\delta E_{\text{even}}/\delta E_{\text{odd}}$ of the energy shifts $E_i \to E_i^{(0)} + \delta E_i$ induced within each parity sector. To linear order in μ_i, we indeed recover the spectral insensitivity to changes as $\delta E_{\text{even}}(\mu_i) = \delta E_{\text{odd}}(\mu_i)$ at φ_i^*. Expanding to second order in μ_i, we however find that the splitting at φ_i^* differs and therefore breaks the degeneracy (figure 7.5e). Consequently, we will not be able to find Majorana Kramers pairs or $\mathbb{Z}_3$ parafermions that are robust against local perturbations as previously for two sites [121]. We note that this is in line with previous conclusions for strong degeneracies in chiral spin chains [112]. To conclude, we consider the conductance signatures at two points along the triply degenerate line (figure 7.5c,d). While the perturbative results suggest a splitting of the levels with the chemical potential, we find in conductance that this splitting can become very small and not possible to resolve due to broadening from temperature effects. Experimentally, we indeed observe that a phase value can be found where a seemingly robust zero-bias conductance peak appears (figure 7.5f). We want to highlight that this behaviour is not to be generally expected, but only along this fine-tuned line of parameters.

7.5 SUMMARY

In this chapter we have studied a superconducting extension of the Fermi-Hubbard model in short arrays of semiconductor-superconductor hybrid quantum dot arrays. In the absence of spin-polarizing magnetic fields, the on-site Coulomb repulsion is the largest energy scale of the system. Tuning the normal and superconducting couplings allows to deliberately tune the system to host degenerate spectra. For both two and three electronic sites we explored the signatures of such degeneracies. In the case of two sites, we found close agreement with the predictions put forward in Ref. [121], suggesting robust Majorana Kramers pairs [123, 223] or $\mathbb{Z}_3$ parafermions at specific parameter configurations. We identify these configurations by experimentally finding robust zero-bias peaks. Notably, such excitations can have applications in topological quantum computing [91–94], but were typically so far only predicted for physical platforms that are more difficult to realise [98–106]. Whether this platform, hosting non-local Kramers pairs, has potential use in this context remains subject of further research. Upon extending the system to three sites, we do find signatures of degeneracies by sweeping the system's larger parameter space. A theoretical analysis shows these to be consistent with strongly degenerate spectra along fine-tuned configurations of the system. In contrast to the two-site system, these degeneracies are however not robust but predicted to split quadratically. This we interpret as being consistent with previous predictions that strong degeneracies in quasi one-dimensional systems are generally not robust against perturbations [94, 227]. Based on the observations, we believe hybrid superconductor - quantum dot systems can allow for analysis of the stability of strong degeneracies through quantum simulation for systems beyond computational feasibility. Furthermore, extending the system to two dimensions, we foresee the platform to be useful in understanding strongly correlated phenomena when subjected to superconducting correlations.

DATA AVAILABILITY

All raw data obtained in relation to this chapter, the code to generate the theoretical results and the scripts to reproduce the figures from the raw data are available on Zenodo [231].

7.6 METHODS

FABRICATION AND YIELD

The presented devices are fabricated on InSbAS with 7 nm epitaxial aluminium, described in detail in [129]. An in-depth account of the fabrication of these specific devices can be found in [127] and [128]. Starting with an InSbAs chip fully covered with aluminium, a Transene D wet etch is used to create the fine structures, followed by the deposition of ohmic Ti/Pd contacts. Next, we deposit 20 nm AlOx via 40 °C atomic layer deposition (ALD). To confine a quasi one dimensional channel, large Ti/Pd depletion gates are evaporated. Device B consists of two depletion gates (one top and one bottom), whereas device A utilises three depletion gate (one top and two bottom). The extra bottom depletion gate simplifies utilising the additional middle ohmic contact and gives independent control over forming the left and right sides of the channel. The channel widths were designed to be ≈200 nm. Following a second ALD layer (20 nm AlOx), we deposit a layer of Ti/Pd finger gates used to control the electrochemical potential energies of the QDs and the hybrid regions. Lastly, a third ALD layer (20 nm AlOx) is deposited, followed by the final Ti/Pd tunnelling gates used to define the quantum dots. Superconducting LC-resonator circuits were fabricated on a separate chip with a silicon substrate, by etching NbTiN. To apply DC voltages, bias tees are created by depositing 20 nm Cr structures with resistances of ≈ 5 kΩ. Further details on the resonator circuits and techniques can be found in [127].

DC TRANSPORT AND RF-REFLECTOMETRY MEASUREMENTS

To efficiently explore the large parameter space of device A, we employed radio frequency (RF) lead reflectometry [145] in addition to DC conductance measurements. To do so, we connect each ohmic contact to an inductor via a bond wire. The inductors are designed with inductances $L_{1,2,3} = 0.2, 0.5, 1.5$ μH, that together with a parasitic capacitance to ground via bond-wires result in resonators with frequencies of $f_{1,2,3} = 723, 505, 248$ MHz. To utilise the fast integration times offered by the resonator circuit, arbitrary waveform generators (AWGs) are used to vary voltages on either the QD plunger gates or to apply a bias on the ohmic contacts using sawtooth pulses with frequencies on the order of 10-50 Hz. A complete overview of the circuit diagram, fridge wirings and filters can be found in [127, 139]. Using a cryogenic directional coupler, we obtain simultaneously the reflected signal of each resonator through multiplexing [208]. For each resonator, both the amplitude and phase response are recorded. We convert this to a single normalized value for each lead (denoted $\tilde{S}_1$, $\tilde{S}_2$ and $\tilde{S}_3$), which corresponds roughly linearly to the conductance through each lead [144, 224, 225]. The data processing procedure is shown in figure 7.7.

Device B was not connected to a resonator chip and only measured using DC and AC transport techniques. The same techniques were applied to device A, with connections routed via 5 kΩ Cr structures, to isolate the DC lines from the RF-circuit. In both devices, the aluminium strips are kept electrically grounded. Each lead is connected to a current meter, which is biased with a digital-to-analogue converter, connected such that both DC and AC voltages can be applied. The offsets of the applied voltage-biases on each lead are corrected via independently measuring the Coulomb peaks in the QDs and looking at the change in sign of the current as a function of applied voltage. The voltage outputs of the current meters are each recorded with both a digital multimeter and a lock-in amplifier. When applying a DC/AC voltage to one lead, all other leads are kept grounded. The AC excitations are applied with frequencies around 20 Hz and an amplitude of 5 µV RMS. Full conductance matrices $G_{ij} = \frac{dI_i}{dV_j}$ are obtained by measuring the response of each I_i to each V_i. Typically, voltage-divider effects arise when applying biases in a multi-terminal set-up. In these measurements we focus on low tunneling regimes ($\mathrm{G} \ll 2\mathrm{e}^2/\mathrm{h}$), such that the device resistance is significant compared to the resistance of other connections to ground and hence we do not correct these multi-terminal effects (expected to be on the order of X). When measuring in RF, conductance measurements are first obtained to confirm whether we were indeed in the low-tunneling regime.

For the measurements in device A, the field perpendicular to the superconducting loop (B_z) is generated using a high-resolution current source, providing a B_z resolution below 0.1 µT. A small (but significant) hysteresis on the order of 5 µT is observed when sweeping B_z in opposite directions. This is counteracted by setting B_z first to −100 µT and then sweeping this field back in the positive direction, such that consecutive experiments where B_z is varied are consistent.

Analytic spectrum along triply degenerate line

In the limit $U \to \infty$ the Hilbert space is restricted to states only containing at most single occupation per site. For $\mu_{i,\sigma} = 0$ this restricted low energy spectrum can be calculated analytically which we will do in the remainder of this section. With the doubly occupied states unavailable, the size of the Hilbert space reduces from 64 down to 27- 13 even and 14 odd states. As outlined in the main text, the Hamiltonian also commutes with the fermion parity operator $[H, P_F] = 0$. Hence, we can separate the Hilbert space into an odd and even fermion parity sector and solve them independently of each other.

Even parity sector

In the even parity sector we find that the Hamiltonian can be split into three blocks. Beginning with the spin mixing block we find:

$$H^{(1)}_{even} = \begin{pmatrix} 0 & \Delta_1 e^{-i\varphi_1} & 0 & \Delta_0 & -\Delta_1 e^{-i\varphi_1} & 0 & -\Delta_0 \\ \Delta_1 e^{i\varphi_1} & 0 & t_0 & 0 & 0 & 0 & 0 \\ 0 & t_0 & 0 & t_1 & 0 & 0 & 0 \\ \Delta_0 & 0 & t_1 & 0 & 0 & 0 & 0 \\ -\Delta_1 e^{i\varphi_1} & 0 & 0 & 0 & 0 & t_0 & 0 \\ 0 & 0 & 0 & 0 & t_0 & 0 & t_1 \\ -\Delta_0 & 0 & 0 & 0 & 0 & t_1 & 0 \end{pmatrix}, \tag{7.6}$$

spanned by the states $\{|000\rangle, |0\uparrow\downarrow\rangle, |\uparrow 0\downarrow\rangle, |\uparrow\downarrow 0\rangle, |0\downarrow\uparrow\rangle, |\downarrow 0\uparrow\rangle, |\downarrow\uparrow 0\rangle\}$. Solving the seventh order characteristic polynomial equation reveals first of all:

$$E^{(1)}_{\text{even},1} = 0. \tag{7.7}$$

Due to time-reversal symmetry, the remainder of the subblock spectrum is twofold degenerate. We find:

$$\begin{aligned} E^{(1)}_{\text{even},2(3)} &= \pm\sqrt{t_0^2 + t_1^2}, \\ E^{(1)}_{\text{even},4(5)} &= \pm(\Delta_0^2 + \Delta_1^2 + \frac{t_0^2 + t_1^2}{2} \\ &\quad + [(\Delta_0^2 + \Delta_1^2)^2 + \frac{(t_0^2 + t_1^2)^2}{4} + (\Delta_0^2 - \Delta_1^2)(t_1^2 - t_0^2) + 4\Delta_0\Delta_1 t_0 t_1 \cos(\varphi)]^{\frac{1}{2}})^{\frac{1}{2}} \\ E^{(1)}_{\text{even},6(7)} &= \pm(\Delta_0^2 + \Delta_1^2 + \frac{t_0^2 + t_1^2}{2} \\ &\quad - [(\Delta_0^2 + \Delta_1^2)^2 + \frac{(t_0^2 + t_1^2)^2}{4} + (\Delta_0^2 - \Delta_1^2)(t_1^2 - t_0^2) + 4\Delta_0\Delta_1 t_0 t_1 \cos(\varphi)]^{\frac{1}{2}})^{\frac{1}{2}} \end{aligned} \tag{7.8}$$

Furthermore, we have:

$$H^{(2)}_{\text{even}} = \begin{pmatrix} 0 & t_0 & 0 \\ t_0 & 0 & t_1 \\ 0 & t_1 & 0 \end{pmatrix}, \tag{7.9}$$

spanned by $\{|0\downarrow\downarrow\rangle, |\downarrow 0\downarrow\rangle, |\downarrow\downarrow 0\rangle\}$, and finally:

$$H^{(3)}_{even} = \begin{pmatrix} 0 & t_0 & 0 \\ t_0 & 0 & t_1 \\ 0 & t_1 & 0 \end{pmatrix} \tag{7.10}$$

in the basis $\{|0\uparrow\uparrow\rangle, |\uparrow 0\uparrow\rangle, |\uparrow\uparrow 0\rangle\}$. Note that $H^{(2)}_{\text{even}}$ and $H^{(3)}_{\text{even}}$ are the same and related by time-reversal symmetry. Consequently, the eigenvalues are the same for each block reading

$$\begin{aligned} E^{(2,3)}_{\text{even},1} &= 0, \\ E^{(2,3)}_{\text{even},2} &= \sqrt{t_0^2 + t_1^2}, \\ E^{(2,3)}_{\text{even},3} &= -\sqrt{t_0^2 + t_1^2}. \end{aligned} \tag{7.11}$$

ODD PARITY SECTOR

In the odd parity sector, the Hamiltonian can similarly be split into three subblocks which can be solved separately. Due to time reversal symmetry, the whole spectrum of the odd parity sector will be two-fold degenerate. The first subblock reading:

$$H^{(1)}_{\text{odd}} = \begin{pmatrix} 0 & \Delta_0 & 0 & 0 & 0 & 0 \\ \Delta_0 & 0 & t_1 & -\Delta_0 & 0 & 0 \\ 0 & t_1 & 0 & 0 & t_0 & 0 \\ 0 & -\Delta_0 & 0 & 0 & \Delta_1 e^{i\varphi_1} & 0 \\ 0 & 0 & t_0 & \Delta_1 e^{-i\varphi_1} & 0 & -\Delta_1 e^{-i\varphi_1} \\ 0 & 0 & 0 & 0 & -\Delta_1 e^{i\varphi_1} & 0 \end{pmatrix}, \tag{7.12}$$

in the basis $\{|\uparrow\downarrow\downarrow\rangle, |00\downarrow\rangle, |0\downarrow 0\rangle, |\downarrow 00\rangle, |\downarrow\uparrow\downarrow\rangle, |\downarrow\downarrow\uparrow\rangle\}$. This yields eigenenergies:

$$\begin{aligned} E^{(1)}_{\text{odd},1} &= 0 \\ E^{(1)}_{\text{odd},2} &= 0 \\ E^{(1)}_{\text{odd},3(4)} &= \pm(\Delta_0^2 + \Delta_1^2 + \frac{t_0^2 + t_1^2}{2} \\ &\quad + [(\Delta_0^2 + \Delta_1^2)^2 + \frac{(t_0^2 + t_1^2)^2}{4} + (\Delta_0^2 - \Delta_1^2)(t_1^2 - t_0^2) - 2\Delta_0\Delta_1 t_0 t_1 \cos(\varphi) - 3\Delta_0\Delta_1]^{\frac{1}{2}})^{\frac{1}{2}} \\ E^{(1)}_{\text{odd},5(6)} &= \pm(\Delta_0^2 + \Delta_1^2 + \frac{t_0^2 + t_1^2}{2} \\ &\quad - [(\Delta_0^2 + \Delta_1^2)^2 + \frac{(t_0^2 + t_1^2)^2}{4} + (\Delta_0^2 - \Delta_1^2)(t_1^2 - t_0^2) - 2\Delta_0\Delta_1 t_0 t_1 \cos(\varphi) - 3\Delta_0\Delta_1]^{\frac{1}{2}})^{\frac{1}{2}} \end{aligned} \tag{7.13}$$

The time reversal symmetric block, written in the basis $\{|\downarrow\uparrow\uparrow\rangle, |00\uparrow\rangle, |0\uparrow 0\rangle, |\uparrow 00\rangle, |\uparrow\downarrow\uparrow\rangle, |\uparrow\uparrow\downarrow\rangle$ has the same form as eq. (7.12). Consequently, the eigenvalues are the same as for the first block. The third and final block written in the basis $\{|\uparrow\uparrow\uparrow\rangle, |\downarrow\downarrow\downarrow\rangle\}$ is diagonal and features two eigenvalues:

$$\begin{aligned} E^{(3)}_{\text{odd},1} &= 0 \\ E^{(3)}_{\text{odd},2} &= 0 \end{aligned} \tag{7.14}$$

ANALYTIC DEGENERACY CONDITION

Finally, we are interested in the condition yielding degeneracy of the groundstates. To achieve this, we solve:

$$E^{(1)}_{\text{odd},6} = E^{(1)}_{even,5} \tag{7.15}$$

to find a relation between t_i, Δ_i. Reducing the equations, this leads to the degeneracy condition:

$$\Delta_0\Delta_1 = -2t_0 t_1 \cos(\varphi), \tag{7.16}$$

which corresponds to eq. (7.5) given in the main text for $\Delta_0 = \Delta_1$ and $t_0 = t_1$. Plugging eq. (7.16) back into the previously calculated eigenvalues, we find that the spectrum becomes at least triply degenerate for each manifold.

7.7 EXTENDED DATA

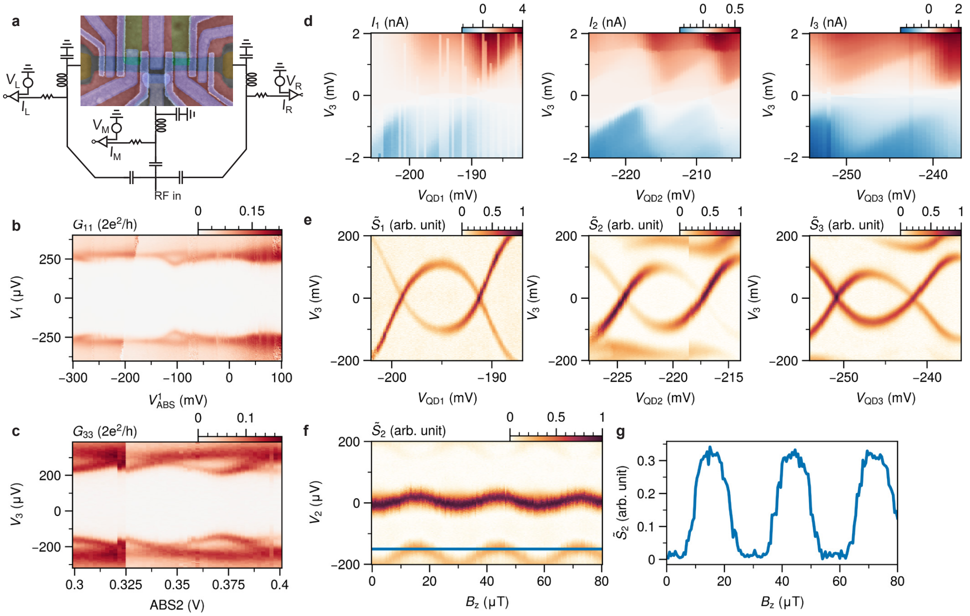

Figure 7.6: **Characterisation device A (a)** SEM of a copy of device A, used to obtain the results presented in the main text. The RF and DC circuit components are included. As first characterisation, the induced superconductivity in the hybrid sections is investigated by activating only the tunneling gates next to each aluminium strip. We then obtain finite-bias spectroscopy of **(b)** the left hybrid segment while sweeping $V^{(1)}_{\mathrm{ABS}}$ and **(c)** the right hybrid segment while sweeping $V^{(2)}_{\mathrm{ABS}}$. In both sides, an induced superconducting gap around 250 μV is observed. **(d)** Next, all tunneling gates are activated to define three QDs. To allow for strong interactions between them, the tunneling barriers between each QD and their neighbouring hybrid segments are kept relatively open. In this regime, no fully Coulomb-blockaded diamonds are observed in the currents measured in (d), obtained with the QD settings used for measurements obtained in the main text . Nevertheless, one can roughly estimate the charging energies in each QD to be on the order of 1.5 mV. **(e)** Lower-bias spectroscopy in the same range as the measurements in (d), showing sub-gap states with an eye-shaped dispersion as a function of the QD plunger gates, typical for proximitized QDs. **(f)** The proximity to two SC leads additionally results in the middle QD's spectrum becoming sensitive to the flux threaded through the SC loop. This effect is corrected in the measurements where the phase is varied. **(g)** Additionally, the oscillations allows for estimating the SC period to be 28 μT, which we use to map B_z to ϕ.

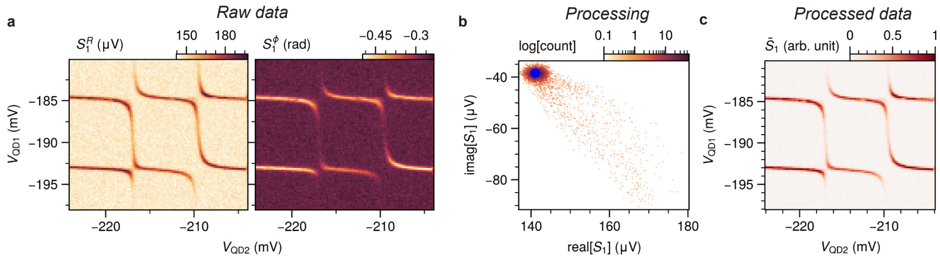

Figure 7.7: **Example of RF-signal processing.** In lead-reflectometry measurements, both the amplitude (S_i^R) and phase S_i^ϕ of the reflected signals is recorded (e.g. $S_1 = S_1^R e^{iS_1^\phi}$). We convert this to a single value to display in the main text, visualised here. **(a)** Raw data corresponding to the measurement shown in figure 7.2a. Both the amplitude response (left) and the phase response (right) are recorded. **(b)** Visualisation of the data processing. First, the complex values S_1 are collected in a 2-d histogram on the complex plane. The value corresponding to Coulomb blockade will show up in this plane as the point with the highest count, indicated here with the blue mark. Consequently we convert each point to the processed data-points $\tilde{S}_1$, defined as the distance of each point to Coulomb blockade. An example for a single data-point is highlighted with the arrow. **(c)** Processed data of (a), identical to the measurement shown in figure 7.2a.

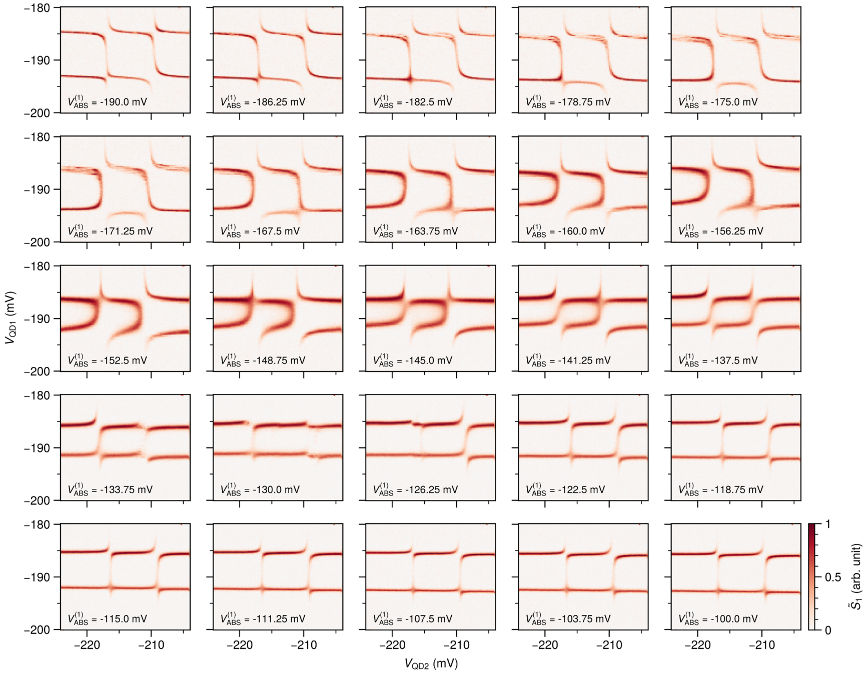

Figure 7.8: **CSDs in extended range for device A.** Figure 7.2 highlights two examples of CSDs obtained for the three-site device, sweeping QD1 and QD2 when QD3 is kept off resonance. Here an extended range is shown, for CSDs obtained for 25 values of $V_{\mathrm{ABS}}^{(1)}$ in the range −190 mV to −100 mV. In particular, these measurements highlight how each quadrant transitions from an ECT dominated to a CAR dominated avoided crossing, indicating that a sweet spot can be reached for each charge configuration in this range.

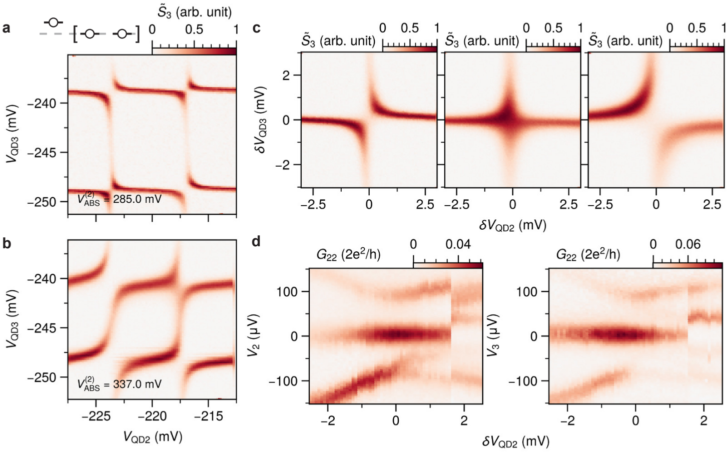

Figure 7.9: **Characterisation of right PMM pair in device A.** In the main text, the left and middle QDs are used to demonstrate a sweet spot in the effective two-site chain. To perform the measurements in Figs. 3-5, the pair formed by the middle and right QD must similarly be at a two-site sweet spot. To find this, the same tuning procedure is used as for the left pair in figure 7.2. **(a)** CSDs obtained with the left QD tuned off resonance, at $V_{\mathrm{ABS}}^{(2)} = 285\,\mathrm{mV}$, showing an ECT dominated avoided crossing in each quadrant. **(b)** CSDs obtained at $V_{\mathrm{ABS}}^{(2)} = 337\,\mathrm{mV}$, now showing CAR dominated avoided crossings. The transition shows that a sweet spot can also be found for each quadrant in this right QD. **(c)** Close-ups of the bottom left quadrant, fine-tuning the ABS **(d)** Finite-bias spectroscopy at the sweet-spot in (c), while sweeping V_{QD2} along the highlighted path. The triplet feature distinguishing these measurements from the high-field case is again (faintly) visibly, indicated by the arrows.

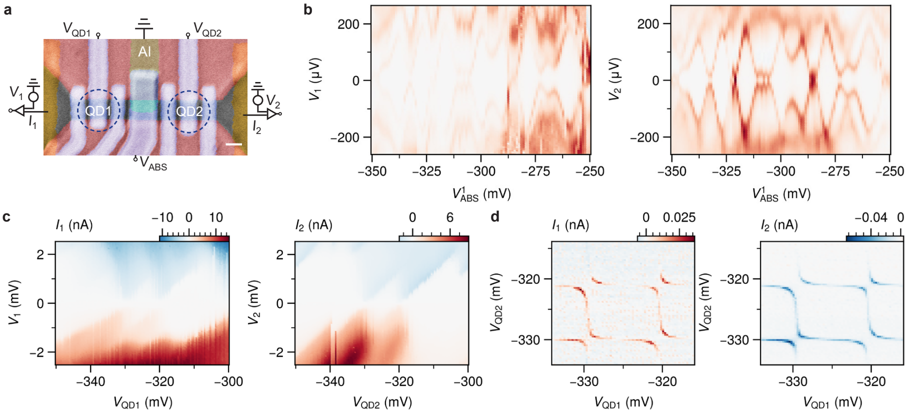

Figure 7.10: **Device B: Basic characterisation. (a)** False colour scanning electron micrograph of device B. **(b)** Characterisation of the the hybrid section, through finite-bias spectroscopy measured from the left and right sides. The spectrum of Andreev bound states is more crowded and shows a larger charging energy, compared to the sections in device A (figure 7.6). Nonetheless, suitable regions in parameter space of $V_{\mathrm{ABS}}^{(1)}$ could be located. **(c)** Measurements of Coulomb diamonds in QD1 and QD2, that are used for the supplementary data in figure 7.11 and figure 7.12. **(d)** Exemplar charge stability diagram for a pair of resonances in QD1 and QD2, with avoided crossings here indicating strong ECT interactions between the QDs.

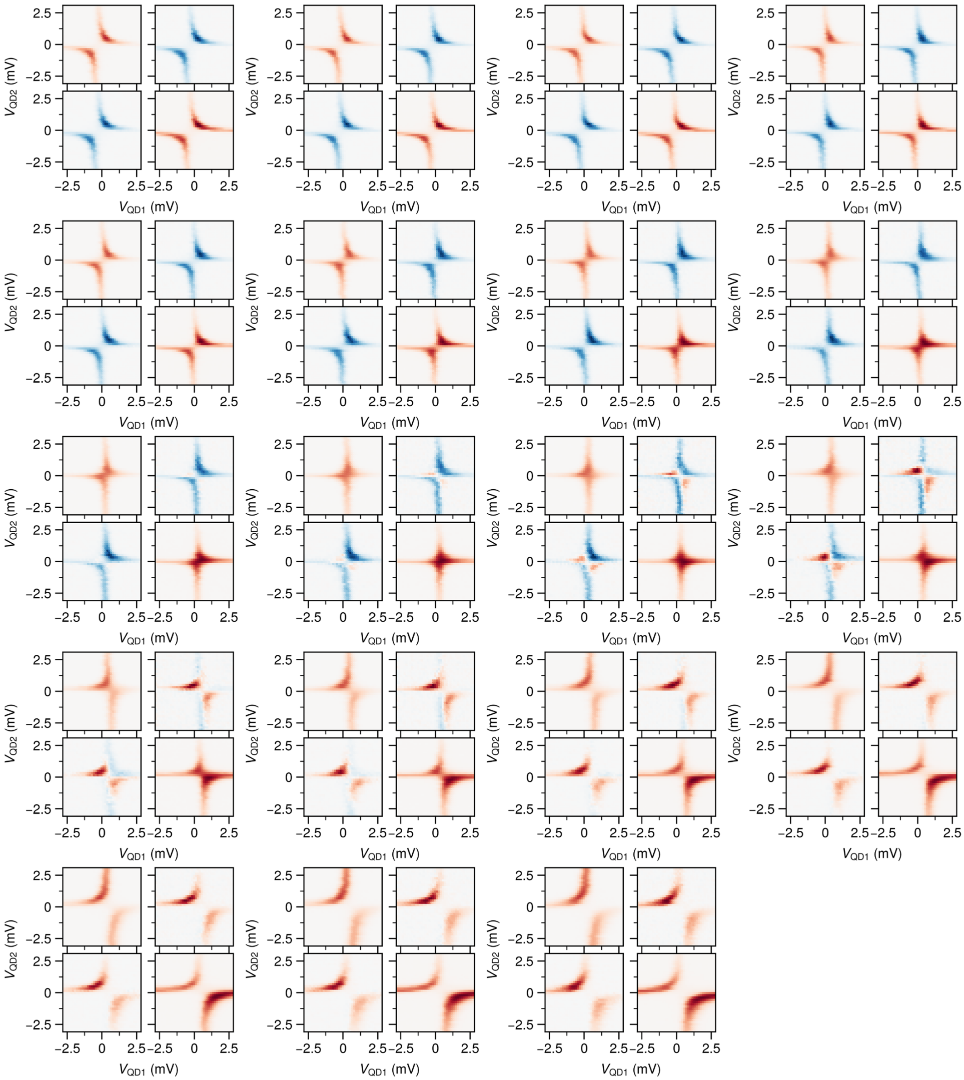

Figure 7.11: **Device B: charge stability diagrams in a wider $V_{\text{ABS}}^{(1)}$ range.** A key finding in [178], was that the CSDs for a two-site chain at a sweet spot at finite field, could not be distinguished from the CSDs at zero magnetic field, contrasting predictions [35] that the non-local conductance could be used to determine the quality of Majoranas. Here we present local and non-local zero-bias conductance CSDs in device B, for a more extensive range of $V_{\text{ABS}}^{(1)}$ around a two-site sweet spot. The lower left charge configuration from figure 7.10d is shown. In particular, as the system transition from an ECT dominated to a CAR dominated regime, a switch is observed between measuring negative non-local conductance to measuring positive non-local conductance. At the sweet spot, crossing forms around μ_{i}=0 where the non-local conductance is zero, owed to the chargeless nature of the excitations at the sweet spot. Notably, the entire trend shown here is identical to measurements obtained at finite magnetic fields [28] (see e.g. figure 5.14).

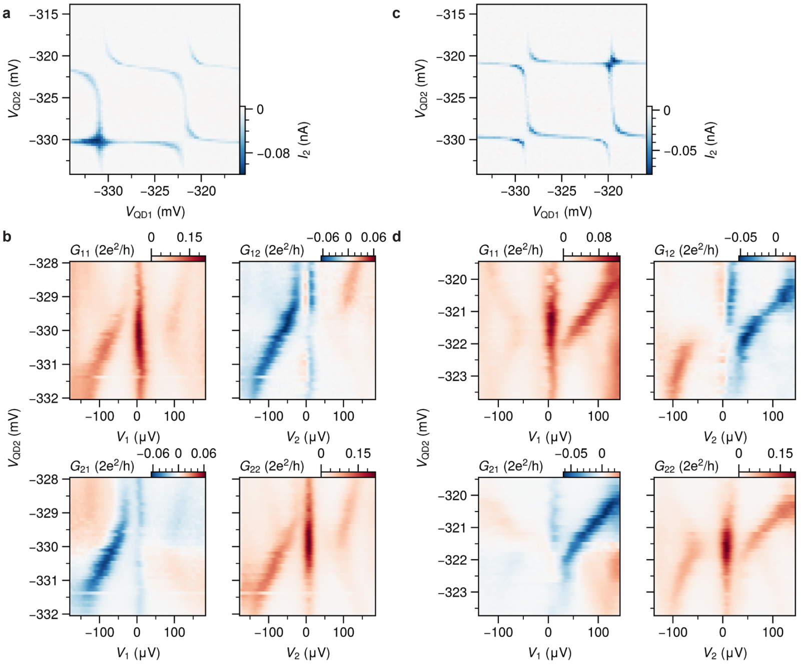

Figure 7.12: **Device B: conductance spectra and role of charge configuration.** In main text figure 7.2, the conductance spectra of the two-site sweet spot as a function of QD plunger gate is presented. In particular, such a measurement reveals the only signature that distinguishes the zero-field and finite-field systems: a particle-hole symmetry breaking feature related to the presence of triplet states in the even subspace. Interestingly, the feature can appear either on the hole-side or electron-side of the applied voltage bias, depending on the charge configurations of the QDs. We reproduce these measurements here for two charge configurations in Device B. **(a)** CSD taken at a voltage $V_{\mathrm{ABS}}^{(1)}$ that corresponds to a sweet spot in the lower left quadrant. **(b)** Full conductance matrix measured as a function of detuning V_{QD2}, along the dashed line in (a). The triplet feature connecting the excited states and the zero energy states appears at negative bias. **(c)** CSD taken at a voltage $V_{\mathrm{ABS}}^{(1)}$ corresponding to a sweet spot in the top right quadrant. **(d)** Full conductance matrix measured as a function of detuning V_{QD2}, along the dashed line in (c). The triplet feature again appears, but now at positive bias, as the excitation has now become 'electron-like' due to the new charge configuration of the QDs.

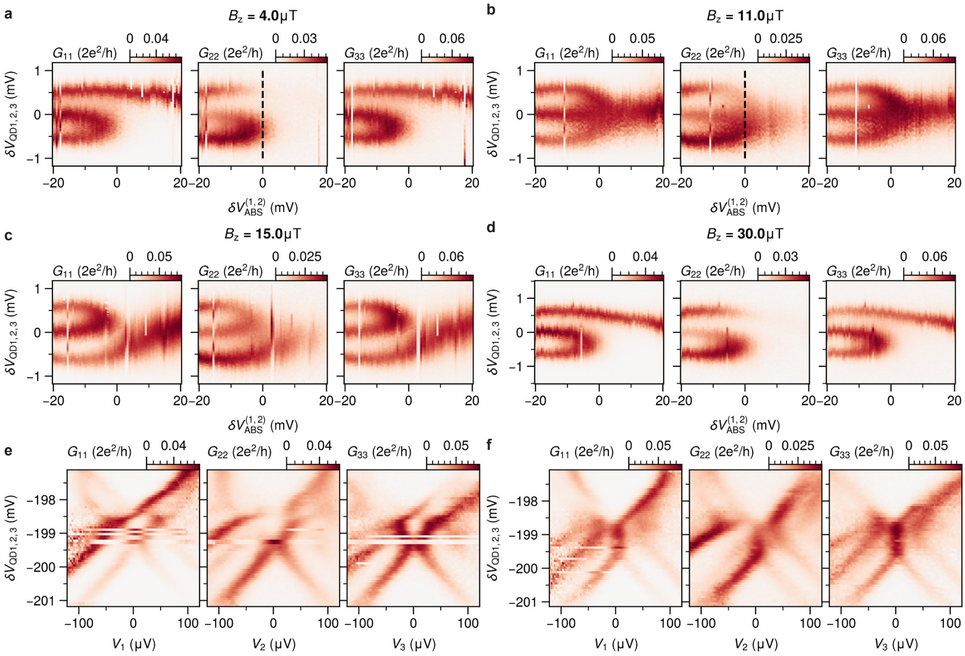

Figure 7.13: **Raw datasets for figure 4.** Figure 7.4 displays zero-bias conductance measurements obtained in a large parameter space of sweeping simultaneously all QD plungers versus sweeping both $V_{\mathrm{ABS}}^{(1)}$ and $V_{\mathrm{ABS}}^{(2)}$ around a sweet spot value (denoted $\delta V_{\mathrm{ABS}}^{(1)}$=0). In the main text, only G_{11} is shown, while G_{22} and G_{33} were measured simultaneously. We show here the full dataset, for **(a)** B_z = 4 μT, **(b)** B_z = 11 μT, **(c)** B_z = 15 μT and **(d)** B_z = 30 μT. In addition, finite bias spectroscopy was obtained along the dashed lines in (a) and (b), when simultaneously sweeping all QD plunger gates, shown in (e) and (f) respectively. At the B_z value corresponding to the ‘special angle’ in (b), the zero-bias conductance appears to split non-linearly, reminiscent of the behaviour expected for this system at finite field.

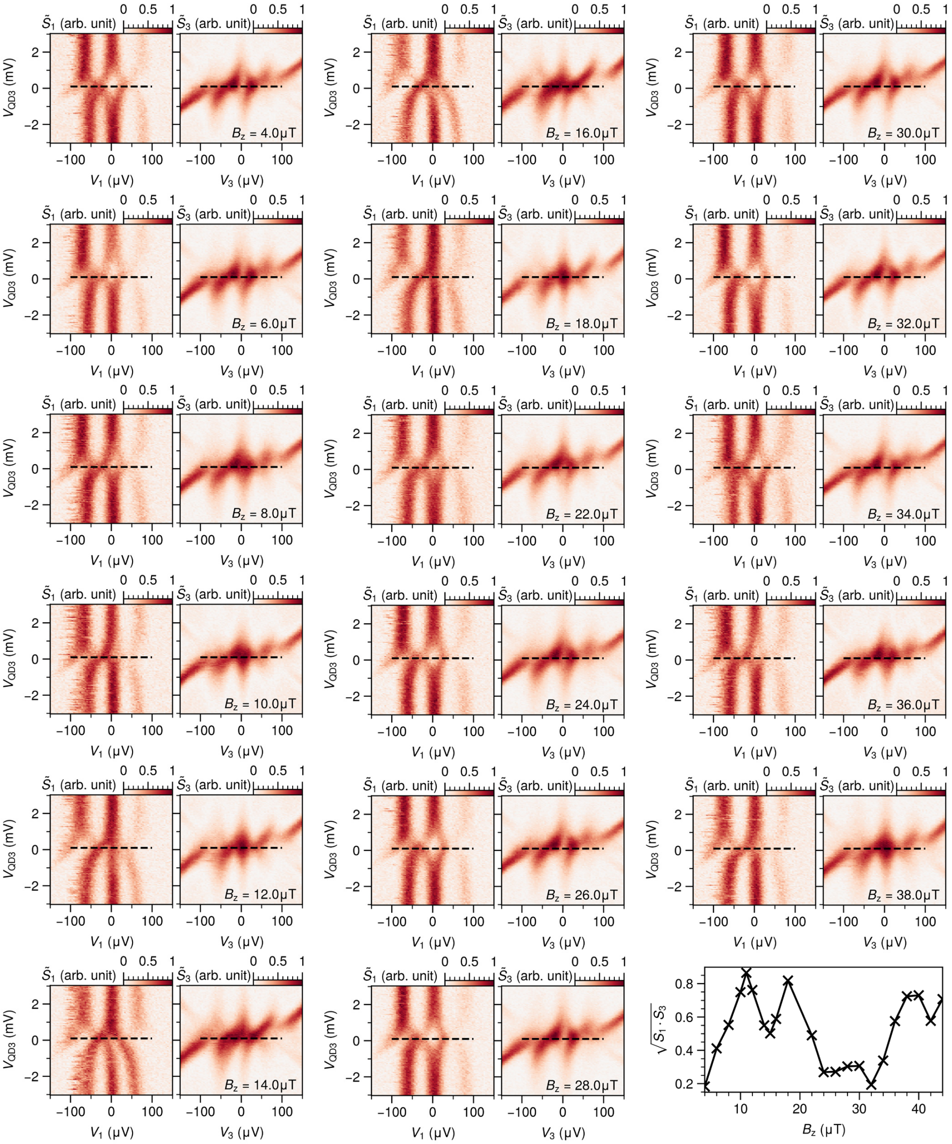

Figure 7.14: **Additional datasets for figure 5 (a)** In main text figure 7.5f, a finite-bias spectroscopy versus detuning V_{QD3} is shown for a value of B_z to match the theoretical 'special angle', where a seemingly stable zero-bias peak appears. Here, we show the evolution of this measurement as a function of B_z,observing the smooth transition from figure 7.3a to figure 7.5f. **(b)** To visualize the trend in closing and re-opening of the splitting of the ZBP as V_{QD3} is brought on resonance, we extract $\sqrt{\tilde{S}_1 \cdot \tilde{S}_2}$ at δV_{QD3}, V_1 and $V_3 = 0$.

8

REMOVING DOMAIN WALLS IN LONGER CHAINS

Having demonstrated in Chapter 5 and Chapter 6 that the physics of the quantum dot - superconductor chain in two-sites behaves as expected when scaling from two to three sites, there is a logical follow-up question: can the system be made even longer? Implementing these structures in qubit architectures is, for instance, expected to result in coherence times that scale exponentially with the lengths of the chains. To scale to longer systems, the phase differences between all superconducting segments in the chain will need to be controlled. While Chapter 6 demonstrates this control by using an external magnetic flux, ideally it can be achieved with control over intrinsic system parameters [200]. In this chapter, we investigate whether the relevant phase differences can be tuned through the spin degree of freedom in each QD, or the chemical potential of the discrete bound states in the hybrid sections. We confirm that both these tuning knobs allow for controlling the phase difference in the couplings between neighbouring QDs, bypassing the requirement to tune an external flux. However, we find that the amplitude of the phase shifts can deviate from a discrete π-shift. We introduce a spatial variation in the spin-orbit field as possible mechanism to explain the observed behaviour and comment on the consequences for experimentally creating long Kitaev chains.

You've done us these lovely spoons.
We were just wondering if you could do us a third one that was a bit bigger.

- Mitchell and Webb

The work in this chapter appears online as: *Using Andreev bound states and spin to remove domain walls in a Kitaev chain*, Wietze D. Huisman†, **Sebastiaan L. D. ten Haaf**†, Chun-Xiao Liu, Qingzhen Wang, Alberto Bordin, Florian J. Bennebroek Evertsz', Bart Roovers, Michael Wimmer and Srijit Goswami, arXiv:2601.12891 [232].
Personal contribution includes assisting in the experiments, performing numerical and analytical analysis and writing the manuscript.
†Authors contributed equally.

8.1 Introduction

The Kitaev chain models a 1D spinless fermionic chain with a p-wave superconducting pairing, which hosts unpaired Majoranas at its edges [14]. These quasiparticles are central to many schemes for fault-tolerant quantum computation [13, 15]. Semiconductor quantum dots coupled via superconductors offer an experimentally tunable realization of the Kitaev chain [33, 35, 37, 38], which has so-far enabled the creation of localized Majoranas in systems with two [28, 80] and three quantum dot (QD) sites [34]. The protection of Majoranas against perturbations scales with the number of sites in the chain, making it highly desirable to extend these arrays. Scaling to longer chains would, for instance, enable implementations of a parity qubit with longer coherence times [33, 34, 177] or demonstrations of the non-abelian exchange of Majorana quasiparticles [180, 233, 234]. A fundamental obstacle for scaling to longer chains is posed by phase differences that arise between neighbouring superconductors. In a Kitaev chain, any π-phase difference between neighbouring superconducting pairings locally closes the excitation gap. This effectively cuts the chain in segments as a so-called domain wall is formed [14, 37]. One ideally requires all phases to be uniform. As we study in Chapter 6 for a three-site system, we can address this problem via a flux-controlled superconducting loop [90, 187]. This is, however, not a practical solution for longer systems: an N-site chain would require independent control over the flux through N-2 superconducting loops.

It was theoretically proposed [200] that Kitaev chains can in fact be scaled without explicit flux control. Instead, control over the spin configuration of the QDs and/or control over the chemical-potential energy of the hybrid segments is predicted to be sufficient to achieve this. Here, we investigate this strategy experimentally, by studying a three-site Kitaev chain in an InSbAs 2DEG *with* a flux-tunable superconducting loop. We follow the protocol in Chapter 6 to create localized Majorana edge modes, and study the flux-response of the excitation gap in the middle quantum dot. By comparing the response to the superconducting flux for different spin configurations, we confirm that changing the spin polarisation of one of the quantum dots introduces a discrete phase shift in the system. Furthermore, we show that changing the chemical potential energy of one of the hybrid segments induces a similar phase shift, providing a second mechanism that can remove a domain wall. Closer inspection reveals that the phase shifts evolve smoothly as a function of the ABS charge, which can result in sweet spots with an arbitrary (non-π) difference in their relative phase. We theoretically analyse how an effective spatial variation in the spin-orbit field gives rise to the smooth phase evolution and derive an analytical expression to compare to the experimental results. Our results show that flux-free scaling of the Kitaev chain can be feasible, but that a deeper understanding of microscopic details of the system is important for implementing the technique.

8.2 The scaling protocol

The Hamiltonian for the general N-site Kitaev chain is given by [14, 37]:

$$H = \sum_{j}^{N} \mu_j c_j^\dagger c_j + \sum_{j}^{N-1} \left(t_j c_j^\dagger c_{j+1} + |\Delta_j| e^{-i\phi_j} c_j^\dagger c_{j+1}^\dagger \right) + h.c.$$

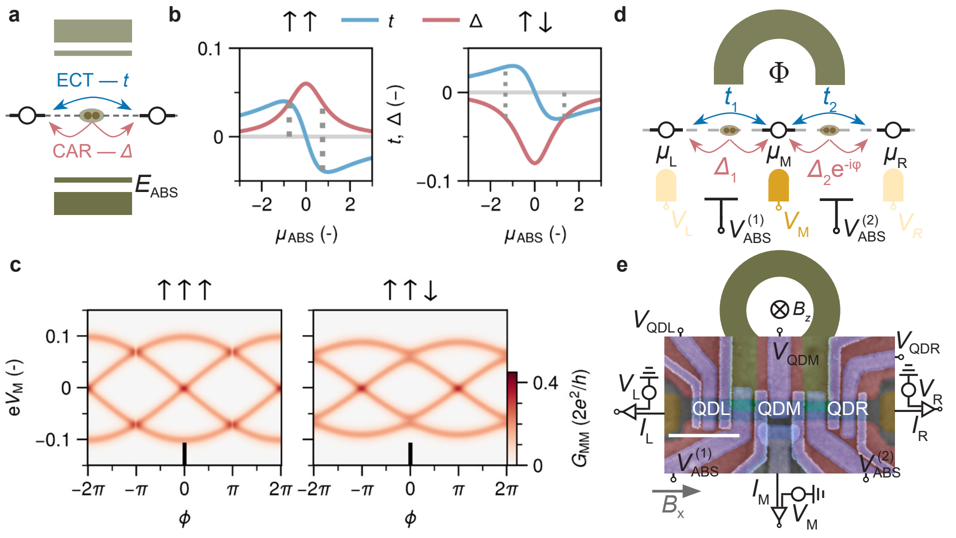

Figure 8.1: **Proposed mechanisms for controlling phase in the Kitaev chain and device layout of a three-site chain. a)** Schematic of ECT and CAR sub-gap processes in a two-site Kitaev chain setup, controlled by an ABS with energy E_{ABS}. **b)** ECT (t) and CAR (Δ) strengths as a function of μ_{ABS} for two different spin configurations. **c)** Simulated conductance spectra on the middle quantum dot of a three-site Kitaev chain, as a function of the phase ϕ. Two different spin configurations are compared, demonstrating the removal of a domain wall through flipping the rightmost spin. **d)** Three-site Kitaev chain schematic showing the two pairs of couplings t_1, Δ_1 and t_2, Δ_2. Phase modulation is enabled by threading a flux Φ through the superconducting loop connecting the two hybrid sections. **e)** SEM of the measured device. An out-of plane magnetic field B_z is used to modulate the flux, with a period of 28 μT. An in-plane magnetic field B_x is applied parallel to the channel, to spin-polarise the quantum dots.

A gauge transformation allows for taking the chemical potentials μ_j and hopping terms t_j to be real and assigning a complex phase ϕ_j only to the superconducting pairings Δ_j [14, 18]. In a 1D system with Rashba spin-orbit coupling, these phases are restricted so that ϕ_j is either 0 or π [37]. For any N, unpaired Majoranas arise on the two outermost sites when $\mu_j = 0$, $|t_j| = |\Delta_j|$, this is referred to as the Majorana sweet spot. When all phases are equal (such that either all $t_j = +\Delta_j$ or all $t_j = -\Delta_j$), the middle sites host an excitation gap that separates the Majorana modes at the edge.

The Kitaev chain can be effectively engineered by coupling spin-polarised QDs via Andreev bound states in a semiconductor–superconductor hybrid segment [28, 177]. Focusing first on a minimal two-site system, the hopping interaction (t) occurs through elastic co-tunnelling (ECT), whereas crossed Andreev reflection (CAR) provides a pairing interaction (Δ) via the creation or splitting of Cooper pairs in the superconductor [25, 27] (figure 8.1a). Crucially, the amplitudes t, Δ of these virtual processes depend differently on the ABS chemical potential energy μ_{ABS}. Additionally, the relative signs of the amplitudes are affected by the spin configuration of the spin-polarised quantum dots. Depending on whether the spins of the QDs are aligned or anti-aligned, either the CAR or the ECT process requires the presence of spin-orbit interactions. As a result, the coupling mechanism differs for different spin configurations. Figure 8.1b shows theoretically calculated t, Δ amplitudes as a function of μ_{ABS}, previously shown in Ref. [200], comparing an equal spin alignment and an opposite spin-alignment in the QDs. For each spin configuration, tuning μ_{ABS} enables either $t = \Delta$ or $t = -\Delta$. Focussing on $\mu_{\mathrm{ABS}} < 0$, changing the spin of one of the QDs similarly changes the relative amplitude from $t = +\Delta$ to $t = -\Delta$ (vice versa for $\mu_{\mathrm{ABS}} > 0$).

The relative sign between t, Δ becomes relevant when considering a Kitaev chain with $N \geq 3$ QD sites. To see this, we turn to a spinful model considering three spinful QDs and two ABSs (see section 8.7). Figure 8.1c shows numerical conductance spectra of the middle quantum dot at a three-site sweet spot, as a function of the phase difference ϕ between the two superconducting pairings. For the left spin configuration, for example, we find a situation where the gap is closed when $\phi = 0$, due to the formation of a domain wall. Changing the spin on the right QD shifts the entire spectrum by a π-phase, removing the domain wall and reopening the excitation gap in the middle QD at $\phi = 0$.

8.3 DEVICE AND EXPERIMENTAL SETUP

A schematic overview and a Scanning Electron Micrograph (SEM) of the measured device are shown in figure 8.1d and figure 8.1e. Three large lithographically defined depletion gates (red) confine a narrow conductance channel across two superconducting strips (green). Narrow gates are used to define three quantum dots on the left, in the middle and on the right of the two superconducting regions. Their chemical potential energies are controlled by V_{QDL}, V_{QDM} and V_{QDR} respectively. The two hybrid sections host discrete Andreev bound states, whose energies are controlled by $V_{\mathrm{ABS}}^{(1)}$ and $V_{\mathrm{ABS}}^{(2)}$. The sections are connected in a loop, enabling an out-of-plane magnetic field B_z to control the flux Φ through the loop. This directly controls the relative phases of the inter-dot couplings between neighbouring QD pairs [90]. Each QD is coupled to a normal contact via a tunnelling barrier, allowing us to probe the local density of states at the edges and in the middle of the chain. Fast measurements are performed using radio-frequency lead reflectometry techniques enabled by off-chip lumped-element resonators, where the reflected phase and amplitude of signal S_{21}^{i} on lead i is recorded. We plot the processed signal $\widetilde{S_{21}^{i}}$, as detailed in section 8.7. In addition, we show measurements of the differential conductance $G_{\mathrm{MM}} = \frac{dI_{\mathrm{M}}}{dV_{\mathrm{M}}}$ through the middle ohmic contact.

8.4 RESULTS

8.4.1 SPIN-INDUCED PHASE SHIFTS

To initialize the system, we identify an isolated orbital in each of the three QDs. An in-plane magnetic field (B_{x}) is applied along the length of the 1D channel, to spin polarise the QDs (Fig. S1). Since each orbital has two spin polarisations, we can study eight different combinations of resonances. We use the combined spin-configuration as label. Following the same protocol as in Chapter 6, the device is first tuned up so that the condition $|t_i| = |\Delta_i|$ is satisfied for each of the two QD pairs (left/middle and middle/right). This is achieved by tuning $V_{\mathrm{ABS}}^{(1)}$ and $V_{\mathrm{ABS}}^{(2)}$ to change the charge and energy of ABSs, which in turn affects the interdot couplings (figure 8.1b,c). The tune-up is completed by setting all V_{QDi} to the charge

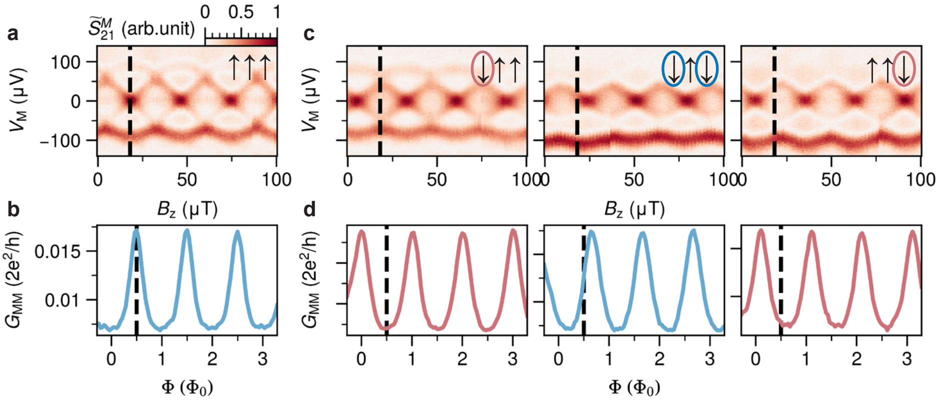

Figure 8.2: **Spin-induced phase shifts. a)** Bias spectroscopy measurement for the middle quantum dot as a function of the out-of-plane magnetic field B_z for a ↑↑↑ spin configuration. **b)** A higher resolution G_{MM} linetrace along $V_M = 0$, expressed in units of the flux quantum Φ_0. We identify a flux where the excitation gap closes. **c)** Repeated measurements of a), for different spin-configurations. **d)** Comparison of G_{MM} linetraces along V_M=0, for the same spin-configurations as in c). Applied magnetic field along B_x is 150 mT. The behaviour is reproducibly observed, shown in figure 8.6.

degeneracy point corresponding to $\mu_i = 0$. To identify the flux corresponding to a phase $\phi = 0$, we measure the finite-bias conductance through the middle quantum dot G_{MM} as a function of B_z (figure 8.2a). The excitation gap in the middle QD closes periodically as a function of B_z, in line with the predicted behaviour shown in figure 8.1c and Refs. [90, 200]. The value of B_z where the excitation gap in the middle QD closes is taken as reference point (indicating ϕ=π), which can be easily extracted from a measurement along $V_M = 0$ (figure 8.2b).

The result in figure 8.2a is obtained for an ↑↑↑ spin configuration. We can select a different spin configuration through the voltages V_{QDi}. For each adjustment, a slight retuning of V_{ABS} is required to maintain the $|t_i| = |\Delta_i|$ condition. We repeat the measurement in figure 8.2a for three different combinations of spin polarisations of the outer QDs, shown in figure 8.2c. For every adjustment of a spin polarisation, we observe that the spectrum shifts by approximately half a flux period, corresponding to a π-shift in the effective phase ϕ. To compare the flux response more closely, we compare linetraces along $V_M = 0$ in figure 8.2d. Focusing on the Φ value indicated by the dashed line, at fixed B_x, the excitation gap in the system is either present or closed depending on the spin-configuration. This in principle demonstrates the desired control: the spin configuration serves as a tool to remove a domain wall, without requiring to tune the external flux. We note, however, that small offsets from $\phi = 0$ or $\phi = \pi$ appear in the bottom two configurations, marking a departure from the discrete $0/\pi$-shift presented in figure 8.1c. This motivates a more in-depth study where we turn to the second predicted control knob: the Andreev bound state charge.

8.4.2 ABS-induced phase shifts

The charge of the Andreev bound states provides a second way to change the relative sign of the t and Δ amplitudes, as highlighted in figure 8.1b. Hence, tuning between the two available $|t| = |\Delta|$ sweet-spots within the range of a single ABS should yield a relative phase shift, while maintaining the same spin-configuration. In contrast to changing the spin of the QDs, this control via V_{ABS} allows for a continuous interpolation between two sweet spots. First, we search for a range in $V^{(2)}_{\text{ABS}}$ where the rightmost QD interacts with a single ABS. figure 8.3a shows a charge stability diagram of two spin-polarised resonances in the right QD interacting with an ABS in the right hybrid segment. As $V^{(2)}_{\text{ABS}}$ is varied, the positions of the QD resonances are modulated, indicating interaction with ABSs in this range [154]. Here, we find that one sweet spot can be clearly identified for the spin-down resonance, while the spin-up resonance allows for determining a sweet spot at two different ABS energies (figure 8.8). At each of these three sweet spots, we obtain a zero-bias conductance measurement as a function of flux, shown in figure 8.3b. Comparing these linetraces, we observe that now both the change in spin and the change of ABS energy result in comparable relative phase shifts. Next, we study the flux dependence of the system throughout a larger range of $V^{(2)}_{\text{ABS}}$ around the two spin-up sweet spots, to interpolate how the system evolves from the result in panel 3b.ii to the shifted trace in panel 3b.iii. Generally then $|t_2| \neq |\Delta_2|$, while we maintain $|t_1| = |\Delta_1|$. Similar to figure 8.3b, we characterise the flux dependence by measuring the response of the zero-bias conductance. The oscillations are fitted to estimate the value B_z where the excitation gap closes (see figure 8.7), which allows to extract a single value $\widetilde{\Phi}$ that characterises the relative flux-shift at each $V^{(2)}_{\text{ABS}}$ point with respect to the dashed line in panel 3b.i. The evolution of this extracted flux-shift $\widetilde{\Phi}$ versus the ABS energy is shown in figure 8.3c.

The extracted flux-shift in figure 8.3c reveals three important observations. First, we find that the flux-shift induced by a spin-flip is similar to the flux-shift acquired by changing the ABS charge from one sweet spot to another. This indicates that the underlying mechanism shown in figure 8.1b appears to be well-understood. However, we also observe that the flux-shift, and therefore the phase, varies smoothly between two-sweet spots as the ABS energy is changed, deviating from the scenario where only phases of 0 or π appear in the system [37]. Given that the exact positions of the two sweet spots along V_{ABS} depend on underlying microscopic details, a smooth phase evolution means that any arbitrary flux-shift can appear in practice. Furthermore, the phase separation of the plateaus at the extremes of the ABS range is larger than π, indicated by the red arrow. The practical implications of this are treated in the Discussion. Below we address how the model underlying figure 8.1c can be adjusted to reproduce this behaviour.

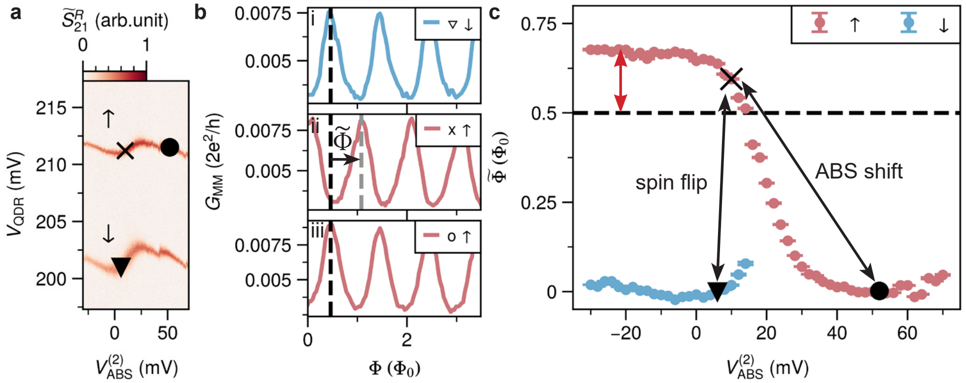

Figure 8.3: **ABS-induced phase shifts. a)** Hybridization between the right ABS and two spin levels of the right quantum dot QDR. Three sweet spots (×, ∘, ▵) are identified from charge stability diagrams of the right and middle quantum dot (figure 8.8). **b)** Flux dependence of the zero-bias conductance G_{MM} on the middle dot, measured at the three sweet spots indicated in a). **c)** Continuous measurement of the extracted flux-shift $\widetilde{\Phi}$ as a function of the right ABS energy. The extracted shift $\widetilde{\Phi}$ is defined with respect to the first conductance peak in the zero-bias trace as indicated in b) (see figure 8.7 for further details about the extraction). The spin-down configuration is only shown for values of $V^{(2)}_{\mathrm{ABS}} < 16\,\mathrm{mV}$, as the extraction was unreliable for the rest of the range. Raw datasets are shown in figure 8.10 and figure 8.11. Measurements were performed at an in-plane field B_x of 200 mT. The flux dependence of the energy spectrum at all values of the ABS energy is shown in figure 8.9.

8.4.3 POSSIBLE ORIGIN OF SMOOTH PHASE EVOLUTION

The above results deviate from the original theoretical result [200] in two clear ways: the system *smoothly* interpolates between two phase plateaus as a function of $V^{(2)}_{\mathrm{ABS}}$, and the separation of the two plateaus corresponds to a total phase-shift larger than π. In a system that respects complex conjugation symmetry, only discrete 0 or π phases arise. A possible mechanism that could break this symmetry, is a spatial variation in the effective spin-orbit field along the chain, which was so far assumed to be constant (perpendicular to the chain). As a starting point, we present here a simple adjustment to the model underlying figure 8.1c that implements this effectively, by introducing an in-plane offset angle θ_{A} between the polarisation-axis of the QDs ($\vec{B}_{\mathrm{QD}}$) and that of the ABS ($\vec{B}_{\mathrm{ABS}}$), with Zeeman energy $E_{\mathrm{Z}}^{\mathrm{ABS}}$. Mapping the full model onto an effective three-site model then allows to obtain an expression for the complex phase-shift $\widetilde{\phi}$ in the system (see section 8.7) as a function of ABS parameters:

$$\widetilde{\phi} = \frac{\pi}{2} - \arctan\left[\frac{\mu_{\mathrm{ABS}} + \mu_0(\theta_{\mathrm{A}}, E_{\mathrm{Z}}^{\mathrm{ABS}})}{\Gamma(\theta_{\mathrm{A}}, E_{\mathrm{Z}}^{\mathrm{ABS}})}\right] \tag{8.1}$$

When $\theta_{\mathrm{A}}, E_{\mathrm{Z}}^{\mathrm{ABS}} = 0$, the dependence on μ_{ABS} is a step-function between 0 and π, centred around $\mu_{\mathrm{ABS}} = 0$. The parameter $\Gamma \propto E_{\mathrm{Z}}^{\mathrm{ABS}} \sin(\theta_{\mathrm{A}})$ smoothens the step-function and $\mu_0 \propto E_{\mathrm{Z}}^{\mathrm{ABS}} \cos(\theta_{\mathrm{A}})$ shifts the centre of the curve away from $\mu_{\mathrm{ABS}} = 0$. In figure 8.4a, we show the dependence on μ_{ABS} for varying θ_{A} at fixed $E_{\mathrm{Z}}^{\mathrm{ABS}}$, highlighting the smoothening effect on the step-function when $\theta_{\mathrm{A}} \neq 0$. The scattered points indicate the two values of μ_{ABS}

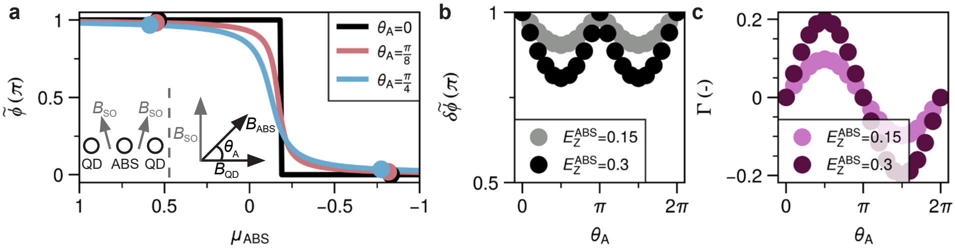

Figure 8.4: **Theoretical analysis of $\tilde{\phi}$ as a function of μ_{ABS}. a)** To explain the experimental result, we propose a spatial variation in the spin-orbit hopping between neighbouring sites as possible source (inset left). For simplicity, we implement this here equivalently through an offset angle θ_{A} between the polarisation of the QDs and the ABS (inset right). The more general case is discussed in section 8.7. The analytically obtained phase-shift $\tilde{\phi}$ (equation (8.1)) is plotted, for various θ_{A}. For each curve, the two μ_{ABS} values are indicated that correspond to a sweet-spot numerically. A fitting of the experimental data to the theoretical result is shown in figure 8.9. **b)** The smoothening of the phase dependence on μ_{ABS} results in a decrease in the phase difference $\delta\tilde{\phi}$ between two sweet-spots, for two values of E_Z^{ABS} in units of the induced superconducting pairing in the ABS. **c)** The smoothening parameter Γ as a function of θ_{A}, for two values of E_Z^{ABS}.

that numerically correspond to sweet spots. Due to the smoothening, the phase separation between the two sweet-spots decreases as a function of θ_{A} and E_Z^{ABS} (figure 8.4b), as they lie more towards the centre of the smoothened curve, similar to figure 8.3c. A plot of Γ as a function of θ_{A} is shown for two values of E_Z^{ABS} in figure 8.4c, where we see that the broadening is maximum when $\theta_{\text{A}} = \pi/2$. Fitting this result to the experimental data captures the overall trend well (figure 8.9). We stress, however, that the larger-than-pi separation of the plateaus in figure 8.3c is not directly described by this mechanism.

8.5 DISCUSSION

The key finding of the experiments presented in this chapter is that both quantum dot spin and ABS charge *can* remove a domain wall in a Kitaev chain device. However, the resulting phase shifts may differ from the ideal value of π. In our model, we find that spatial variations in the alignment of the spin-orbit field can be a possible explanation for these deviations. We believe this to be a physically reasonable assumption, which may for example arise through variations in the electrical fields or microscopic differences in the QDs/tunnel barriers. An anisotropic g-tensor along the chain could also produce this, although in this specific material the in-plane g-factor is expected to be isotropic [235]. The larger-than-π variation may arise if the spin-orbit field itself is affected by the V_{ABS} gate voltage, or through the presence of multiple Andreev bound states. To minimize the deviations induced by spin-orbit misalignments, this effect should be taken into account in the design of future experiments. Specifically, our results suggest that complex geometries for applications such as braiding experiments should consist of predominantly parallel chains, allowing a single field $\vec{B}$ to be perpendicular to $\vec{B}_{\text{SO}}$ everywhere.

We emphasize that further work is needed for a complete understanding of the exact underlying mechanism. We expect, for instance, that an effective change in the offset angle θ_A may be observed when using different ABS orbitals as mediator of the interdot coupling. Further, we find experimentally that $\widetilde{\Phi}$ is affected by the direction of the external in-plane magnetic field used to spin-polarise the QDs, shown in figure 8.13. Importantly, phase shifts extending beyond half a flux period become visible only when tracking the phase dependence as a function of a continuous parameter, most clearly seen in the raw data shown in figure 8.9. For the data in figure 8.2 on the other hand, whether the phase-shifts are smaller or larger than π remains ambiguous. Ref. [90] reports similar deviations from π-shifts in a similar device, but can not resolve the exact amplitude for the same reason. We hope further experiments can resolve the outstanding questions.

The main purpose of the investigated protocol is to remove domain walls in long Kitaev chains and maximize the bulk excitation gap, without requiring an external flux. The main consequence of the observed deviations from π-shifts, is that the technique can lead to a reduced excitation gap on the middle site compared to the maximum when the effective phase $\phi = 0$. We show this reduction explicitly in figure 8.12. As an example, we can quantitatively analyse the reduction in the excitation gap for the results in figure 8.2. By extracting the phases of the ↓↑↑ and ↓↑↓ configurations in figure 8.2, we find that the phase difference between the states deviates from π by approximately 30%, or 4 µT (figure 8.14). This in turn leads to a decrease in the excitation gap from approximately 50 µeV to 38 µeV. A larger deviation from π translates directly to a larger reduction in the energy gap. However, as long as the phase shift is non-zero, it may be used to avoid a situation where the excitation gap closes. Compared to fine-tuned flux control over multiple loops, with the drawbacks of requiring additional control lines and accounting for cross-talk [236, 237], we believe this presented technique to be the preferred alternative.

8.6 SUMMARY

We have studied the phase-dependent energy spectra of different spin-configurations of a three-site Kitaev chain. Through flux-dependent measurements, we observe that phase shifts close to π can be achieved by changing the spin occupation on either of the outer QDs. These phase shifts would allow to avoid domain walls, enabling the scaling to longer Kitaev chains without the need for external flux control. Interestingly, upon further investigation, we find that the relative phase varies smoothly with the ABS charge, which can give rise to arbitrary phase shifts between sweet-spots. We theoretically show that a spatial variation in the spin-orbit field can be a possible mechanism for the observed continuous transition. This finding helps to understand the origin of phase shifts that deviate from π, and helps to understand conditions under which the spin-flip protocol can be used reliably in future experiments.

DATA AVAILABILITY

All raw data obtained in relation to this chapter and the scripts to produce the figures are available on Zenodo [238].

8.7 METHODS

DEVICE FABRICATION

The investigated device was fabricated using the techniques described in detail in [129] and [128]. The aluminium loop structure is defined in an InSbAs-Al chip by wet etching, followed by the deposition of three ohmic Ti/Pd contacts. After deposition of 20 nm AlOx via 40 °C atomic layer deposition (ALD), three large Ti/Pd depletion gates are evaporated: one large top depletion gate and two bottom depletion gates each extending halfway. The bottom consists of two gates in order to independently form the left and right halves of the channel, separated by a thin channel where the middle lead is placed. The channel width is designed to be 200 nm. Following a second ALD layer (20 nm AlOx), a first layer of six Ti/Pd finger gates is evaporated. These are used for controlling the electrochemical potential energies of the QDs and hybrid regions and for defining the tunneling barrier for the middle contact. A third ALD layer (20 nm AlOx) is deposited, followed by evaporation of the remaining six Ti/Pd finger gates that define the three QDs. For RF-measurements, superconducting LC-resonator circuits are fabricated on a separate chip with a silicon substrate by etching NbTiN. To apply DC voltages, bias tees are created by depositing 20 nm Cr structures with resistances of $\approx 5\,\mathrm{k\Omega}$.

The measured device was cooled down a total of twelve times over the course of 1.5 years. The initial cool-downs focussed on the results presented in Refs. [187] and [139]. The results presented in figure 8.2 and figure 8.3 were obtained in the seventh and twelfth cooldown, where we focussed systematically on the phase-shifts in the system. The effects of changing spin or ABS charge to shift the phase was observed in earlier cool-downs, but not addressed systematically in those measurements. A summary of all observed phase shift data, including data from the earlier cool-downs four and six, is shown in figure 8.6.

DC TRANSPORT MEASUREMENTS

Measurements are performed in a dilution refrigerator with a base temperature of 20 mK. We expect the effective electron temperature to be on the order of 50-100 mK. Transport measurements presented in the main text are performed in AC and DC using a four-terminal set-up (three ohmic contacts plus two aluminium strips connected in a loop). The aluminium strips induce a gap of $\approx 250\,\mu\mathrm{V}$ and are kept electrically grounded. Each ohmic lead is connected to a current meter and biased through a digital-to-analogue converter and both DC and AC voltages can be applied. Offsets of the applied voltage-bias on each lead are corrected via independently measuring the Coulomb peaks in the QDs and looking at the change in sign of the current. The voltage outputs of the current meters are recorded with three digital multimeters and three lock-in amplifiers. When applying a DC voltage to one lead (e.g., V_L), the other leads (i.e., V_M and V_R) are kept grounded. AC excitations are applied with amplitudes around 5 µV RMS and a frequency of 23 Hz. In this way, the conductance of the middle lead $G_\mathrm{MM} = \frac{\mathrm{d}I_\mathrm{M}}{\mathrm{d}V_\mathrm{M}}$ is obtained by measuring the response of I_M to V_M. Small offsets in measured conductances arise using the lock-in amplifiers, due to capacitances to ground within the electronics. These offsets are calibrated using Coulomb blockaded measurements and corrected. Voltage-divider effects are not corrected, since we focus on low tunneling regimes ($G \ll 2e^2/h$) where the device resistance is large compared to the resistances of the fridge lines and the current meters, such that the multi-terminal effect is small.

RF-reflectometry measurements

For fast characterisation of the device, we employ radio-frequency (RF) lead reflectometry [145] in addition to the DC/AC conductance measurements. Each ohmic contact is connected to an inductor, designed with varying inductances $L_{\mathrm{L,M,R}} = 0.2, 0.5, 1.5\ \mu\mathrm{H}$, that together with a parasitic capacitance to ground via bond-wires result in resonators with frequencies of $f_{\mathrm{L,M,R}} = 723, 505, 248$ MHz. The complete circuit diagram including the fridge wiring and filters is presented in Ref. [139]. Using a directional coupler, we obtain the reflected signal of each lead. We denote with S_{21}^{L}, S_{21}^{M} and S_{21}^{R} the normalised reflected signals of the left, middle and right lead respectively, which correspond roughly linearly to conductance. All three signals can be measured simultaneously through multiplexing [208], using the circuit shown in figure 8.5. The amplitude and phase of the complex reflected signal are translated into a single quantity $\widetilde{S}_{21}^{\mathrm{i}}$ and normalized, following Ref. [139]. In combination with saw-tooth pulses on the QD plunger gates, generated by arbitrary waveform generators, this allows for scanning the parameter space many times faster than through DC measurements.

Measurement procedures

Magnetic fields are applied using a 3D vector magnet. The field perpendicular to the superconducting loop (B_{z}) is generated using a high-resolution current source, giving a B_{z} resolution below 0.1 µT (providing sufficient resolution for the flux period of 28 µT). A small (but significant) hysteresis on the order of 5 µT is observed when sweeping B_{z} in opposite directions. This is counteracted by setting B_{z} first to −20 µT and then sweeping this field back in the positive direction, such that consecutive experiments where B_{z} is varied are consistent. To spin-polarise the QDs, a magnetic field of 150 to 200 mT is applied parallel to the channel (B_{x}). Due to an imperfection in the alignment, this introduces a small B_{z} component as well, on the order of 80 flux quanta. It was not possible to accurately correct this offset for this work, and so we are unable to determine the B_{x} value that corresponds to precisely 0 flux through the loop. To accurately determine this point of zero flux in future work, we recommend significantly smaller loop sizes.

In the following sections, we briefly outline the details and procedures used to acquire the results in figure 8.2 and figure 8.3.

Spin-flip procedure

First, the tune-up procedure described in the main text is followed to ensure $|t_1| = |\Delta_1|, |t_2| = |\Delta_2|$ and all $\mu_i = 0$. Next, the flux dependent energy spectrum and zero-bias conductance in figure 8.2a and b are measured sequentially. The full energy spectrum is measured using RF-techniques, to allow for faster data collection, while the zero-bias features are specifically recorded through slower conductance measurements, ensuring more accurate phase extraction from fitting. In-between these two measurements, the flux-controlling magnetic field B_{z} is set to −20 µT to mitigate any hysteresis effects. Next, we flip the spin on, for example, the left QD by changing its chemical potential energy. A slight adjustment is then made to the energy of the ABS that couples to the left QD, re-ensuring the $|t_1| = |\Delta_1|$ condition. Appropriate charge stability diagrams are collected to confirm that we are back at the sweet spot. We ensure that this adjustment to the ABS energy is small compared to its full extent. We now repeat the flux dependent spectrum measurement, allowing us to identify the spin-flip induced phase shift.

ABS shift procedure

To obtain the dataset in figure 8.3c, a sequence of steps is taken to correct for cross capacitances and renormalization effects. The aim is to study the effective phase-shift experienced by the system when changing $V_{\text{ABS}}^{(2)}$. After identifying a range where $V_{\text{ABS}}^{(2)}$ modulates the energy of an ABS, we set $V_{\text{ABS}}^{(2)}$ to a starting point of $-30\,\text{mV}$. Here the effective couplings are $|t_1| = |\Delta_1|$, but $|t_2| \neq |\Delta_2|$. We then take the following sequence of steps:

1. Tune V_{QDR} to select the down-spin resonance on QDR.
2. Record charge stability diagrams (CSDs) for both QDL-QDM and QDM-QDR, to keep track of the dominant interdot coupling and identify where the two-site sweet spots occur (see figure 8.8).
3. Recalibrate all V_{QDi} to their respective $\mu_i = 0$ points.
4. Set the magnetic field B_z (controlling the flux) to $-20\,\mu\text{T}$, to mitigate any hysteresis effects.
5. Measure the zero-bias conductance on the middle QD (G_{MM}) as a function of the external flux.
6. Reset B_z to $-20\,\mu\text{T}$ and measure the finite-bias energy spectrum ($\tilde{S}_{21}^{\text{M}}$) as a function of B_z.
7. Retune V_{QDR} to select the up-spin resonance and repeat steps (2)-(6).
8. Increase $V_{\text{ABS}}^{(2)}$ by $2\,\text{mV}$, to adjust the ABS charge and energy.
9. Repeat steps (1)-(8) until the end of the chosen $V_{\text{ABS}}^{(2)}$ range is reached.

THEORETICAL RESULTS

The calculations in figure 8.1c are reproduced from the results presented in Ref. [200], which extends the model from Refs. [35, 239]. To model the device, consisting of 3 quantum dots and 2 hybrid segments, a five-site model is considered in a many-body Fock basis where charging energy and spin are included on each site. In the perturbative limit with large charging and Zeeman energies, this model maps exactly to the 3-site Kitaev chain [36]. We refer to the aforementioned references for details. To reproduce the experimental data in figure 8.3c, we extend the model by introducing an effective variation in the spin-orbit field. Below we introduce the general model used and derive equation (8.1) as presented in the main text.

PHASE SHIFTS WITH A SPATIALLY VARYING SPIN-ORBIT FIELD

A general approximation in modelling the system is that the spin-orbit field (along $\hat{y}$) is perpendicular to the chain and the applied Zeeman field (along $\hat{z}$). Here, we describe the complex phase that arises when this constrained is relaxed. In the experimental system, the charging energy of the QDs is typically the largest energy scale in the system. In order to simplify the discussion, we neglect charging energy and work in the BdG representation [36]. We consider the subsystem consisting of three tunnel coupled sites:

$$H = H^1_{\mathrm{QD}} + H^{1,2}_{\mathrm{T}} + H^2_{\mathrm{QD}} + H^{2,3}_{\mathrm{T}} + H^3_{\mathrm{QD}} \tag{8.2}$$

where sites 1,3 include a Zeeman energy E^{QD}_Z and a chemical potential μ^i_{QD}, written:

$$H^i_{\mathrm{QD}} = \psi_i^\dagger \left[\mu^i_{\mathrm{QD}} \tau_z \sigma_0 + E^{\mathrm{QD}}_{\mathrm{Z}} \tau_0 \sigma_z\right] \psi_i \tag{8.3}$$

with $\psi_i = (c_{i,\uparrow}, c_{i,\downarrow}, c^\dagger_{i,\downarrow}, -c^{i,\dagger}_{i,\uparrow})$ the subspace basis for site i, τ_i the Pauli matrices for particle-hole space and σ_i the Pauli matrices for spin. The middle site has in addition an induced superconducting pairing Δ and a generally lower Zeeman energy E^{ABS}_Z:

$$H^2_{\mathrm{QD}} = H_{\mathrm{ABS}} = \psi_i^\dagger \left[\mu_{\mathrm{ABS}} \tau_z \sigma_0 + E^{\mathrm{ABS}}_{\mathrm{Z}} \tau_0 \sigma_z + \Delta \tau_x \sigma_0\right] \psi_i \tag{8.4}$$

To couple neighbouring sites i,j, we implement the most general hopping matrix (respecting time reversal symmetry) with normal hopping t and spin-rotating hopping t_{SO} around a unit vector $\vec{n}_{i,j}$. The spin precession angle θ_{ij} is set by $\tan\theta_{ij} = \frac{t}{t_{\mathrm{SO}}}$. The tunneling Hamiltonian is then given by:

$$H^{i,j}_T = \psi_i \left[t \tau_z \sigma_x + t_{\mathrm{SO}} \tau_z \vec{\sigma} \cdot \vec{n}_i\right] \psi_j \tag{8.5}$$

where $\vec{\sigma} = [\sigma_x, \sigma_y, \sigma_z]$. Typically $\vec{n}$ is set to $[0,1,0]$, reflecting a purely 1D Rashba spin-orbit term. Here we consider the general case $\vec{n} = [n_x, n_y, n_z]$. Lastly, we set $\mu^i_{\mathrm{QD}} = E^{\mathrm{QD}}_{\mathrm{Z}}$, assuming the QDs are weakly coupled to the ABS [79]. We are interested in the complex phase that remains when mapping this spinful three-site system to a spinless two site system. To derive this, we use Pymablock to perform a Schrieffer-Wolff transformation [240, 241] and project out the middle site and the undesired spin. This leaves an effective ECT coupling t_{eff} and effective CAR coupling Δ_{eff} between the two sites. We can write these coupling terms as:

$$\begin{aligned} t_{\mathrm{eff}} &= \frac{c_1 \mu_{\mathrm{ABS}} + c_2 E^{\mathrm{ABS}}_{\mathrm{Z}}}{(E^{\mathrm{ABS}}_{\mathrm{Z}})^2 - \Delta^2 - (\mu_{\mathrm{ABS}})^2} \\ \Delta_{\mathrm{eff}} &= \frac{\Delta t_{\mathrm{SO}} c_3}{(E^{\mathrm{ABS}}_{\mathrm{Z}})^2 - \Delta^2 - (\mu_{\mathrm{ABS}})^2} \end{aligned} \tag{8.6}$$

where the complex coefficients c_1,c_2,c_3 are given by:

$$\begin{aligned} c_1 &= t^2 + t^2_{\mathrm{SO}} \left(\vec{n}_1 \cdot \vec{n}_2 - 2(\vec{n}_1 \cdot \vec{n}_2)_{\hat{z}}\right) - i \left[t t_{\mathrm{SO}} (\vec{n}_1 + \vec{n}_2)_{\hat{z}} + t^2_{\mathrm{SO}} (\vec{n}_1 \times \vec{n}_2)_{\hat{z}}\right] \\ c_2 &= t^2_{\mathrm{SO}} \vec{n}_1 \cdot \vec{n}_2 - t^2 + i \left[t t_{\mathrm{SO}} (\vec{n}_1 + \vec{n}_2)_{\hat{z}} - t^2_{\mathrm{SO}} (\vec{n}_1 \times \vec{n}_2)_{\hat{z}}\right] \\ c_3 &= [t_{so} (\vec{n}_1 \times \vec{n}_2)_{\hat{y}} - t(\vec{n}_1 + \vec{n}_2)_{\hat{y}}] + i[t(\vec{n}_1 + \vec{n}_2)_{\hat{x}} - t_{\mathrm{SO}} (\vec{n}_1 \times \vec{n}_{2\hat{x}})] \end{aligned} \tag{8.7}$$

Since we are only interested in the change in complex phase as a function of μ_{ABS}, we can neglect Δ_{eff} as it only contributes a constant offset. This leaves the phase contribution from t_{eff}, which we can write in the form:

$$\arg(t_{\text{eff}}) = \arg(c_1) + \arg\left(\mu_{\text{ABS}} + E_Z^{\text{ABS}}\mathfrak{R}\left(\frac{c_2}{c_1}\right) + iE_Z^{\text{ABS}}\mathfrak{I}\left(\frac{c_2}{c_1}\right)\right) \tag{8.8}$$

From here, we extract the change in phase $\widetilde{\phi}$ as a function of μ_{ABS}, where we only need to consider the right term in equation (8.8):

$$\widetilde{\phi}(\mu_{\text{ABS}}) = \frac{\pi}{2} - \arctan\left(\frac{\mu_{\text{ABS}} + E_{\text{Z}}^{\text{ABS}}\mathfrak{R}(\frac{c_1}{c_2})}{E_{\text{Z}}^{\text{ABS}}\mathfrak{I}(\frac{c_1}{c_2})}\right) + \phi_0 \tag{8.9}$$

where ϕ_0 is the constant offset added by the phase contribution of Δ_{eff} and $\arg(c_1)$. This result is the general form of the result equation (8.1) presented in the main text.

GAUGE TRANSFORMATION FROM A SPIN-ORBIT FIELD TO A ZEEMAN FIELD

The above result relies on the physically reasonable assumption that a realistic device may have a general spatially varying spin orbit-field that is not necessarily strictly perpendicular to the chain. To simplify the discussion in the main text, we present a simpler case where the spin-orbit field is fixed to be perpendicular and instead the Zeeman field in the ABS is rotated in the y-z plane, captured by a single angle θ_{A}. We show here the equivalence between these two cases via a unitary transformation, where the latter matches a specific orientation of a spatially varying spin-orbit field. With the magnetic field in H_{ABS} misaligned in the z-y plane with an angle θ_{A} we have the following Hamiltonian for the middle site:

$$H_{\text{ABS}}^{\theta} = \psi_i^{\dagger}\left[\mu_{\text{ABS}}\tau_z\sigma_0 + \Delta\tau_x\sigma_0 + E_{\text{Z}}^{\text{ABS}}\cos(\theta_{\text{A}})\tau_0\sigma_z + E_{\text{Z}}^{\text{ABS}}\sin(\theta_{\text{A}})\tau_0\sigma_y\right]\psi_i \tag{8.10}$$

while the tunneling Hamiltonians, fixing $\vec{n} = [0,1,0]$, are:

$$H_T^{i,j} = \psi_i(t\tau_z\sigma_x + it_{\text{SO}}\tau_z\sigma_y)\psi_j \tag{8.11}$$

with $t = t_0\cos\theta_{\text{SO}}$ and $t_{\text{SO}} = t_0\sin\theta_{\text{SO}}$. We can express these matrices as $T = e^{i\theta_{\text{SO}}\sigma_y}$. Utilizing the unitary transformation U that diagonalizes H_{ABS}^{θ} (equation (8.10)) we can transform the tunneling Hamiltonians $H_T^{1,2}$ and $H_T^{2,3}$ using:

$$TU = e^{i\theta_{\text{SO}}\sigma_y}e^{i\frac{\theta_A}{2}\sigma_x} \qquad U^{\dagger}T = e^{-i\frac{\theta_A}{2}\sigma_x}e^{i\theta_{\text{SO}}\sigma_y} \tag{8.12}$$

To match this to the general tunneling Hamiltonian equation (8.5), we then need to solve:

$$e^{i\theta_{12}\vec{\sigma}\cdot\vec{n}_{1,2}} = e^{i\theta_{\text{SO}}\sigma_y}e^{i\frac{\theta_A}{2}\sigma_x} \qquad e^{i\theta_{23}\vec{\sigma}\cdot\vec{n}_{2,3}} = e^{-i\frac{\theta_A}{2}\sigma_x}e^{i\theta_{\text{SO}}\sigma_y} \tag{8.13}$$

which yields the solution:

$$\begin{aligned}\vec{n}_1 &= \frac{1}{\sin(\theta_{12})}\left[\cos(\theta_{\text{SO}})\sin(\theta_{\text{A}}/2),\ \sin(\theta_{\text{SO}})\cos(\theta_{\text{A}}/2),\ \sin(\theta_{\text{SO}})\sin(\theta_A/2)\right]\\ \vec{n}_2 &= \frac{1}{\sin(\theta_{23})}\left[-\cos(\theta_{\text{SO}})\sin(\theta_{\text{A}}/2),\ \sin(\theta_{\text{SO}})\cos(\theta_{\text{A}}/2),\ \sin(\theta_{\text{SO}})\sin(\theta_{\text{A}}/2)\right]\end{aligned} \tag{8.14}$$

and $\theta_{12} = \theta_{23}$. The Zeeman field alignment in the ABS can thus be interpreted as an effective spin-orbit field variation, where the spin-precession is equal but around two vectors pointing symmetrically in different vectors. While this is physically less plausible as underlying mechanism, it captures the essence of the experimental result.

Phase shift with offset in QD-ABS polarisation axis

We now repeat the extraction of the complex phase in the system as a function of μ_{ABS}, with the simpler Hamiltonian terms equation (8.10) and equation (8.11). Again performing a Schrieffer-Wolff transformation, we obtain new expressions for the effective couplings Δ_{eff} and t_{eff}:

$$\Delta_{\mathrm{eff}} = \frac{2\Delta t t_{\mathrm{SO}}}{(E_{\mathrm{Z}}^{\mathrm{ABS}})^2 - \Delta^2 - (\mu_{\mathrm{ABS}})^2} \tag{8.15}$$

and:

$$t_{\mathrm{eff}} = \frac{E_{\mathrm{Z}}^{\mathrm{ABS}}(t^2 + t_{\mathrm{SO}}^2)\cos(\theta_{\mathrm{A}}) + (t^2 - t_{\mathrm{SO}}^2)\mu_{\mathrm{ABS}}}{(E_{\mathrm{Z}}^{\mathrm{ABS}})^2 - (\Delta)^2 - (\mu_{\mathrm{ABS}})^2} + i\frac{2E_{\mathrm{Z}}^{\mathrm{ABS}} t t_{\mathrm{SO}} \sin(\theta_{\mathrm{A}})}{(E_{\mathrm{Z}}^{\mathrm{ABS}})^2 - (\Delta)^2 - (\mu_{\mathrm{ABS}})^2} \tag{8.16}$$

Since the expression for CAR is real, the remaining phase in the system is given by:

$$\widetilde{\phi}(\mu_{\mathrm{ABS}}) = \arg(t_{\mathrm{eff}}) = \arctan\left(\frac{\Im(t_{\mathrm{eff}})}{\Re(t_{\mathrm{eff}})}\right) = \frac{\pi}{2} - \arctan\left(\frac{\mu_{\mathrm{ABS}} + \mu_0}{\Gamma}\right) \tag{8.17}$$

with $\Gamma = 2E_z^{\mathrm{ABS}} \frac{t t_{\mathrm{SO}}}{t^2 - t_{\mathrm{SO}}^2} \sin(\theta_{\mathrm{A}})$ and $\mu_0 = E_{\mathrm{Z}}^{\mathrm{ABS}} \frac{t^2 + t_{so}^2}{t^2 - t_{so}^2} \cos(\theta_{\mathrm{A}})$ as shown in main text. We again stress that this result only predicts a total change in $\widetilde{\phi}$ of π when sweeping μ_{ABS}. In order to fit the equation in figure 8.9, we add a fitting parameter $\delta\widetilde{\phi}$ which sets the separation between the two phase plateaus.

Alternative considerations

The above result, considering a spatial variation in the spin-orbit field, can be a plausible explanation for the experimental result. We stress, however, that further experimental work is needed to pinpoint the exact mechanism, and that alternative effects may need to be considered. A similar connection between phase and charge arises, for example, in electron scattering processes involving a screened impurity in a metal. In this context, the *Friedel sum rule* connects the phase $\tilde{\phi}$ gained by an incoming electron to the charge of the impurity $\langle \hat{N} \rangle$ via [242]:

$$\tilde{\phi} = \pi \langle \hat{N} \rangle \tag{8.18}$$

Since the ABS in our system is essentially a spin-impurity strongly coupled to a superconductor, as considered in the typical YSR-state picture [154], we posit that similar effects may arise when the excited state of the system is a screened doublet. A similar consideration was recently discussed in Ref. [243]. In the superconducting atomic limit, the charge of the ABS can be readily extracted as a function of μ_{ABS}. This would give the following relation between phase and μ_{ABS}:

$$\widetilde{\phi} = \frac{2|v|^2}{\pi} = \pi\left(1 - \frac{\mu_{\mathrm{ABS}}}{\sqrt{\mu_{\mathrm{ABS}}^2 + \Delta^2}}\right) \tag{8.19}$$

Notably, since the total, smooth increase in charge across an ABS in the singlet ground state is $2e$, the phase shift induced by this mechanism would in fact be more than π (namely 2π). Nevertheless, this does not account for the seemingly arbitrary separation observed in figure 6.3. We include it here as a speculative comparison, fitted against the experimental data in figure 8.9. We further note that smooth phase evolutions as a function of chemical potential are well-known in transport through a single quantum dot in an interference loop, where a similar discussion arose [244–246].

8.8 EXTENDED DATA

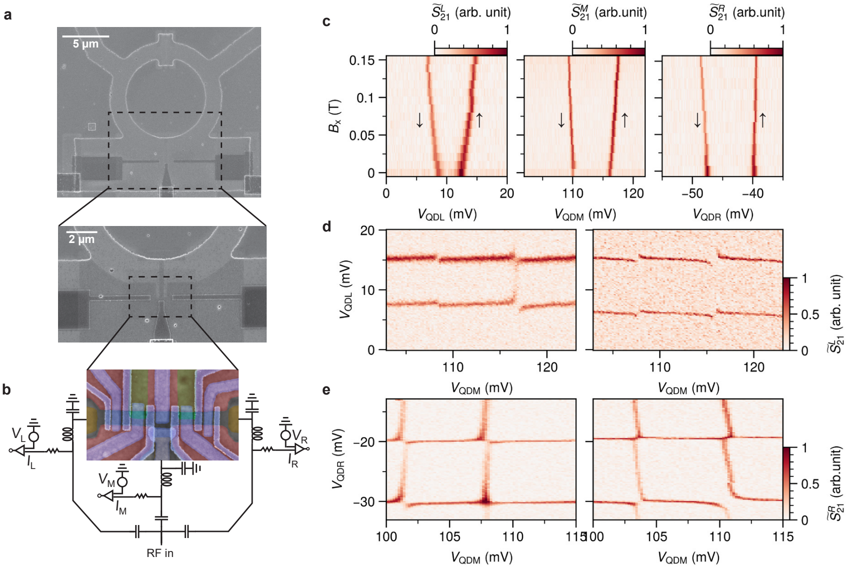

Figure 8.5: **Device and characterization a)** Scanning electron microscopy (SEM) of the measured device, showing the full flux loop (top) and the part of the loop that connects to the device region (bottom). Light areas indicate remaining Aluminium, while the three darker strips are the Ti/Pd device leads **b)** Zoomed in false-coloured SEM of the active region after all three gate depositions. Off-chip lumped element resonators are connected to all three normal leads, allowing for fast reflectometry measurements. **c)** Zeeman splitting of all three QDs used for the measurements of figure 8.2, showing the energy splitting of the two spin states. **d)** Charge stability diagrams of the left and middle QD, showing both CAR (left) and ECT (right) coupling, indicating the existence of sweet spots for both spin states on the left QD. **e)** Charge stability diagrams of the middle and right QD, showing similar behaviour.

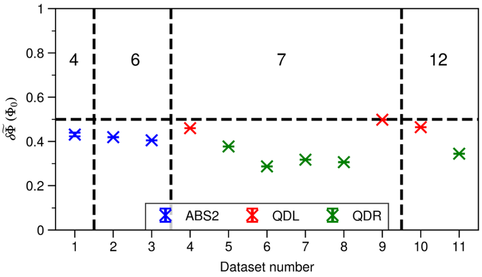

Figure 8.6: **Compilation of datasets demonstrating phase shift reproducibility.** The flux difference $\delta\widetilde{\Phi}(\Phi_0)$ is defined as the flux shift between two differently tuned 3-site chains, where the flux $\widetilde{\Phi}$ of each is extracted using the procedure shown in figure figure 8.7. Different colours indicate which element of the system is responsible for the phase shift. The numbers in the top half of the plot specify the total number of thermal cycles that were performed before the data was measured. All points are projected onto $\delta\widetilde{\Phi} < \frac{\Phi_0}{2}$, since we are unable to distinguish between shifts larger or smaller than π from the relative shifts only. The horizontal dashed line indicates and ideal π-shift.

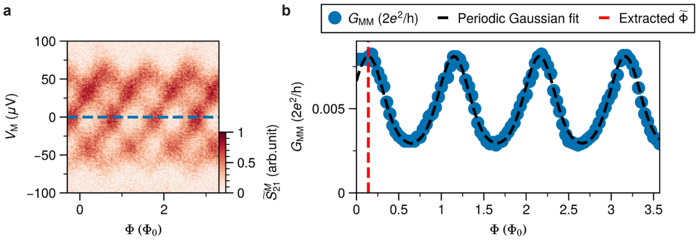

Figure 8.7: **Procedure of extracting $\widetilde{\Phi}$. a)** An example of a flux dependent energy spectrum of a tuned up 3-site chain. **b)** The flux dependent zero bias conductance is fitted to a periodically repeated Gaussian of the form $A_0 + Ae^{-\frac{(\Phi^* - \frac{\Phi_0}{2})^2}{2\sigma^2}}$, where $\Phi^* = (\Phi - \widetilde{\Phi} + \frac{\Phi_0}{2}) \pmod{\Phi_0}$. The extracted flux $\widetilde{\Phi}$ for this example is indicated by the red dashed line. For some of the data in figure 8.6, this extraction is performed on the reflectometry signal S_{21}^{M}, rather than the conductance G_{MM}. There, it was found that inverted Gaussians ($A < 0$) were a better fit, likely due to the non-linear relation between S_{21}^{M} and G_{MM}.

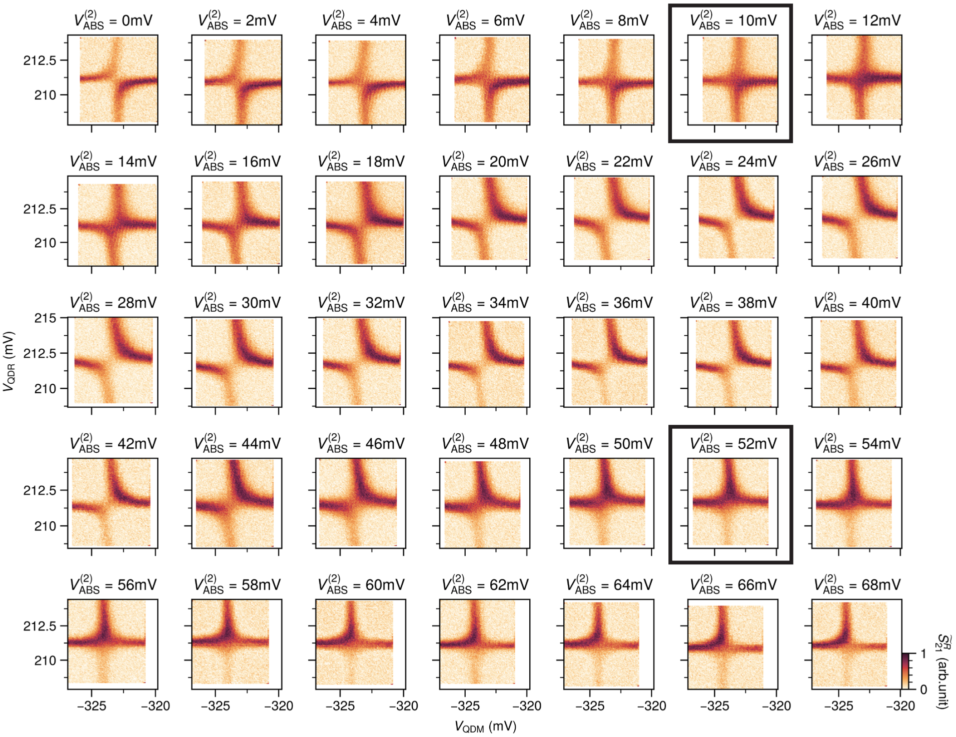

Figure 8.8: **Interaction between the middle QD and the up-spin of the right QD for varying ABS energy.** Full set of CSDs used to identify relevant regimes. Starting at $V_{ABS}^{(2)} = 0$, we observe transitions from $\Delta > t$ to $\Delta < t$ and back to $\Delta > t$, indicating the existence of two sweet spots at $V_{ABS}^{(2)} \approx 10\,\text{mV}$ and $V_{ABS}^{(2)} \approx 52\,\text{mV}$, highlighted by the black squares.

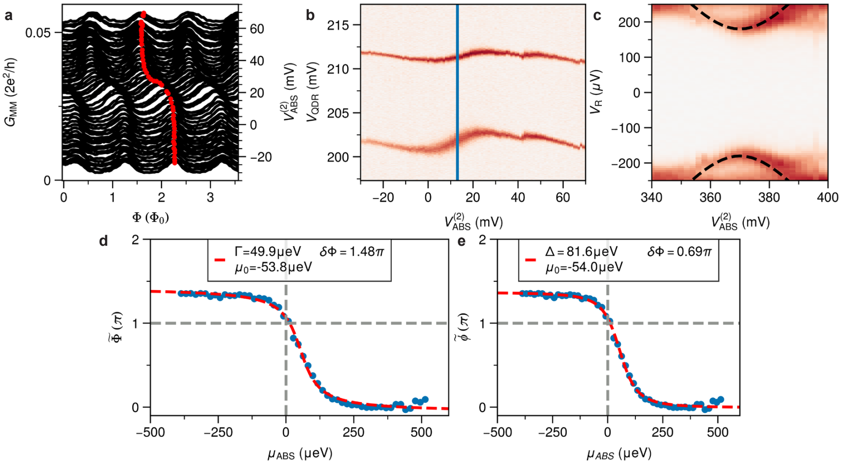

Figure 8.9: **Fitting the flux-dependent conductance measurements as a function of $V_{\mathrm{ABS}}^{(2)}$.** **a)** Compilation of the raw measurements that are used to extract the flux-shift $\widetilde{\Phi}$ presented in figure 8.3c, following the measurement procedure described in section 8.7. Every linetrace is offset by 0.002 $\frac{e^2}{h}$. The selected peaks used to extract $\widetilde{\Phi}$ in figure 8.3c are overlaid. From the continuous measurement it is clear that the total shift exceeds $\Phi_0/2$. To fit the extracted data to the theoretical results, we first map $V_{\mathrm{ABS}}^{(2)}$ to chemical potential μ_{ABS}. **b)** From the charge stability diagram between V_{QDR} and $V_{\mathrm{ABS}}^{(2)}$ (figure 8.3a) we can determine the value $V_{\mathrm{ABS}}^{(2)}$ corresponding to $\mu_{\mathrm{ABS}} = 0$. **c)** Tunneling spectroscopy allows to estimate the leverarm to convert $V_{\mathrm{ABS}}^{(2)}$ to μ_{ABS}. **d)** Fitting of the experimentally observed flux-shift $\widetilde{\Phi}$ as a function of μ_{ABS}, to the derived trend equation (8.1). Since the experimental data shifts between two plateaus separated by more than π, an arbitrary fitting parameter $\delta\Phi$ needed to be included that captures this effect (see section 8.7). **e)** Similarly, we fit the experimental data to the Friedel phase shift (equation (8.19)) , again with an arbitrary scaling parameter $\delta\Phi$. We note that this equation similarly described the data reasonably well, but the validity is speculative.

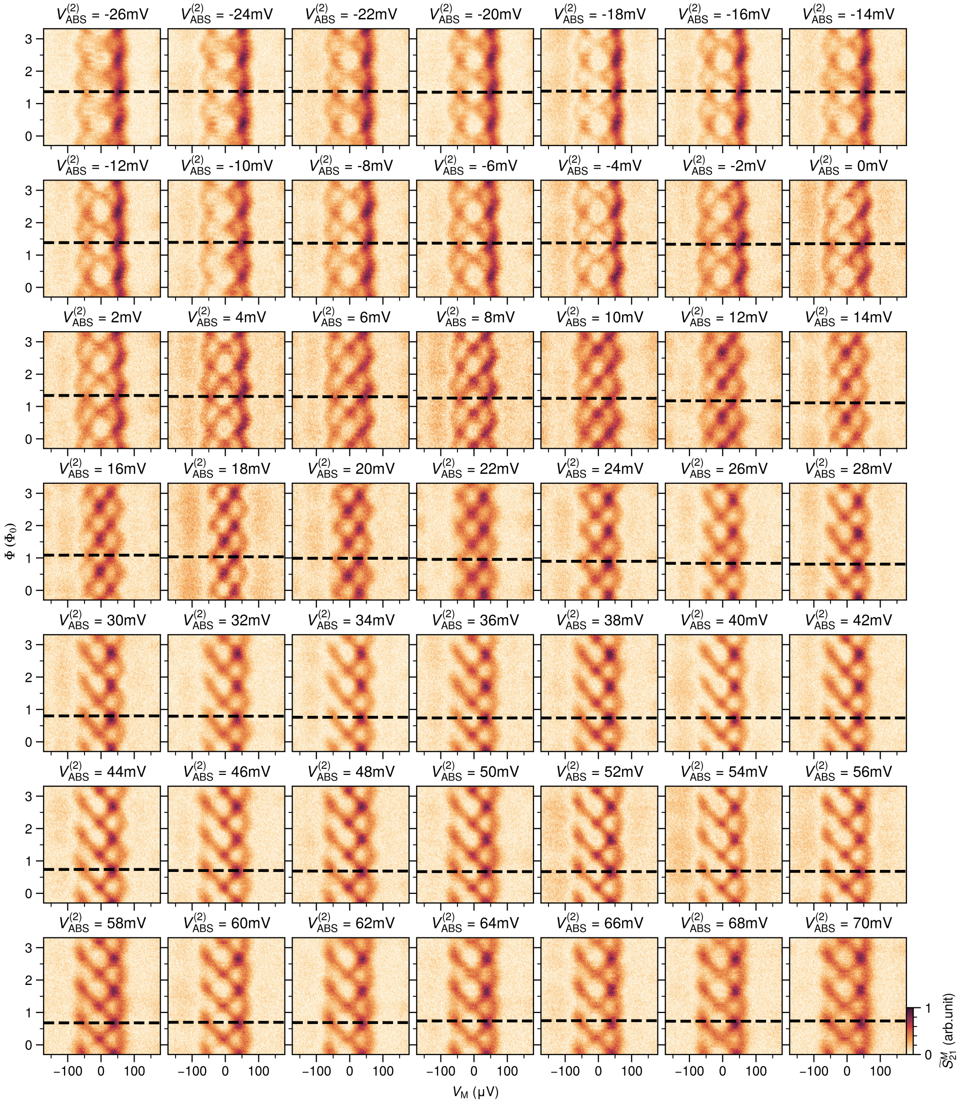

Figure 8.10: **Flux-dependent bias spectroscopy of the ↑-spin for different $V^{(2)}_{\mathrm{ABS}}$.** Finite bias spectroscopy explicitly showing the smooth flux-shift of the up spin presented in figure 8.3c. Horizontal dashed lines indicate a flux where the gap is maximized.

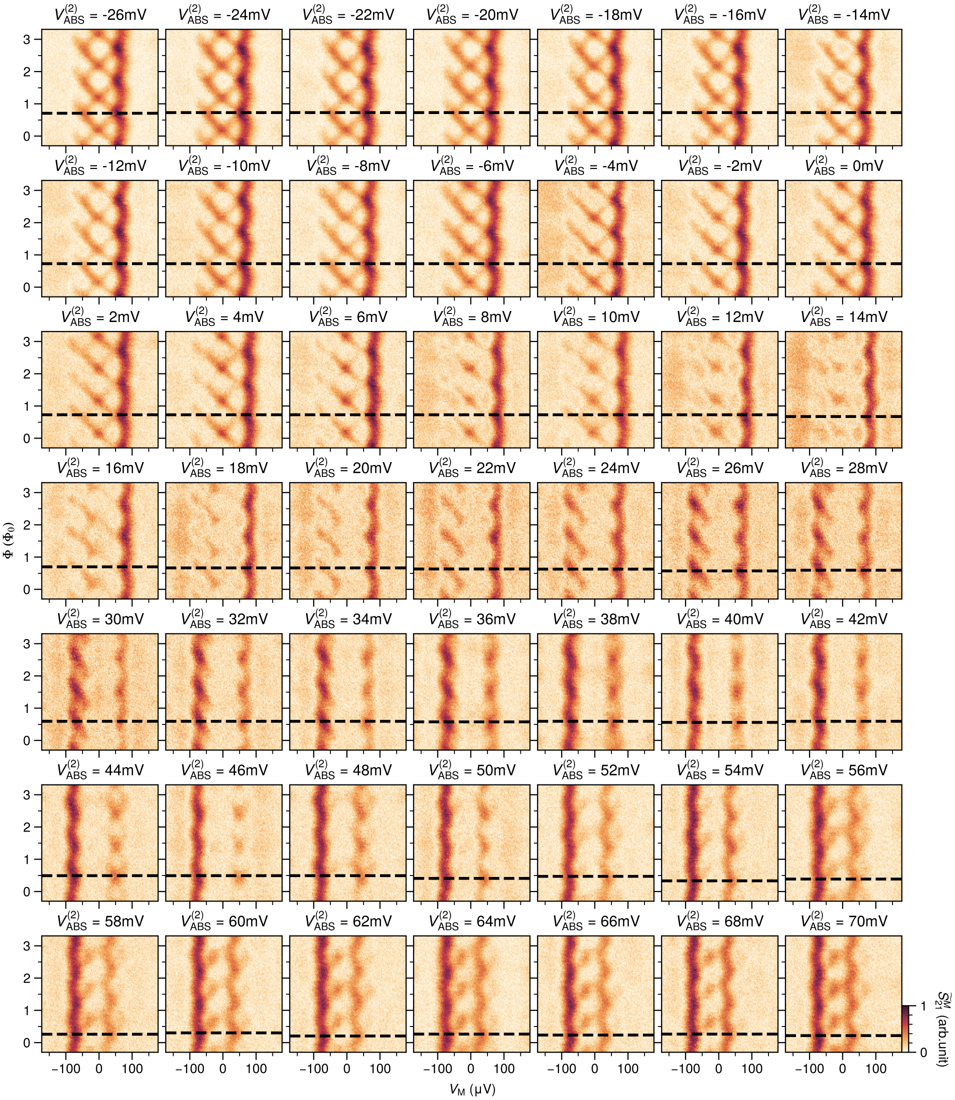

Figure 8.11: **Flux-dependent bias spectroscopy of the ↓-spin for different** $V_{\mathrm{ABS}}^{(2)}$. Horizontal dashed lines indicate a flux where the gap is maximized. The extraction along $V_{\mathrm{M}}=0$ becomes unreliable for $V_{\mathrm{ABS}}^{(2)} < 16\,\mathrm{mV}$.

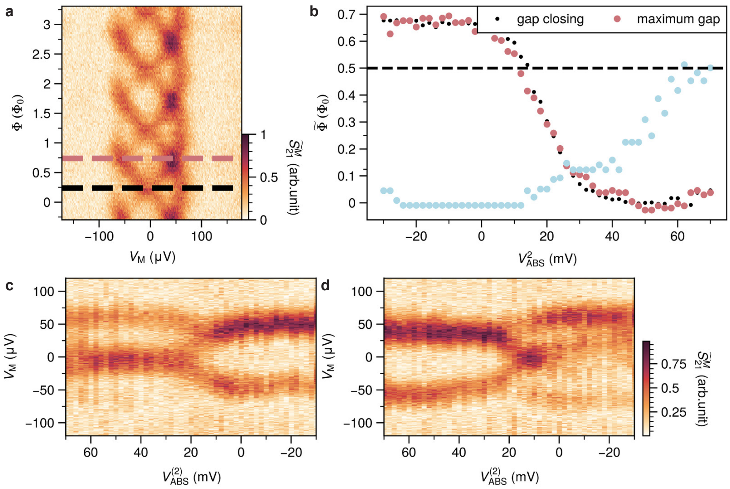

Figure 8.12: **Alternative phase extraction method** In the main text we choose the phase where the gap closes as reference point to track phase shifts in the system. To ensure our result does not depend on the choice of reference point, we compare here with an alternative choice where the gap is maximal instead. We were unable to satisfyingly automate this process and instead utilise a manual extraction for this analysis. **a)** Finite bias spectroscopy at $V_{\mathrm{ABS}}^{(2)} = 70\,\mathrm{mV}$. Points where the gap is either closed or maximal are highlighted as reference. **b)** Phase-shifts as a function of the ABS energy, comparing the two methods. In both cases the evolution follows very similar trends and we find that the choice of extraction method does not affect the conclusions made in the main text. The manually selected phases are shown as dashed lines in figure figure 8.10 and figure 8.11. To see the effect of the larger-than-pi shift, we extract S_{21} linetraces at fixed flux Φ as a function of $V_{\mathrm{ABS}}^{(2)}$. **c)** and **d)** show these traces, starting at the black line and pink line in a) respectively. In c), when the gap starts closed, the gap is reopened by tuning $V_{\mathrm{ABS}}^{(2)}$. In d), the opposite occurs, where the gap is closed at 10 mV Note that the gap reopens again, precisely because the induced phase-shift exceeds a π-shift.

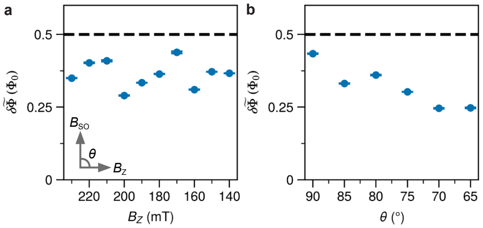

Figure 8.13: **Phase difference between two spin configurations as a function of the Zeeman field strength and orientation. a)** Varying Zeeman field at an angle close to perpendicular to the spin-orbit field ($\theta = 90°$). Significant variation in the extracted phase difference is attributed to the effect of B_Z on the energy of the ABS. **b)** Varying the orientation θ of $B_Z = 200$ mT with respect to the spin-orbit field. The two datasets measured in a) and b) are measured in electrostatically different configurations.

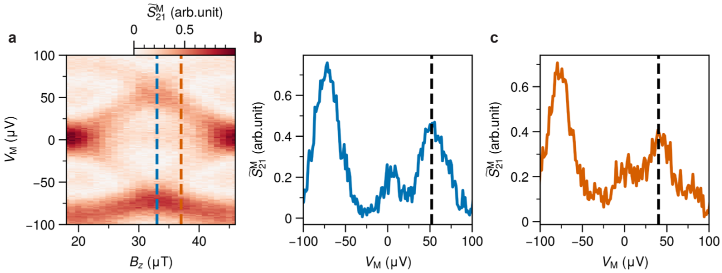

Figure 8.14: **Estimation of the excitation gap reduction resulting from the π shift deviation. a)** Flux dependent spectroscopy of a 3-site chain. **b,c)** Extracted linecuts taken at the maximum energy gap and at a 4 μT deviation respectively. Using b) and c) we estimate a reduction in energy gap from 50 μeV to 38 μeV.

9

OUTLOOK

"Roads? Where we are going, we won't need roads."

- Dr. Emmett Brown

The results presented in this thesis demonstrate that short Kitaev chains can be realized in a two-dimensional electron gas (2DEG) with strong spin–orbit coupling and a large Landé g-factor. This implementation, based on quantum dots coupled via Andreev bound states, enables direct comparison with all parameters of the Kitaev chain model and reveals good agreement between theory and experiment. These advances build directly upon the pioneering work achieved with InSb nanowires [26, 28], which first established the key experimental techniques. The reproducibility of the approach, together with a deterministic tune-up procedure, paves the way for experiments probing the fundamental properties of Majorana bound states. Although the demonstrated techniques will require the fine-tuning of many gate voltages, several promising proposals have now become experimentally accessible [177, 180, 181] thanks to the progress in fabrication and control.

The main motivation for developing these techniques on the 2DEG platform lies in the fundamental limitations ultimately encountered in nanowire-based systems. While advanced fabrication and tuning methods have, for instance, enabled the realization of flux-controlled three-site chains in nanowires [90], scaling to longer systems becomes increasingly challenging. This difficulty arises from the lack of suitable spectral probes (such as the central probe in Chapter 6) and from geometric constraints that restrict nanowire-based QD–ABS chains to essentially one-dimensional, linear arrangements. In this outlook, we highlight two experiments that we expect will explicitly require the 2DEG platform, that can probe the fundamental properties of Majoranas - the features that make them of great experimental interest. Both experiments demand extending the methods developed in this thesis beyond three sites and beyond one-dimensional geometries. First, we outline the expected challenges and necessary developments for scaling the system in section 9.1. Next, we discuss an experimental setup designed to demonstrate the anyonic nature of Majoranas in section 9.2. Finally, we detail experiments in section 9.3 that can probe a key manifestation of the non-locality of the Kitaev chain: the fractionalized entropy associated with individual Majoranas.

9.1 SCALING BEYOND SHORT 1D CHAINS

In this thesis we showed that the technique for tuning a two-site Kitaev chain to a sweet-spot could be readily extended to a three-site chain by pairwise finetuning the couplings between neighbouring QDs. To tune a general N-site Kitaev chain device to a sweet spot, the requirement remains to have control over all chemical potential energies of the QDs and all nearest-neighbour t and Δ couplings. In principle, due to the stabilizing nature of the Kitaev chain with increasing N, the required accuracy on achieving $t = \Delta$ and $\mu = 0$ becomes less stringent. However, overarching conditions on the quantum dots' properties remain: selected resonances must have a sufficiently large level spacing, charging energy and Zeeman energy. For the experiments in Chapter 6, for instance, many QD resonances were ruled out due to not satisfying these conditions or due to instabilities in the electrostatic landscape. Adding the fact that the QD-ABS couplings for different resonances can wildly vary (see figure 3.9), and therefore need to be calibrated per orbital, there does not appear any easy short-cuts in terms of gate-voltages that can be neglected or that can be shared among different QDs. Furthermore, a few problems can arise in longer chains that will cause the system to deviate from the ideal Kitaev model:

- **Long range coupling** - A key assumption in building the Kitaev chain in the quantum dot arrays, is that coupling interactions only take place between neighbouring QD sites. Any longer-range couplings (such as next-nearest-neighbour couplings) will hinder the scalability and tuning procedures [82, 226].

- **Domain walls** - As demonstrated in the three-site chain in Chapter 6, a π-phase difference in the nearest-neighbour coupling terms closes the excitation gap in the central quantum dot. In turn, this destroys the 'protection' of the localized Majorana modes. In longer chains, this issue remains: the relative sign of all nearest neighbour couplings must be the same (the chain should be *sign-ordered*). Any π-phase along the chain creates a so-called *domain wall*, which effectively segments the chain. The protocol studied in Chapter 8 addresses this issue, but we find that microscopic properties of the device may complicate things.

- **Inhomogeneous spin-orbit angles** - In both the two-site and three-site systems we observed a spin-orbit field $\vec{B}_{\mathrm{SO}}$ effectively perpendicular to the 1D channel, such that an external magnetic field $\vec{B}_{\mathrm{ext}}$ could be applied along the channel, maximizing the effect of spin-orbit coupling. In principle, it is not determined whether the most significant effect of spin-orbit coupling arises through hybridization of spin-states of different quantum dot orbitals, or through spin-precession in tunneling processes between neighbouring sites. Any large variation in $\vec{B}_{\mathrm{SO}}$ along the chain can drastically limit the size of the bulk-gap, or prevent scaling the chain altogether.

The latter point may not be an issue in linear systems, as it is well possible that the dominant effect arises during tunnelling processes so that $\vec{B}_{\mathrm{SO}}$ is generally perpendicular to the channel. When extending the system in two-dimensions however, it certainly becomes an important consideration. We discuss this in more detail below in section 9.1.2. The first two points should have measurable effects and can possibly be mitigated. As an example, we highlight below a tune-up procedure of a six-site Kitaev chain device.

9.1.1 TUNING UP A SIX-SITE CHAIN

Figure 9.1a shows a possible design of a six-site Kitaev chain device, extending the design used for the two- and three-site chains in this thesis. We assume here that the aim would be to measure conductance spectra at each QD, requiring an ohmic contact for every QD site. Such a device requires at the minimum a control over 29 separate gate voltages (two depletion gates, sixteen tunneling gates and eleven plunger gates).

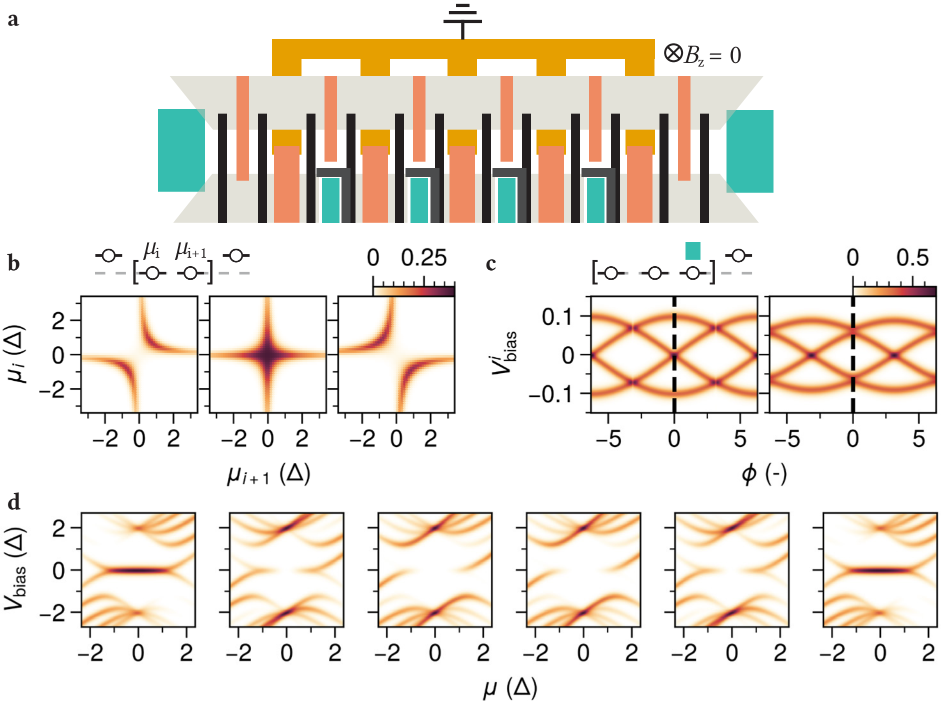

Figure 9.1: **A six-site Kitaev chain device (a)** Schematic overview of the components required for a six-site Kitaev chain device, with the ability to measure tunneling spectroscopy at each QD site. **(b)** When long-range couplings do not play a significant role, the coupling between all QDs can be tuned pairwise in the same way as for the two-site chain, keeping the unused QDs off-resonance. **(c)** The conductance through the middle QD in a three-site subsystems can determine the presence of domain walls, which may be removed using the procedure detailed in Chapter 8. **(d)** Numerical simulation of conductance spectra upon detuning μ for an ideal tune-up: achieving the $t = \Delta$ sweet-spot condition for each QD pair, without any phase differences. A robust zero-bias-conductance peak should be visible on the outermost sites, while all four inner sites show an excitation gap.

Disorder in the depletion gates may complicate the formation of the long channel (see figure 3.5) so that it may be beneficial to split them, requiring control over even more gate voltages. Tuning this large parameter space to the desired regime by hand would be a gargantuan task. It is clear that the fast RF-methods used in Chapter 6 and Chapter 7 will be required in order to characterise this system within any reasonable time-frame. Furthermore, automation will certainly be needed in order to perform these experiments. Much progress has been made in the past years on automating the process of creating and characterising quantum dots [247–251]. The presence of a spectral probe at each QD site should allow for implementing and extending these techniques. For this to be successful, any spurious charges in such a device that can cause drifts or jumps in the quantum dot and hybrid potentials should be minimized to avoided, so that tuned/characterised components remain in the desired parameter regime. The dielectric instabilities observed in the device studied in Chapter 6 for instance, would make scaling the system close to impossible.

Once quantum dots are formed, the next step is to calibrate the coupling between neighbouring QDs. In principle, each QD pair can be calibrated in isolation, by setting all other QDs off resonance. Then, the procedure shown in Chapter 5 can be used to find the sweet-spot for each pair via measuring CSDs (figure 9.1b). Here, the presence of any longer-range interaction will become apparent: the sweet-spot ABS gate value of any of the QD pairs should not depend on ABS gate voltages of other pairs (each QD pair should be tunable independently). Long-range interactions may be suppressed by decreasing the tunnel coupling of QDs to the hybrid regions, at the cost of lowering the bulk excitation gap. The automation of this process through machine-learned recognition of these types of measurements and optimizing a $|t - \Delta|$ cost function has recently been investigated theoretically [252, 253] and experimentally [254].

In principle this procedure can be performed in sequence down the chain. A problem can arise due to the effective phase of the coupling between neighbouring QD pairs, due to the phase difference between neighbouring superconducting probes. The effect of this is shown in figure 9.1c, showing the conductance spectrum of the middle QD in a three-site subsystem, as a function of the phase. If one is unlucky, the bulk-gap is closed without any external flux through the loop connecting the superconductors. Correcting this can be done by threading a flux through each loop (extending the method in Chapter 6) or via current biasing [237], but doing so for every loop adds overhead in addition to cross-talk that may greatly complicate the procedure [236]. The more elegant solution to this problem was explored in Chapter 8 following Ref. [200], where we found that the ABS charge or quantum dot spin-configuration can result in phase -shifts that remove the domain wall, without requiring any additional fluxes.

Finally, we highlight the beautiful experiment that could be enabled by successfully tuning a six-site device in figure 9.1d. In the six-site sweet spot, unpaired Majoranas should arise on the outermost QDs, while the remaining four QDs remain gapped. Detuning all QDs simultaneously should show zero-bias conductance peaks on the outer QDs that remain stable over a large voltage range. While this experiment does not necessarily reveal any new physics compared to the three-site chain, there are interesting considerations in this longer system. Notably, the separation between the outer QDs will be on the order of 2 μm, beyond the coherence length of InSbAs or aluminium. This raises interesting questions about the non-local excitation in the system, which is constructed from the Majoranas on the leftmost and rightmost sites. Furthermore, the coherence time of the Kitaev chain in a qubit context is expected to scale exponentially with chain length - noise coupling to both Majoranas simultaneously over the 2 μm distance indeed seems exceedingly less likely. The timescale limiting experiments is in that case likely set by *quasiparticle poisoning*, free quasiparticles from the superconductor. It will be interesting to see how this mechanism plays a role in this long system.

9.1.2 SPIN-ORBIT INTERACTIONS IN 2D ARRAYS

The previous section discusses the linear scaling of a Kitaev chain device. A possibly reasonable assumption is that angle of the effective spin orbit field $\vec{B}_{\mathrm{SO}}$, which allows for the effective p-wave superconducting pairing between neighbouring QDs, is consistent across the chain. This means that a single in-plane magnetic field direction exists which is nowhere parallel to $\vec{B}_{\mathrm{SO}}$. The experiments discussed in the next two section will require extending the system in a second dimension, where this assumption may break down. One can for example imagine a geometry where two QDs are coupled via an Andreev bound state through an angle of 90°, so that $\vec{B}_{\mathrm{ext}}$ cannot be perpendicular to both QDs simultaneously.

For the design of these devices it will be important to determine whether spin-precession arises mainly in tunneling processes, or whether for instance a significant p-wave component of the Andreev bound state wavefunction allows for the triplet CAR pairing between neighbouring QDs. Figure 9.2 highlights a possible experiment to resolve this. In Chapter 4, we studied the blockade of spin-polarised CAR and ECT, which involves using two QDs coupled to an ABS as spin-filters. Notably, a blockade can also arise when studying direct transport between a QD and an ABS, when applying a voltage bias $E_{\mathrm{ABS}} < -eV_{\mathrm{bias}} < \Delta_{\mathrm{ind}}$. The setup is sketched in figure 9.2a. By applying a magnetic field so that the orbital in the QD is polarised, the spin-polarised current through the QD into the ABS can be studied as a function of magnetic field angle. This measurement is shown in figure 9.2b. Extracting the maximum current for each resonance separately, shows that the current associated with the ↓ resonance is suppressed when $\vec{B}_{\mathrm{SO}}$ is perpendicular to the channel. This is a result of *Andreev blockade* [255, 256], where the singlet Cooper pair states cannot be formed due to the availability of only spin-↓ electrons, so that the flow of sub-gap current into the superconductor is not possible (figure 9.2c). This experiment can be repeated from the opposite side, to get an independent measurement of the spin-orbit blockade of transport via the second QD (figure 9.2d,e). In this instance, we find that the same angle θ results in a blockade of current, which agrees with the overall spin-orbit blockade angle of CAR and ECT studied in Chapter 4. These types of measurements may help resolve the origin of triplet CAR when coupling QDs to an ABS at differing angles. An SEM of a device that may be used to implement this is shown in figure 9.2f.

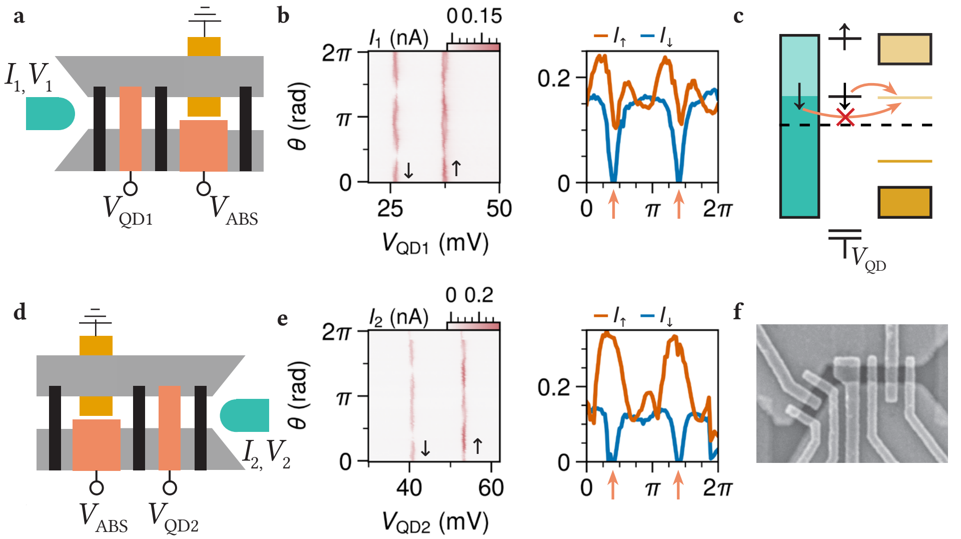

Figure 9.2: **Independent measurement of the spin-orbit angle.** **(a)** Relevant components for measuring the spin-orbit direction in a QD-ABS system. **(b)** Measurement of current arising from local-Andreev reflection as a function of external field-angle. **(c)** Schematic of situation gives rise to 'Andreev blockade' when the magnetic field is aligned with the spin-orbit angle. Only the ↓ resonance experiences blockade when a positive voltage bias is applied. **(d)** For comparison, the measurement can be repeated through the quantum dot coupled to the other side, shown schematically. **(e)** Measurement of Andreev blockade via the QD coupled to the right of an ABS, showing here the same blockade angle for current via de ↓ resonance. **(f)** SEM of an angled device, which could compare the measurements (b) and (e) for the two QDs coupled at different angles. This may help to disentangle the dominant spin-orbit fields in these transport processes.

9.1.3 HIDDEN π-PHASE IN A KITAEV T-JUNCTION

A more subtle effect of extending the Kitaev chain in two-dimensions, relates to the general extra phases that appear when embedding fermionic systems beyond one dimension. This is a direct consequence of the fundamental restriction that fermionic operators cannot be consistently ordered on graphs with branching vertices, without introducing additional sign factors or gauge degrees of freedom [108, 257], which has close relation to the process of extending the Jordan-Wigner transformation to two dimensions [258]. Notably, this ordering phase has observable consequences that will need to be accounted for in Kitaev chain experiments beyond 1-D. To demonstrate this, we show here properties of the Kitaev T-junction - a three-site Kitaev chain with an additional site coupled to the central site. The relevance of this structure will become clear shortly in section 9.2, where such a junction is utilized for braiding of two Majoranas. The Hamiltonian of this system is:

$$H_{\text{T-junction}} = \sum_{i=1}^{4} \mu_i c_i^\dagger c_i + \sum_{i=1}^{2} \left(t_i c_i^\dagger c_{i+1} + \Delta_i c_i^\dagger c_{i+1}^\dagger + \text{h.c.} \right) + \left(\Delta_{24} c_2^\dagger c_4^\dagger + t_{24} c_2^\dagger c_4 + \text{h.c.} \right) \quad (9.1)$$

Naively, one would expect to require $t_i = \Delta_i$ such that the entire system is sign-ordered, to avoid creating accidental domain walls between neighbouring pairs. As sketched in figure 9.3a, indeed this situation appears fully symmetric. A problem arises, however, due to the branch at site 2, coupling the pairs (1,2), (2,3) and (2,4). To see this, we consider the possible three-site subsystems in figure 9.3b. Enforcing for instance the ordering (1-2-3-4), the subsystems in b.ii and b.iii will have a relative π-phase due to the relative order of sites 2 and 4. Unlike in 1D no change in ordering can remove this phase, such that it will have a physical consequences. To observe this in a real system, we propose the experiments shown numerically in figure 9.3c,d. We assume that one can couple 4 quantum dots in a T-junction via 3 superconducting segments, that all t, Δ coupling amplitudes can be tuned to be equal and that the relative phases between each segment can be determined and controlled. We then initialize the system as follows:

1. With μ_4 off resonance, tune the relative phases of the subsystem (9.3b.i) to be equal.
2. With μ_3 off resonance, tune the relative phases of the subsystem (9.3b.ii) to be equal.

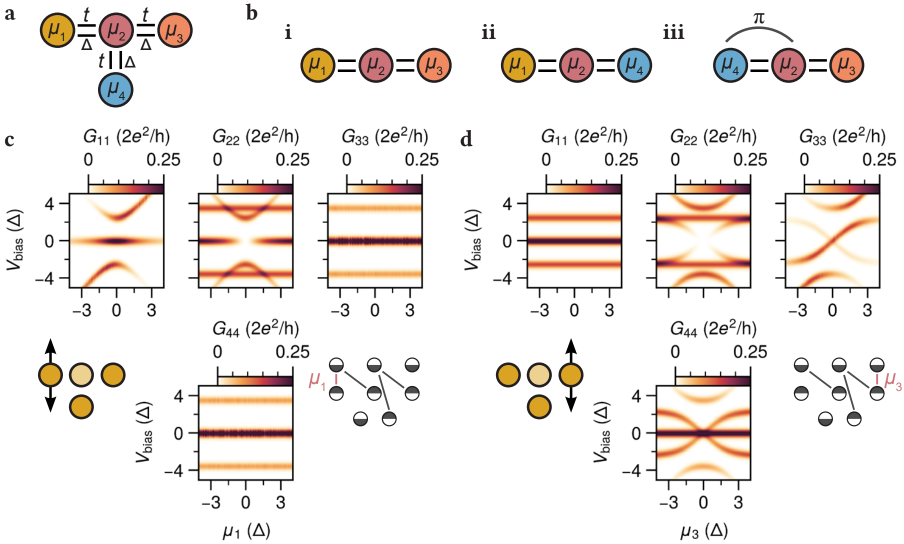

Figure 9.3: **Hidden asymmetry in a T-junction (a)** Components of a Kitaev T-junction: four quantum dots with chemical potential μ_i are coupled via equal elastic co-tunneling (t) and crossed Andreev reflection (Δ) terms. **(b)** To visualize the issues arising from fermion ordering, we can consider detuning each of the outer QDs to effectively create a three-site subsystem, giving i. Detuning μ_4 ii. Detuning μ_3 iii. Detuning μ_1. Here it becomes clear that there is no consistent ordering that will preserve the same sign structure between case (ii) and (iii) - a hidden π phase has appeared. To see the effect of this, we show numerically calculated conductance spectra at each of the four sites, comparing **(c)** the effect of detuning μ_1 and **(d)** the effect of detuning μ_3. In (c), the zero-bias conductance peak gradually decays in G_{11} and appears in G_{22}, as we observed for the well-behaved sign-ordered chain in Chapter 6. In (d) on the other hand, a completely different response is observed, even though the system in (a) appears at first glance symmetric. Due to the extra π-phase enforced by fermion ordering, detuning μ_3 causes the zero-bias conductance peak to split. The Majorana basis picture again provides an intuitive visualisation where the zero-energy modes in the system are located.

Next, we can compare the effect of detuning the QDs while measuring the tunneling conductance on all 4 sites. When detuning μ_1 in this scenario (figure 9.3)c, the expected behaviour is identical to that observed for the sign-ordered 3-site chain presented in Chapter 6: the zero energy mode observed on QD1 is gradually shifted to QD2 while QD3 and QD4 are unaffected. A stark difference is expected when instead detuning μ_3 (figure 9.3d): the detuning instead causes an immediate splitting of the ZBP on the detuned site, even though at first glance the system would appear to be symmetric with respect to swapping site 1 and site 3. The asymmetry becomes more apparent when considering the connected nodes in the Majorana basis. There, we quickly see that turning on μ_1 creates a Majorana localized on site 1 and 2, while turning on μ_3 couples to the delocalized Majorana living on site 2 and site 4.

The presence of the π-phase was previously addressed in Ref [174] in the context of networks of Majorana nanowires. It is important to note that the discussion here does not explicitly include spin-orbit interactions and magnetic field, which will be present in a realistic system. As we saw in Chapter 8, the combination of these elements will also contribute to the complex phases arising in the system. As noted in [174], Rashba spin-orbit may for example automatically ensure that a $\pi/2$ phase is generated at the T-junction, resolving the π-phase issue shown in figure 9.3. The above experiment can also serve to study how these factors come into play in a realistic device.

9.2 NON-ABELIAN ANYONIC EXCHANGE OF MAJORANAS

Assuming that we can resolve the above issues and are able to implement the Kitaev chain in 2D arrays, we can start to consider experiments probing the fundamental properties of Majoranas. Throughout this thesis, the main focus has been demonstrating the 'stability' of Majoranas, whereby a local variation in electrostatic potential does not affect splitting of the zero energy modes. This manifested as robust zero-bias conductance peaks when detuning QD gate voltages. The stability is great for *storing* quantum information: if one can encode quantum information in the joined parity of two Kitaev chains, it is to some degree protected against local noise. What really sets Majoranas apart from electrons, however, is in their exchange statistics.

In three dimensions, only two different types of particles can exist: fermions and bosons. Moving one particle around another in three dimensions is topologically equivalent to doing nothing at all, restricting the possible phases acquired under particle exchange to 1 or -1. In two dimensions this is not the case: it was shown that particles can exist that acquire any arbitrary phase under exchange, dubbed *anyons* [259, 260]. Majoranas, arising at a non-trivial degenerate ground-state, are predicted to be *non-Abelian* anyons. The exchange of Majoranas results in a non-trivial phase arising in the degenerate ground-state of their hosting system, and the order of exchange of Majoranas affects the outcome of these operations. These property lie at the foundation of proposals for fault-tolerant quantum computation [13, 15]. So far, the exchange of anyonic particles has been simulated on larger quantum processors [261–263] and evidence of anyonic properties has been observed in fractional quantum Hall states [264]. The direct demonstration of the exchange of two anyonic quasi-particles has, however, as of yet not been shown experimentally.

To observe the anyonic, non-Abelian nature of Majoranas, a system with a minimum of four Majoranas is required. One can consider, for example, connecting two Kitaev chains in the globally even parity sector, so that the ground state is the state $|00\rangle$ (both chains even) or $|11\rangle$ (both states odd). The effect of exchanging n Majoranas is algebraically equivalent to the Braid group B_n [265], hence the exchange of Majoranas is generally referred to as *braiding*. The effect of exchange Majorana i and j in a system with 4 Majoranas is thus governed by the operators B_4^{ij}, which affect the ground-state as follows:

$$B_4^{12}|00\rangle = \frac{1+i}{\sqrt{2}}|00\rangle \qquad B_4^{23}|00\rangle = \frac{1}{\sqrt{2}}(|00\rangle + i|11\rangle) \tag{9.2}$$

The aim of braiding experiments is to demonstrate that a non-trivial phase arises on the ground-state due to exchange of Majoranas (anyonic property) and that this phase depends on the order of different exchanges (non-abelian property).

9.2.1 GATE-BASED BRAIDING

A compelling way to perform the above braiding operations, is to physically move Majoranas around each other in two dimensions. This is been proposed to be possible through manipulating the chemical potential energies in a system to 'push' Majoranas around [174, 180]. In Chapter 6, we demonstrated that the Majorana wavefunctions can indeed be shifted between neighbouring sites without splitting the zero-energy modes, provided that an excitation gap is present in the receiving quantum dot. This would lie at the foundation of the braiding scheme considered in Ref. [180], drawn schematically in figure 9.4a.

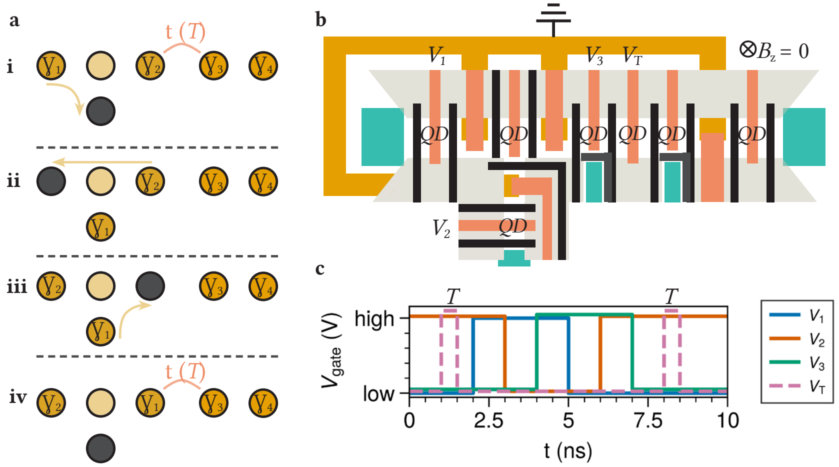

Figure 9.4: **Gate based braiding of Majoranas (a)** Schematic overview of a braiding procedure, adapted from [180]. A y-junction is tunnel coupled to an N-site chain, each tuned to their sweet-spot so that 4 Majoranas are present. By manipulating the electrochemical potential of each QD, γ_1 and γ_2 change positions. **(b)** Example of a device architecture required to implement such a protocol experimentally, omitting readout tools. **(c)** Pulse sequences on the gate voltages in the device illustrated in (b), to implement the exchange of two Majoranas illustrated in (a).

The experiment requires two Kitaev chains at a sweet spot, with a tunable coupling t between the two chains that can be turned on or off. The full procedure is detailed in [180], but the essence is the following: by initializing the two Kitaev chains in a specific parity ground state through turning on the coupling t for some time T, the phase acquired through swapping γ_1 and γ_2 can be detected when reading out the ground-state of the system after completing the sequence in figure 9.4a. A device layout that could be used to implement such a procedure is sketched in figure 9.4b. Here, an additional quantum dot is included that can control the coupling between the two Kitaev chains via the voltage V_{T}, with better tunability and reduced cross talk compared to a single finger gate. Creating and characterising such a device by itself would already be an achievement and will require non-trivial fabrication techniques, for example to contact the leftmost lead inside the superconducting loop as done in Ref. [236] or to route all the finger gates without shorting the system [266]. To perform the experiment, fast pulses need to be applied to the plunger gate voltages, shown in figure 9.4. These should be performed slow enough so that the transfer of Majoranas is adiabatic, but fast enough as to not be affected by the coherence time of the two-site subsystem, expected to be on the order of ≈1-10 ns [80]. The exact shape of these pulses can be optimized [233] to allow for faster charge transfer, while remaining in the adiabatic regime. We intentionally omit the precise readout procedure here, which is currently another field of active research. Recent experiments have shown that quantum capacitance of the superconductor can be used to readout the parity of a two-site Kitaev chain [267]. This could similarly be implemented in the geometry shown here and other suitable methods have been proposed [179, 181].

9.3 OBSERVING THE FRACTIONAL ENTROPY OF MAJORANAS

Another interesting aspect of the Kitaev chain, is that the unpaired Majoranas at the edge in principle form a *non-local* Fermion. The wavefunction of this state lives only on the two edges of the chain. Whether this state is occupied cannot be inferred from any measurements that involves only either edge of the chain: the excitation stores *non-local information.* This has interesting consequences for the fundamental physical property of entropy, which counts the number of microscopic configurations of a system. For a regular system, the Boltzmann entropy is defined as $S = k_B \ln \Theta$, where Θ is the number of microstates. Any regular two-level system has an entropy of $S = k_{\mathrm{B}} \ln(2)$, which is thus generally the smallest possible entropy increment. Each Majorana individually however, can be shown to contribute an entropy of only $S = \frac{1}{2} k_B \ln(2)$. This fractionalized entropy is in fact a general signature of topologically non-trivial systems [268–270]. In the context of the Kitaev chain this can be understood as each Majorana ‘storing’ halve the information of their combined fermionic excitation.

An exciting advance in recent years has been the development of an experimental technique that can accurately resolve changes in entropy. This technique has been shown to be able to resolve the $k_B \ln(3)$ and $k_B \ln(2)$ entropy plateaus of a quantum dot [271], later adapted for more general systems [272, 273]. At the same time, theoretical proposes were put forth on how to apply such a technique to measure the fractional Majorana entropy [274, 275]. It seems like a natural progression to extend the techniques developed for measuring the entropy of quantum dots, to the quantum-dot based Kitaev chains developed in this thesis.

The core of the technique is applying Maxwells equation to relate the change in entropy of a system to a temperature dependent change in average occupation N:

$$\left.\frac{\partial N}{\partial T}\right|_{\mu} = -\left.\frac{\partial S}{\partial \mu}\right|_{T} \quad \Rightarrow \quad \Delta S_{\mu_1 \to \mu_2} = \int_{\mu_1}^{\mu_2} \frac{dN}{dT} d\mu \tag{9.3}$$

In other words, the change in orbital occupation as a result of temperature broadening, is related to the change in entropy when shifting the electrochemical energy. For a quantum dot, the intuition is as follows: if any temperature broadening of an attached reservoir causes an increase in the occupation of the quantum dot, one can infer that there is a large number of states available near E_F. In turn, this means that detuning the quantum dot (μ) will have an effect on the entropy, since this then reduces the number of available states. The strategy is thus as follows:

1. Couple a quantum dot to a system such that its chemical potential μ changes the total entropy S (for instance through capacitive action on the system).
2. Measure the change in occupation N with respect to a change in temperature.

In order to vary the temperature, Refs.[271, 273] rely on driving a current through a nearby reservoir which raises the average electron temperature on very short time scales. The next step is to find a way to make the entropy dependent on the N. A subtle point arises here, since detuning only a single QD in the Kitaev chain does not remove the Majorana (the system remains degenerate), while detuning both QDs removes both Majoranas (corresponding to a trivial $\Delta S = k_B \ln(2)$). Instead, the presence of one of the Majoranas needs to be masked, which can be achieved through a strong coupling to the reservoir, requiring $\delta < \Gamma < k_b T$. Figure 9.5a,b show two possible experimental setups that can be used to measure the fractional entropy contribution of a single Majorana[1].

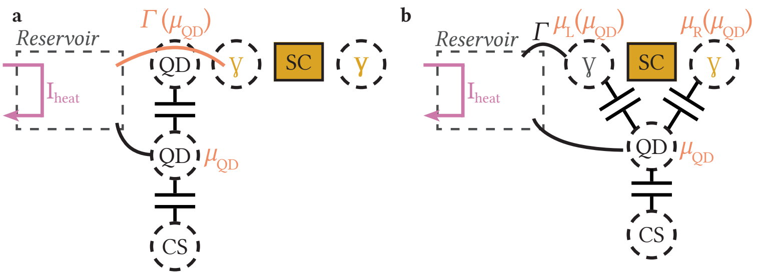

Figure 9.5: **Measurement setups for measuring fractional entropy of Majoranas.** The fractional entropy of Majoranas can be detected in two related, but distinct ways. **(a)** A two-site Kitaev chain is coupled to a quantum dot, which controls the coupling Γ to a temperature-controlled reservoir. The coupling can be turned on or off due to a capacitive coupling to another quantum dot. **(b)** A Kitaev chain is coupled to a reservoir with a constant $\Gamma > T$, masking the entropy of one Majorana. An additional quantum dot couples to both QDs of the Kitaev chain, so that the extra QD can push the Kitaev chain out of the sweet spot.

---

[1] Schematics based on discussions with Joshua Folk and Silvia Lüscher Folk.

ACKNOWLEDGMENTS

Writing this thesis has been a joyful journey that allowed me to explore the world of condensed matter research, travel to great places and meet many inspiring people. The journey began back in 2021 during my MSc in the lab of Leo, and continued in the neighbouring lab of Srijit, leading to numerous fruitful collaborations in the “Kitaev team”. I am grateful to many people, whom I will gladly acknowledge in this final chapter.

To start, **Srijit**, I am extremely happy that you brought me on board after my MSc project. When I asked around whether joining your lab would be a good idea, I found out your students happily return to drink a beer with you after leaving. In addition to the promise of a cool project and learning that you enjoy playing darts, this was all the convincing I needed. You gave me the freedom to explore, while keeping me focussed on finishing projects. You taught me the importance of engaging scientific storytelling, so that I may now be able to write a proper introduction on my own. I hope to one day find out that you have opened your own restaurant/bar in Delft, so that I can stop by and beat you in darts. **Michael**, over the years we started working together more closely, which has been a great experience. Thank you for taking me seriously as I slowly attempted to get a grip on the theoretical side of my projects. You are one of the kindest professors I have met and it was very valuable to have you as my promotor. **Leo**, unfortunately we did not get to interact much during my MSc project, so I was very glad to see you gradually reappear in the weekly meetings and even the lab. Your approach to research and experience has been extremely insightful.

Onto my dear paranymphs - **David**, I am glad to make this the second time that the term “boxershort-cocktail-VAP” appears in a scientific document, as that is where our friendship started over 10 years ago (or was it the “badjas-das VAP”?). As I have joked, you have been my life coach from the start: someone whose humour I deeply appreciate and who reminded me there are countless exciting things to pursue. My general thought has been: if it seems like a good idea to David, it probably is. Therefore, joining your lab as a MSc student and becoming colleagues was an easy choice. Stay groovy and keep on finding the humour in the most absurd of places. **Qing**, you were the first person I spoke to about joining Srijit’s lab and I immediately knew you were a great guy. You quickly taught me everything about fabrication and experiments so that I could make a running start. Struggling through our first paper together and leaning how to trick Srijit into fixing our text was a pleasure. I will cherish our runs together where you, the marathon runner, philosophised about life, while I attempted to catch my breath. Lastly, you’ll forever be a hero for saving our experiment by coming out of *TPKV* to retrieve the chip I dropped into the wet bench at 17:30 on a Friday.

Next, I would like to thank all the other amazing people I worked with in and outside Delft. **Alberto**, I could not have wished for a better person to introduce me to experimental research and nano-fabrication. Your enthusiasm for every success, big or small, has certainly motivated me to stay after our initial project. Watching you go from the ups and downs of the early project to completing a very successful PhD has been inspiring and well-deserved. You are truly someone who can achieve anything when you put your mind to it. I hope Switzerland suits Lucia and you and I hope to see you on the slopes next year (or even better: that we can finally go ice skating on natural ice!). **Tom**, you took me under your wing that faithful summer when SAG appeared less-than-ideal and Kitaev chains emerged. After following you around for two days you entrusted me with the measurements, telling me: “Tonight you may be the first person in the world to measure true Majoranas, good luck”. Later, you convinced me that I could do a PhD and introduced me to Srijit. I cannot sufficiently emphasise your role in bringing this thesis to fruition. **Guan**, you are one of the smartest people I know and it was inspiring to work with you as a starting PhD student. **Ivan**, you combine the broadest (technical) knowledge of pretty much any topic with the most chill and laid-back attitude. Although our work-schedules at one point were nearly opposite (it is still a shame we did not try the world-record fabrication round), it was great to share an office with you. **Christian**, although you are every time too humble, I want to thank and credit you again for setting up the next generation of RF-experiments for the lab. **Rebecca** and **DJ**, you were wonderful office mates in the second half of my PhD. Both of you bring an amazing amount of energy to work. This was not great for my ability to focus, but perfect for my enjoyment of coming to the office. Rebecca, I truly hope the flip-chip community one day embraces the Broodje Kaas© naming convention. DJ, I will miss you asking me every question that comes to your mind (*"Hoe werkt het Nederlandse koningshuis?"*) that trick me into talking about random events I know far too little about myself for hours. I still hope that I will soon lose our bet and have to return to Delft to jump in the canal. Moving across the hallway to the rival office: **Yining**, it was great both starting around the same time as apprentices of Qing. You are a very chill and dedicated person that we can always count on in the lab/office. **Wietze**, your ‘*nuchtere Hollander*’ vibe is a much needed addition to the lab. You are getting too good at darts and I wish you would stop practising. I thank you for handling my *muggenziften* in completing our last project together. **Sebas**, you have been a consistent reminder that the most important thing in science communication is to include *memes* in your presentations. You can and should give yourself more credit as a researcher, you’re going to go far old man. Don’t get distracted by the *noise*. I loved our California road trip with Francesco, Yining and Wietze in the back, cruising through the mountains while listening to Charlie XCX and you in the front trying not to puke. **Francesco**, you have one of the best experimental intuitions of anyone I know. More importantly, you are an amazing and fun person to work with. It is a shame our scientific collaboration in terms of output has been limited to the epoxy gift for David. On the other hand, that project is outlasting both our PhDs, so it may be for the best. May the best tradition of *Italian lunch* live on when you and Nick start the Kitaev company©. **Nick**, I am very happy that you have been a constant presence throughout my entire PhD. You can take the work very seriously and push for great results, but also understand the importance of having fun (also, ‘don’t be a baby’). **Greg**, I am absolutely certain you make for a great lab leader, best of luck building your materials empire in Santa Barbara. **Sebastian**, my other namesake in the E-wing. Trying to keep up with you and **Mert** on the theory side taught me so much and it was a great pleasure to work on our final project together. Many thanks for indulging me and my theory obsessions. Your laugh

resonating through the E-wing will certainly be missed. **Chunxiao**, it was invaluable having you around as in-house theorist of the Kitaev team. You are very pleasant to work with and it is much appreciated you made time to answer all our theory questions despite seemingly always running ten projects already. **Juan**, you are a super chill guy, it was super nice we got paired up in Capri. **Jaap** and **Figen**, I have to mention of course our legendary road trip from Las Vegas to San Francesco with Qing. We somehow squeezed a two-week schedule into three days and saw the entire state of Nevada and California, while somehow still finding time to relax and grab a beer and sing karaoke. Even though we had not been in room together before with the four of us, it clicked straight away and felt like a crazy adventure. **Bart**, I was very glad you decided to stay after your MSc project. You are always the most positive person, which is a delight. I think any other person with the task of maintaining the UTS may have ragequit. **Florian**, **Vincent** and **Antonio**, it is amazing to see the next generation of crazy measurements that you are running while maintaining the fun atmosphere that I've come to love. I am excited to see what the next few years will bring. Then last of this section but definitely not least: the people who keep the labs running and the research flowing. **Raymond S.**, **Raymond V.**, **Olaf**, **Jason**, **Erik**, **Tom**, thanks for your invaluable contributions and support in keeping the systems running and developing the new experiments (and for your endless patience in answering questions). If I ever was productive, it was definitely in part due to the presence and support of great MSc students. Starting with **Philip**, I supervised you at a point at which I barely understood the measurements myself: thank you for your patience in being supervised by me. **Praveen** and **Eoin**, you brought a great amount of fun energy to the lab. **Tijl** and **Vincent**, I don't know what I was thinking when I agreed to supervise two MSc projects at the same time, but I certainly do not regret it. Seeing you both grow into your projects and getting excited to run the measurements was a great motivation for me as well. **Tijl**, you are a very kind and thorough person. Even though you had setbacks in the measurements and in your health, you stayed very dedicated (*"Is it okay if I miss days of research when I am in the hospital?"*) and you completed a great MSc thesis with one of the most visually appealing presentations I have seen. **Vincent**, your approach to physics experiments is the same as your approach to being a defender in football: storming any problem head on with full confidence, worrying about details later (a successful approach I must add!). I do hope you never again traumatize the Italians by preparing frozen pizza in the microwave.

One of the big perks of doing research has been travelling the world to meet others working on the same niche topics. **Gorm**, it was a great pleasure to run into you at many conferences. Whether it is about Shiba chains or about the subtleties of the Danish language, talking to you is always a joy. **Rouven**, although you eventually came to Delft and even joined the football team, our collaboration happened entirely via zoom, which worked surprisingly well. It was very nice to join in on the project with David and you. **Georgios**, thank you for having me visit your lab for six weeks during my second year. Visiting Vienna and Klosterneuberg (by train of course!) and experiencing a different environment was exactly what I needed at that time. I probably joined the most chaotic, legendary meeting of all time on the first day that I was there. You seem to have figured out the perfect balance of being a PI and being a researcher. **Maksim** and **Paul**, I had a lot of fun joining your projects during that time, going running with **Jaime**, playing football

with **Marco** and having drinks on Friday with the entire lab. **Josh**, in addition to being on my defence committee, I really appreciated the warm welcome you and **Silvia** gave me when I visited Vancouver. Even though I was very jet-lagged and only happened to come because Srijit had the misfortune of having to go to Hawaii, I had a very pleasant time and really enjoyed learning more about the work in your lab and discussing experiments.

Hoezeer ik van het onderzoek genoten heb, ben ik blij dat er ook heel veel mensen zijn geweest die er voor hebben gezorgd dat ik meer dan genoeg andere dingen heb beleefd. De jaarlijkse wintersport squad, *Hot Rod*, *Da Vinci '15*, *de Dinnies*, *de Leo's*, *de Quantum Warriors*, *HVV'5* (nu met heuze trainer!), de oud-bewoners van de *VKK* en de *Nieuwe Rijn* en alle andere vrienden en familie: heel veel dank voor de nodige afleiding, beweging en vooral het plezier. **Hester**, ik wist al dat jij mijn meest creatieve vriendin bent, oneindig veel dank voor het ontwerpen van de prachtige cover van dit proefschrift.
Tot slot wil ik graag mijn fijne, betrokken familie kan bedanken. **Fenna** and **Nienke**, ik heb jullie vroeger vaak *geragebait* door te zeggen dat wat jullie op school deden minder cool was dan wat ik deed (*"Doen jullie dat nu pas? Dat deed ik twee jaar geleden al"*). Ik ben trots dat jullie mij allebei inmiddels hebben ingehaald terwijl ik in het lab aan het spelen was. Nienke, ik ben blij dat jij in het zoeken van je eigen succesvolle weg altijd binnen dezelfde muren in Delft uitkwam; ik heb veel gehad aan onze vele koffies samen (ook al leek ik waarschijnlijk vrijwel altijd gestrest). Fenna, op iets meer afstand ben ik dankbaar dat jij als lieve zus altijd het moreel kompas van ons gezin bent gebleven. **Pap** en **mam**, al heb ik het niet vaak toegegeven, is mijn pad tot PhD'er toch wel zeker geïnspireerd door jullie verhalen uit jullie tijd in Leiden. Hoewel deze verhalen zich meestal beperkten tot dezelfde drie anekdotes, was ik toch zeer benieuwd om eens in kijkje te nemen in dat leven. Veel dank voor alle interesse in mijn werk, wat zich zelfs heeft geuit in het proeflezen van papers en dit proefschrift. Tot slot, liefste **Char**. Niemand heeft vaker de woorden "alleen nog even een meting aanzetten" of "mijn proefschrift is bijna af" gehoord dan jij. Ik kan je echt niet genoeg bedanken voor je steun en geduld de afgelopen jaren, maar bovenal voor alle fijne momenten en leuke dingen die we samen hebben meegemaakt. Ik leer nog elke dag heel veel van jou, dank je dat elke dag samen met jou weer een nieuw avontuur is.

Bas
Delft, February 2026

A

NUMERICAL TRANSPORT CALCULATIONS

To obtain the numerical transport calculations throughout this thesis, code was developed for calculating the conductance of a system described by a many-body Hamiltonian in a Fock basis [276]. This is a three step process that entails:

1. Constructing the matrix representation of a Hamiltonian in a given many-body basis.
2. Solving for the eigenvalues and eigenvectors either through exact diagonalization or by approximating the lowest N eigenstates and eigenvalues.
3. Calculating the currents that would flow if ohmic leads were attached to the system, by solving a rate equation.

A variety of open source packages exist with similar purposes [277–279], this separate code was developed specifically for the types of problems of experimental interest in the context of this thesis. We describe here briefly how the calculations are implemented.

DATA STRUCTURE

The aim is to minimize the data required to describe the system and restrict the required computations to binary operations, which can be implemented efficiently. To store the Fock states, we use a binary representation so that each integer represents a unique state. We take a Fock state representing the occupation of L spinful fermionic sites $|\phi\rangle = |n_{0,\downarrow}, n_{0,\uparrow}, \ldots, n_{L-1,\downarrow}, n_{L-1,\uparrow}\rangle$ ($\hat{n}_{i,\sigma} = c^{\dagger}_{i,\sigma} c_{i,\sigma}$) and map it to the binary string $(n_{L-1,\uparrow} n_{L-1,\downarrow} \ldots n_{0,\uparrow} n_{0,\downarrow}) \in \{0,1\}^L$, storing the corresponding integer:

$$|0\rangle = 0\ (0) \quad |{\downarrow}\rangle = 1\ (1) \quad |{\uparrow}\rangle = 10\ (2) \quad |0, {\downarrow\uparrow}, 0, {\uparrow}\rangle = 10001100\ (140) \tag{A.1}$$

The binary is read with the least significant bit corresponding to the first site, so that the representation is independent of the number of sites in the system.

For fermionic creation and annihilation operators we similarly use a binary representation, stored as nested lists of integers to represent products and sums of operators. Each operator

$c^\dagger_{i,\sigma}, c_{i,\sigma}$ is mapped uniquely to a binary with the least significant bit specifying whether it is a creation or annihilation operator and the remaining bits storing the bit-position in the Fock state binary the operator should act on ($= 2i+\sigma$). In this convention:

$$c^\dagger_{0,\downarrow} = 0\ (0) \quad c_{0,\downarrow} = 1\ (1) \quad c_{2,\downarrow} = 1001\ (9) \quad c^\dagger_{3,\uparrow} = 1110\ (14) \tag{A.2}$$

As convention, the empty list represents the null operator and the nested empty list represents the identity operator:

$$\hat{0} = [\ ] \quad \hat{I} = [[\ ]] \tag{A.3}$$

which allows for defining a consistent multiplication and addition scheme. All operators are then represented in a unique fashion by a non-empty nested list:

$$c^\dagger_{0,\downarrow} = [[0]] \quad c_{0,\uparrow} = [[3]] \quad c^\dagger_{0,\downarrow}c_{0,\downarrow} + c^\dagger_{2} = [[1,0],[5]] \tag{A.4}$$

Each sublist is stored with the rightmost operator in the first position. For each operator sequence an additional list is stored for any prefactors. Normal ordering can be implemented by sorting each list in descending order, separated by parity, which allows for tracking the number of swaps to determine the correct signs.

$$\begin{aligned} c_{1,\downarrow}c_{2,\downarrow}c^\dagger_{0,\uparrow}c^\dagger_{1,\downarrow}c_{0,\uparrow} &= [[3,4,2,9,5]] \\ :c_{1,\downarrow}c_{2,\downarrow}c^\dagger_{0,\uparrow}c^\dagger_{1,\downarrow}c_{0,\uparrow}: &= [[9,3,2],[9,5,3,4,2]] = c^\dagger_{0,\uparrow}c_{0,\uparrow}c_{2,\downarrow} + c^\dagger_{0,\uparrow}c^\dagger_{1,\downarrow}c_{0,\uparrow}c_{1,\downarrow}c_{2,\downarrow} \end{aligned} \tag{A.5}$$

Finally, we implement the action of an operator on a state in their binary representation through algorithm 1:

Algorithm 1 Action of an *operator* on a Fock *state* in the binary representations.

```
check_bit = operator & 1                              ▷ Determine creation or annihilation
flip_bit_position = operator ≫ 1          ▷ Shift operator by 1 to get position of bit to flip
flip_bit = 1≪ flip_bit_position                              ▷ Send a 1 to correct position
destroyed = ((flip_bit & state)==0)==check_bit         ▷ Check if operator destroys state
if ~ destroyed then
    sign = hamming_weight(state & ( flip_bit -1)) & 1        ▷ Determine fermionic parity
    new_state = state ⊕ flip_bit                   ▷ Flip the relevant bit to create new state
    return $new\_state, sign$
else
    return $-1, sign$                                      ▷ Return -1 for a destroyed state
end if
```

This provides an efficient mapping $f(operator, fock\ states) \rightarrow fock\ states$ that allows to construct a sparse representation of the Hamiltonian. For example, acting the operator $c^\dagger_{0,\uparrow}$ on a subset of Fock states:

$$c^\dagger_{0,\uparrow}\{|0,0\rangle, |0,\downarrow\rangle, |\uparrow,0\}\rangle \rightarrow f(2,[0,4,2]) = [2,6,-1] \rightarrow \{|\uparrow,0\rangle, |\uparrow,\downarrow\rangle, 0\} \tag{A.6}$$

yields the mapping 0→2 and 4 → 6 while state 2 is destroyed (represented as -1). In a complete Fock-ordered basis, the Hamiltonian indices correspond one-to-one to the integer representations of the states themselves. In any other arbitrary basis an additional hash table is required that tracks which state corresponds to which position.

Solving the eigenstates and eigenvalues

The sparse Hamiltonian representation stores the row and column indices corresponding to non-zero entries as a result of the action of the operator sequence on a given Fock state basis. Next, we require to obtain the eigenvalues and eigenvectors $\{|\alpha\rangle, E_\alpha\}$. For smaller systems, the full matrix can be straightforwardly constructed from the sparse representation and diagonalized through conventional methods. For larger systems, however, this becomes unfeasible due to exponential scaling of the Hilbert space. If one is only interested in the k lowest eigenstates, a more efficient method is available, known as *Lanczos algorithm*. This method relies on constructing a so-called *Krylov space* [280]:

$$\mathcal{K}_m(H,v) = \mathrm{span}(v, Hv, H^2v, \dots, H^{m-1}v) \tag{A.7}$$

and constructing a new $m \times m$ matrix T, such that the eigenvalues of T correspond to the m extremal eigenvalues of H, relying on the dominance of extremal eigenvalues in higher powers of H. Benefits of this method are that it only requires implementing the matrix-vector product Hv and that it stores at most three full vectors at a given time throughout the algorithm.

An interesting note is that further memory efficiency can be gained by exploiting the structure of a Hamiltonian when working in a Fock-ordered basis. In a system with only particle-conserving terms (mod 2), the matrix of an n-site system H_n has the following recursive structure:

$$H_n = \begin{pmatrix} H_{n-1} & P_n \\ P_n^T & H_{n-1} + \mu_n I_{n-1} \end{pmatrix} \tag{A.8}$$

where P_n are the couplings between the new site n and the $n-1$ sites in the subsystem and μ_n the self-energies of the new site. Through this the positions of terms in P_n can be inferred from P_{n-1} by bit shifting: if an operator acting on site i couples the states $\cdots 001100 \cdots$ and $\cdots 010100$, then the same-type operator on site $i+1$ will couple the same states bit-shifted by 1 ($\ll 1$). For a system with at most k-nearest neighbour interactions, the Hamiltonian entries can be obtained efficiently from the $k \times k$ subsystem.

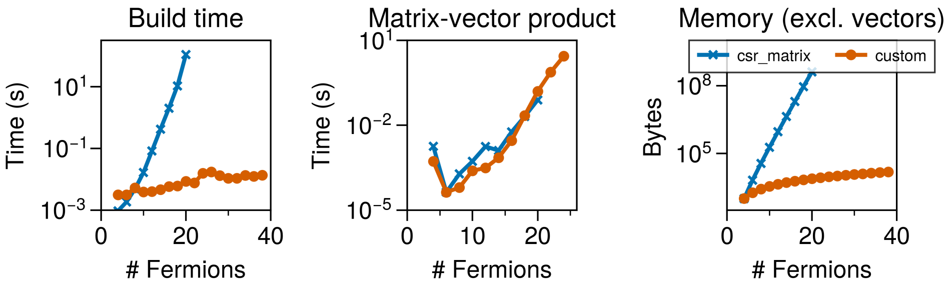

Figure A.1: **Memory and speed comparison for implementing the matrix-vector product for Lanczos algorithm.**

This reduces the amount of pre-calculated data that needs to be stored in order to implement a fast matrix-vector product for the Lanczos algorithm. As an example, we compare in figure A.1 the memory requirement and speed of performing a single matrix-vector product with a pre-calculated sparse matrix (implemented here with the commonly used *csr_matrix* from the *scipy* package.) versus the low-memory implementation. We note that the method enables a faster construction and reduced memory storage, without losing speed in the matrix-vector product compared to scipy's implementation. The matrix-vector product time still scales exponentially with system size, as expected.

SOLVING THE RATE EQUATION

Once the eigenvalues and eigenvectors are obtained, it remains to calculate the currents through the system when it is weakly coupled to normal metal leads. The full system is described by:

$$H = H_0 + H_L + H_T \tag{A.9}$$

where H_0 is the fermionic system of interest, H_L the metal leads and H_T a tunneling Hamiltonian coupling the two systems. To calculate the current, we solve the rate equation as described in Ref [281][1]. First, we determine the transition rates between states α and β as a result of tunneling an electron with spin σ from a lead at site j to the system, distinguishing the addition (+) or removal (-) of electrons to the system:

$$\begin{aligned} \Gamma^{j\sigma+}_{\beta\alpha} &= 2\pi \sum_{f_\beta, i_\alpha} |\langle f_\beta | H_T^{j\sigma+} | i_\alpha \rangle|^2 W_{i,\alpha} \delta(E_{f_\beta} - E_{i_\alpha}) \\ &\approx 2\pi t_j^2 \nu_j \left| T^{j\sigma+}_{\beta\alpha} \right|^2 n_F(E_\beta - E_\alpha - \mu_j) \end{aligned} \tag{A.10}$$

Here n_F is the Fermi-Dirac distribution, μ_j the chemical potential of lead j, $T^{j\sigma+}_{\beta\alpha} = \langle \beta | c^\dagger_{j\sigma} | \alpha \rangle$ and t_j the tunneling rate associated with lead j. Similarly:

$$\begin{aligned} \Gamma^{j\sigma-}_{\beta\alpha} &= 2\pi \sum_{f_\beta, i_\alpha} |\langle f_\beta | H_T^{j\sigma-} | i_\alpha \rangle|^2 W_{i,\alpha} \delta(E_{f_\beta} - E_{i_\alpha}) \\ &\approx 2\pi t_j^2 \nu_j \left| T^{j\sigma-}_{\beta\alpha} \right|^2 \left[1 - n_F(E_\alpha - E_\beta - \mu_j) \right] \end{aligned} \tag{A.11}$$

with $T^{j\sigma-}_{\beta\alpha} = \langle \beta | c_{j\sigma} | \alpha \rangle$. Then, the total transition rates are given by the summing the contributions of different leads, spins and electron/hole transport $\Gamma_{\beta\alpha} = \sum_{j,\sigma,\delta} \Gamma^{j\sigma\delta}_{\alpha,\beta}$. Using these transitions rates, the probability distribution P_a can be calculated for the occupation of state α:

$$\frac{\mathrm{d}}{\mathrm{d}t} P_\alpha = -\sum \Gamma_{\beta\alpha} P_\alpha + \sum_{\beta \neq \alpha} \Gamma_{\alpha\beta} P_\beta = 0 \tag{A.12}$$

The first term in the sum concerns transitions from state α to other states and the second term the reverse. These processes should be balanced in the steady state, hence $\frac{\mathrm{d}}{\mathrm{d}t} P_\alpha = 0$. Lastly, the normalization condition should be satisfied:

$$\sum_\alpha P_\alpha = 1 \tag{A.13}$$

Finally, this allows to obtain the current in lead l via:

$$I_l = (-e) \sum_{\beta,\alpha} (\Gamma^{l+}_{\beta,\alpha} - \Gamma^{l-}_{\beta,\alpha}) P_\alpha \tag{A.14}$$

---

[1] We summarize here a collection of notes kindly provided by dr. Chun-Xiao Liu.

B

Topology in the Kitaev chain

The transition from a trivial phase to a phase with unpaired Majorana edge modes in the Kitaev chain is an example of a *topological* phase transition. While not necessary to understand the experimental work in this thesis, it can be worth understanding how and why topology actually comes into play. In particular, this provides context for Chapter 6, where we focus on distinguishing the edges and bulk of the three site Kitaev chain system.

The Pfaffian as topological invariant

To understand where topology enters the discussion, we will follow here Kitaev's original description [14]. This requires introducing a few mathematical tools and general truths about Hamiltonians in the Majorana basis, so that they can be applied to the Kitaev chain. In Chapter 2, we started by writing down Kitaev's toy model in fermionic language, and transforming it to a Hamiltonian in a basis of Majorana operators. An important realization is that *any* quadratic fermionic Hamiltonian H can be written in a Majorana basis, in the form:

$$H = \frac{i}{4}\sum_{j,k} A_{j,k}\gamma_j\gamma_k \tag{B.1}$$

where γ_j, γ_k are Majorana operators that map to fermionic operators and where A is always an *anti-symmetric* matrix ($A^T = -A$), provided that the fermionic Hamiltonian is Hermitian. A fundamental property of anti-symmetric matrices is that they can be decomposed entirely into 2x2 blocks via an orthogonal transformation W [282, 283], such that:

$$B = WAW^T = \bigoplus_{m=1}^{N} \begin{pmatrix} 0 & E_m \\ -E_m & 0 \end{pmatrix} \tag{B.2}$$

In this form it is easy to see that the eigenvalues are $\pm E_m$ pairs and that the eigenvectors are linear combinations of pairs of Majorana operators. Furthermore, if any $E_m = 0$, this automatically results in the appearance of two unpaired Majoranas at zero energy. Given this block diagonal structure, a simple basis transformation to a set of operators $b_m^\dagger, b_m$ can be performed such that $H = \sum_m E_m(b_m^\dagger b_m - \frac{1}{2})$. This representation is known as the canonical form, which consists of independent fermionic modes with energies E_m. The

ground state in this canonical form is the vacuum $|0\rangle$.
Now, every antisymmetric matrix has an associated property called the Pfaffian [284], which is a continuous function of their matrix entries that satisfies $\mathrm{Pf}(B)^2 = \det(B)$ [285]. For the transformation in equation (B.2), this property carries through as:

$$\mathrm{Pf}(B) = \mathrm{Pf}(WAW^T) = \det(W)\mathrm{Pf}(A) \tag{B.3}$$

Important for our purposes, is that the sign of the Pfaffian $\mathrm{sgn}[\mathrm{Pf}(\mathrm{A})]$ relates directly to the parity of the ground state [14, 286]. For the form in equation (B.2), the Pfaffian is the simple expression $\mathrm{Pf}(B) = \prod_{\mathrm{m}} E_{\mathrm{m}}$. Since all $E_{\mathrm{m}} > 0$ this means $\mathrm{sgn}[\mathrm{Pf}(\mathrm{B})] = 1$, consistent with the ground state in the canonical form being the (even parity) vacuum. It also reveals an interesting connection: $\mathrm{Pf}(B) = 0$ would immediately imply that at least one $E_m = 0$, which in turn tells us that unpaired Majoranas are present. Given the relation in equation (B.3), it further imposes a condition on the original system and its transformation:

$$\mathrm{sgn}\left[\det(\mathrm{W})\right] = \mathrm{sgn}\left[\mathrm{Pf}(A)\right] \tag{B.4}$$

As W is an orthogonal transformation ($\det(W) = \pm 1$), the sign of the Pfaffian of A therefore tells us whether the system can be smoothly rotated to the canonical vacuum (i.e. $\det(W) = 1$, trivial) or not (i.e. $\det(W) = -1$, non-trivial).

The sign of the Pfaffian thus carries important information. Since the Pfaffian of A is continuous in the underlying Hamiltonian parameters, its sign can only change if it passes through zero. Whenever it crosses through zero, unpaired Majoranas appear *somewhere* in the system. The final piece of the puzzle is the realization that these Majoranas are pinned to the edges. If one takes any system H for which $\mathrm{sgn}[\mathrm{Pf}(A)] = -1$ and connects it to a trivial system ($\mathrm{sgn}[\mathrm{Pf}(B)] = 1$, e.g. the vacuum), the only way to go from the non-trivial system to the trivial system is by passing through a point with $\mathrm{sgn}[\mathrm{Pf}] = 0$. Therefore, unpaired Majoranas have to arise at the interface! This ties a negative sign of the Pfaffian of a system specifically to the presence of Majorana *edge* modes.

What remains, is to show how this behaves for the Kitaev chain in the Majorana basis (equation (2.4)). To simplify, we take an N-site chain and connect the last site to the first site so that the system becomes translationally invariant. This allows for deriving via its bulk-properties that [14]:

$$\mathrm{sgn}\left[\mathrm{Pf}(\mathrm{H}_{\mathrm{kitaev}})\right] = -1 \Leftrightarrow |\mu| < 2t \tag{B.5}$$

For the Kitaev chain in the limit $N \to \infty$, the sign of the Pfaffian is thus non-trivial when $|\mu| < 2t$. Furthermore, the presence of the Majoranas at the edge of the system is dictated entirely by the properties of the bulk system. This is what is known as a *bulk-edge correspondence.* Only closing the bulk energy gap of the system can change the topological invariant and remove the Majoranas from the system. This is what is meant with the statement that Majoranas are *topologically protected.*

C

MISCELLANEOUS RESULTS

Throughout the experimental investigations a few studies or observations remained inconclusive or incomplete, generally due to lack of time or due to undesired dilution refrigerator events. Rather than letting these datasets disappear in the void, we include here three sets of measurements that have close relation to the experimental chapters, but that require further work before drawing proper conclusions. We aim to briefly convey the general point of these measurements and the open questions that remain, which may serve to motivate future experiments (the secret outlook beyond the outlook).

The following three experiments are highlighted:

1. Observed non-sinusoidal dependence of CAR and ECT amplitudes on the angle of an applied external magnetic field, relating to Chapter 4.
2. Observation of strong interaction between a quantum dot and a low-energy Andreev bound state to create a so-called Shiba chain, relating to Chapter 5.
3. Measurements of negative differential conductance measurements pertaining to dynamical transport blockades at zero field, relating to Chapter 7.

ANHARMONIC DEPENDENCE OF CROSSED ANDREEV REFLECTION AND ELASTIC CO-TUNNELLING ON MAGNETIC FIELD ROTATIONS.

In Chapter 4, we present a series of measurements characterizing the subgap transport processes of CAR and ECT mediated by an Andreev bound state. By using quantum dots as spin-filters, we distinguish the spin-dependent rates of CAR and ECT via currents flowing in two ohmic contacts attached to each quantum dot. These currents depend on the energy and charge of the Andreev bound state, modulated by its chemical potential energy μ_{ABS}, but also on spin-orbit interactions: spin precession is required, for example, to form a Cooper pair using two quantum dots polarised to the same spin resonance. When aligning the external magnetic field perpendicular to the channel, same-spin CAR and opposite-spin ECT are completely suppressed. Rotating the field, both these processes are recovered. This allowed us to infer that the effective spin-orbit field is aligned perpendicular to our channel. In previous experiments [26], the current resulting from ECT and CAR followed a sinusoidal or cosinusoidal trend as a function of the magnetic field angle. The measurements shown in this thesis in Chapter 4 on the other hand, already subtly deviated from a clear sine or cosine behaviour. In a similar device as in Chapter 4, an additional dataset was collected where we find an even more drastic deviation, shown in figure C.1a. Focussing for example on the ECT rate for the ↑↑ configuration, clear extra harmonics appear:

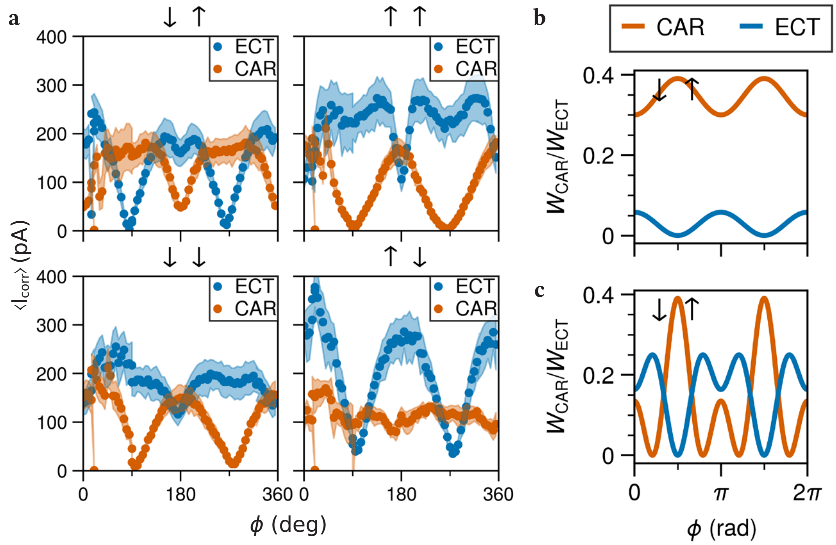

Figure C.1: **Non-sinusoidal field angle dependence of CAR and ECT. (a)** CAR and ECT measurements obtained in a similar device as presented in Chapter 4, repeating the same procedure as in figure 6.4, for a different electrostatic configuration. A clear non-sinusoidal dependence is observed in all four spin-configurations. As possible explanation, we compare two results from the model presented in section 2.2.3 which explicitly takes the spin-precession angle $\Delta\theta$ between the QDs and the ABS as input parameter. We fix μ_{ABS} and E_Z and vary the starting orientation ϕ in equation (2.28). **(b)** When the spin-precession angle is small ($\Delta\theta = 0.1\pi$), the dependence of CAR and ECT on field angle is roughly sinusoidal/cosinusoidal. **(c)** When the spin-precession angle is closer to $\pi/2$ ($\Delta\theta = 0.3\pi$), higher harmonics start to appear.

A possible, trivial, origin of this deviating behaviour can be a non-harmonic dependence of the ABS energy on the magnetic field angle, which also affects the CAR and ECT amplitudes. Alternatively, in Chapter 2 we discussed a simple model that allows to calculate the expected rates of CAR and ECT as a function of the spin-precession angle $\Delta\theta(r, \alpha_{\mathrm{SO}})$ that captures the amount of spin-precession over a distance r in a Rashba spin-orbit field with strength α_{SO}. When $\Delta\theta$ is small, the dependence of CAR and ECT on the angle of the applied external magnetic field angle (with respect to $\vec{B}_{\mathrm{SO}}$), is indeed roughly (co)sinusoidal, shown in figure C.1b (repeated from section 2.2.3). Interestingly, when we set $\Delta\theta$ to be larger, a clear deviation from this behaviour appears (figure C.1c), that resembles some of the experimental features. Considering that the spin-orbit length in InSbAs is on the order of a few 100 nm, comparable to the separation between the QDs and the ABS, it is plausible that the spin-precession in tunneling between them is relatively large. A better understanding of this mechanism may serve to answer the following questions:

- How important is spin-precession in tunnelling compared to spin-orbit effects in the ABS orbital?
- Can we use this understanding to adapt the device geometry and dimensions for maximizing the $t = \Delta$ condition?

The Shiba chain in a QD-ABS system

Throughout this thesis we use quantum dots as source of zero-energy modes, and a higher-energy Andreev bound state to couple them. A stable degenerate ground-states arises due to the ability to balance the coupling between even and odd parity subspaces via control over the ABS charge and energy, as demonstrated in Chapter 5. Notably, this is not a unique way to emulate the Kitaev chain. In fact, the same types of devices used to create a two-site Kitaev chain may be used to create a three-site Kitaev chain if one is able to incorporate the ABS itself as a zero energy state, also referred to as a Shiba chain [38, 287]. Such a system was studied for example in an InSb nanowire device in Ref. [58]. Here, we briefly highlight how the two-site Kitaev chain studied in Chapter 5 can be utilised in a similar manner.

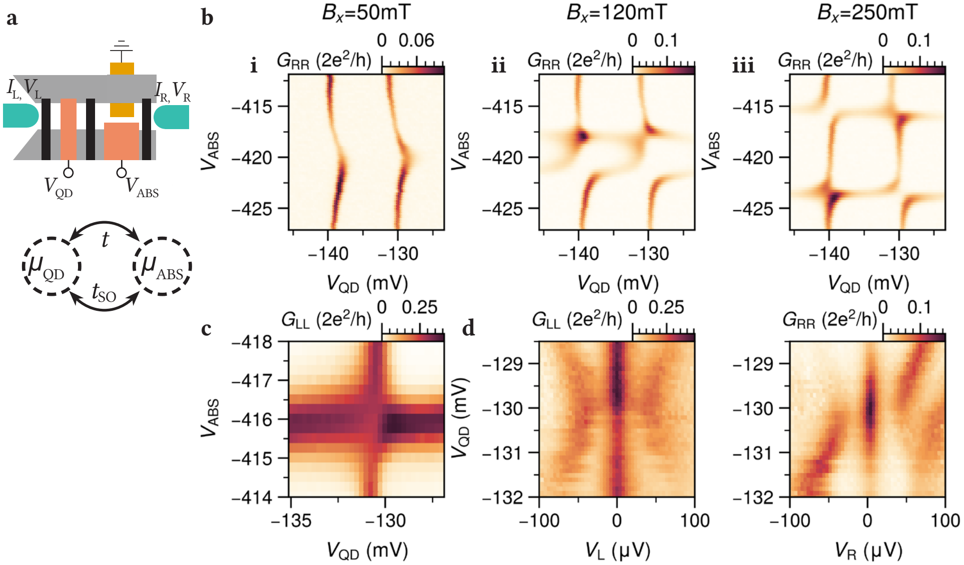

Figure C.2: **Tuning a Shiba chain (a)** Top: overview of relevant device components. Bottom: Relevant tuning parameters. Data was obtained on device A detailed in Chapter 5. **(b)** Charge stability diagrams between a QD and an ABS as a function of magnetic field. As the magnetic field increases, the ABS is pulled down in energy and avoided crossings start to appear. **(c)** The magnetic field allows to balance the ratio of t and t_{SO}, resulting in a crossing in the CSD similar to figure 5.2. **(d)** With V_{ABS} on resonance and detuning V_{QD}, this results in stable correlated ZBPs protected by a finite energy gap, similar to observed behaviour in the QD-ABS-QD system shown in figure 5.3.

Instead of coupling two quantum dots via a finite energy ABS, a zero-energy excitation can be created in the ABS itself and couple directly to either of the QDs (figure C.2). The competition between the odd and even subspaces is then driven by the ratio of the normal-hopping t and the spin-precessing hopping t_{SO} [287], instead of ECT and CAR,. In general, the Andreev bound states in the devices studied in this thesis are in the singlet ground state and do not have a singlet-doublet degeneracy at zero bias. However, depending on the device design, the charging energy in the hybrid segment can vary (see figure 3.7). This can significantly lower the energy of the doublet states relative to the singlet state. In addition, the external magnetic field required to spin-polarise the ABS doublet will additionally lower its energy. The consequence of this can be clearly seen in figure C.2, where we present three charge stability diagrams of a quantum dot orbital tunnel coupled to an ABS in the hybrid segment. At lows fields the ABS remains in the singlet ground state and the interaction with the QD only results in the characteristic modulation of the QD resonances as a function of V_{ABS}. When the magnetic field is increased, a singlet-doublet transition is driven by V_{ABS} and avoided crossings appear in the QD-ABS CSD, where the direction of the avoided crossing is determined by the ratio t/t_{SO} in each quadrant. This ratio is sensitive to the amplitude of the magnetic field and hence can serve to tune to a sweet-spot. Focussing for example on the top right corner, we find such a sweet spot at 180 mT, shown in figure C.2c. Just like in the QD-ABS-QD system in figure 5.3, the system hosts stable zero bias peaks at this sweet spot. Detuning for instance V_{QD} reveals stable zero-bias conductance peaks, protected by an excitation gap that now depends on the absolute t/t_{SO} amplitudes. Given these measurements and Ref. [58], the Shiba chain approach could be a reasonable alternative method for studying Majoranas. In this direction, there are plenty questions left to address experimentally:

- Tuning to a sweet spot via amplitudes of the external magnetic field is not possible for a three-site chain, since independent control is needed over the pairwise interactions. Is there a systematic way to deterministically find sweet-spots that does work for longer systems?

- Extending to a three site Shiba chain (i.e. a QD-ABS-QD system), there will be next-nearest neighbour couplings due to the existence of CAR and ECT. How detrimental are these processes and can they be suppressed?

- In principle the excitation gap at the sweet spot can be larger compared to the QD-ABS-QD chain, since it is set by first-order t,t_{SO} processes rather than the second-order CAR and ECT mechanisms. How large can the excitation gap be in this system and how is it optimized?

- The current device design was not optimized for building a 'Shiba chain' - could a design where every QD is in proximity to the superconductor (like in Ref.[38]) be beneficial?

- Is the lack of finetuned control over t/t_{SO} compensated by requiring less gate voltages to create a longer chain (which are less sensitive to imperfect tuning)?

NEGATIVE LOCAL DIFFERENTIAL CONDUCTANCE DUE TO DYNAMICAL TRANSPORT BLOCKADES

A key finding in Chapter 5 is that key signatures of Majoranas in a two-site Kitaev chain device (stable ZBPs and quadratically dispersing higher-energy excitations) persist when removing the external magnetic field used to spin-polarise the quantum dots. In Chapter 7 we study this system at zero field in more detail. There we demonstrate that the key distinguishing features in the conductance spectrum of the QD-ABS-QD system at high and low fields are related to the presence of triplet states at zero field, which do not partake in transport when the QDs are spin polarised. An interesting aspect of these excited triplet states ($|\downarrow\downarrow\rangle$, $|\uparrow\uparrow\rangle$ and $|\downarrow\uparrow\rangle + |\uparrow\downarrow\rangle$) is that the system cannot relax to the ground state via de superconductor, which requires a singlet pair of electrons to form a Cooper pair. This gives rise to interesting dynamical blockades, illustrated in figure C.3a. Both the triplet state extended across the two QDs or a triplet state in the QD-ABS subsystem will not be able to relax in transport to the ground-state via the superconductor without a mechanism that allows spin to relax. Since a finite bias is required to enter the triplet state, this is expected to give rise to *negative* local differential conductance (NLDC) [120, 288]. As soon as the voltage bias is sufficient to enter a triplet state, the current will decrease due to the delay in completing a transport cycle.

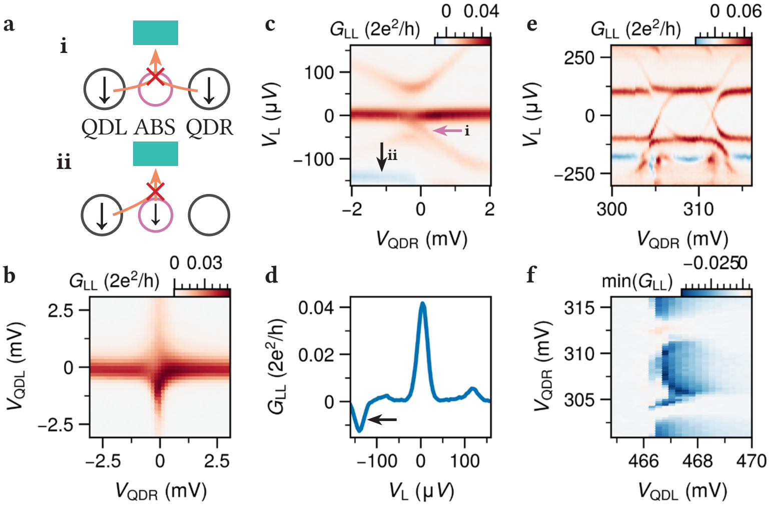

Figure C.3: **Negative local differential conductance in QD-ABS-QD junction.** **(a)** Schematic overview of possible triplet blockades in the QD-ABS-QD system (see Ref [51] for device details) **(b)** Charge stability diagram indicating the studied system is tuned to a zero-field sweet spot ($t = \sqrt{2}\Delta$). **(c)** Finite bias spectroscopy as a function of V_{QDR}, with V_{QDL} on resonance. The typical zero-field feature owed to excited triplet states is indicated by the red arrow. Negative local differential conductance is observed at a higher bias transition. **(d)** Linetrace as indicated. **(e)** Linetrace as a function of V_{QDR} in a larger range, with V_{QDL} off resonance. **(f)** The minimum value of G_{LL} for bias traces obtained as a function V_{QDL} and V_{QDR} (i.e. the minimum measured in repeated measurements of (d). The transport blockade depends non-trivially on the chemical potential of both QDs, similar to the theoretical study presented in [120].

We show here the observed NLDC in a two-site system at zero field, measured at a sweet spot shown in figure C.3b. To start, we measure local conductance G_{LL} as a function of bias, while sweeping V_{QDR} and keeping V_{QDL} (figure C.3c). In this example, we observe the expected features: a stable ZBP, dispersing excited states and an additional conductance feature marked *i*, which marks the presence of the triplet states. Notably, we do not observe an NLDC here, just as we did not observe this in Chapter 5 and Chapter 7. Instead, we observe NLDC at a higher bias, marked *ii*, which likely corresponds to a triplet blockade formed via the QD and the ABS. Figure C.2d highlights a linetrace at fixed V_{QDR}, showing the clear negative peak in G_{LL}. By exploring a larger parameter space, we can map out the settings of V_{QDL} and V_{QDR} that result in NLDC. In figure C.3e, we sweep V_{QDR} across two resonances with V_{QDL} off resonance and find that the dynamic blockade appears to be lifted for specific values of the right QD. Repeating these measurements for a larger range of V_{QDL}, we obtain the minimum in conductance in the QDL-QDR phase space, shown in figure C.3. This shows that the blockade depends on the both QDL and QDR, in a seemingly non-trivial manner. These measurements raise the following questions, that can be interesting to study:

- Why is the transport blockade only visible for the QD-ABS transport? Does it imply a longer spin lifetime in the hybrid compared to the QD?
- Can the tunnelling rates be adjusted so that the transport blockade also appears for the QD-QD triplet?
- How does the chemical potential of the right QD lift the triplet blockade?

BIBLIOGRAPHY

REFERENCES

[1] Saunders Mac Lane. *Categories for the Working Mathematician*, volume 5 of *Graduate Texts in Mathematics*. Springer, New York, NY, 2nd edition, 1998.

[2] David Deutsch. Quantum theory, the Church–Turing principle and the universal quantum computer. *Proceedings of the Royal Society of London. A. Mathematical and Physical Sciences*, 400(1818):97–117, 1985.

[3] Lov K. Grover. Quantum mechanics helps in searching for a needle in a haystack. *Phys. Rev. Lett.*, 79:325–328, Jul 1997.

[4] Peter W. Shor. Polynomial-time algorithms for prime factorization and discrete logarithms on a quantum computer. *SIAM Review*, 41(2):303–332, 1999.

[5] Rolf Landauer, Mark Edward Welland, and James Kazimierz Gimzewski. Is quantum mechanics useful? *Philosophical Transactions of the Royal Society of London. Series A: Physical and Engineering Sciences*, 353(1703):367–376, 1995.

[6] M. I. Dyakonov. Quantum computing: A view from the enemy camp. *Optics and Spectroscopy*, 95(2):261–267, Aug 2003.

[7] Xavier Waintal. The quantum house of cards. *Proceedings of the National Academy of Sciences*, 121(1):e2313269120, 2024.

[8] Andrew Steane. Multiple-particle interference and quantum error correction. *Proceedings of the Royal Society of London. Series A: Mathematical, Physical and Engineering Sciences*, 452(1954):2551–2577, 1996.

[9] Peter W. Shor. Fault-tolerant quantum computation. *Proceedings of the 37th Annual Symposium on Foundations of Computer Science (FOCS)*, pages 56–65, 1996. Presented in 1996, published in 1997.

[10] Dorit Aharonov and Michael Ben-Or. Fault-tolerant quantum computation with constant error. *SIAM Journal on Computing*, 38(4):1207–1282, 2008. Preliminary version appeared in STOC 1997.

[11] R. W. Hamming. Error detecting and error correcting codes. *The Bell System Technical Journal*, 29(2):147–160, 1950.

[12] Michael H. Freedman, Alexei Kitaev, Michael J. Larsen, and Zhenghan Wang. Topological quantum computation. *Bulletin of the American Mathematical Society*, 40(1):31–38, 2003.

[13] Chetan Nayak, Steven H. Simon, Ady Stern, Michael Freedman, and Sankar Das Sarma. Non-abelian anyons and topological quantum computation. *Rev. Mod. Phys.*, 80:1083–1159, Sep 2008.

[14] A Yu Kitaev. Unpaired Majorana fermions in quantum wires. *Physics-Uspekhi*, 44, 2001.

[15] A.Yu. Kitaev. Fault-tolerant quantum computation by anyons. *Annals of Physics*, 303(1):2–30, 2003.

[16] Roman M. Lutchyn, Jay D. Sau, and S. Das Sarma. Majorana fermions and a topological phase transition in semiconductor-superconductor heterostructures. *Phys. Rev. Lett.*, 105:077001, Aug 2010.

[17] Yuval Oreg, Gil Refael, and Felix von Oppen. Helical liquids and Majorana bound states in quantum wires. *Phys. Rev. Lett.*, 105:177002, Oct 2010.

[18] Jason Alicea. New directions in the pursuit of Majorana fermions in solid state systems. *Reports on Progress in Physics*, 75(7):076501, jun 2012.

[19] David Aasen, Michael Hell, Ryan V. Mishmash, Andrew Higginbotham, Jeroen Danon, Martin Leijnse, Thomas S. Jespersen, Joshua A. Folk, Charles M. Marcus, Karsten Flensberg, and Jason Alicea. Milestones toward Majorana-based quantum computing. *Phys. Rev. X*, 6:031016, Aug 2016.

[20] Leo Kouwenhoven. Perspective on Majorana bound-states in hybrid superconductor-semiconductor nanowires. *Modern Physics Letters B*, 39(03):2540002, 2025.

[21] Chun-Xiao Liu, Jay D. Sau, Tudor D. Stanescu, and S. Das Sarma. Andreev bound states versus Majorana bound states in quantum dot-nanowire-superconductor hybrid structures: Trivial versus topological zero-bias conductance peaks. *Phys. Rev. B*, 96:075161, Aug 2017.

[22] Adriaan Vuik, Bas Nijholt, Anton R. Akhmerov, and Michael Wimmer. Reproducing topological properties with quasi-Majorana states. *SciPost Phys.*, 7:061, 2019.

[23] Haining Pan and S. Das Sarma. Physical mechanisms for zero-bias conductance peaks in Majorana nanowires. *Phys. Rev. Res.*, 2:013377, Mar 2020.

[24] Seongjin Ahn, Haining Pan, Benjamin Woods, Tudor D. Stanescu, and Sankar Das Sarma. Estimating disorder and its adverse effects in semiconductor Majorana nanowires. *Phys. Rev. Mater.*, 5:124602, Dec 2021.

[25] Chun-Xiao Liu, Guanzhong Wang, Tom Dvir, and Michael Wimmer. Tunable superconducting coupling of quantum dots via Andreev bound states in semiconductor-superconductor nanowires. *Phys. Rev. Lett.*, 129, 12 2022.

[26] Guanzhong Wang, Tom Dvir, Grzegorz P. Mazur, Chun-Xiao Liu, Nick van Loo, Sebastiaan L. D. ten Haaf, Alberto Bordin, Sasa Gazibegovic, Ghada Badawy, Erik P. A. M. Bakkers, Michael Wimmer, and Leo P. Kouwenhoven. Singlet and triplet Cooper pair splitting in hybrid superconducting nanowires. *Nature*, 612(7940):448–453, Dec 2022.

[27] Alberto Bordin, Guanzhong Wang, Chun-Xiao Liu, Sebastiaan L. D. ten Haaf, Nick van Loo, Grzegorz P. Mazur, Di Xu, David van Driel, Francesco Zatelli, Sasa Gazibegovic, Ghada Badawy, Erik P. A. M. Bakkers, Michael Wimmer, Leo P. Kouwenhoven, and Tom Dvir. Tunable crossed Andreev reflection and elastic cotunneling in hybrid nanowires. *Phys. Rev. X*, 13:031031, Sep 2023.

[28] Tom Dvir, Guanzhong Wang, Nick van Loo, Chun Xiao Liu, Grzegorz P. Mazur, Alberto Bordin, Sebastiaan L. D. ten Haaf, Ji Yin Wang, David van Driel, Francesco Zatelli, Xiang Li, Filip K. Malinowski, Sasa Gazibegovic, Ghada Badawy, Erik P.A.M. Bakkers, Michael Wimmer, and Leo P. Kouwenhoven. Realization of a minimal Kitaev chain in coupled quantum dots. *Nature*, 614:445–450, 2 2023.

[29] Nico Leumer, Magdalena Marganska, Bhaskaran Muralidharan, and Milena Grifoni. Exact eigenvectors and eigenvalues of the finite Kitaev chain and its topological properties. *Journal of Physics: Condensed Matter*, 32(44):445502, aug 2020.

[30] W. P. Su, J. R. Schrieffer, and A. J. Heeger. Solitons in polyacetylene. *Phys. Rev. Lett.*, 42:1698–1701, Jun 1979.

[31] W. P. Su, J. R. Schrieffer, and A. J. Heeger. Soliton excitations in polyacetylene. *Phys. Rev. B*, 22:2099–2111, Aug 1980.

[32] Suraj S. Hegde and Smitha Vishveshwara. Majorana wave-function oscillations, fermion parity switches, and disorder in Kitaev chains. *Phys. Rev. B*, 94:115166, Sep 2016.

[33] Martin Leijnse and Karsten Flensberg. Parity qubits and poor man's Majorana bound states in double quantum dots. *Phys. Rev. B*, 86, 10 2012.

[34] Alberto Bordin, Chun-Xiao Liu, Tom Dvir, Francesco Zatelli, Sebastiaan L. D. ten Haaf, David van Driel, Guanzhong Wang, Nick van Loo, Yining Zhang, Jan Cornelis Wolff, Thomas Van Caekenberghe, Ghada Badawy, Sasa Gazibegovic, Erik P. A. M. Bakkers, Michael Wimmer, Leo P. Kouwenhoven, and Grzegorz P. Mazur. Enhanced Majorana stability in a three-site Kitaev chain. *Nature Nanotechnology*, 20(6):726–731, Jun 2025.

[35] Athanasios Tsintzis, Rubén Seoane Souto, and Martin Leijnse. Creating and detecting poor man's Majorana bound states in interacting quantum dots. *Phys. Rev. B*, 106, 11 2022.

[36] Juan Daniel Torres Luna, Sebastian Miles, A. Mert Bozkurt, Chun-Xiao Liu, Antonio L. R. Manesco, Anton R. Akhmerov, and Michael Wimmer. Pareto-optimality of majoranas in hybrid platforms, 2025.

[37] Jay D. Sau and S. Das Sarma. Realizing a robust practical Majorana chain in a quantum-dot-superconductor linear array. *Nature Communications*, 3(1):964, Jul 2012.

[38] Ion C. Fulga, Arbel Haim, Anton R. Akhmerov, and Yuval Oreg. Adaptive tuning of Majorana fermions in a quantum dot chain. *New Journal of Physics*, 15, 4 2013.

[39] J. Bardeen, L. N. Cooper, and J. R. Schrieffer. Theory of superconductivity. *Phys. Rev.*, 108:1175–1204, Dec 1957.

[40] A. F. Andreev. The thermal conductivity of the intermediate state in superconductors. *Soviet Physics – JETP*, 19(5):1228–1231, 1964.

[41] I. O. Kulik. Macroscopic Quantization and the Proximity Effect in S-N-S Junctions. *Soviet Journal of Experimental and Theoretical Physics*, 30:944, January 1969.

[42] John Bardeen and Jared L. Johnson. Josephson current flow in pure superconducting-normal-superconducting junctions. *Phys. Rev. B*, 5:72–78, Jan 1972.

[43] C. W. J. Beenakker. Universal limit of critical-current fluctuations in mesoscopic josephson junctions. *Phys. Rev. Lett.*, 67:3836–3839, Dec 1991.

[44] J. A. Sauls. Andreev bound states and their signatures. *Philosophical Transactions of the Royal Society A: Mathematical, Physical and Engineering Sciences*, 376(2125):20180140, 2018.

[45] L. Hofstetter, S. Csonka, J. Nygård, and C. Schönenberger. Cooper pair splitter realized in a two-quantum-dot y-junction. *Nature*, 461(7266):960–963, Oct 2009.

[46] L. Hofstetter, S. Csonka, A. Baumgartner, G. Fülöp, S. d'Hollosy, J. Nygård, and C. Schönenberger. Finite-bias Cooper pair splitting. *Phys. Rev. Lett.*, 107:136801, Sep 2011.

[47] Anindya Das, Yuval Ronen, Moty Heiblum, Diana Mahalu, Andrey V. Kretinin, and Hadas Shtrikman. High-efficiency Cooper pair splitting demonstrated by two-particle conductance resonance and positive noise cross-correlation. *Nature Communications*, 3(1):1165, Nov 2012.

[48] L. G. Herrmann, F. Portier, P. Roche, A. Levy Yeyati, T. Kontos, and C. Strunk. Carbon nanotubes as Cooper-pair beam splitters. *Phys. Rev. Lett.*, 104:026801, Jan 2010.

[49] J. Schindele, A. Baumgartner, and C. Schönenberger. Near-unity Cooper pair splitting efficiency. *Phys. Rev. Lett.*, 109:157002, Oct 2012.

[50] Guanzhong Wang, Tom Dvir, Nick van Loo, Grzegorz P. Mazur, Sasa Gazibegovic, Ghada Badawy, Erik P. A. M. Bakkers, Leo P. Kouwenhoven, and Gijs de Lange. Nonlocal measurement of quasiparticle charge and energy relaxation in proximitized semiconductor nanowires using quantum dots. *Phys. Rev. B*, 106:064503, Aug 2022.

[51] David van Driel, Guanzhong Wang, Alberto Bordin, Nick van Loo, Francesco Zatelli, Grzegorz P. Mazur, Di Xu, Sasa Gazibegovic, Ghada Badawy, Erik P. A. M. Bakkers, Leo P. Kouwenhoven, and Tom Dvir. Spin-filtered measurements of Andreev bound states in semiconductor-superconductor nanowire devices. *Nature Communications*, 14(1):6880, Oct 2023.

[52] J Bauer, A Oguri, and A C Hewson. Spectral properties of locally correlated electrons in a Bardeen-Cooper-Schrieffer superconductor. *Journal of Physics: Condensed Matter*, 19(48):486211, nov 2007.

[53] Tobias Meng, Serge Florens, and Pascal Simon. Self-consistent description of Andreev bound states in Josephson quantum dot devices. *Phys. Rev. B*, 79:224521, Jun 2009.

[54] Eduardo J. H. Lee, Xiaocheng Jiang, Manuel Houzet, Ramón Aguado, Charles M. Lieber, and Silvano De Franceschi. Spin-resolved Andreev levels and parity crossings in hybrid superconductor–semiconductor nanostructures. *Nature Nanotechnology*, 9(1):79–84, Jan 2014.

[55] J. Gramich, A. Baumgartner, and C. Schönenberger. Andreev bound states probed in three-terminal quantum dots. *Phys. Rev. B*, 96:195418, Nov 2017.

[56] Arno Bargerbos, Marta Pita-Vidal, Rok Žitko, Jesús Ávila, Lukas J. Splitthoff, Lukas Grünhaupt, Jaap J. Wesdorp, Christian K. Andersen, Yu Liu, Leo P. Kouwenhoven, Ramón Aguado, Angela Kou, and Bernard van Heck. Singlet-doublet transitions of a quantum dot Josephson junction detected in a transmon circuit. *PRX Quantum*, 3:030311, Jul 2022.

[57] Arno Bargerbos, Marta Pita-Vidal, Rok Žitko, Lukas J. Splitthoff, Lukas Grünhaupt, Jaap J. Wesdorp, Yu Liu, Leo P. Kouwenhoven, Ramón Aguado, Christian Kraglund Andersen, Angela Kou, and Bernard van Heck. Spectroscopy of spin-split Andreev levels in a quantum dot with superconducting leads. *Phys. Rev. Lett.*, 131:097001, Aug 2023.

[58] David van Driel, Bart Roovers, Francesco Zatelli, Alberto Bordin, Guanzhong Wang, Nick van Loo, Jan Cornelis Wolff, Grzegorz P. Mazur, Sasa Gazibegovic, Ghada Badawy, Erik P.A.M. Bakkers, Leo P. Kouwenhoven, and Tom Dvir. Charge sensing the parity of an Andreev molecule. *PRX Quantum*, 5:020301, Apr 2024.

[59] A. Bordin. *Engineering the Kitaev chain.* Dissertation (tu delft), Delft University of Technology, 2025.

[60] Alberto Bordin, Xiang Li, David van Driel, Jan Cornelis Wolff, Qingzhen Wang, Sebastiaan L. D. ten Haaf, Guanzhong Wang, Nick van Loo, Leo P. Kouwenhoven, and Tom Dvir. Crossed Andreev reflection and elastic cotunneling in three quantum dots coupled by superconductors. *Phys. Rev. Lett.*, 132:056602, Feb 2024.

[61] L. H. Thomas. The motion of the spinning electron. *Nature*, 117(2945):514–514, Apr 1926.

[62] John C. Slater. *Quantum Theory of Atomic Structure*, volume 1 of *International Series in Pure and Applied Physics.* McGraw-Hill, 1960.

[63] Roland Winkler. *Spin–Orbit Coupling Effects in Two-Dimensional Electron and Hole Systems*, volume 191 of *Springer Tracts in Modern Physics.* Springer, Berlin, 2003.

[64] R. H. Parmenter. Symmetry properties of the energy bands of the zinc blende structure. *Phys. Rev.*, 100:573–579, Oct 1955.

[65] G. Dresselhaus. Spin-orbit coupling effects in zinc blende structures. *Phys. Rev.*, 100:580–586, Oct 1955.

[66] Yu. A. Bychkov and É. I. Rashba. Properties of a 2D electron gas with lifted spectral degeneracy. *Soviet Journal of Experimental and Theoretical Physics Letters*, 39:78, January 1984.

[67] R. Hanson, L. P. Kouwenhoven, J. R. Petta, S. Tarucha, and L. M. K. Vandersypen. Spins in few-electron quantum dots. *Rev. Mod. Phys.*, 79:1217–1265, Oct 2007.

[68] C. Fasth, A. Fuhrer, L. Samuelson, Vitaly N. Golovach, and Daniel Loss. Direct measurement of the spin-orbit interaction in a two-electron inas nanowire quantum dot. *Phys. Rev. Lett.*, 98:266801, Jun 2007.

[69] K. C. Nowack, F. H. L. Koppens, Yu. V. Nazarov, and L. M. K. Vandersypen. Coherent control of a single electron spin with electric fields. *Science*, 318(5855):1430–1433, 2007.

[70] Henrik A. Nilsson, Philippe Caroff, Claes Thelander, Marcus Larsson, Jakob B. Wagner, Lars-Erik Wernersson, Lars Samuelson, and H. Q. Xu. Giant, level-dependent g-factors in InSb nanowire quantum dots. *Nano Letters*, 9(9):3151–3156, Sep 2009.

[71] Ming-Hao Liu, Ching-Ray Chang, and Son-Hsien Chen. Spin precession due to spin-orbit coupling in a two-dimensional electron gas with spin injection via ideal quantum point contact. *Phys. Rev. B*, 71:153305, Apr 2005.

[72] Supriyo Datta and Biswajit Das. Electronic analog of the electro-optic modulator. *Applied Physics Letters*, 56(7):665–667, 02 1990.

[73] Melina Luethi, Henry F. Legg, Daniel Loss, and Jelena Klinovaja. From perfect to imperfect poor man's Majoranas in minimal Kitaev chains. *Phys. Rev. B*, 110:245412, Dec 2024.

[74] M. Tinkham. *Introduction to Superconductivity*. Dover Books on Physics Series. Dover Publications, 2004.

[75] Yu Luh. Bound state in superconductors with paramagnetic impurities. *Acta Physica Sinica*, 21:75–91, 1965.

[76] Hiroyuki Shiba. Classical spins in superconductors. *Progress of Theoretical Physics*, 40(3):435–451, 09 1968.

[77] A I Rusinov. Superconductivity near a magnatic impurity. *JETP Lett. (USSR) (Engl. Transl.), 9: 85-7(Jan. 20, 1969).*, 12 1968.

[78] D. van Driel. *Quantum Dots Coupled to Andreev Bound States*. Dissertation (tu delft), Delft University of Technology, 2024.

[79] Chun-Xiao Liu, A Mert Bozkurt, Francesco Zatelli, Sebastiaan L. D. ten Haaf, Tom Dvir, and Michael Wimmer. Enhancing the excitation gap of a quantum-dot-based Kitaev chain. *Commun. Phys.*, 7(1):235, 2024.

[80] Francesco Zatelli, David van Driel, Di Xu, Guanzhong Wang, Chun-Xiao Liu, Alberto Bordin, Bart Roovers, Grzegorz P. Mazur, Nick van Loo, Jan C. Wolff, A. Mert Bozkurt, Ghada Badawy, Sasa Gazibegovic, Erik P. A. M. Bakkers, Michael Wimmer, Leo P. Kouwenhoven, and Tom Dvir. Robust poor man's Majorana zero modes using Yu-Shiba-Rusinov states. *Nature Communications*, 15(1):7933, Sep 2024.

[81] Elsa Prada, Pablo San-Jose, Michiel W. A. de Moor, Attila Geresdi, Eduardo J. H. Lee, Jelena Klinovaja, Daniel Loss, Jesper Nygård, Ramón Aguado, and Leo P. Kouwenhoven. From Andreev to Majorana bound states in hybrid superconductor–semiconductor nanowires. *Nature Reviews Physics*, 2(10):575–594, Oct 2020.

[82] Viktor Svensson and Martin Leijnse. Quantum dot based Kitaev chains: Majorana quality measures and scaling with increasing chain length. *Phys. Rev. B*, 110:155436, Oct 2024.

[83] N. Sedlmayr and C. Bena. Visualizing Majorana bound states in one and two dimensions using the generalized Majorana polarization. *Phys. Rev. B*, 92:115115, Sep 2015.

[84] S. V. Aksenov, A. O. Zlotnikov, and M. S. Shustin. Strong Coulomb interactions in the problem of Majorana modes in a wire of the nontrivial topological class bdi. *Phys. Rev. B*, 101:125431, Mar 2020.

[85] Rodrigo A. Dourado, Jeroen Danon, Martin Leijnse, and Rubén Seoane Souto. Measuring coherence factors of states in superconductors through local current. *Phys. Rev. B*, 112:174515, Nov 2025.

[86] M. Alvarado, A. Levy Yeyati, Ramón Aguado, and R. Seoane Souto. Characterizing local Majorana properties using Andreev states. *Phys. Rev. B*, 112:L241403, Dec 2025.

[87] Elsa Prada, Ramón Aguado, and Pablo San-Jose. Measuring Majorana nonlocality and spin structure with a quantum dot. *Phys. Rev. B*, 96:085418, Aug 2017.

[88] David J. Clarke. Experimentally accessible topological quality factor for wires with zero energy modes. *Phys. Rev. B*, 96:201109, Nov 2017.

[89] Rubén Seoane Souto, Athanasios Tsintzis, Martin Leijnse, and Jeroen Danon. Probing Majorana localization in minimal Kitaev chains through a quantum dot. *Phys. Rev. Res.*, 5:043182, Nov 2023.

[90] Alberto Bordin, Florian J. Bennebroek Evertsz', Bart Roovers, Juan D. Torres Luna, Wietze D. Huisman, Francesco Zatelli, Grzegorz P. Mazur, Sebastiaan L. D. ten Haaf, Ghada Badawy, Erik P. A. M. Bakkers, Chun-Xiao Liu, Rubén Seoane Souto, Nick van Loo, and Leo P. Kouwenhoven. Probing Majorana localization of a phase-controlled three-site Kitaev chain with an additional quantum dot. *Nature Communications*, Feb 2026.

[91] Pin Gao, Ying-Ping He, and Xiong-Jun Liu. Symmetry-protected non-abelian braiding of Majorana Kramers pairs. *Phys. Rev. B*, 94:224509, Dec 2016.

[92] Constantin Schrade and Liang Fu. Quantum computing with Majorana Kramers pairs. *Phys. Rev. Lett.*, 129:227002, Nov 2022.

[93] Hongfa Pan, Jinxiong Jia, and Zhenhua Qiao. Fusion rules for Majorana Kramers pairs in time-reversal invariant topological superconductors. *Phys. Rev. B*, 111:115414, Mar 2025.

[94] Jason Alicea and Paul Fendley. Topological phases with parafermions: Theory and blueprints. *Annual Review of Condensed Matter Physics*, 7(Volume 7, 2016):119–139, 2016.

[95] Adrian Hutter and Daniel Loss. Quantum computing with parafermions. *Phys. Rev. B*, 93:125105, Mar 2016.

[96] Michael H. Freedman, Michael Larsen, and Zhenghan Wang. A Modular Functor Which is Universal for Quantum Computation. *Commun. Math. Phys.*, 227(3):605–622, 2002.

[97] David J. Clarke, Jason Alicea, and Kirill Shtengel. Exotic non-Abelian anyons from conventional fractional quantum hall states. *Nature Communications*, 4(1):1348, Jan 2013.

[98] Chris L. M. Wong and K. T. Law. Majorana kramers doublets in $d_{x^2-y^2}$-wave superconductors with rashba spin-orbit coupling. *Phys. Rev. B*, 86:184516, Nov 2012.

[99] Fan Zhang, C. L. Kane, and E. J. Mele. Time-reversal-invariant topological superconductivity and Majorana Kramers pairs. *Phys. Rev. Lett.*, 111:056402, Aug 2013.

[100] Anna Keselman, Liang Fu, Ady Stern, and Erez Berg. Inducing time-reversal-invariant topological superconductivity and fermion parity pumping in quantum wires. *Phys. Rev. Lett.*, 111:116402, Sep 2013.

[101] Xiong-Jun Liu, Chris L. M. Wong, and K. T. Law. Non-abelian Majorana doublets in time-reversal-invariant topological superconductors. *Phys. Rev. X*, 4:021018, Apr 2014.

[102] Arbel Haim, Anna Keselman, Erez Berg, and Yuval Oreg. Time-reversal-invariant topological superconductivity induced by repulsive interactions in quantum wires. *Phys. Rev. B*, 89:220504, Jun 2014.

[103] Jelena Klinovaja, Amir Yacoby, and Daniel Loss. Kramers pairs of Majorana fermions and parafermions in fractional topological insulators. *Phys. Rev. B*, 90:155447, Oct 2014.

[104] Jelena Klinovaja and Daniel Loss. Time-reversal invariant parafermions in interacting Rashba nanowires. *Phys. Rev. B*, 90:045118, Jul 2014.

[105] Constantin Schrade, A. A. Zyuzin, Jelena Klinovaja, and Daniel Loss. Proximity-induced π josephson junctions in topological insulators and kramers pairs of majorana fermions. *Phys. Rev. Lett.*, 115:237001, Dec 2015.

[106] Manisha Thakurathi, Pascal Simon, Ipsita Mandal, Jelena Klinovaja, and Daniel Loss. Majorana kramers pairs in rashba double nanowires with interactions and disorder. *Phys. Rev. B*, 97:045415, Jan 2018.

[107] Pierre Pfeuty. The one-dimensional Ising model with a transverse field. *Annals of Physics*, 57(1):79–90, 1970.

[108] P. Jordan and E. Wigner. Über das Paulische äquivalenzverbot. *Zeitschrift für Physik*, 47(9):631–651, Sep 1928.

[109] T. D. Schultz, D. C. Mattis, and E. H. Lieb. Two-dimensional Ising model as a soluble problem of many fermions. *Rev. Mod. Phys.*, 36:856–871, Jul 1964.

[110] Kartik Chhajed. From Ising model to Kitaev chain. *Resonance*, 26(11):1539–1558, Nov 2021.

[111] Jeff Murugan, Zayd Pandit, and Hendrik J. R. Van Zyl. On complexity and duality. *Journal of High Energy Physics*, 2025(3):62, Mar 2025.

[112] Paul Fendley. Parafermionic edge zero modes in $\mathbb{Z}_n$-invariant spin chains. *Journal of Statistical Mechanics: Theory and Experiment*, 2012(11):P11020, nov 2012.

[113] H. A. Kramers and G. H. Wannier. Statistics of the two-dimensional ferromagnet. part i. *Phys. Rev.*, 60:252–262, Aug 1941.

[114] Eduardo H. Fradkin and L. P. Kadanoff. Disorder variables and parafermions in two-dimensional statistical mechanics. *Nucl. Phys. B*, 170:1–15, 1980.

[115] F. Y. Wu and Y. K. Wang. Duality transformation in a many-component spin model. *Journal of Mathematical Physics*, 17(3):439–440, 03 1976.

[116] A.B. Zamolodchikov and Dubna (USSR) Joint Inst. for Nuclear Research. Kramers-wannier transform for z(n) symmetric systems. *Zh. Eksp. Teor. Fiz.*, 75:341–345, 1978.

[117] H. S. Green. A generalized method of field quantization. *Phys. Rev.*, 90:270–273, Apr 1953.

[118] Paul Fendley. Free parafermions. *Journal of Physics A: Mathematical and Theoretical*, 47(7):075001, jan 2014.

[119] Murray T. Batchelor, Robert A. Henry, and Xilin Lu. A brief history of free parafermions. *AAPPS Bulletin*, 33(1):29, Nov 2023.

[120] Zoltán Scherübl, András Pályi, and Szabolcs Csonka. Transport signatures of an Andreev molecule in a quantum dot–superconductor–quantum dot setup. *Beilstein Journal of Nanotechnology*, 10:363–378, 2019.

[121] A. Mert Bozkurt, Sebastian Miles, Sebastiaan L. D. ten Haaf, Chun-Xiao Liu, Fabian Hassler, and Michael Wimmer. Interaction-induced strong zero modes in short quantum dot chains with time-reversal symmetry. *SciPost Phys.*, 18:206, 2025.

[122] C. D. Batista and G. Ortiz. Generalized jordan-wigner transformations. *Phys. Rev. Lett.*, 86:1082–1085, Feb 2001.

[123] Thomas E. O'Brien, Anthony R. Wright, and Menno Veldhorst. Many-particle Majorana bound states: Derivation and signatures in superconducting double quantum dots. *physica status solidi (b)*, 252(8):1731–1742, 2015.

[124] Raphael L. R. C. Teixeira and Luis G. G. V. Dias da Silva. Edge $\mathbb{Z}_3$ parafermions in fermionic lattices. *Phys. Rev. B*, 105:195121, May 2022.

[125] Yuan Yao and Akira Furusaki. Parafermionization, bosonization, and critical parafermionic theories. *Journal of High Energy Physics*, 2021(4):285, Apr 2021.

[126] Simone Traverso, Christoph Fleckenstein, Maura Sassetti, and Niccolò Traverso Ziani. An exact local mapping from clock-spins to fermions. *SciPost Phys. Core*, 6:055, 2023.

[127] Ivan Kulesh. *Superconducting proximity and confinement in a two-dimensional electron gas.* PhD thesis, Delft University of technology, 2025.

[128] Qingzheng Wang. *Topological superconductivity in InSbAs two-dimensional electron gases.* PhD thesis, Delft University of technology, 2024. In prepration.

[129] Christian M. Möhle, Chung Ting Ke, Qingzhen Wang, Candice Thomas, Di Xiao, Saurabh Karwal, Mario Lodari, Vincent Van De Kerkhof, Ruben Termaat, Geoffrey C. Gardner, Giordano Scappucci, Michael J. Manfra, and Srijit Goswami. InSbAs two-dimensional electron gases as a platform for topological superconductivity. *Nano Letters*, 21:9990–9996, 12 2021.

[130] J. Shabani, M. Kjaergaard, H. J. Suominen, Younghyun Kim, F. Nichele, K. Pakrouski, T. Stankevic, R. M. Lutchyn, P. Krogstrup, R. Feidenhans'l, S. Kraemer, C. Nayak, M. Troyer, C. M. Marcus, and C. J. Palmstrøm. Two-dimensional epitaxial superconductor-semiconductor heterostructures: A platform for topological superconducting networks. *Phys. Rev. B*, 93:155402, Apr 2016.

[131] M. Kjaergaard, F. Nichele, H. J. Suominen, M. P. Nowak, M. Wimmer, A. R. Akhmerov, J. A. Folk, K. Flensberg, J. Shabani, C. J. Palmstrøm, and C. M. Marcus. Quantized conductance doubling and hard gap in a two-dimensional semiconductor–superconductor heterostructure. *Nature Communications*, 7(1):12841, Sep 2016.

[132] Hideaki Takayanagi and Tsuyoshi Kawakami. Superconducting proximity effect in the native inversion layer on InAs. *Phys. Rev. Lett.*, 54:2449–2452, Jun 1985.

[133] Chanh Nguyen, James Werking, Herbert Kroemer, and Evelyn L. Hu. InAs-AlSb quantum well as superconducting weak link with high critical current density. *Applied Physics Letters*, 57(1):87–89, 07 1990.

[134] P. Krogstrup, N. L. B. Ziino, W. Chang, S. M. Albrecht, M. H. Madsen, E. Johnson, J. Nygård, C. M. Marcus, and T. S. Jespersen. Epitaxy of semiconductor–superconductor nanowires. *Nature Materials*, 14(4):400–406, Apr 2015.

[135] William F. Schiela, Peng Yu, and Javad Shabani. Progress in superconductor-semiconductor topological Josephson junctions. *PRX Quantum*, 5:030102, Sep 2024.

[136] Sergej Schuwalow, Niels B. M. Schröter, Jan Gukelberger, Candice Thomas, Vladimir Strocov, John Gamble, Alla Chikina, Marco Caputo, Jonas Krieger, Geoffrey C. Gardner, Matthias Troyer, Gabriel Aeppli, Michael J. Manfra, and Peter Krogstrup. Band structure extraction at hybrid narrow-gap semiconductor-metal interfaces. *Advanced Science*, 8(4):2003087, 2021. © 2020 The Authors. Advanced Science published by Wiley-VCH GmbH.

[137] William Mayer, William F. Schiela, Joseph Yuan, Mehdi Hatefipour, Wendy L. Sarney, Stefan P. Svensson, Asher C. Leff, Tiago Campos, Kaushini S. Wickramasinghe, Matthieu C. Dartiailh, Igor Žutić, and Javad Shabani. Superconducting proximity effect in InAsSb surface quantum wells with in situ Al contacts. *ACS Applied Electronic Materials*, 2(8):2351–2356, Aug 2020.

[138] Sjoerd Telkamp, Zijin Lei, Tommaso Antonelli, Christian Reichl, Ilya Besedin, Georg Jakobs, Stefan Fält, Christian Marty, Rüdiger Schott, and Werner Wegscheider. An InAsSb surface quantum well with in-situ deposited Nb as a platform for semiconductor-superconductor hybrid devices, 2025.

[139] Ivan Kulesh, Sebastiaan L. D. ten Haaf, Qingzhen Wang, Vincent P. M. Sietses, Yining Zhang, Sebastiaan R. Roelofs, Christian G. Prosko, Di Xiao, Candice Thomas, Michael J. Manfra, and Srijit Goswami. Flux-controlled two-site Kitaev chain. *Phys. Rev. Lett.*, 135:056301, Jul 2025.

[140] Yuxuan Jiang, Maksim Ermolaev, Seongphill Moon, Gela Kipshidze, Gregory Belenky, Stefan Svensson, Mykhaylo Ozerov, Dmitry Smirnov, Zhigang Jiang, and Sergey Suchalkin. g-factor engineering with InAsSb alloys toward zero band gap limit. *Phys. Rev. B*, 108:L121201, Sep 2023.

[141] Supriyo Datta. *Electronic Transport in Mesoscopic Systems.* Cambridge Studies in Semiconductor Physics and Microelectronic Engineering. Cambridge University Press, 1995.

[142] Guanzhong Wang, Jouri Bommer, and Michiel de Moor. Notes on transport measurements using a lock-in. Technical report, Delft University of Technology, October 2023.

[143] Esteban A. Martinez, Andreas Pöschl, Esben Bork Hansen, May An Y. van de Poll, Saulius Vaitiekėnas, Andrew P. Higginbotham, and Lucas Casparis. Measurement circuit effects in three-terminal electrical transport measurements, 2021.

[144] Davydas Razmadze, Deividas Sabonis, Filip K. Malinowski, Gerbold C. Ménard, Sebastian Pauka, Hung Nguyen, David M.T. van Zanten, Eoin C.T. O′Farrell, Judith Suter, Peter Krogstrup, Ferdinand Kuemmeth, and Charles M. Marcus. Radio-frequency methods for Majorana-based quantum devices: Fast charge sensing and phase-diagram mapping. *Phys. Rev. Appl.*, 11:064011, Jun 2019.

[145] Florian Vigneau, Federico Fedele, Anasua Chatterjee, David Reilly, Ferdinand Kuemmeth, M. Fernando Gonzalez-Zalba, Edward Laird, and Natalia Ares. Probing quantum devices with radio-frequency reflectometry. *Applied Physics Reviews*, 10(2):021305, 02 2023.

[146] Guido Burkard, Thaddeus D. Ladd, Andrew Pan, John M. Nichol, and Jason R. Petta. Semiconductor spin qubits. *Reviews of Modern Physics*, 95(2), June 2023.

[147] Yining Zhang, Ivan Kulesh, Sebastiaan L. D. ten Haaf, Nick van Loo, Francesco Zatelli, Tijl Degroote, Christian G. Prosko, and Srijit Goswami. Gate reflectometry in a minimal Kitaev chain device, 2025.

[148] Chun-Xiao Liu. Quantum capacitance and parity switching of a quantum-dot-based Kitaev chain, 2026.

[149] H. van Houten, C. W. J. Beenakker, and A. A. M. Staring. Coulomb-blockade oscillations in semiconductor nanostructures. In H. Grabert and M. H. Devoret, editors, *Single Charge Tunneling*, volume 294 of *NATO ASI Series B*. Plenum, New York, 1992.

[150] Leo P. Kouwenhoven, Charles M. Marcus, Paul L. McEuen, Seigo Tarucha, Robert M. Westervelt, and Ned S. Wingreen. *Electron Transport in Quantum Dots*, pages 105–214. Springer Netherlands, Dordrecht, 1997.

[151] Laura M. Roth, Benjamin Lax, and Solomon Zwerdling. Theory of optical magneto-absorption effects in semiconductors. *Phys. Rev.*, 114:90–104, Apr 1959.

[152] A.F. Volkov, P.H.C. Magnée, B.J. van Wees, and T.M. Klapwijk. Proximity and Josephson effects in superconductor-two-dimensional electron gas planar junctions. *Physica C: Superconductivity*, 242(3):261–266, 1995.

[153] Anders Jellinggaard, Kasper Grove-Rasmussen, Morten Hannibal Madsen, and Jesper Nygård. Tuning Yu-Shiba-Rusinov states in a quantum dot. *Phys. Rev. B*, 94:064520, Aug 2016.

[154] K. Grove-Rasmussen, G. Steffensen, A. Jellinggaard, M. H. Madsen, R. Žitko, J. Paaske, and J. Nygård. Yu–Shiba–Rusinov screening of spins in double quantum dots. *Nature Communications*, 9(1):2376, Jun 2018.

[155] Qingzhen Wang, Sebastiaan L. D. ten Haaf, Ivan Kulesh, Di Xiao, Candice Thomas, Michael J. Manfra, and Srijit Goswami. Triplet correlations in Cooper pair splitters realized in a two-dimensional electron gas. *Nature Communications*, 14(1):4876, Aug 2023.

[156] Patrik Recher, Eugene V. Sukhorukov, and Daniel Loss. Andreev tunneling, Coulomb blockade, and resonant transport of nonlocal spin-entangled electrons. *Phys. Rev. B*, 63:165314, Apr 2001.

[157] Nikolai M. Chtchelkatchev, Gianni Blatter, Gordey B. Lesovik, and Thierry Martin. Bell inequalities and entanglement in solid-state devices. *Phys. Rev. B*, 66:161320, Oct 2002.

[158] Bernd Braunecker, Pablo Burset, and Alfredo Levy Yeyati. Entanglement detection from conductance measurements in carbon nanotube Cooper pair splitters. *Phys. Rev. Lett.*, 111:136806, Sep 2013.

[159] Waldemar Kłobus, Andrzej Grudka, Andreas Baumgartner, Damian Tomaszewski, Christian Schönenberger, and Jan Martinek. Entanglement witnessing and quantum cryptography with nonideal ferromagnetic detectors. *Phys. Rev. B*, 89:125404, Mar 2014.

[160] F. Brange, O. Malkoc, and P. Samuelsson. Minimal entanglement witness from electrical current correlations. *Phys. Rev. Lett.*, 118:036804, Jan 2017.

[161] Piotr Busz, Damian Tomaszewski, and Jan Martinek. Spin correlation and entanglement detection in Cooper pair splitters by current measurements using magnetic detectors. *Phys. Rev. B*, 96:064520, Aug 2017.

[162] R. S. Deacon, A. Oiwa, J. Sailer, S. Baba, Y. Kanai, K. Shibata, K. Hirakawa, and S. Tarucha. Cooper pair splitting in parallel quantum dot Josephson junctions. *Nature Communications*, 6(1):7446, Jul 2015.

[163] Z. B. Tan, D. Cox, T. Nieminen, P. Lähteenmäki, D. Golubev, G. B. Lesovik, and P. J. Hakonen. Cooper pair splitting by means of graphene quantum dots. *Phys. Rev. Lett.*, 114:096602, Mar 2015.

[164] S. Metti, C. Thomas, D. Xiao, and M. J. Manfra. Spin-orbit coupling and electron scattering in high-quality $InSb_{1-x}As_x$ quantum wells. *Phys. Rev. B*, 106:165304, Oct 2022.

[165] Jeroen Danon, Anna Birk Hellenes, Esben Bork Hansen, Lucas Casparis, Andrew P. Higginbotham, and Karsten Flensberg. Nonlocal conductance spectroscopy of Andreev bound states: Symmetry relations and bcs charges. *Phys. Rev. Lett.*, 124:036801, Jan 2020.

[166] Andreas Pöschl, Alisa Danilenko, Deividas Sabonis, Kaur Kristjuhan, Tyler Lindemann, Candice Thomas, Michael J. Manfra, and Charles M. Marcus. Nonlocal conductance spectroscopy of Andreev bound states in gate-defined InAs/Al nanowires. *Phys. Rev. B*, 106:L241301, Dec 2022.

[167] R. S. Deacon, Y. Tanaka, A. Oiwa, R. Sakano, K. Yoshida, K. Shibata, K. Hirakawa, and S. Tarucha. Kondo-enhanced Andreev transport in single self-assembled InAs quantum dots contacted with normal and superconducting leads. *Phys. Rev. B*, 81:121308, Mar 2010.

[168] J. Gramich, A. Baumgartner, and C. Schönenberger. Resonant and inelastic Andreev tunneling observed on a carbon nanotube quantum dot. *Phys. Rev. Lett.*, 115:216801, Nov 2015.

[169] W. G. van der Wiel, S. De Franceschi, J. M. Elzerman, T. Fujisawa, S. Tarucha, and L. P. Kouwenhoven. Electron transport through double quantum dots. *Rev. Mod. Phys.*, 75:1–22, Dec 2002.

[170] S. Nadj-Perge, S. M. Frolov, J. W. W. van Tilburg, J. Danon, Yu. V. Nazarov, R. Algra, E. P. A. M. Bakkers, and L. P. Kouwenhoven. Disentangling the effects of spin-orbit and hyperfine interactions on spin blockade. *Phys. Rev. B*, 81:201305, May 2010.

[171] J. Danon and Yu. V. Nazarov. Pauli spin blockade in the presence of strong spin-orbit coupling. *Phys. Rev. B*, 80:041301, Jul 2009.

[172] Arunav Bordoloi, Valentina Zannier, Lucia Sorba, Christian Schönenberger, and Andreas Baumgartner. Spin cross-correlation experiments in an electron entangler. *Nature*, 612(7940):454–458, Dec 2022.

[173] M. C. Hels, B. Braunecker, K. Grove-Rasmussen, and J. Nygård. Noncollinear spin-orbit magnetic fields in a carbon nanotube double quantum dot. *Phys. Rev. Lett.*, 117:276802, Dec 2016.

[174] Jason Alicea, Yuval Oreg, Gil Refael, Felix von Oppen, and Matthew P. A. Fisher. Non-abelian statistics and topological quantum information processing in 1d wire networks. *Nature Physics*, 7(5):412–417, May 2011.

[175] Qingzhen Wang and Sebastiaan L. D. ten Haaf. Data repository for “Triplet Cooper pair splitting in a two-dimensional electron gas", 2022. https://zenodo.org/doi/10.5281/zenodo.7311374.

[176] Christian M. Moehle, Prasanna K. Rout, Nayan A. Jainandunsing, Dibyendu Kuiri, Chung Ting Ke, Di Xiao, Candice Thomas, Michael J. Manfra, Michał P. Nowak, and Srijit Goswami. Controlling Andreev bound states with the magnetic vector potential. *Nano Letters*, 22(21):8601–8607, Nov 2022.

[177] Athanasios Tsintzis, Rubén Seoane Souto, Karsten Flensberg, Jeroen Danon, and Martin Leijnse. Majorana qubits and non-abelian physics in quantum dot–based minimal Kitaev chains. *PRX Quantum*, 5:010323, Feb 2024.

[178] Sebastiaan L. D. ten Haaf, Qingzhen Wang, A. Mert Bozkurt, Chun-Xiao Liu, Ivan Kulesh, Philip Kim, Di Xiao, Candice Thomas, Michael J. Manfra, Tom Dvir, Michael Wimmer, and Srijit Goswami. A two-site Kitaev chain in a two-dimensional electron gas. *Nature*, 630(8016):329–334, Jun 2024.

[179] Gábor Széchenyi and András Pályi. Parity-to-charge conversion for readout of topological Majorana qubits. *Phys. Rev. B*, 101:235441, Jun 2020.

[180] Péter Boross and András Pályi. Braiding-based quantum control of a Majorana qubit built from quantum dots. *Phys. Rev. B*, 109:125410, Mar 2024.

[181] Chun-Xiao Liu, Haining Pan, F. Setiawan, Michael Wimmer, and Jay D. Sau. Fusion protocol for Majorana modes in coupled quantum dots. *Phys. Rev. B*, 108:085437, Aug 2023.

[182] K. Grove-Rasmussen, H. I. Jørgensen, B. M. Andersen, J. Paaske, T. S. Jespersen, J. Nygård, K. Flensberg, and P. E. Lindelof. Superconductivity-enhanced bias spectroscopy in carbon nanotube quantum dots. *Phys. Rev. B*, 79:134518, Apr 2009.

[183] R. S. Deacon, Y. Tanaka, A. Oiwa, R. Sakano, K. Yoshida, K. Shibata, K. Hirakawa, and S. Tarucha. Tunneling spectroscopy of Andreev energy levels in a quantum dot coupled to a superconductor. *Phys. Rev. Lett.*, 104:076805, Feb 2010.

[184] Li Dai, Watson Kuo, and Ming-Chiang Chung. Extracting entangled qubits from Majorana fermions in quantum dot chains through the measurement of parity. *Scientific Reports*, 5(1):11188, Jun 2015.

[185] D. Michel Pino, Rubén Seoane Souto, and Ramón Aguado. Minimal Kitaev-transmon qubit based on double quantum dots. *Phys. Rev. B*, 109:075101, Feb 2024.

[186] Sebastiaan L. D. ten Haaf. Data and Code for "A two-site Kitaev chain in a two-dimensional electron gas", 2024. https://zenodo.org/doi/10.5281/zenodo.10801215.

[187] Sebastiaan L. D. ten Haaf, Yining Zhang, Qingzhen Wang, Alberto Bordin, Chun-Xiao Liu, Ivan Kulesh, Vincent P. M. Sietses, Christian G. Prosko, Di Xiao, Candice Thomas, Michael J. Manfra, Michael Wimmer, and Srijit Goswami. Observation of edge and bulk states in a three-site Kitaev chain. *Nature*, 641(8064):890–895, May 2025.

[188] C. L. Kane and E. J. Mele. Quantum spin hall effect in graphene. *Phys. Rev. Lett.*, 95:226801, Nov 2005.

[189] M. Z. Hasan and C. L. Kane. Colloquium: Topological insulators. *Rev. Mod. Phys.*, 82:3045–3067, Nov 2010.

[190] Xiao-Liang Qi and Shou-Cheng Zhang. Topological insulators and superconductors. *Rev. Mod. Phys.*, 83:1057–1110, Oct 2011.

[191] B. I. Halperin. Quantized hall conductance, current-carrying edge states, and the existence of extended states in a two-dimensional disordered potential. *Phys. Rev. B*, 25:2185–2190, Feb 1982.

[192] Xiao-Gang Wen. Topological orders and edge excitations in fractional quantum hall states. *Advances in Physics*, 44(5):405–473, 1995.

[193] Chun-Xiao Liu, Jay D. Sau, Tudor D. Stanescu, and S. Das Sarma. Andreev bound states versus Majorana bound states in quantum dot-nanowire-superconductor hybrid structures: Trivial versus topological zero-bias conductance peaks. *Phys. Rev. B*, 96:075161, Aug 2017.

[194] Christopher Reeg, Olesia Dmytruk, Denis Chevallier, Daniel Loss, and Jelena Klinovaja. Zero-energy Andreev bound states from quantum dots in proximitized Rashba nanowires. *Phys. Rev. B*, 98:245407, Dec 2018.

[195] Adriaan Vuik, Bas Nijholt, Anton R. Akhmerov, and Michael Wimmer. Reproducing topological properties with quasi-Majorana states. *SciPost Phys.*, 7:061, 2019.

[196] Sankar Das Sarma and Haining Pan. Disorder-induced zero-bias peaks in Majorana nanowires. *Phys. Rev. B*, 103:195158, May 2021.

[197] Jian Li, Hua Chen, Ilya K. Drozdov, A. Yazdani, B. Andrei Bernevig, and A. H. MacDonald. Topological superconductivity induced by ferromagnetic metal chains. *Phys. Rev. B*, 90:235433, Dec 2014.

[198] Stevan Nadj-Perge, Ilya K. Drozdov, Jian Li, Hua Chen, Sangjun Jeon, Jungpil Seo, Allan H. MacDonald, B. Andrei Bernevig, and Ali Yazdani. Observation of Majorana fermions in ferromagnetic atomic chains on a superconductor. *Science*, 346(6209):602–607, 2014.

[199] Zhi-Hai Liu, Chuanchang Zeng, and H. Q. Xu. Coupling of quantum-dot states via elastic cotunneling and crossed Andreev reflection in a minimal Kitaev chain. *Phys. Rev. B*, 110:115302, Sep 2024.

[200] Chun-Xiao Liu, Sebastian Miles, Alberto Bordin, Sebastiaan L. D. ten Haaf, Grzegorz P. Mazur, A. Mert Bozkurt, and Michael Wimmer. Scaling up a sign-ordered Kitaev chain without magnetic flux control. *Phys. Rev. Res.*, 7:L012045, Feb 2025.

[201] Bradraj Pandey, Gaurav Kumar Gupta, Gonzalo Alvarez, Satoshi Okamoto, and Elbio Dagotto. Diabatic error and propagation of Majorana zero modes in interacting quantum dots systems, 2025.

[202] Bradraj Pandey, Satoshi Okamoto, and Elbio Dagotto. Nontrivial fusion of Majorana zero modes in interacting quantum-dot arrays. *Phys. Rev. Res.*, 6:033314, Sep 2024.

[203] Bradraj Pandey, Nitin Kaushal, Gonzalo Alvarez, and Elbio Dagotto. Majorana zero modes in Y-shape interacting Kitaev wires. *npj Quantum Materials*, 8(1):51, Sep 2023.

[204] Motohiko Ezawa. Even-odd effect on robustness of Majorana edge states in short Kitaev chains. *Phys. Rev. B*, 109:L161404, Apr 2024.

[205] Melina Luethi, Henry F. Legg, Daniel Loss, and Jelena Klinovaja. The fate of poor man's Majoranas in the long Kitaev chain limit, 2025.

[206] Haining Pan, Sankar Das Sarma, and Chun-Xiao Liu. Rabi and Ramsey oscillations of a Majorana qubit in a quantum dot-superconductor array. *Phys. Rev. B*, 111:075416, Feb 2025.

[207] Sebastiaan L. D. ten Haaf. Data and Code for "Observation of edge and bulk states in a three site Kitaev chain", 2025. https://zenodo.org/doi/10.5281/zenodo.15020006.

[208] J. M. Hornibrook, J. I. Colless, A. C. Mahoney, X. G. Croot, S. Blanvillain, H. Lu, A. C. Gossard, and D. J. Reilly. Frequency multiplexing for readout of spin qubits. *Applied Physics Letters*, 104(10):103108, 03 2014.

[209] Luka Pavešič, Ramón Aguado, and Rok Žitko. Strong-coupling theory of quantum-dot Josephson junctions: Role of a residual quasiparticle. *Phys. Rev. B*, 109:125131, Mar 2024.

[210] C. W. J. Beenakker. Theory of Coulomb-blockade oscillations in the conductance of a quantum dot. *Phys. Rev. B*, 44:1646–1656, Jul 1991.

[211] Anders Jellinggaard, Kasper Grove-Rasmussen, Morten Hannibal Madsen, and Jesper Nygård. Tuning Yu-Shiba-Rusinov states in a quantum dot. *Phys. Rev. B*, 94:064520, Aug 2016.

[212] Sebastiaan L. D. ten Haaf, Sebastian Miles, Qingzhen Wang, A. Mert Bozkurt, Ivan Kulesh, Yining Zhang, Christian G. Prosko, Michael Wimmer, and Srijit Goswami. Probing ground-state degeneracies of a strongly interacting Fermi-Hubbard model with superconducting correlations, 2025.

[213] J. Hubbard and Brian Hilton Flowers. Electron correlations in narrow energy bands. *Proceedings of the Royal Society of London. Series A. Mathematical and Physical Sciences*, 276(1365):238–257, 1963.

[214] Daniel P. Arovas, Erez Berg, Steven A. Kivelson, and Srinivas Raghu. The hubbard model. *Annual Review of Condensed Matter Physics*, 13(Volume 13, 2022):239–274, 2022.

[215] Patrick A. Lee, Naoto Nagaosa, and Xiao-Gang Wen. Doping a Mott insulator: Physics of high-temperature superconductivity. *Reviews of Modern Physics*, 78(1):17–85, January 2006. Publisher: American Physical Society.

[216] Tilman Esslinger. Fermi-Hubbard Physics with Atoms in an Optical Lattice. *Annual Review of Condensed Matter Physics*, 1(Volume 1, 2010):129–152, August 2010. Publisher: Annual Reviews.

[217] Michael Johanning, Andrés F Varón, and Christof Wunderlich. Quantum simulations with cold trapped ions. *Journal of Physics B: Atomic, Molecular and Optical Physics*, 42(15):154009, July 2009.

[218] Sebastian Schmidt and Jens Koch. Circuit QED lattices: Towards quantum simulation with superconducting circuits. *Annalen der Physik*, 525(6):395–412, 2013.

[219] Andrew A. Houck, Hakan E. Türeci, and Jens Koch. On-chip quantum simulation with superconducting circuits. *Nature Physics*, 8(4):292–299, April 2012. Publisher: Nature Publishing Group.

[220] Shuo Yang, Xin Wang, and S. Das Sarma. Generic Hubbard model description of semiconductor quantum-dot spin qubits. *Physical Review B*, 83(16):161301, April 2011. Publisher: American Physical Society.

[221] T. Hensgens, T. Fujita, L. Janssen, Xiao Li, C. J. Van Diepen, C. Reichl, W. Wegscheider, S. Das Sarma, and L. M. K. Vandersypen. Quantum simulation of a Fermi–Hubbard model using a semiconductor quantum dot array. *Nature*, 548(7665):70–73, August 2017. Publisher: Nature Publishing Group.

[222] Tim Byrnes, Na Young Kim, Kenichiro Kusudo, and Yoshihisa Yamamoto. Quantum simulation of Fermi-Hubbard models in semiconductor quantum-dot arrays. *Physical Review B*, 78(7):075320, August 2008. Publisher: American Physical Society.

[223] Anthony R. Wright and Menno Veldhorst. Localized many-particle Majorana modes with vanishing time-reversal symmetry breaking in double quantum dots. *Phys. Rev. Lett.*, 111:096801, Aug 2013.

[224] DJ Reilly, CM Marcus, MP Hanson, and AC Gossard. Fast single-charge sensing with a rf quantum point contact. *Applied Physics Letters*, 91(16), 2007.

[225] M Jung, MD Schroer, KD Petersson, and Jason R Petta. Radio frequency charge sensing in InAs nanowire double quantum dots. *Applied Physics Letters*, 100(25), 2012.

[226] Rodrigo A. Dourado, Martin Leijnse, and Rubén Seoane Souto. Majorana sweet spots in three-site Kitaev chains. *Phys. Rev. B*, 111:235409, Jun 2025.

[227] Adam S. Jermyn, Roger S. K. Mong, Jason Alicea, and Paul Fendley. Stability of zero modes in parafermion chains. *Phys. Rev. B*, 90:165106, Oct 2014.

[228] Steven Howes, Leo P. Kadanoff, and Marcel Den Nijs. Quantum model for commensurate-incommensurate transitions. *Nuclear Physics B*, 215(2):169–208, 1983.

[229] S. Ostlund. Incommensurate and commensurate phases in asymmetric clock models. *Phys. Rev. B*, 24:398–405, Jul 1981.

[230] Isidora Araya Day, Sebastian Miles, Hugo K. Kerstens, Daniel Varjas, and Anton R. Akhmerov. Codebase release 2.1 for Pymablock. *SciPost Phys. Codebases*, pages 50–r2.1, 2025.

[231] Sebastiaan L. D. ten Haaf and Sebastian Miles. Data and Code for “Probing ground-state degeneracies of a strongly interacting Fermi-Hubbard model with superconducting correlations", 2025. https://zenodo.org/doi/10.5281/zenodo.17872114.

[232] Wietze D. Huisman, Sebastiaan L. D. ten Haaf, Chun-Xiao Liu, Qingzhen Wang, Alberto Bordin, Florian J. Bennebroek Evertsz’, Bart Roovers, Michael Wimmer, and Srijit Goswami. Using Andreev bound states and spin to remove domain walls in a Kitaev chain, 2026.

[233] Svend Krøjer, Rubéen Seoane Souto, and Karsten Flensberg. Demonstrating Majorana non-Abelian properties using fast adiabatic charge transfer. *Phys. Rev. B*, 105:045425, Jan 2022.

[234] Sebastian Miles, Francesco Zatelli, A. Mert Bozkurt, Michael Wimmer, and Chun-Xiao Liu. Braiding Majoranas in a linear quantum dot-superconductor array: Mitigating the errors from Coulomb repulsion and residual tunneling, 2025.

[235] S. Metti, C. Thomas, and M. J. Manfra. Electronic g factor and tunable spin-orbit coupling in a gate-defined InSbAs quantum dot. *Phys. Rev. B*, 108:235306, Dec 2023.

[236] Christian G. Prosko, Wietze D. Huisman, Ivan Kulesh, Di Xiao, Candice Thomas, Michael J. Manfra, and Srijit Goswami. Flux-tunable Josephson effect in a four-terminal junction. *Phys. Rev. B*, 110:064518, Aug 2024.

[237] Magnus R. Lykkegaard, Anders Enevold Dahl, Tyler Lindemann, Michael J. Manfra, Karsten Flensberg, and Charles M. Marcus. Phase-biased Andreev diffraction grating. *Phys. Rev. Lett.*, 135:066301, Aug 2025.

[238] Sebastiaan L. D. ten Haaf and Wietze D. Huisman. Data and Code for “Controlling phase with Andreev bound states and spin to remove domain walls in a Kitaev chain", 2025. https://zenodo.org/doi/10.5281/zenodo.17857948.

[239] Fernando Domínguez and Alfredo Levy Yeyati. Quantum interference in a cooper pair splitter: The three sites model. *Physica E: Low-dimensional Systems and Nanostructures*, 75:322–329, 2016.

[240] Isidora Araya Day, Sebastian Miles, Hugo K. Kerstens, Daniel Varjas, and Anton R. Akhmerov. Pymablock: An algorithm and a package for quasi-degenerate perturbation theory. *SciPost Phys. Codebases*, page 50, 2025.

[241] Isidora Araya Day, Sebastian Miles, Hugo K. Kerstens, Daniel Varjas, and Anton R. Akhmerov. Codebase release 2.1 for Pymablock. *SciPost Phys. Codebases*, pages 50–r2.1, 2025.

[242] David C. Langreth. Friedel sum rule for Anderson's model of localized impurity states. *Phys. Rev.*, 150:516–518, Oct 1966.

[243] Masashi Hashimoto, Yasuhiro Yamada, Yoichi Tanaka, Yoshimichi Teratani, Takuro Kemi, Norio Kawakami, and Akira Oguri. Nonlocal Andreev transport through a quantum dot in a magnetic field: Interplay between Kondo, Zeeman, and Cooper-pair correlations. *Phys. Rev. B*, 109:035404, Jan 2024.

[244] R. Schuster, E. Buks, M. Heiblum, D. Mahalu, V. Umansky, and Hadas Shtrikman. Phase measurement in a quantum dot via a double-slit interference experiment. *Nature*, 385(6615):417–420, Jan 1997.

[245] A. Yacoby, M. Heiblum, D. Mahalu, and Hadas Shtrikman. Coherence and phase sensitive measurements in a quantum dot. *Phys. Rev. Lett.*, 74:4047–4050, May 1995.

[246] A. Levy Yeyati and M. Büttiker. Aharonov-Bohm oscillations in a mesoscopic ring with a quantum dot. *Physical Review B*, 52:R14360–R14363, 1995.

[247] Justyna P. Zwolak, Thomas McJunkin, Sandesh S. Kalantre, J.P. Dodson, E.R. MacQuarrie, D.E. Savage, M.G. Lagally, S.N. Coppersmith, Mark A. Eriksson, and Jacob M. Taylor. Autotuning of double-dot devices in situ with machine learning. *Phys. Rev. Appl.*, 13:034075, Mar 2020.

[248] R. Durrer, B. Kratochwil, J.V. Koski, A.J. Landig, C. Reichl, W. Wegscheider, T. Ihn, and E. Greplova. Automated tuning of double quantum dots into specific charge states using neural networks. *Phys. Rev. Appl.*, 13:054019, May 2020.

[249] H Moon, D T Lennon, J Kirkpatrick, N M van Esbroeck, L C Camenzind, Liuqi Yu, F Vigneau, D M Zumbühl, G A D Briggs, M A Osborne, D Sejdinovic, E A Laird, and N Ares. Machine learning enables completely automatic tuning of a quantum device faster than human experts. *Nat Commun*, 11(1):4161, August 2020.

[250] V. Nguyen, S. B. Orbell, D. T. Lennon, H. Moon, F. Vigneau, L. C. Camenzind, L. Yu, D. M. Zumbühl, G. A. D. Briggs, M. A. Osborne, D. Sejdinovic, and N. Ares. Deep reinforcement learning for efficient measurement of quantum devices. *npj Quantum Information*, 7(1):100, Jun 2021.

[251] Justyna P. Zwolak and Jacob M. Taylor. Colloquium: Advances in automation of quantum dot devices control. *Rev. Mod. Phys.*, 95:011006, Feb 2023.

[252] Rouven Koch, David van Driel, Alberto Bordin, Jose L. Lado, and Eliska Greplova. Adversarial hamiltonian learning of quantum dots in a minimal Kitaev chain. *Phys. Rev. Appl.*, 20:044081, Oct 2023.

[253] Jacob Benestad, Athanasios Tsintzis, Rubén Seoane Souto, Martin Leijnse, Evert van Nieuwenburg, and Jeroen Danon. Machine-learned tuning of artificial kitaev chains from tunneling spectroscopy measurements. *Phys. Rev. B*, 110:075402, Aug 2024.

[254] David van Driel, Rouven Koch, Vincent P. M. Sietses, Sebastiaan L. D. ten Haaf, Chun-Xiao Liu, Francesco Zatelli, Bart Roovers, Alberto Bordin, Nick van Loo, Guanzhong Wang, Jan Cornelis Wolff, Grzegorz P. Mazur, Tom Dvir, Ivan Kulesh, Qingzhen Wang, A. Mert Bozkurt, Sasa

Gazibegovic, Ghada Badawy, Erik P. A. M. Bakkers, Michael Wimmer, Srijit Goswami, Jose L. Lado, Leo P. Kouwenhoven, and Eliska Greplova. Cross-platform autonomous control of minimal Kitaev chains, 2024.

[255] David Pekker, Po Zhang, and Sergey M. Frolov. Theory of Andreev blockade in a double quantum dot with a superconducting lead. *SciPost Phys.*, 11:081, 2021.

[256] Po Zhang, Hao Wu, Jun Chen, Sabbir A. Khan, Peter Krogstrup, David Pekker, and Sergey M. Frolov. Signatures of Andreev blockade in a double quantum dot coupled to a superconductor. *Phys. Rev. Lett.*, 128:046801, Jan 2022.

[257] Sergey B. Bravyi and Alexei Yu. Kitaev. Fermionic quantum computation. *Annals of Physics*, 298(1):210–226, 2002.

[258] F Verstraete and J I Cirac. Mapping local Hamiltonians of fermions to local Hamiltonians of spins. *Journal of Statistical Mechanics: Theory and Experiment*, 2005(09):P09012, sep 2005.

[259] J. M. Leinaas and J. Myrheim. On the theory of identical particles. *Il Nuovo Cimento B (1971-1996)*, 37(1):1–23, Jan 1977.

[260] Frank Wilczek. Quantum mechanics of fractional-spin particles. *Phys. Rev. Lett.*, 49:957–959, Oct 1982.

[261] Shibo Xu, Zheng-Zhi Sun, Ke Wang, Liang Xiang, Zehang Bao, Zitian Zhu, Fanhao Shen, Zixuan Song, Pengfei Zhang, Wenhui Ren, Xu Zhang, Hang Dong, Jinfeng Deng, Jiachen Chen, Yaozu Wu, Ziqi Tan, Yu Gao, Feitong Jin, Xuhao Zhu, Chuanyu Zhang, Ning Wang, Yiren Zou, Jiarun Zhong, Aosai Zhang, Weikang Li, Wenjie Jiang, Li-Wei Yu, Yunyan Yao, Zhen Wang, Hekang Li, Qiujiang Guo, Chao Song, H. Wang, and Dong-Ling Deng. Digital simulation of projective non-abelian anyons with 68 superconducting qubits. *Chinese Physics Letters*, 40(6):060301, jun 2023.

[262] T. I. Andersen, Y. D. Lensky, K. Kechedzhi, I. K. Drozdov, A. Bengtsson, S. Hong, A. Morvan, X. Mi, A. Opremcak, R. Acharya, R. Allen, M. Ansmann, F. Arute, K. Arya, A. Asfaw, and J. et al. Atalaya. Non-abelian braiding of graph vertices in a superconducting processor. *Nature*, 618(7964):264–269, Jun 2023.

[263] Mohsin Iqbal, Nathanan Tantivasadakarn, Ruben Verresen, Sara L. Campbell, Joan M. Dreiling, Caroline Figgatt, John P. Gaebler, Jacob Johansen, Michael Mills, Steven A. Moses, Juan M. Pino, Anthony Ransford, Mary Rowe, Peter Siegfried, Russell P. Stutz, Michael Foss-Feig, Ashvin Vishwanath, and Henrik Dreyer. Non-abelian topological order and anyons on a trapped-ion processor. *Nature*, 626(7999):505–511, Feb 2024.

[264] R. L. Willett, K. Shtengel, C. Nayak, L. N. Pfeiffer, Y. J. Chung, M. L. Peabody, K. W. Baldwin, and K. W. West. Interference measurements of non-abelian e/4 and abelian e/2 quasiparticle braiding. *Phys. Rev. X*, 13:011028, Mar 2023.

[265] E. Artin. Theory of braids. *Annals of Mathematics*, 48(1):101–126, 1947.

[266] Wonill Ha, Sieu D. Ha, Maxwell D. Choi, Yan Tang, Adele E. Schmitz, Mark P. Levendorf, Kangmu Lee, James M. Chappell, Tower S. Adams, Daniel R. Hulbert, Edwin Acuna, Ramsey S. Noah, Justine W. Matten, Michael P. Jura, Jeffrey A. Wright, Matthew T. Rakher, and Matthew G. Borselli. A flexible design platform for Si/SiGe exchange-only qubits with low disorder. *Nano Letters*, 22(3):1443–1448, Feb 2022.

[267] Nick van Loo, Francesco Zatelli, Gorm O. Steffensen, Bart Roovers, Guanzhong Wang, Thomas Van Caekenberghe, Alberto Bordin, David van Driel, Yining Zhang, Wietze D. Huisman, Ghada Badawy, Erik P. A. M. Bakkers, Grzegorz P. Mazur, Ramón Aguado, and Leo P. Kouwenhoven. Single-shot parity readout of a minimal Kitaev chain. *Nature*, 650(8101):334–339, Feb 2026.

[268] Alexei Kitaev and John Preskill. Topological entanglement entropy. *Phys. Rev. Lett.*, 96:110404, Mar 2006.

[269] Michael Levin and Xiao-Gang Wen. Detecting topological order in a ground state wave function. *Phys. Rev. Lett.*, 96:110405, Mar 2006.

[270] N. R. Cooper and Ady Stern. Observable bulk signatures of non-abelian quantum hall states. *Phys. Rev. Lett.*, 102:176807, Apr 2009.

[271] Nikolaus Hartman, Christian Olsen, Silvia Lüscher, Mohammad Samani, Saeed Fallahi, Geoffrey C. Gardner, Michael Manfra, and Joshua Folk. Direct entropy measurement in a mesoscopic quantum system. *Nature Physics*, 14(11):1083–1086, Nov 2018.

[272] Yaakov Kleeorin, Holger Thierschmann, Hartmut Buhmann, Antoine Georges, Laurens W. Molenkamp, and Yigal Meir. How to measure the entropy of a mesoscopic system via thermoelectric transport. *Nature Communications*, 10(1):5801, Dec 2019.

[273] Timothy Child, Owen Sheekey, Silvia Lüscher, Saeed Fallahi, Geoffrey C. Gardner, Michael Manfra, Andrew Mitchell, Eran Sela, Yaakov Kleeorin, Yigal Meir, and Joshua Folk. Entropy measurement of a strongly coupled quantum dot. *Phys. Rev. Lett.*, 129:227702, Nov 2022.

[274] Sergey Smirnov. Majorana tunneling entropy. *Phys. Rev. B*, 92:195312, Nov 2015.

[275] Eran Sela, Yuval Oreg, Stephan Plugge, Nikolaus Hartman, Silvia Lüscher, and Joshua Folk. Detecting the universal fractional entropy of Majorana zero modes. *Phys. Rev. Lett.*, 123:147702, Oct 2019.

[276] Sebastiaan L. D. ten Haaf. KitaevTool. `https://github.com/SebTenHaaf/KitaevTool`, 2025.

[277] Gediminas Kiršanskas, Jonas Nyvold Pedersen, Olov Karlström, Martin Leijnse, and Andreas Wacker. Qmeq 1.0: An open-source python package for calculations of transport through quantum dot devices. *Computer Physics Communications*, 221:317–342, 2017.

[278] Phillip Weinberg and Marin Bukov. QuSpin: a Python package for dynamics and exact diagonalisation of quantum many body systems part I: spin chains. *SciPost Phys.*, 2:003, 2017.

[279] Jarrod R McClean, Nicholas C Rubin, Kevin J Sung, Ian D Kivlichan, Xavier Bonet-Monroig, Yudong Cao, Chengyu Dai, E Schuyler Fried, Craig Gidney, Brendan Gimby, Pranav Gokhale, Thomas HÃ¤ner, Tarini Hardikar, VojtÄ›ch Havlaek, Oscar Higgott, Cupjin Huang, Josh Izaac, Zhang Jiang, Xinle Liu, Sam McArdle, Matthew Neeley, Thomas O'Brien, Bryan O'Gorman, Isil Ozfidan, Maxwell D Radin, Jhonathan Romero, Nicolas P D Sawaya, Bruno Senjean, Kanav Setia, Sukin Sim, Damian S Steiger, Mark Steudtner, Qiming Sun, Wei Sun, Daochen Wang, Fang Zhang, and Ryan Babbush. OpenFermion: the electronic structure package for quantum computers. *Quantum Science and Technology*, 5(3):034014, jun 2020.

[280] Cornelius Lanczos. An iteration method for the solution of the eigenvalue problem of linear differential and integral operators. *J. Res. Natl. Bur. Stand. B*, 45:255–282, 1950.

[281] M. Leijnse and M. R. Wegewijs. Kinetic equations for transport through single-molecule transistors. *Phys. Rev. B*, 78:235424, Dec 2008.

[282] D. C. Youla. A normal form for a matrix under the unitary congruence group. *Canadian Journal of Mathematics*, 13:694–704, 1961.

[283] Roger A. Horn and Charles R. Johnson. *Matrix Analysis.* Cambridge University Press, Cambridge, 2 edition, 2013. Corollary 2.6.6.

[284] H. Weyl. *The Classical Groups: Their Invariants and Representations.* Number nr. 1,dl. 1 in Princeton Landmarks in Mathematics and Physics. Princeton University Press, 1946. Pfaffian introduced on page 166.

[285] N.G. de Bruijn. On some multiple integrals involving determinants. *Journal of the Indian Mathematical Society. New Series*, 19:133–151, 1955.

[286] Aurélien Grabsch, Yevheniia Cheipesh, and Carlo W. J. Beenakker. Pfaffian formula for fermion parity fluctuations in a superconductor and application to Majorana fusion detection. *Annalen der Physik*, 531(10):1900129, 2019.

[287] Sebastian Miles, David van Driel, Michael Wimmer, and Chun-Xiao Liu. Kitaev chain in an alternating quantum dot-Andreev bound state array. *Phys. Rev. B*, 110:024520, Jul 2024.

[288] James Eldridge, Marco G. Pala, Michele Governale, and Jürgen König. Superconducting proximity effect in interacting double-dot systems. *Phys. Rev. B*, 82:184507, Nov 2010.

Curriculum Vitæ

Sebastiaan Laurens Daniël ten Haaf

1997/03/21	Date of birth in Rijswijk, The Netherlands
2011-2014	**The British School Muscat, Oman**
2014-2017	**BSc in Physics, Leiden University** *BSc Thesis*: "The effect of curvature on diffusion in solid supported lipid bilayers" (Supervisor: Prof. dr D.J. Kraft) Honours college Bèta and Life Science
2019-2021	**MSc in Physics, Leiden University** *Specialisation*: Quantum Matter and Optics *MSc Thesis 1*: "Filter cavity design for filtering photons at 1 MHz separation" (Supervisor: Prof. dr. D. Bouwmeester) *MSc Thesis 2*: "Delocalized Andreev Bound States in coupled quantum dots" (Supervisor: Prof. dr. J. van Ruijtenbeek)
2022-2026	**PhD in Applied Physics, Delft University of Technology** *Thesis*: Majoranas can be lonely - engineering the Kitaev chain in a two-dimensional electron gas *Promotor*: Prof. dr. Michael Wimmer *Co-promotor*: Dr. Srijit Goswami

List of Publications

Journal publications and preprints

🗎 Included in this thesis.
† Equal Contribution.

18. *Probing Majorana localization of a phase-controlled three-site Kitaev chain with an additional quantum dot*
Alberto Bordin†, Florian J. Bennebroek Evertsz'†, Bart Roovers†, Juan D. Torres Luna†, Wietze D. Huisman, Francesco Zatelli, Grzegorz P. Mazur, **Sebastiaan L. D. ten Haaf**, Ghada Badawy, Erik P. A. M. Bakkers, Chun-Xiao Liu, Ruben Seoane Souto, Nick van Loo and Leo P. Kouwenhoven
Nature Communications (2026)

🗎 17. *Using Andreev bound states and spin to remove domain walls in a Kitaev chain*
Wietze D. Huisman†, **Sebastiaan L. D. ten Haaf**†, Chun-Xiao Liu, Qingzhen Wang, Alberto Bordin, Florian J. Bennebroek Evertsz', Bart Roovers, Michael Wimmer and Srijit Goswami
arXiv:2601.12891 (2026)

🗎 16. *Probing ground-state degeneracies of a strongly interacting Fermi-Hubbard model with superconducting correlations*
Sebastiaan L. D. ten Haaf†, Sebastian Miles†, Qingzhen Wang, A. Mert Bozkurt, Ivan Kulesh, Yining Zhang, Christian G. Prosko, Michael Wimmer and Srijit Goswami
arXiv:2512.13242 (2025)

15. *Gate reflectometry in a minimal Kitaev chain device*
Yining Zhang, Ivan Kulesh, **Sebastiaan L. D. ten Haaf**, Nick van Loo, Francesco Zatelli, Tijl Degroote, Christian G. Prosko and Srijit Goswami
arXiv:2508.06403 (2025)

14. *Flux-controlled two-site Kitaev chain*
Ivan Kulesh†, **Sebastiaan L. D. ten Haaf**†, Qingzhen Wang, Vincent P. M. Sietses, Yining Zhang, Sebastiaan R. Roelofs, Christian G. Prosko, Di Xiao, Candice Thomas, Michael J. Manfra and Srijit Goswami
Phys. Rev. Lett. 135, 056301 (2025)

13. *Interaction-induced strong zero modes in short quantum dot chains with time-reversal symmetry*
A. Mert Bozkurt, Sebastian Miles, **Sebastiaan L. D. ten Haaf**, Chun-Xiao Liu, Fabian Hassler and Michael Wimmer
SciPost Phys. 18, 206 (2025)

🗎 12. *Observation of edge and bulk states in a three-site Kitaev chain*
Sebastiaan L. D. ten Haaf, Yining Zhang, Qingzhen Wang, Alberto Bordin, Chun-Xiao Liu, Ivan Kulesh, Vincent P. M. Sietses, Christian G. Prosko, Di Xiao, Candice Thomas, Michael J. Manfra, Michael Wimmer and Srijit Goswami
Nature 641, 890-895 (2025)

11. *Enhanced Majorana stability in a three-site Kitaev chain*
    Alberto Bordin†, Chun-Xiao Liu†, Tom Dvir, Francesco Zatelli, **Sebastiaan L. D. ten Haaf**, David van Driel, Guanzhong Wang, Nick van Loo, Yining Zhang, Jan Cornelis Wolff, Thomas van Caekenberghe, Ghada Badawy, Sasa Gazibegovic Erik P. A. M. Bakkers, Chun-Xiao Liu, Ruben Seoane Souto, Nick van Loo and Leo P. Kouwenhoven
    Nature Nanotechnology 20, 726-731 (2025)

10. *Scaling up a sign-ordered Kitaev chain without magnetic flux control*
    Chun-Xiao Liu, Sebastian Miles, Alberto Bordin, **Sebastiaan L. D. ten Haaf**, Grzegorz P. Mazur, A. Mert Bozkurt and Michael Wimmer
    Phys. Rev. Research 7, L012045 (2025)

9. *Enhancing the excitation gap of a quantum-dot-based Kitaev chain*
   Chun-Xiao Liu, A. Mert Bozkurt, Francesco Zatelli, **Sebastiaan L. D. ten Haaf**, Tom Dvir and Michael Wimmer
   Communications Physics 7, 235 (2024)

🗎 8. *A two-site Kitaev chain in a two-dimensional electron gas*
   Sebastiaan L. D. ten Haaf†, Qingzhen Wang†, A. Mert Bozkurt, Chun-Xiao Liu, Ivan Kulesh, Philip Kim, Di Xiao, Candice Thomas, Michael J. Manfra, Tom Dvir, Michael Wimmer and Srijit Goswami
   Nature 630, 329-334 (2024)

7. *Cross-platform autonomous control of minimal Kitaev chains*
   David van Driel, Rouven Koch, Vincent P. M. Sietses, **Sebastiaan L. D. ten Haaf**, Chun-Xiao Liu, Francesco Zatelli, Bart Roovers, Alberto Bordin, Nick van Loo, Guanzhong Wang, Jan Cornelis Wolff, Grzegorz P. Mazur, Tom Dvir, Ivan Kulesh, Qingzhen Wang, A. Mert Bozkurt, Sasa Gazibegovic, Ghada Badawy, Erik P. A. M. Bakkers, Michael Wimmer, Srijit Goswami, Jose L. Lado, Leo P. Kouwenhoven and Eliska Greplova
   arXiv:2405.04596 (2024)

6. *Crossed Andreev reflection and elastic cotunneling in three quantum dots coupled by superconductors*
   Alberto Bordin, Xiang Li, David van Driel, Jan Cornelis Wolff, Qingzhen Wang, **Sebastiaan L. D. ten Haaf**, Guanzhong Wang , Nick van Loo , Leo P. Kouwenhoven and Tom Dvir
   Phys. Rev. Lett. 132, 056602 (2024)

5. *Lipid membranes supported by polydimethylsiloxane substrates with designed geometry*
   Melissa Rinaldin, **Sebastiaan L. D. ten Haaf**, Ernst J. Vegter, Casper van der Wel, Piermarco Fonda, Luca Giomi and Daniela J. Kraft
   Soft Matter 20, 7379-7366 (2024)

🗎 4. *Triplet correlations in Cooper pair splitters realized in a two-dimensional electron gas*
   Qingzhen Wang†, **Sebastiaan L. D. ten Haaf**†, Ivan Kulesh, Di Xiao, Candice Thomas, Michael J. Manfra and Srijit Goswami
   Nature Communications 14, 4876 (2023)

3. *Tunable crossed Andreev reflection and elastic cotunneling in hybrid nanowires*
   Alberto Bordin†, Guanzhong Wang†, Chun-Xiao Liu†, **Sebastiaan L. D. ten Haaf**, Nick van Loo, Grzegorz P. Mazur, Di Xu, David van Driel, Francesco Zatelli, Sasa Gazibegovic, Ghada Badawy, Erik P. A. M. Bakkers, Michael Wimmer, Leo P. Kouwenhoven and Tom Dvir
   Phys. Rev. X 13, 031031 (2023)

2. *Realization of a minimal Kitaev chain in coupled quantum dots*
   Tom Dvir†, Guanzhong Wang†, Nick van Loo†, Chun-Xiao Liu, Grzegorz P. Mazur, Alberto Bordin, **Sebastiaan L. D. ten Haaf**, Ji-Yin Wang, David van Driel, Francesco Zatelli, Xiang Li, Filip K. Malinowski, Sasa Gazibegovic, Ghada Badawy, Erik P. A. M. Bakkers, Michael Wimmer and Leo P. Kouwenhoven
   Nature 614, 445-450 (2023)

1. *Singlet and triplet Cooper pair splitting in hybrid superconducting nanowires*
   Guanzhong Wang†, Tom Dvir†, Grzegorz P. Mazur†, Chun-Xiao Liu, Nick van Loo, **Sebastiaan L. D. ten Haaf**, Alberto Bordin, Sasa Gazibegovic, Ghada Badawy, Erik P. A. M. Bakkers, Michael Wimmer and Leo P. Kouwenhoven
   Nature 612, 448-453 (2022)

PATENTS

1. *Method of creating Majorana bound states in a quantum-dot chain*
   Michael Wimmer, Chun-Xiao Liu, Sebastian Miles, David van Driel, Bart Roover and **Sebastiaan L. D. ten Haaf**
   EP24761258 (originally NL2035759) filed 07-09-2023, received 13-02-2025

The whole world at your fingertips,
the ocean at your door

- Bo Burnham